Titre: Title:	Mechanistic studies of stress corrosion cracking in austenitic stainless steels and in 70Cu-30Zn
Auteur: Author:	Xiaozhu Wu
Date:	1998
Type:	Mémoire ou thèse / Dissertation or Thesis
Référence: Citation:	Wu, X. (1998). Mechanistic studies of stress corrosion cracking in austenitic stainless steels and in 70Cu-30Zn [Ph.D. thesis, École Polytechnique de Montréal]. PolyPublie. https://publications.polymtl.ca/8889/

UNIVERSITÉ DE MONTRÉAL

MECHANISTIC STUDIES OF STRESS CORROSION CRACKING IN AUSTENITIC STAINLESS STEELS AND IN 70CU-30ZN

XIAOZHU WU
DÉPARTEMENT DE GÉNIE PHYSIQUE
ET DE GÉNIE DES MATÉRIAUX
ÉCOLE POLYTECHNIQUE DE MONTRÉAL

THÈSE PRÉSENTÉE EN VUE DE L'OBTENTION
DU DIPLÔME DE PHILOSOPHIAE DOCTOR (Ph.D.)
(GÉNIE MÉTALLURGIQUE)
JUILLET 1998

UNIVERSITÉ DE MONTRÉAL

ÉCOLE POLYTECHNIQUE DE MONTRÉAL

Cette thèse intitulée:

MECHANISTIC STUDIES OF STRESS CORROSION CRACKING IN AUSTENITIC STAINLESS STEELS AND IN 70CU-30ZN

présentée par: WU Xiaozhu

en vue de l'obtention du diplôme de: Philosophiae Doctor

a été dûment acceptée par le jury d'examen constitué de:

M. SAVADOGO Oumarou, D.d'ETAT, président

M. DICKSON J. Ivan, Ph.D., membre et directeur de recherche

M. VERREMAN Yves, Ph.D., membre

M. ZHENG Wenyue, Ph.D., membre

To my parents, Yuda and Liwei

Acknowledgment

I would like to express my sincere appreciation to Professor J. Ivan Dickson, my thesis supervisor, for his guidance and constant encouragement throughout this research. Without his understanding and support, I would not have successfully completed my Ph.D. study. I also appreciate many helpful comments he made to improve this manuscript.

I was grateful to Ms. Li Shiqiong, a good friend of mine despite our differences in age, for her valuable suggestions and helpfulness in SCC tests. I benefited a lot from the discussions with her in my early stage study.

Thanks also go to Eric Boutin in the laboratory of $(CM)^2$ in Ecole Polytechnique and Jian Li in Queen's University, who performed respectively texture measurements and EBSPs analysis in δ–ferrite which were important for this study.

During the course of my Ph.D. study, personnel and friends in Département de Métallurgie et de Génie des Matériaux gave me enthusiastic support. I would like to repeat my acknowledgment for the help I received from many of them. I especially wish to thank André Désilets, Carole Massicotte, René Veillette, Josée Laviolette and Jacques Desrochers for their assistance in experiments and their help in the preparation of this thesis.

Finally, I would like to thank Lhoucine Azzi and Richard Chambon, for their great helps in preparing the French version of the extended abstract.

Résumé

Cette thèse met l'accent sur l'analyse des aspects fractographiques de la corrosion sur contrainte (CSC) en fonction des variables mécaniques et microstructurales, dans le but d'avoir une meilleure compréhension des mécanismes qui se produisent en CSC. Des échantillons d'aciers inoxydables (316L et 310) et 70Cu-30Zn ont été soumis à des tests de CSC dans une solution aqueuse de $MgCl_2$ à 154°C et dans des solutions d'amoniaques à 23°C respectivement. Les espèces critiques nécessaires à la fissuration présentes dans l'environnement de ces deux systèmes ont été identifiées. Le comportement en CSC de la ferrite–δ, contenue dans l'acier inoxydable austénitique 316L, et celui du 70Cu-30Zn dans des conditions de recuit et après laminage à froid ont été étudiés. Finalement, les processus de croissance, d'arrêt et de réinitiation ont été analysés au cours de la CSC de l'acier inoxydable 310 et du 70Cu-30Zn.

Une série d'essais de traction dans l'air, sur des échantillons d'aciers inoxydables 316L et 310 préfissurés en CSC partielle, a été réalisée à différentes vitesses de déplacement et après différents intervalles de temps entre les essais de traction post-CSC (PCSC) et les essais de CSC. Il a été montré que l'hydrogène absorbé au cours d'essais antérieurs est responsable de la rupture cristallographique en traction. Pour l'acier inoxydable 316L, la fissuration cristallographique dans la ferrite–δ s'est produite à une certaine distance du fond de fissure de CSC. Cette apparence au type clivage est très semblable à la fissuration cristallographique produite par l'hydrogène dans la ferrite. Mais dans l'austénite, la fissuration cristallographique s'est produite seulement en fond de fissure de CSC, ou dans une région entourant les palettes de ferrite–δ. La fissuration *cristallographique* dans l'acier inoxydable 310 complètement

austénitique est moins cristallographique, et est présente dans des régions isolées en avant du fond de fissure de CSC. La plupart de ces régions sont sur des plans à 45° de la contrainte de traction et près d'inhomogénéité de composition. L'étendue des zones de fissuration cristallographique PCSC augmente dans l'acier inoxydable 316L avec l'augmentation du facteur d'intersité de contrainte K et celle de l'intervalle de temps entre les essais de traction PCSC et de CSC, ainsi qu'avec la diminution des vitesses de déplacement en traction. Les zones de la fissuration cristallographique PCSC dans l'acier inoxydable 310 ont presque les mêmes dimensions dans toutes les conditions d'essais. Mais elles sont plus petites que celles de l'acier inoxydable 316L, parce que la présence de ferrite–δ augmente leurs dimensions.

La participation de l'hydrogène à la CSC des aciers inoxydables dans la solution de $MgCl_2$ a été montrée par la fractographie similaire dans l'austénite produite pendant la CSC et la PCSC, la fractographie similaire dans rubans de 316 chargés par l'hydrogène et immergés dans la solution de $MgCl_2$, et les variations similaires des propriétés dans ces rubans.

La fissuration en CSC de la ferrite–δ dans les échantillons d'orientation ST d'acier inoxydable 316L présente une rupture transgranulaire dans la ferrite–δ et interfaciale entre la ferrite–δ et l'austénite. Beaucoup de lignes du glissement formant comme des ondes sont présentes sur le côté de la ferrite–δ aux interfaces, elles correspondent au chemin de rupture transgranulaire. Les lignes d'arrêt de la fissuration, avec la même orientation que ces lignes de glissement ont été trouvées sur le côté de la ferrite–δ aux interfaces. Ceci indique que les lignes de glissement en forme d'ondes et les lignes d'arrêt correspondent momentanément à des fonds de fissuration pendant la propagation interfacielle en CSC. La propagation interfacielle est discontinue. La participation de l'hydrogène absorbé dans la CSC a aussi été démontrée par l'initiation en avant du fond de fissure aux interfaces δ–γ. Les aspects fractographiques de la rupture en CSC et de la fissuration cristallographique PCSC dans la ferrite–δ sont différents. Mais ces différences pouvent être expliquées par l'interaction de l'hydrogène et des dislocations vis dans la ferrite–δ et par la distribution de l'hydrogène près

des l'interfaces δ–γ. Le mouvement des dislocations vis est augmenté par l'hydrogène produit par les réactions de CSC.

Des mesures photogrammétriques sur les surfaces de rupture sont utilisées pour déterminer la cristallographie de la CSC et la PCSC transgranulaire dans la ferrite–δ. La texture de la ferrite–δ et les lignes de Kikuchi en électrons rétrodiffusées (EBSPs) obtenues dans les régions de PCSC de la ferrite–δ ont aussi été analysées pour obtenir des informations cristallographiques complémentaires. Les plans moyens de fissuration en CSC sont {110} avec des directions de propagation microscopique <110> dans la ferrite–δ. Les microfacettes, les composantes des plans moyens de fissuration et des stries sur les lignes du rivières, sont aussi les plans de glissement {110} et {112}. La cristallographie de PCSC a été déterminée par les plans et les directions {100}<100>, {100}<110> et {100}<210>. Comparées au clivage produit à basse température, les deux orientations microfacettes qui s'emboîtent et qui constituent les microfacettes {100} devraient être aussi des plans de glissement.

Les échantillons préfissurés de 70Cu-30Zn ont été testés dans une solution d'ammoniaque désoxygénée qui contient peu d'ions Cu^{2+}. Les essais ont montré que les ions Cu^{2+} aussi bien que l'oxygène sont les espèces critiques pour la propagation dans ce système. Les essais de CSC dans une solution d'ammoniaque contenant de l'oxygène et ne produisant pas de ternis montrent l'influence de la microstructure et du facteur d'intensité de contrainte K au fond de fissure sur les modes de fissuration dans le laiton 70Cu-30Zn. Des fissurations intergranulaire et transgranulaire sont observées dans les échantillons recuits. La fissuration intergranulaire a lieu dans les régions où K est faible, mais la fissuration transgranulaire a lieu dans les régions où K est élevé. La fissuration intergranulaire est aussi favorisée dans les régions près de la surface latérale où la concentration d'oxygène est plus grande. Une prédéformation importante cause un pourcentage très important de fissuration transgranulaire et change la fissuration intergranulaire en une fissuration quasi-intergranulaire.

L'augmentation de K au fond de fissure n'influence apparemment pas le mode de fissuration dans les éprouvettes laminées à froid.

Pour mesurer la relation entre la vitesse de propagation en CSC et le facteur d'intensité de contrainte K, une méthode mécanique a été développée en mesurant la complaisance sur des éprouvettes standard CT pendant les essais de CSC. La vitesse de propagation a tendance à augmenter avec l'augmentation de K pour les éprouvettes à l'état recuit. Pour les échantillons laminés à froid, le plateau où la vitesse de propagation est indépendante de K est plus visible. Ceci est en accord avec les observations fractographiques qui ont montré que la propagation de CSC dépend de la configuration des dislocations au fond de fissure. Que la fracture soit intergranulaire ou transgranulaire dépend essentiellement des dislocations en fond de fissure, qui ont été produites soit par la contrainte appliquée soit par le laminage à froid.

Le processus de propagation par CSC a été étudié en imposant une contrainte périodique de petite amplitude à la contrainte constante, afin de marquer le fond de fissure de CSC sur les éprouvettes d'acier inoxydable 310 et de 70Cu-30Zn. Dans le laiton, l'addition d'une contrainte périodique provoque souvent une transition du mode de fissuration. Ces transitions de fissuration intergranulaire à quasi-intergranulaire et à transgranulaire ont suivi les orientations cristallographiques sur les joints de grains ou près des joints de grains. Le fond de fissure intergranulaire, indiqué sur les joints de grains par les traces des surcharges, montre que dans certaines régions il coincide avec les traces de glissement sur les joints de grains. Ceci suggère que la propagation en CSC intergranulaire, comme la CSC transgranulaire, est aussi associée à du glissement localisé.

Une étude fractographique détaillée des traces en fond de fissure produites par les légères surcharges confirme l'existence d'un fond de fissure cristallographique en CSC transgranulaire de l'acier inoxydable 310 et du 70Cu-30Zn. Les sites de reinitiation observés,

après l'addition d'une contrainte périodique, sont tous au fond de fissure dans le laiton, mais parfois jusqu'à approximativement 1 μm en avant du fond de fissure dans l'acier inoxydable 310. La propagation partant d'un site un peu en avant du fond de fissure et allant vers le fond de fissure n'est pas observée dans les deux matériaux. Les marques d'arrêt qui se produisent spontanément pendant la propagation en CSC ont seulement été trouvées quelques fois dans des ramifications des fissures dans la présente étude. Ceci indique qu'elles ne sont pas représentatives de la propagation en CSC.

Les interactions environnement-dislocations et leurs effets sur la rupture par CSC sont discutés. L'absorption d'hydrogène dans le système acier inoxydable / solution aqueuse de $MgCl_2$ et l'adsorption d'une espèce d'ions, possiblement Cu^{2+}, dans le système laiton / ammoniac jouent un rôle très important sur la rupture en CSC. La rupture macroscopique fragile est produite par un processus de glissement local en fond de fissure, bien que les interactions environnement-dislocations soient différentes dans les deux systèmes. L'environnement favorise les mouvements de dislocations en fond de fissure et provoque un empilement des dislocations sur les plans de glissement localisé. Combiné à une possible réduction de force de cohésion provoquée par l'environnement, les empilements de dislocations conduisent à une décohésion sur les plans de glissement à cause de leur propre champ de contrainte, et à une décohésion sur des plans intersectant les plans de glissement à cause du champ de contrainte élastique induit par les empilements.

Abstract

This thesis focuses on the fractographic aspects of stress corrosion cracking (SCC) as a function of microstructural and mechanical variables to provide a better understanding of SCC mechanisms. Stainless steels (316L and 310) and 70Cu-30Zn underwent SCC tests in a $MgCl_2$ aqueous solution at 154°C and in concentrated ammonia solutions at room temperature respectively. The critical environmental species involved in these two systems were identified. Then the SCC behavior of the bcc δ–ferrite containing in 316L austenitic stainless steel and of 70Cu-30Zn in annealed and cold-worked conditions was studied. Finally, the growth, arrest and reinitiation processes were analyzed during the SCC of 310 stainless steel and 70Cu-30Zn.

A series of tensile tests in air on specimens of 316L and 310 stainless steels partially cracked by SCC were carried out at different displacement rates and different time intervals between SCC tests and the post-SCC (PSCC) tensile tests. Absorbed hydrogen from previous SCC tests was shown to be involved in the tensile fracture by the presence of crystallographic cracking. In 316L stainless steel, the PSCC crystallographic cracking appeared both in the δ–ferrite and in the austenite (γ), at the SCC crack tips and ahead of SCC crack tips. The crystallographic cracking occurred in the δ–ferrite within a certain distance from the previous SCC crack tip. Its cleavage-like appearance is very similar to the crystallographic cracking produced by hydrogen. But in the austenite, the PSCC crystallographic cracking only occurred at the previous SCC crack tip or in the areas surrounding the crystallographically fractured δ–ferrite platelets. The PSCC cracking in completely austenitic 310 stainless steel was less crystallographic. It appeared in isolated regions, most of which were on the plane approximately 45° to the tensile

stress and near composition inhomogeneities. The size of the PSCC crystallographic cracking in 316L stainless steel tended to increase with increasing K, with increasing time interval between the SCC tests and the PSCC tensile fracture at least up to three months, and with decreasing tensile displacement rate. The size of the PSCC crystallographic cracking in 310 stainless steel was approximately the same for all the test conditions, but was generally smaller than the size in 316L stainless steel. The presence of δ–ferrite phase increased the size of PSCC crystallographic cracking zone.

The involvement of hydrogen in SCC of stainless steels in boiling $MgCl_2$ solution is rationalized by the similar fractography of austenite fractured in SCC and in PSCC crystallographic cracking, by the similar fractography of 316 stainless steel ribbons cracked during hydrogen charging and during immersion in the $MgCl_2$ solution, as well as by the similar tendency of tensile property changes in those ribbons.

The SCC cracking of the δ–ferrite phase in ST orientated specimens of 316L stainless steel presented interfacial fracture along the δ-γ interfaces and transgranular fracture within the δ–ferrite. Many wavy slip traces appeared on the δ–ferrite side of the interfacial boundaries and corresponded to the path of the transgranular fracture in the δ–ferrite. Crack arrest lines, which had a similar trend to the wavy slip traces were also found on the δ–ferrite side of the interfacial boundaries. This indicates that both wavy slip traces and crack arrest lines are the instant crack fronts during SCC propagation. The interfacial SCC propagation is discontinuous. The absorbed hydrogen involved in SCC was also demonstrated by the crack initiation ahead of the macroscopic crack front at δ-γ interfaces. The fractographic features of SCC and PSCC crystallographic cracking in the δ–ferrite were different. However, these difference can be explained by the hydrogen-screw dislocation interaction in the δ phase, as well as by the hydrogen distribution near δ-γ interfaces. The activity of screw dislocations in the δ–ferrite is enhanced by the hydrogen produced from the SCC reactions.

Photogrammetric analysis on the fracture surfaces was employed to determine the crystallography of transgranular SCC and PSCC in δ–ferrite, with complementary information provided by the measurement of the texture tendency in the δ–ferrite and by the electron back scattered patterns (EBSPs) obtained from the PSCC regions. The average cracking planes of SCC was {110} with the microscopic propagation directions of <110> and <111> in the δ-ferrite. The microfacets composed of the average cracking planes and the serrations on the river lines were determined as {110} and {112} slip planes. The crystallography of PSCC in δ-ferrite was determined as {100}<100>, {100}<110> and (100}<210>, but the {100} planes were made up of many interlocked microfacets which should correspond to slip planes.

Precracked 70Cu-30Zn specimens were tested in a deoxygenated ammonia solution in which the cupric ion concentration was very low. This test determined that cupric complex ions or equivalently oxygen is a critical species for the apparent SCC crack propagation in this system. By performing SCC tests in an oxygenated, non-tarnishing ammonia solution, the influence of microstructural variation and of the crack tip K on the cracking patterns of SCC in 70Cu-30Zn was examined. The SCC of 70Cu-30Zn in the annealed condition showed both intergranular and transgranular fracture. The intergranular fracture tended to occur in lower K regions, while the transgranular fracture tended to occur in higher K regions. The intergranular fracture was also favored in the near surface regions where the concentration of dissolved oxygen was higher. In the cold-worked condition, the amount of deformation prior to the SCC tests influenced the fracture patterns. Heavy cold work greatly increased the amount of transgranular fracture and changed intergranular fracture to quasi-intergranular fracture. But the increase of crack tip K had much less influence on the cracking features in heavily cold-worked materials.

In order to measure the relationship between the SCC crack propagation velocity and the crack tip K, a fracture mechanics technique was developed by using the

compliance measurement method on standard CT specimens during constant load SCC tests. The crack propagation velocity appeared to increase with increasing K in the annealed condition, while the plateau region where the crack propagation velocity is independent of K was more clear in the cold worked condition. This is consistent with the fractographic observations in that the SCC propagation is closely associated with the dislocation configurations at the crack tip. The occurrence of intergranular or transgranular fracture is essentially determined by the crack tip dislocations, either produced by the applied stress or by previous cold work.

The SCC propagation process was studied by imposing small periodic load pulses on the essential constant applied load to mark the SCC crack front of 310 stainless steel and of annealed 70Cu-30Zn. The load pulses often induced cracking pattern transitions in 70Cu-30Zn. Transitions from intergranular fracture to quasi-intergranular fracture and to transgranular fracture occurred along the crystallographic orientations on the grain boundaries or in the vicinity of these boundaries. The intergranular crack front, indicated by the load pulse traces on grain boundaries, showed that in some regions the intergranular crack front locally coincided with slip traces on the grain boundaries. This suggests that intergranular SCC propagation, similar to transgranular SCC, is associated with localized slip.

The detailed fractographic study of crack front markings produced by small load pulses confirmed the presence of a crystallographic crack front in transgranular SCC fracture of 310 stainless steel and of 70Cu-30Zn. The reinitiation sites observed were all at the SCC crack tip in 70Cu-30Zn, but were occasionally up to approximately 1 μm away from the crack tip in 310 stainless steel. No reverse propagation was found in both materials at crack reinitiation sites. The crack arrest markings which spontaneously occurred during SCC propagation were only found in crack branches in the present study. This

indicates that they are not a general phenomenon during SCC propagation under constant load.

The environment-dislocation interactions and their effects on the SCC fracture is discussed. The absorption of hydrogen in stainless steels / $MgCl_2$ system and the adsorption of cupric complex ions in the 70Cu-30Zn / ammonia system play very important roles on the SCC fracture. Although the environment-dislocation interactions are specific in each material / environment system, the macroscopically brittle SCC fracture is produced by the localized slip process at the crack tip. The environment enhances dislocation activity at the SCC crack tip which results in dislocation pileups on localized slip planes. Combined with the possible bond strength reduction induced by the environmental effect, the dislocation pileups lead to slip plane decohesion on the pileup plane by their core stress field and decohesion on the intersected slip planes by the elastic stress field of this pileup.

Condensé en français

Cette thèse met l'accent sur l'analyse des aspects fractographiques de la corrosion sur contrainte (CSC) en fonction des variables mécaniques et microstructurales, dans le but d'obtenir une meilleure compréhension des mécanismes de fissuration qui se produisent en CSC. Des éprouvettes d'aciers inoxydables austénitiques (316L et 310) ont été soumises à des essais de CSC dans une solution aqueuse de $MgCl_2$ à 154°C et des éprouvettes de laiton 70Cu-30Zn ont été soumises à des essais de CSC dans des solutions d'ammoniaque à 23°C. Les espèces critiques pour produire cette fissuration, présentes dans l'environnement de ces deux systèmes, ont été identifiées. Les comportements en CSC de ces matériaux ont été étudiés, incluant le comportement de la ferrite–δ, contenue dans l'acier inoxydable austénitique 316L. Pour le 70Cu-30Zn, le comportement du matériau recuit à été comparé à celui du matériau écroui à froid par laminage. Finalement, les phénomènes de croissance, d'arrêt et de réinitiation de la fissure ont été analysés au cours de la CSC de l'acier inoxydable austénitique 310 et du 70Cu-30Zn.

Une série d'essais de traction dans l'air, sur des éprouvettes d'aciers inoxydables 316L et 310 préfissurés en CSC, ont été réalisés à différents taux de déplacement et après différents intervalles de temps après la CSC. Ces essais ont souvent montré une fissuration cristallographique post-corrosion sous contrainte (PCSC), par la présence de rupture cristallographique au fond de la fissure de CSC et en avant de ce fond de fissure. Il a été montré que l'hydrogène absorbé au cours d'essais antérieurs est en partie responsable de la rupture en traction. Pour l'acier inoxydable 316L, de la fissuration cristallographique PCSC dans la ferrite–δ s'est souvent produite à une petite distance du fond de fissure de CSC. Mais dans l'austénite, la fissuration cristallographique s'est produite seulement au fond de la fissure de CSC ou dans des régions entourant les palettes fissurées de ferrite–δ. Pour

l'acier inoxydable 310, qui est complètement austénitique, une fissuration cristallographique était parfois présente dans des régions isolées en avant du fond de fissure de CSC. La plupart de ces régions étaient sur des plans à 45° de la contrainte de traction et étaient situés près d'inhomogénéités de composition. Parfois un court essai de fatigue a également été réalisé après un essai de CSC afin de marquer le fond de fissure de CSC. Une fissuration cristallographique PCSC s'est également produite en avant du fond de cette fissure de fatigue.

Les détails fractographiques de la rupture PCSC ont été étudiés par microscopie électronique à balayage, en employant des observations stéréofractographiques. Dans l'acier inoxydable 316L, les zones de fissuration cristallographique PCSC dans la ferrite–δ sont perpendiculaires à l'axe de traction. Des microfacettes sont présentes sur les facettes moyennes et généralement s'emboîtent bien sur deux surfaces de rupture correspondantes. Cette apparence est très semblable à la fissuration cristallographique produite par l'hydrogène dans la ferrite. Les microfacettes produites par la fissuration cristallographique PCSC de l'austénite sont plus petites et plus déformées que celles produites en CSC. Autrement, les deux ruptures ont des caractéristiques de fissuration très similaires. La fissuration PCSC dans l'acier inoxydable 310 souvent n'est pas très typique d'une fissuration cristallographique. Les microfacettes sont accompagnées par de la déformation plastique ou sont liées par des microvides. Quelques régions de PCSC d'apparence cristallographique à faible grossissement présentent des microvides qui sont plus petites que les cupules voisines. Ces variations microfractographiques ont résulté des différentes concentrations locales d'hydrogène dans la région en avant du fond de fissure. L'aspect cristallographique est d'autant plus prononcé que la concentration d'hydrogène est importante. Des caractéristiques ressemblant au clivage dans la ferrite–δ sont dues à la sensibilité de cette phase cubique centrée à fissurer en présence d'hydrogène. La présence de ferrite–δ augmente aussi la concentration d'hydrogène dans l'austénite voisine. La fissuration cristallographique est donc souvent apparue dans des régions austénitiques bordant la ferrite–δ. Dans l'acier inoxydable 310 qui est complètement austénitique, la

concentration locale d'hydrogène requise pour la fissuration cristallographique a été obtenue par les interactions entre les dislocations et l'hydrogène. Donc, la fissuration cristallographique PCSC est apparue dans les régions avec de nombreuses dislocations activées, tel que les plans de cisaillement maximum et aussi près d'inhomogénéités de composition.

L'étendu des zones de fissuration cristallographique PCSC augmente dans l'acier inoxydable 316L avec l'augmentation du facteur d'intensité de contrainte K et de l'intervalle de temps (jusqu'à 3 mois) entre les essais de traction PCSC et de CSC, ainsi qu'avec la diminution des taux de déplacement en traction. Les mouvements de dislocations transportent l'hydrogène le long de plans de glissement, permettant une fissuration cristallographique dans des régions en avant du fond de fissuration de CSC. Dans le cas où la fissure de CSC aurait été ouverte directement dans la solution aqueuse de $MgCl_2$ sous une vitesse de déplacement rapide dès la fin de l'essai de CSC, une rupture ductile aurait été obtenue en avant de la fissure de CSC. En effet, l'hydrogène n'aurait pas pu diffuser assez vite pour pouvoir suivre le mouvement des dislocations et ainsi permettre une fragilisation. Les zones de la fissuration cristallographique PCSC dans l'acier inoxydable 310 ont presque les mêmes dimensions pour toutes les conditions d'essais. Mais elles sont plus petites que celles dans l'acier inoxydable 316L, parce que la présence de la ferrite–δ, qui est plus sensible à l'hydrogène augmente ces dimensions dans ce dernier acier.

Des essais de traction sur des rubans minces d'acier inoxydable 316 ont été réalisés pour des conditions où les rubans étaient polarisés cathodiquement ou étaient immergés dans une solution aqueuse de $MgCl_2$ à 154°C. Les changements de propriétés en traction de ces rubans, particulièrement l'allongement à la rupture, avaient tendance à être similaire à ceux polarisés cathodiquement dans une solution de H_2SO_4. L'allongement augmente avec une augmentation de l'intervalle de temps entre le chargement et l'essai de traction dans l'air. Le recuit avant que les rubans viennent en contact avec la solution de $MgCl_2$ a aussi

augmenté l'allongement, mais une prédéformation diminue l'allongement. Ce résultat indique que l'hydrogène est produit évolué dans la solution de $MgCl_2$ aux piqûres des corrosions ou dans une fissure de CSC au potentiel de corrosion libre. Une grande densité de dislocation augmente l'influence de l'hydrogène qui favorise une rupture plus cristallographique.

Les aspects fractographiques changent graduellement avec la concentration d'hydrogène dans les rubans fissurés en traction. Des grandes facettes cristallographiques ou de la fissuration intergranulaire sont obtenues dans les régions près des surfaces latérales de rubans qui sont polarisés cathodiquement dans la solution de $MgCl_2$. A ces endroits, la concentration d'hydrogène est plus élevée. Des petites facettes cristallographiques déformées sont produites à cause d'une concentration d'hydrogène moins élevée dans les régions voisines des surfaces des rubans polarisés cathodiquement, et aussi dans les régions entre la CSC et la rupture ductile dans les rubans qui étaient immergés dans la solution de $MgCl_2$. Ces petites facettes déformées sont semblables à celles obtenues dans la rupture cristallographique PCSC de l'austénite dans l'acier inoxydable 316L. Les lignes de glissement sur les grandes facettes indiquent que ces facettes sont des plans de glissement {111}. Les aspects fractographiques similaires et la même cristallographie de fissuration obtenue dans les rubans qui sont chargés par l'hydrogène et qui sont immergés dans la solution de $MgCl_2$ confirme que l'hydrogène participe à la CSC de l'acier inoxydable dans la solution de $MgCl_2$. De plus, les observations suggèrent que l'interaction hydrogène-dislocation soit essentiel pour la CSC et pour la rupture provoquée par l'hydrogène.

Donc, la participation de l'hydrogène à la CSC des aciers inoxydables dans la solution de $MgCl_2$ a été démontrée par la fractographie similaire de l'austénite produite lors de la CSC et de la PCSC, par la fractographie similaire dans des rubans d'acier inoxydable 316 chargés par l'hydrogène et immergés dans la solution de $MgCl_2$ et par les variations similaires des propriétés mécaniques dans ces rubans.

Les observations fractographiques sur la ferrite–δ dans l'acier inoxydable 316L ont montré que les ruptures de CSC associées à cette phase sont parfois transgranulaires et parfois le long des interfaces entre la ferrite–δ et l'austénite. Les lignes ondulées de glissement, présentes sur le côté de la ferrite–δ de ces interfaces, correspondent parfois au chemin de rupture transgranulaire dans cette ferrite. Les facettes primaires lors de la rupture transgranulaire sont souvent inclinées approximativement à 45° par rapport à l'axe de traction et forment des pics et des vallées réguliers. Les stries perpendiculaires aux lignes de rivières sont généralement absentes, mais il y a beaucoup de lignes de rivières microscopiques qui sont parallèles aux lignes de rivières macroscopiques. Beaucoup de lignes d'arrêt de fissuration, avec la même orientation que les lignes onduleuses de glissement ont été trouvées sur le côté de la ferrite–δ dans les régions de fissuration interfacielle. Ceci indique que ces lignes onduleuses de glissement et ces lignes d'arrêt correspondent momentanément à des fronts de fissuration pendant la propagation en CSC interfacielle. La propagation interfacielle est donc discontinue. La participation de l'hydrogène absorbé dans la CSC a aussi été montrée par l'initiation de la fissuration interfacielle en avant du fond de la fissure précédente.

Les aspects fractographiques de la rupture en CSC et de la fissuration cristallographique PCSC dans la ferrite–δ sont différents. Mais ces différences peuvent être expliquées par l'interaction de l'hydrogène et des dislocations vis dans la ferrite–δ et par la distribution de l'hydrogène près des interfaces δ–γ. Le mouvement des dislocations vis dans la ferrite–δ est augmenté par l'hydrogène absorbé lors de la CSC.

Des mesures photogrammétriques sur des surfaces de rupture ont été employées pour déterminer la cristallographie de la CSC et de la PCSC transgranularie dans la ferrite–δ. La texture de la ferrite–δ et les lignes de Kikuchi en électrons retrodiffusées (EBSPs) obtenu dans les régions de PCSC de la ferrite–δ ont aussi été analysées pour obtenir d'informations cristallographiques complémentaires. Les plans moyens de

fissuration dans la ferrite–δ en CSC sont {110} avec des directions de propagation microscopique <110> et <111>. Les microfacettes sont aussi sur des plans de glissement {110} et {112}. La cristallographie de la fissuration PCSC dans la ferrite–δ a été déterminée comme étant {100}<100>, {100}<110> et {100}<210>. En contraste au clivage produit à basse température, ces plans {100} sont constitués par des séries de microfacettes en alternance qui s'emboîtent sur les surfaces de rupture opposées. Les résultats indiquent que ces microfacettes devraient correspondre à des plans de glissement.

Les échantillons préfissurés de 70Cu-30Zn ont été testés dans une solution d'ammoniaque deoxygené qui contient peu d'ions Cu^{2+}. Aucune propagation n'a été observée après des centaines d'heures. Les essais ont montré que les ions Cu^{2+} aussi bien que l'oxygène sont les espèces critiques pour la propagation apparente dans ce système. Les essais de CSC dans une solution d'ammoniaque contenant de l'oxygène et ne produisant pas de ternis montrent l'influence de la microstructure et du facteur d'intensité de contrainte K au fond de fissure sur les modes de fissuration dans le laiton 70Cu-30Zn. De la fissuration intergranulaire et transgranulaire sont observées dans les échantillons recuits. La fissuration intergranulaire a lieu dans les régions où K est faible, et la fissuration transgranulaire a lieu dans les régions où K est élevé. La fissuration intergranulaire est aussi favorisée dans les régions près de la surface latérale où la présence d'oxygène est abondante. Dans les éprouvettes laminées à froid, le montant de déformation avant les essais de CSC influence le mode de fissuration. Une prédéformation importante cause un pourcentage très important de fissuration transgranulaire et change la fissuration intergranulaire en une fissuration quasi-intergranulaire. L'augmentation de K au fond de fissure n'influence apparemment pas le mode de fissuration dans les éprouvettes laminées à froid. Ceci indique que les modes de fissuration sont fortement influencées par les dislocations en fond de fissure, produites par la contrainte appliquée lors des essais de CSC ou par le laminage à froid avant ces essais.

Pour mesurer la relation entre de vitesse de propagation en CSC et le facteur d'intensité de contrainte K, une méthode mécanique a été développée en mesurant la complaisance sur des éprouvettes normalisées CT pendant les essais de CSC. La vitesse de propagation a tendance à augmenter avec l'augmentation de K pour les éprouvettes à l'état recuit. Pour les échantillons laminés à froid, le plateau où la vitesse de propagation est indépendante de K est plus visible. Ceci est en accord avec les observations fractographiques qui ont montré que la propagation en CSC dépend de la configuration des dislocations au fond de fissure. Dans le laiton recuit avec peu de dislocations, le montant de dislocations nécessaire pour la propagation devrait être fourni par la contrainte appliquée. Un K élevé produit plus de dislocations qui provoquent une propagation plus rapide. Pour le laiton laminé à froid, la densité de dislocations au fond de fissure ne dépend que peu d'une petite augmentation de contrainte, particulièrement lorsque K est faible.

Le processus de propagation par CSC a été étudié en imposant une contrainte périodique de petite amplitude à la contrainte constante, afin de marquer le fond de fissure de CSC sur les éprouvettes d'acier inoxydable 310 et de 70Cu-30Zn. L'étude fractographique montre que les fronts de fissuration transgranulaire sont parallèles aux stries qui sont les intersections des plans de glissement {111} dans ces deux matériaux. Donc la propagation transgranulaire devrait se faire en suivant ces plans de glissement. Dans le laiton, l'addition d'une contrainte périodique provoque souvent une transition du mode de fissuration. Ces transitions de fissuration intergranulaire à quasi-intergranulaire et à transgranulaire suivent les orientations cristallographiques sur les joints de grains ou près des joints de grains. Des fronts de fissuration cristallographique sont aussi parfois trouvés sur des joints de grains, et ces lignes sont parallèles au moins localement aux lignes de glissement présentes sur ces joints. Ceci indique que la fissuration intergranulaire par CSC suit des plans de glissement très près du joint de grain. Les sites de reinitiation observés, après l'addition d'une contrainte périodique, sont tous au fond de fissure dans le laiton, mais parfois un peu en avant du fond de fissure dans l'acier inoxydable 310. La propagation partant d'un site un peu en avant du fond de fissure et allant vers le fond de

fissure n'a jamais été observé dans ces deux matériaux. Les marques d'arrêt qui se produisent spontanément pendant la propagation en CSC ont seulement été trouvées quelques fois dans les ramifications des fissures à K élevé. Donc, ces marques d'arrêt de fissures sont provoquées seulement par une grande déformation plastique en fond de fissure et ne sont pas représentatives de la propagation en CSC.

Les interactions environment-dislocations et leurs effets sur la rupture par CSC sont discutés. L'absorption d'hydrogène dans le système acier inoxydable / solution aqueuse de $MgCl_2$ et l'adsorption d'une espèce d'ions, possiblement Cu^{2+}, dans le système laiton / ammoniac jouent un rôle très important sur la rupture en CSC. Les espèces adsorbées et absorbées peuvent faciliter les mouvements de dislocations en fond de fissure et réduire la force de cohésion sur les plans de glissement. La rupture qui macroscopiquement à une apparence fragile est produite par un processus de glissement local en fond de fissure, bien que les interactions environment-dislocations soient différentes dans les deux systèmes. L'environnement localise les mouvements de dislocations en fond de fissure et provoque un empilement des dislocations sur les plans de glissement localisé. Le champ de contrainte au cœur de l'empilement des dislocations produit une contrainte normale sur le plan d'empilement. Combiné à la réduction de force de cohésion provoquée par l'environnement, cette contrainte normale peut provoquer la décohésion du plan de glissement. Dans le même temps, le champ élastique dû à l'empilement des dislocations provoque une contrainte normale sur un plan intersectant à approximativement 70° le plan de d'empilement. Ceci provoque la décohésion sur ce plan, qui est un autre plan de glissement {111} dans les métaux cubiques faces centrées. La décohésion répétée sur ces deux plans de glissement produit une fissuration en CSC qui alterne entre ces deux plans de glissement {111}.

Table of Contents

List of Figures

List of Tables

Introduction

Despite intensive mechanistic studies during the last half-century, the fundamental process of stress corrosion cracking (SCC) still remains of significant engineering concern to prevent its occurrence and of academic interest due to its complexity. Because SCC occurs in a corrosive environment in which general corrosion is usually suppressed, that is, the ratio of visibly corroded areas to passivated areas is very small on the surface, it is generally agreed that SCC is initiated by the break-up of the surface film, which may be a passive film, a dealloyed spongy layer or any kind of film produced by the environment-surface interactions. However, there is no consensus on how the resulting crack propagates into the material. Since the fractography of cleavage-like transgranular SCC in fcc materials was widely investigated by electron microscopy in 1970s, many mechanisms have been proposed to interpret the observed cracking aspects. Most of these mechanisms, regardless of the microscopic processes they are based on, such as dissolution, adsorption, surface film fracture, hydrogen-induced cracking or hydrogen-induced dislocation activity at the crack tip, interpret the fracture surfaces as cleavage occurring on {100} or {110} planes.

However, in inert environment cleavage rarely occurs in fcc metals even at low temperatures. In a few cases [1] that real cleavage was observed in austenitic stainless steels at low temperatures, it often occurred on {111} slip planes. Such {111} slip planes have also been demonstrated [2-5], first by the detailed SCC crystallography study carried out in Ecole Polytechnique, to be the microscopic SCC cracking planes in fcc metals. The {100} and {110} cracking facets, considered as the cleavage planes in fcc metals, are generally composed of different alternating {111} slip systems. This evidence indicates that cleavage-based SCC mechanisms should be reconsidered.

The dislocation density was found to be much higher in regions in contact with aqueous SCC environments [6,7], and it has been proposed [8] that a critical dislocation density is required for SCC. TEM observations made near the SCC fracture surfaces revealed [9,10] that, besides their high density, dislocations tended to arrange themselves in a coplanar manner. This phenomenon was observed even in copper, a metal with a high stacking fault energy, and is in sharp contrast with the behavior in inert environment where a dislocation free zone exists directly at the crack tip [11-13]. Obviously, the environment plays a role in determining the dislocation configurations. A question therefore arises as to how the damaging species changes the dislocation arrangement and does this in turn influence the fracture appearance? There is evidence that dislocations are activated by certain environments. The most unambiguous reports are the *in situ* TEM dislocation observations in hydrogen environment [14-17]. In SCC of non-ferrous metals where the hydrogen effect is often precluded, the evidence is rather indirect and the damaging species are often not very clear. Mechanistic connection between the environmental effects on dislocation behaviour, slip localization and SCC is not well established.

Another ambiguous aspect concerning SCC crack propagation is its discontinuous character. The discontinuity was indicated by acoustic emission [18,19], transient current [20] and fractographic analysis [18,21-23]. It was observed mostly in tests involved high

plastic deformation at the crack tip. In SCC tests carried out under the yield strength or without imposed plastic deformation, the crack arrest markings were generally absent [6,24]. This indicates the possibility that the testing technique may induce artifacts during crack propagation.

Various mechanistic interpretations reflect the complexity of SCC problems and the specificity of each material / environment system. In order to avoid the ambiguity and address the fundamentals, further assessment of individual systems is necessary to determine the critical environmental species influencing cracking. Because of the uncertainty and the difficulty of direct observations of dislocation propagation relationships, it is worthwhile to exam intergranular propagation and the propagation in bcc metals, which will help shed light on the generality of the propagation mechanism. It is also useful to determine whether the propagation discontinuities exist as an integral part of the propagation mechanism.

Therefore, the first objective of this thesis work was to identify the specific environmental species involved in two SCC systems, namely austenitic stainless steels in chloride solution and a fcc 70Cu-30Zn brass in concentrated ammonia solution. For the former, it has been debated for a long time whether hydrogen is involved in this system, while in the latter it is almost certain that the SCC occurs without the presence of hydrogen. Subsequently, the cracking features of the bcc δ–ferrite phase contained in one of the austenitic stainless steels studied was observed and compared with the fcc austenite. The SCC behavior of 70Cu-30Zn in annealed and cold worked conditions was investigated. The purpose of this part of work was to examine the relationship between localized slip and the propagation patterns. Finally, the growth, arrest and reinitiation process were analyzed in order to obtain additional information on the propagation mechanism.

This thesis will start with a literature review which summarizes the important developments in the mechanistic studies of hydrogen-induced cracking, SCC and relevant areas. Chapter 2 will describe the experimental methods employed in the present study. The experimental results obtained by these methods will be presented in chapters 3 to 7. Each chapter includes a discussion section to analyze and evaluate the results and to compare them with other published studies. A general discussion will be given in Chapter 8, in which some details of the essential microscopic SCC processes are discussed. The final chapter outlines the conclusions of this study.

Chapter 1

Literature Review

1.1 HYDROGEN-INDUCED CRACKING

Hydrogen can reduce the physical and mechanical properties of materials to a degree that renders them unattractive, unreliable or dangerous. Hydrogen degradation or embrittlement of iron was reported as early as 1873. This form of hydrogen damage has been observed most often in iron and steels, primarily in quenched and tempered steels, in precipitation-hardened steels or in steels which have high strength. Also, it has been recognized as an important failure mechanism in austenitic stainless steels for the past decade. In parallel with the development of experimental techniques and the use of the electron microscope, hydrogen embrittlement is no longer an accurate term to describe the damage process because in some cases hydrogen was observed to facilitate plastic flow. Instead, hydrogen-induced cracking and hydrogen-related fracture have been accepted as more general terms.

1.1.1 Hydrogen in iron and steels

The hydrogen atom is the smallest in diameter and the simplest in electronic structure among the elements. It stays in metals in a variety of forms, such as dissolved interstitial atoms, hydrides, and nonequilibrium phases trapped at defects.

Among transition metals, iron has the lowest solubility for hydrogen. The maximum dissolved hydrogen at high temperature is only 6 at.%. Crystal structure influences hydrogen solubility in iron. The transformation of $\alpha \rightarrow \gamma$ or $\delta \rightarrow \gamma$ increases hydrogen solubility. Shown in Fig. 1.1 [25], hydrogen solubility data for stainless steels fall into two groups corresponding to the microstructures: one for austenitic steels and one for ferritic and martensitic steels. Data for ferritic steels are close to those for α-iron; while the austenitic steels have a solubility that is a factor of 3 to 20 greater. The alloying elements influence the hydrogen solubility in stainless steels, among which Ni has the least effect [26,27].

Due to the extremely low solubility of hydrogen in iron and steels, hydride is not formed or at least is unstable in pure iron, carbon steels, and low-concentration alloys. Under high-fugacity condition, austenitic stainless steels can form "pseudo-hydrides" [28]. These "pseudo-hydrides" are in fact high-concentration solid solutions formed in the presence of a miscibility gap.

Hydrogen diffusing in a non-ideal metal or alloy interacts with lattice defects. Many of these defects have strong interactions with hydrogen, which result in the localization of hydrogen. Depending on the interactions between hydrogen and lattice defects, the hydrogen traps can be classified as strong, moderate and week [29]. Point defects such as C, N interstitials are weak traps for hydrogen. Substitionals solute atoms such as Si and Ti are moderate traps, whereas vacancies are strong traps. Dislocation cores interact strongly with hydrogen, but the dislocation elastic field does so much more weakly. Two-

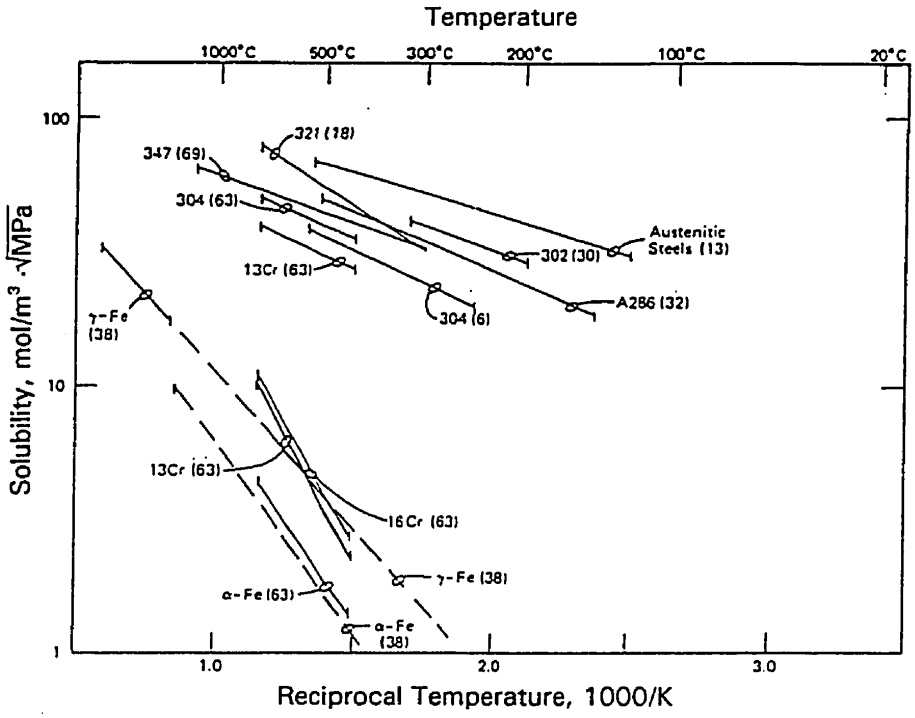

Figure 1.1 Hydrogen solubility in stainless steels.

dimensional imperfections such as grain boundaries, phase boundaries, and free surfaces are all strong traps for hydrogen. The hydrostatic stress field ahead of a crack tip is a weak trap [29].

Trapping increases the solubility, but it is only marginally measured below 600 K for a trap density 10^{25} m^{-3} and would be negligible for smaller trap densities [30]. Fig. 1.2 shows the hydrogen diffusivity in austenitic steels [25]. The diffusivities are lower than extrapolated values for pure γ-iron and vary with alloy composition. Overall, trapping effects in austenitic steels are not as pronounced as in ferritic steels.

At long range relative to the atomic spacing, hydrogen interacts with defects in crystals through its elastic strain field which is spherically symmetrical in iron [31]. The amount of hydrogen in the elastic field of edge dislocations, the so-called Cottrell atmosphere, is quite low. The number of hydrogen atoms per unit length of dislocations is only 5×10^{-4} at room temperature [32]. For screw dislocations, which do not have a hydrostatic field, only the segments bowed away from pure screw dislocations can interact with hydrogen. Hence the interaction is relatively weak and short-ranged. At short range, hydrogen interacts with dislocations in a nonlinear elastic manner and "chemically" through localized bonding. The local interactions can be described phenomenologically in terms of a binding energy.

1.1.2 Effects of hydrogen on plasticity and fracture

The loss of plasticity caused by hydrogen charging is considered as one of the important symptoms of hydrogen embrittlement in metals. In fact, conventional indices of ductility, such as the elongation and the reduction in area at fracture, are always decreased by hydrogen, but other measurements give less clear results. The inconsistencies are due to the high complexity of the plastic behavior of hydrogen-charged metals.

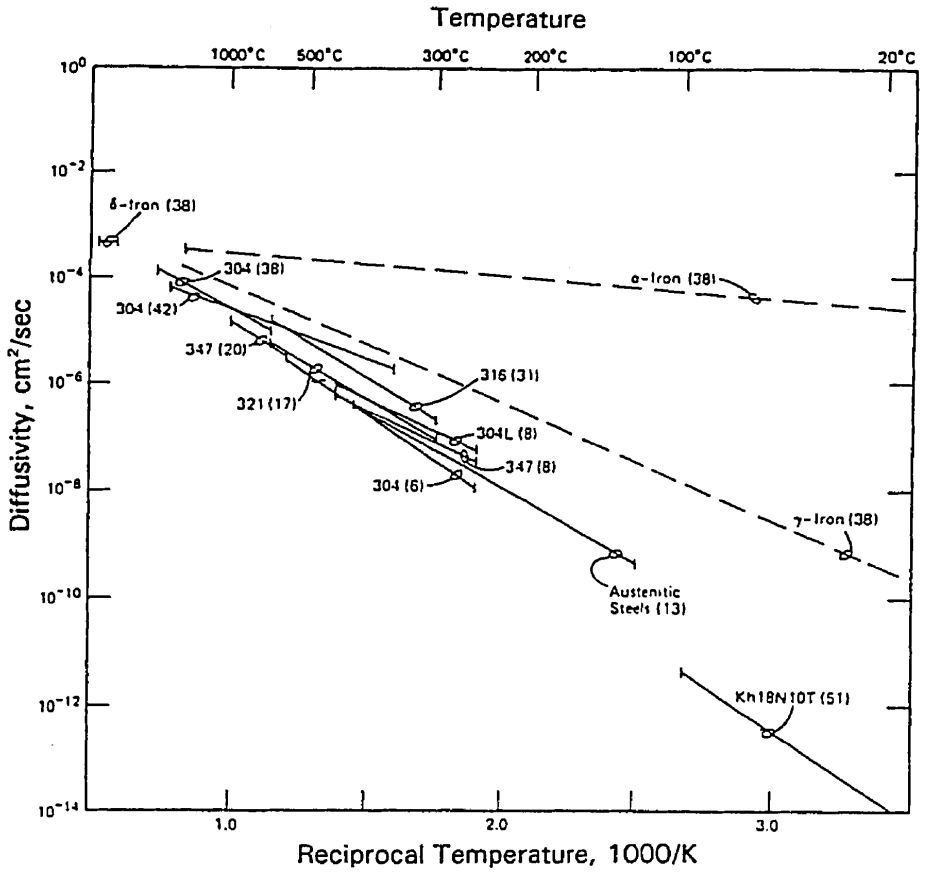

Figure 1.2 Hydrogen diffusivity in stainless steels.

1.1.2.1 Hydrogen-dislocation interactions during plastic deformation

The effects of hydrogen on dislocations ahead of a crack were studied by Birnbaum *et al* [14–17] using an *in situ* transmission electron microscopy (TEM) technique. On adding hydrogen gas to the environmental cell, dislocation sources began to operate and dislocations began to increase their velocities. Removal of the hydrogen gas resulted in cessation of the dislocation motion. The effect of the hydrogen was to reduce the stress for dislocation motion. Enhanced dislocation velocities resulting from hydrogen were observed for screw, edge, and mixed dislocations and for dislocations that were in tangles, in slip bands and far from other dislocations. Because similar behavior was observed for dislocations in fcc, bcc, and hcp crystal structures and in alloys as well as in pure metal, Birnbaum *et al* suggested that the increase in dislocation velocities by hydrogen is a general phenomenon.

It was proposed [33] that dislocations could transport hydrogen at rates faster than lattice diffusion during plastic deformation. The transported hydrogen could be trapped in voids, leading to the increase of internal pressure and to fracture. Increase in the hydrogen diffusivity [34] and in the release rate from iron [35] by deformation have been observed.

In general, there are two types of behavior in hydrogen transport by dislocations [36]. In the first, the hydrogen is introduced into the material and equilibrated with all traps or defects well before the plastic deformation. The surface is supposed to be close to the site of hydrogen egress. When this closed system is mechanically loaded so that dislocation motion starts, some of the hydrogen trapped at dislocations is returned to the lattice. If the velocity of dislocation is sufficiently high, all of the hydrogen will be left behind in the lattice and perhaps be partially absorbed by static traps. For velocities near or less than the critical value, some of the hydrogen will remain with the moving dislocation. Because the hydrogen chemical potential of a moving dislocation is less than that in the

surrounding material, there will be a driving force for hydrogen diffusion back to the dislocation. Previously moving dislocations which are stopped become sinks for hydrogen.

In the second case, the hydrogen is presented to the surface at the same time that deformation begins. This system is open, with hydrogen entry accompanying deformation. Dislocations will emit hydrogen for three physical reasons as they move into the material: (i) the charging medium chemical potential is greater than that within the material; (ii) dislocations move faster than the critical breakaway velocity; and (iii) dislocations annihilate each other and intersect with other defects. Thus, in contrast to the first case, dislocations, whether moving or stopped, act as hydrogen sources.

1.1.2.2 Hydrogen distribution at the crack tip

Assuming a CCT sample is made of a perfect elasto-plastic material (the work hardening coefficient is zero), Kitagawa and Kojima [37] theoretically analyzed the elasto-plastic stress and strain near the crack tip and the hydrogen distribution at the crack tip by solving the non-linear hydrogen diffusion equations including trapping effects. The maximum hydrostatic stress σ_h traps more hydrogen as K increases. Under a certain stress, the saturated hydrogen concentration at the point of maximum σ_h is nearly equal to the total hydrogen concentration in the region near the crack tip.

The calculations made by Sofronis and McMeeking [38] indicate that hydrogen is more likely to be present in the near-tip region rather than in the maximum hydrostatic stress region. The recent work of Wu *et al.* [39] showed that there are two hydrogen concentration peaks in front of a crack tip under mode I loading: one is adjacent to the crack tip and is attributed to dislocation trapping; the other one is at a distance away from the crack tip and is attributed to the hydrostatic dilatation.

Considering that there is always a flux of hydrogen atoms passing through the crack tip even at a steady state of charging, Turnbull *et al* [40] found that the peak amount of hydrogen is at the crack tip but it is lower than the value predicted for an idealized boundary condition. Hydrogen concentration and its distribution at the crack tip is influenced by applied stress intensity factor K, and increases with increasing K.

1.1.2.3 The influence of hydrogen on the yield strength of metals

The most controversial issue on the hydrogen-influenced plastic properties concerns the yield strength. Depending on the experimental conditions, the yield strength can be decreased, increased or unaffected. It is extremely sensitive to the purity of hydrogen-charged iron. For high purity iron single crystals and polycrystals, some results have shown convincingly that softening occurs during dynamic charging and precharging of hydrogen at temperatures greater than 190 K [41], but hardening ensues after a transient softening below 190 K, as schematically illustrated in Fig. 1.3. At low strains, hydrogen reduces both the flow stress and the strain hardening rate relative to hydrogen-free conditions. At higher strains, opposite effects are observed [41].

Impure iron and low strength steels show a reduced yield strength when charged by hydrogen at high fugacity. At low hydrogen fugacities, the effect of hydrogen is to raise the flow stress in these materials [42]. For high strength steels, hydrogen has little effect on the yield strength which is controlled by microstructural features. Hydrogen promotes the onset of plastic instability in steels in two ways [43]: by the formation of concentrated shear bands along characteristic slip traces and by the multiplication of these bands through the nucleation of new shear bands.

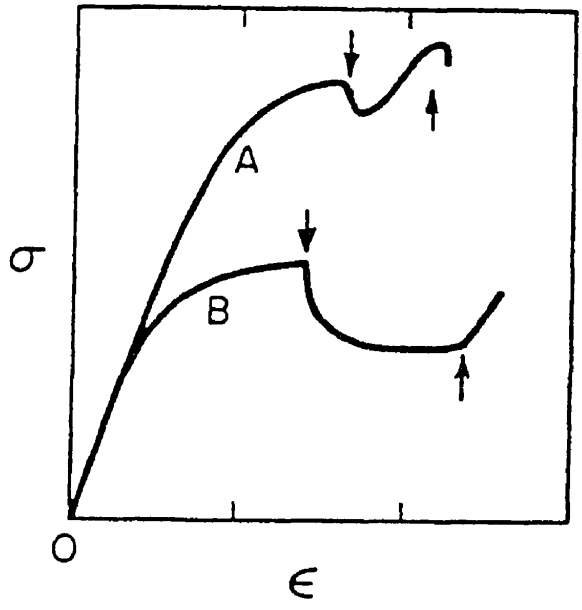

Figure 1.3 Form of the stress-strain curves for high purity iron at (a) T < 190 K and (b) T > 190 K. The down and up arrows represent respectively initiation and cessation of charging with hydrogen during a tensile test.

1.1.2.4 Interpretations of hydrogen effects on yield strength

There are many hypotheses for the rationalization of the hardening-softening behavior, although not all the mechanisms have direct experimental support. Softening can be explained by enhanced motion of screw dislocations by easier kink formation [30,44], enhanced injection of dislocations at free surfaces and a reduced internal stress which leads to the relaxation of the long range stresses (interactions with dislocations) [45].

However, softening was observed in systems in which there are no strong dislocation-lattice interactions. This suggests that the explanation of easier kink nucleation is not correct. An elastic shielding mechanism was proposed to explain the generality of softening [28]. In this mechanism, hydrogen diffuses to positions of low free energy and forms high-concentration

atmospheres around dislocation, solutes and precipitates. The binding energy permits the atmospheres to form and to move with the dislocations in the temperature ranges when embrittlement occurs. The significant interactions are therefore between dislocations and defects including *the atmospheres*. The concentrations and configurations of the hydrogen atmospheres respond to the stress fields of all of the lattice defects. The reconfiguration will reduce the energy of the entire system. In general, the effect of hydrogen atmospheres at dislocations is to decrease the interactions of elastic defects at short range but to have no effect at large distances.

An explanation of hardening at low temperatures is that hydrogen segregation at edge dislocations hampers their motion [45]. But the mechanism of the hardening at room temperature is not as evident. There are other possible explanations [30]. For example, because of its presence in dislocation cores, hydrogen could make dislocation intersections more difficult; hydrogen could also be trapped in vacancies and stabilize them, retarding recovery processes and leading to hardening. It is also possible that hydrogen increases the pinning and viscous dragging to dislocation cores by carbon atoms.

As slip localization and either hardening or softening induced by hydrogen were observed in 304 and 310 stainless steels, Ni and high purity Al, Birnbaum [46] suggested that the tensile test could not determine the true flow stress in the presence of slip localization induced by hydrogen. The macroscopic flow stress measured in a tensile test can be increased or decreased, depending on the magnitude of the hydrogen-induced dislocation velocity increase and on the degree of slip localization. If the increase in flow stress resulting from strain localization is not counteracted by its decrease induced by an increase in dislocation mobility, macroscopic hardening occurs. The hardening reflects the slip localization rather than the effects of hydrogen on this behavior. This interpretation has been supported by the hardening and enhanced dislocation mobility by hydrogen in stainless steels and in Al.

1.1.3 Mechanisms of hydrogen induced cracking

Hydrogen-induced cracking has been studied in recent years in many systems. Despite this effort, there is still incomplete understanding of the mechanisms by which hydrogen-induced cracking occurs. In this section, some important mechanisms are presented.

1.1.3.1 Hydrogen related phase change mechanisms

Westlake [47] first proposed that cracking could proceed by the formation and cracking of a hydride near the crack tip. Gahr *et al.*[48] then showed that the hydrostatic stress field ahead of a stressed crack tip could stabilize the hydride even when it is unstable in the absence of stress, and demonstrated embrittlement by hydride cracking in niobium. Qualitatively, the mechanism can be described as follows:

Under the applied stress, the chemical potential of the solute hydrogen and the hydride are reduced at tensile stress concentrations, such as crack tips. Hydrogen diffuses to these regions and hydrides then form at the crack tip. The phase change is accompanied by a decrease in the critical stress intensity for crack propagation because hydrides are generally brittle phases. The crack propagates into the hydride by cleavage until the hydride-solid solution boundary is reached. At this point, the crack enters a ductile phase with a high K_{IC} and the crack stops until more hydride is formed. The process repeats itself, resulting in discontinuous crack growth through the stress-induced hydride phase and with hydride formation along the crack path.

In a qualitative sense, other stress-induced brittle phases can cause similar embrittlement as hydrides. One important case is the hydrogen-enhanced transformation of martensites in stainless steels. The fracture surfaces of "hydrogen-embrittled" stainless

steels are clearly different from that in the absence of hydrogen and the *in situ* TEM studies have shown that martensites are formed in front of the crack tip and along the crack sides. Hydrogen-induced cracking in metastable stainless steels have been associated with hydrogen-enhanced transformation of the γ-fcc phase to the α'-bcc and ε-hcp martensites [49,50]. It was speculated that hydrogen entry into the lattice may promote the transformation of metastable austenite to martensite.

1.1.3.2 Hydrogen-enhanced local plasticity (HELP) mechanism

Because of the loss of macroscopic ductility and of relatively low-resolution studies of the fracture surfaces, the hydrogen-induced cracking was considered as a "brittle fracture" in many cases. It was Beachem [51] who first suggested, on the basis of careful fractographic examination, that hydrogen embrittlement of steels was in fact associated with locally enhanced plasticity at the crack tip. In recent years, this point of view has been supported by the work of Lynch [52,53] and Birnbaum *et al* [14–17], in a variety systems. Using both fractographic evidence and *in situ* TEM studies, it has been shown that the HELP mechanism is a viable failure mechanism for a large number of pure metals and alloys, mainly those do not form hydrides. However, Lynch considers that the HELP mechanism is a surface phenomenon (adsorption), while Birnbaum *et al.* consider that it occurs in the volume of the material as well as near the surface.

The HELP mechanism is operative for hydrogen in solid solution and for gaseous hydrogen environments. In both cases, either adsorbed hydrogen at the crack tip surfaces weakens interatomic bonds, or high concentration of hydrogen due to the stress field in front of a crack tip reduces the local flow stress, therefore facilitating the nucleation of dislocations in the vicinity of the crack tips. The shear localization leads to fracture by plastic-failure processes, either by microvoid formation and their coalescence with the main crack [52], or by the fracture along alternating slip planes [54,55]. Higher resolution

observations also showed that many intergranular fractures are not confined to the grain boundaries [56,57] in the presence of hydrogen but are situated in the vicinity of grain boundaries. Thus, the HELP mechanism can interpret fractures without distinguishing between the intergranular and transgranular fracture patterns.

1.1.3.3 Decohesion mechanism

This mechanism originated with Pfeil [58] in 1926 and was substantially extended by Troiano [59,60] and later by Oriani [61,62]. The concept of this model is based on hydrogen affecting the bonding forces between metal atoms. Recognizing that embrittlement does not arise from hydrogen uniformly distributed in solid solution, it was proposed that hydrogen diffuses to regions of positive triaxial stress ahead of the crack tip, and accumulates to reach a large local hydrogen concentration. Sufficient local hydrogen concentration reduces bond strength and facilitates the nucleation of microcracks within these regions. The resulting microcrack rejoins the main crack and also advances out of the region of hydrogen accumulation, then becomes arrested by plastic deformation (Fig. 1.4). The process repeats, leading to discontinuous propagation.

Oriani modified this model [62] by quantifying the magnitude of elastic stresses which are necessary to produce sufficient hydrogen accumulation, and the location of the sites of crack nucleation. He considered that local stress concentration could reach $E/10$ at a few atomic distances from a crack tip. Such a large stress concentration led to a sufficient amount of hydrogen to reduce the cohesive force. In contrast to the model of Troiano, Oriani considered that crack propagation is continuous, proceeding at a rate determined by the transport processes involved in accumulating the necessary hydrogen concentration.

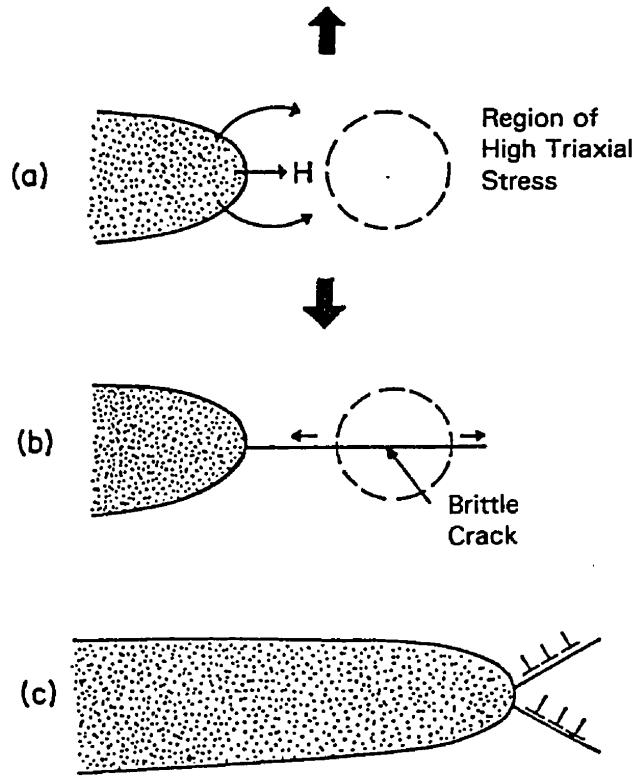

Figure 1.4 Schematic illustration of the hydrogen-induced decohesion model.

1.1.3.4 Internal pressure theory

According to the model proposed by Zappfe *et al.* [63] and Tetelman [64], hydrogen-induced cracking is caused by precipitation of molecular hydrogen in internal defects followed by a substantial build-up of pressure. The presence of such internal pressure, estimated as high as 10^5 atmospheres [65], allows the formation and growth of a microcrack at a lower value of the externally applied stress. Subsequently, the pressure inside a crack decreases as the crack extends. This in turn results in an arrest in crack growth until the internal pressure reincreases to a critical value. Because time is required for the necessary diffusion of hydrogen atoms to the crack until its recombination to form molecular hydrogen, the crack growth process is discontinuous. The stop-and-start process should therefore leave evidence on the fracture surfaces.

1.1.3.5 Hydrogen transported by dislocation

Hydrogen transported by dislocations was first proposed by Azou and Bastien [33] and then developed by Tien *et al.* [66,67]. Tien *et al.* assumed that hydrogen atoms are bound to mobile dislocations as a Cottrell atmosphere. The atmosphere can then be stripped off or deposited at other traps such as grain boundaries, inclusions and microvoids, and therefore contribute to decohesion and embrittlement. They simply specified that the velocity of the dislocations must be less than the critical breakaway velocity v_c to carry the Cottrell atmosphere.

They specifically suggested that for steels large supersaturations could develop, and substantial pressure could arise in voids, promoting failure by an internal pressure theory. In contrast, Johnson and Hirth [68] analyzed the supersaturation produced by dislocation transport and found the supersaturation was very small (~0.001) in voids at

room temperature in iron and steels. Consequently, the pressurization of the voids was possible only at large external hydrogen fugacities.

Bernstein and Thompson [69] suggested that for single phase materials where no defects or heterogeneities have strong interactions with hydrogen, long term supersaturation induced by dislocation transport does not appear possible. But such an effect is both likely and predictable at second phase particles and poisoned grain boundaries. There exists a critical condition where stable supersaturation may or may not occur depending on the material and test conditions. It is evident [34,70] that, for example, in plastically deformed nickel, dislocation transport of hydrogen is the predominant mechanism and that the transport rates are several orders higher than in unstrained nickel where lattice diffusion is the predominant mechanism.

1.1.3.6 Hydrogen-induced cleavage

This mechanism was proposed to explain SCC in stainless steels [9]. Hydrogen diffuses to the triaxial stress area at the crack tip, producing a hydrogen accumulation region (HAR). It was observed that the dislocation configuration is planar at the fracture surface while it is cellular away from the fracture surface. Therefore the stacking fault energy is believed to be lower at the crack tip due to the presence of the HAR. Planar slip on intersecting {111} planes produces Lomer-Cottrell locks which lie on {100} and hinder the oncoming dislocations. High stress acting on Lomer-Cottrell locks cleaves the {100} planes, then the crack joins up to the main crack (Fig. 1.5).

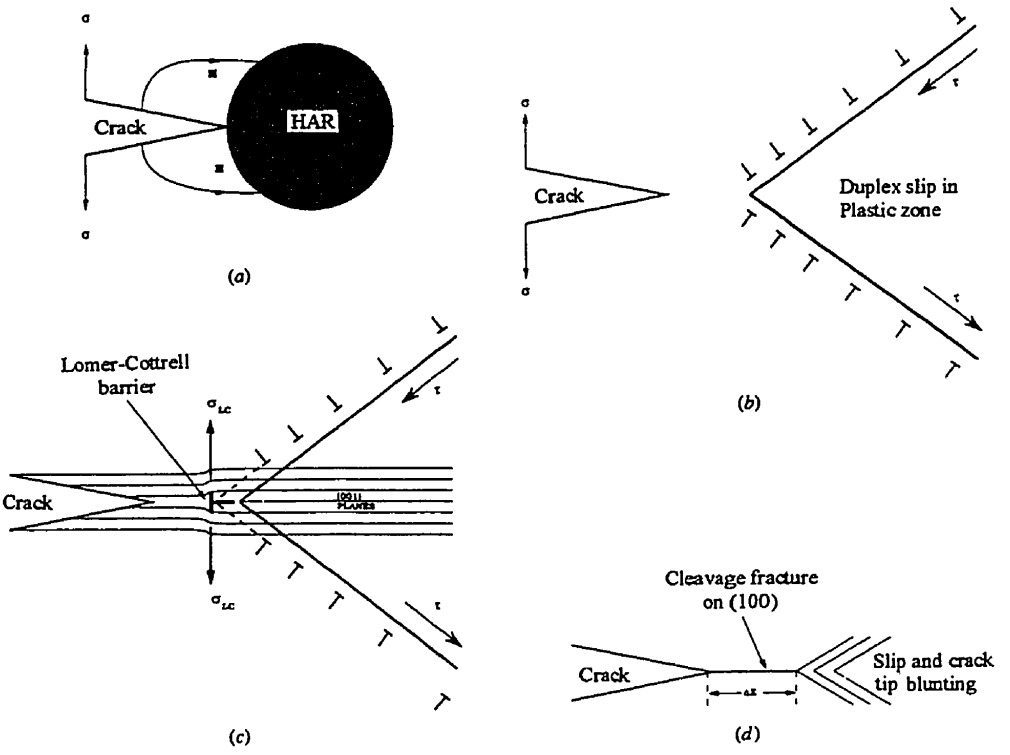

Figure 1.5 Schematic illustration of the hydrogen-induced cleavage model.

1.2 STRESS CORROSION CRACKING

Stress corrosion cracking (SCC) is a failure phenomenon that occurs because of the simultaneous presence of stress, generally a tensile stress, a specific environment and a susceptible material. The stress required for SCC is much smaller than the yield strengths of the materials, while the cracking velocities, generally between 10^{-8} to 10^{-4} m/s, are much higher than the corrosion rates in the absence of stress but less than the mechanical fracture velocities under overload conditions. The cracks frequently exhibit multiple branching. In order for SCC to occur, a threshold stress or stress intensity and a critical potential must be exceeded. Moreover, the key damaging species in the environment need not be present in large concentrations.

1.2.1 Stress corrosion cracking in stainless steels

SCC is found in many alloys and in many types of environments. Stainless steels in particular have suffered from this form of failure because of their widespread use in a variety of environments. The chloride ion which is often unavoidable in aqueous environment is very harmful to the stainless steels once a small pit exists on the surface. As a result, there have been many failures resulted from the presence of chloride, often in unexpected locations. Therefore, chloride cracking has become the most studied type of SCC failure in stainless steels.

1.2.1.1 Environmental variations in aqueous chloride solutions

The corrosion environment plays an essential role in determining whether SCC occurs, and how fast the rate of the cracking process is. In the case of SCC of austenitic stainless steels in aqueous chloride solutions, a number of environmental factors can be identified:

1) pH value

The SCC process involves an active (or at least not conventionally passive) state within the crack. Much of the experimental work on chloride cracking has been carried out in artificial environments, such as boiling $MgCl_2$ solutions to accelerate the cracking process. The pH values at the crack tip in hot $MgCl_2$ solution are between 1.2 to 2.5, and characteristically in the range of 1.4 to 1.6 within the crevice regardless of the pH value of the corroding solution [71]. The low pH behavior is accompanied by the formation of an oxide film. Baker *et al* [71] suggested this film was the result of the following reaction:

$$2Cr^{3+} + 3H_2O \rightarrow Cr_2O_3 + 6H^+. \qquad (1\text{-}1)$$

2) Chloride ion concentration

The presence of chloride increases the anodic dissolution and decreases the passivity of the material [72], as the anodic polarization curve shows (Fig. 1.6). Increasing the chloride

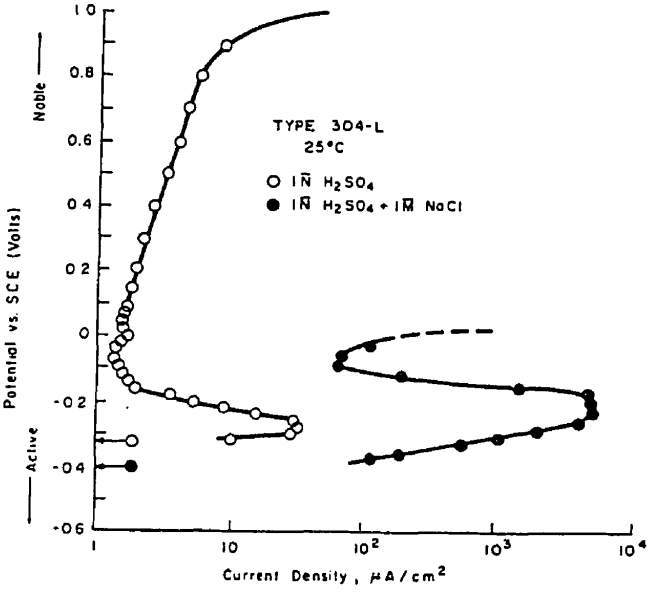

Figure 1.6 Potentionstatic anodic polarization curves of 304 stainless steel in solutions with and without Cl^- ions.

concentration increases the rate of cracking [73]. The chloride concentration also affects the crack initiation, because there is a close correlation between SCC and the onset of pitting corrosion. In boiling $MgCl_2$ solution, the high chloride activity lowers the amount of local hydrolysis of chromium ions which is required to form a passive film. The passive state is so fragile, that the material stays in a passive-to-active transition stage, and a trenching type of corrosion at slip steps can occur without pitting. But in low chloride concentration and/or low temperature, conventional pitting becomes necessary to generate the acidity and high chloride concentration within the pit [74].

3) Temperature

SCC in austenitic stainless steels occurs in very dilute aqueous chloride solutions at temperatures as low as 75°C and as high as above 200°C [75–78]. The cracking resembles conventional chloride SCC in boiling $MgCl_2$ solution, often employed as a standard solution. Low temperature SCC is clearly initiated in a crevice, implying that the crevice in dilute chloride solutions has the same active or semiactive state as that within pits in high chloride solutions. The reduction of the chloride concentration required for SCC at temperature above 200°C reflects a less acidic crack environment required at that temperature to achieve an active state and probably also the faster kinetics of the anodic reactions.

4) Potential

It was frequently noted [79,80] that the SCC process in austenitic stainless steels could be delayed or prevented by the application of a cathodic current, that is, cathodic protection. But Russell *et al* [81] found later that the stage II velocity is indifferent to a small change of cathodic potential. The effect of anodic polarization has not been as clear cut. Anodic polarization was reported either to accelerate [82] or not to affect [79] the cracking kinetics. The observations of Kohl [83] on the effect of anodic polarization shed some light on these seemingly contradictory conclusions. He determined that potentiostatic

anodic polarization reduced the initiation time tenfold or more but had a much smaller effect on the crack propagation rate in 44% $MgCl_2$ solution. Thus, it is likely that the failure time is controlled by the crack propagation when little or no effect of anodic polarization is found, while the fracture required long initiation times are accelerated by anodic polarization.

1.2.1.2 Hydrogen evolution in chloride solution

The concept that hydrogen is involved in SCC was proposed 40 years ago. From the thermodynamics view, if the electrode potential of the metal inside a crack is lower than the hydrogen equilibrium potential in the relevant solution, evolution of hydrogen may occur at the crack tip. Hydrogen evolution from stainless steels undergoing cracking in boiling $MgCl_2$ was observed [66].

Smith *et al* [84] found the pH value of the crack tip to be in the range of 3.5 to 3.9 when they analyzed the hydrogen potential of the crack tip in 4340 steel. They stated that water at the advancing crack is thermodynamically unstable and hydrogen can be liberated during SCC. Since the pH value is about 1 during SCC of 316 stainless steel in boiling $MgCl_2$ solution [81], the thermodynamic condition is suitable for the occurrence of hydrogen evolution. Some tests have confirmed that hydrogen evolution is the primary cathodic reaction during SCC of austenitic stainless steels in 42% $MgCl_2$ [85] and measured the hydrogen distribution at the SCC crack tip in boiling LiCl solution [86].

1.2.1.3 SCC of duplex stainless steels

The SCC properties of duplex stainless steels are related to complex electrochemical and mechanical interactions between the two phases. Regarding the electrochemical interactions, ferrite is generally observed to be anodic to the austenite, at least in boiling $MgCl_2$

solution. The difference in corrosion potential between austenite and ferrite in duplex steels is much bigger than that between austenitic and ferritic steels. This electrochemical coupling would thus prevent the attack of the austenite, which can be preferentially deformed at low stress [87,88]. It was suggested that duplex stainless steels in $MgCl_2$ solution are not subject to hydrogen embrittlement at 143°C, because the hydrogen evolution reaction $H + H \rightarrow H_2$ or $H + H^+ + e \rightarrow H_2$ is overwhelmingly predominant in the cathodic reaction at that temperature. The reactions prevent the entry of hydrogen into the alloys [88].

Alloying compositions and the amount of ferritic phase influence the SCC resistance in duplex stainless steels. As summarized in reference 88, Si has a favorable effect in both $MgCl_2$ and $CaCl_2$ solutions, but gives a detrimental effect in NaCl solution. Mo and Cu are also detrimental to the SCC resistance in $MgCl_2$ solution. In chloride solution, the required amount of ferrite to have a good SCC resistance is in the range of 10–20% in Cr-Ni-Mn steels.

In contrast to the behavior in $MgCl_2$ solution, the ferrite phase has a more noble pitting potential than austenite in chloride solution containing H_2S [89] because of its high Cr and Mo contents. The effect of H_2S on duplex steels is to decrease the dissolution and the entry of hydrogen by the formation of a sulfide film, while in mechanically depassivated ferrite, H_2S increases the dissolution rate and enhances hydrogen entry [90].

Thus, the good resistance of SCC in duplex stainless steels can be explained depending on its mechanical and electrochemical behavior in $MgCl_2$ solution and in solution containing H_2S:

1) In the first solution [87,88], the anodic ferrite protects the austenite from corrosion. At low stress, ferrite is not sufficiently strained to favor crack initiation because of its higher yield strength than austenite. The SCC occurs only at high stress when ferrite can be fractured under both corrosion and mechanical effects.

2) In solution contain H_2S, austenite is attacked both chemically and mechanically prior to ferrite at low stress. The cracking is mainly controlled by the localized anodic dissolution of the austenite, which is not very sensitive to hydrogen embrittlement. Slow propagation deteriorates the crack microenvironment, ferrite may be depassivated and may protect austenite from cracking [89]. At high applied stress, the ferrite phase undergoes mechanical depassivation. The localized dissolution and hydrogen embrittlement in ferrite cause rapid cracking [90].

1.2.2 Stress corrosion cracking in copper alloys

The failure of copper alloys in aqueous ammonia solution represents the classical example of SCC. This failure has been considered as requiring the presence of ammonia, moisture and oxygen. SCC of copper alloys can also occur in copper sulphate solution [75] and in many salt solutions under slow strain rate test conditions with anodic polarization [76]. Two kinds of ammonia solutions exist, depending on the composition: (i) non-tarnishing solution in which the metal undergoes active anodic dissolution in the absence of a detectable surface film, and (ii) tarnishing solution in which the metal becomes covered by a film. This black tarnish film is an epitaxed layer of cuprous oxide [91,92] and preferentially penetrates along the grain boundaries [93]. Immersion of copper and α-brass in oxygenated aqueous ammonia leads initially to active dissolution in the absence of the tarnish film. The rate of dissolution increases with the time of immersion until the solution attains a critical concentration of dissolved copper. At that point, the specimen surfaces become coated with the characteristic tarnish film.

1.2.2.1 Dissolution in non-tarnishing solution

The process [94] involves the anodic dissolution of Cu and Zn:

$$Cu + 2NH_3 \rightarrow Cu(NH_3)_2^+ + e; \quad (1\text{-}2)$$

$$Zn + 4NH_3 \rightarrow Zn(NH_3)_4^{2+} + 2e; \quad (1\text{-}3)$$

and the cathodic reduction of the cupric complexes:

$$Cu(NH_3)_5^{2+} + e \rightarrow Cu(NH_3)_2^{+} + 3NH_3. \quad (1\text{-}4)$$

The cuprous complex ion produced in reaction (1-2) is unstable in the presence of oxygen, being oxidized to the cupric state by reaction:

$$2Cu(NH_3)_2^{+} + \tfrac{1}{2}O_2 + H_2O + 6NH_3 \rightarrow 2Cu(NH_3)_5^{2+} + 2OH^{-}. \quad (1\text{-}5)$$

The reduction of cupric ion generates cuprous complexes in reaction (1-4), which in turn react with oxygen to generate cupric complexes by reaction (1-5). The process is termed autocatalytic, and increases the dissolution rate as shown in Fig. 1.7. The presence of zinc in α-brass does not substantially change the above electrochemical behavior. This dissolution process is summarized in Fig. 1.8.

Thus, if the solution contains significant concentrations of dissolved copper, the anodic dissolution process is controlled by the transport of the cathodic reactants, the cupric complex, to the surface. Oxygen plays a key role in the dissolution process in that it reoxidizes the cuprous ions produced in anodic reaction (1-2), and therefore increases the copper dissolution. In solution containing no dissolved copper, oxygen reduction is the controlling process until the cupric complex ions increase sufficiently, then the reduction of these ions becomes the predominant cathodic process [95].

1.2.2.2 Film formation in tarnishing solution

The inflection in Fig. 1.7 corresponds to the formation of the tarnish film in brass. This critical copper content is essentially constant for solution containing more than 6N ammonia, but decreases with decreasing ammonia concentration in the range 0.5 to 5 N [95]. The presence of dissolved copper is necessary for tarnishing to occur.

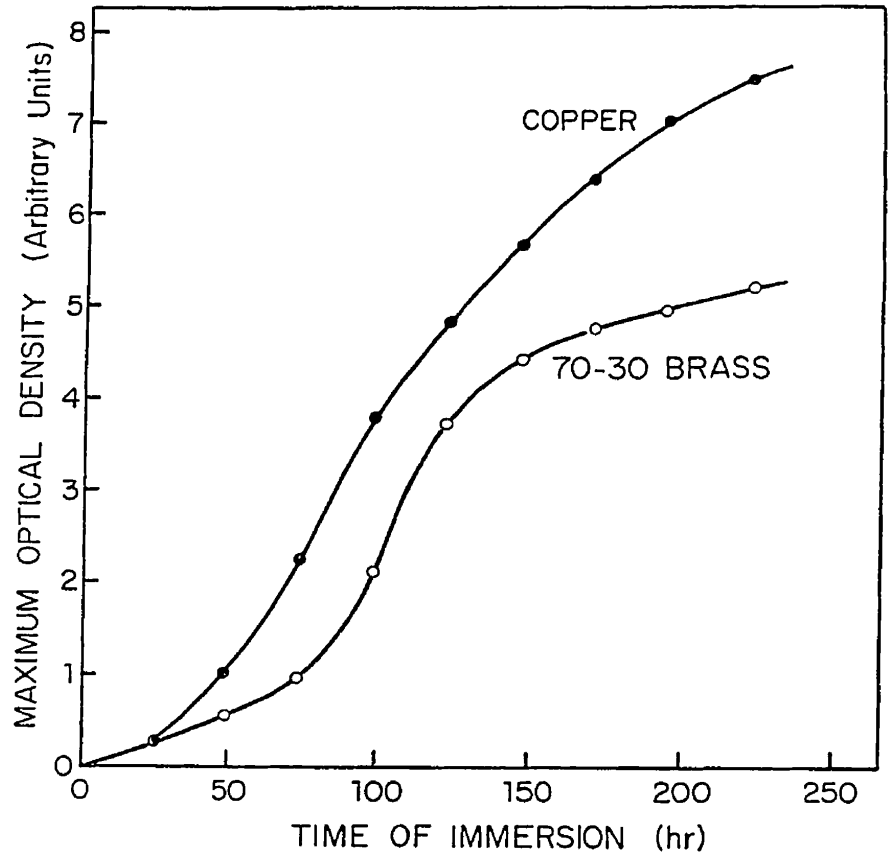

Figure 1.7 Relationship between maximum optical density, which is proportional to the dissolved copper concentration of the solution, and time of immersion of unstressed specimens of copper and Cu-30Zn in oxygenated 15M aqueous ammonia.

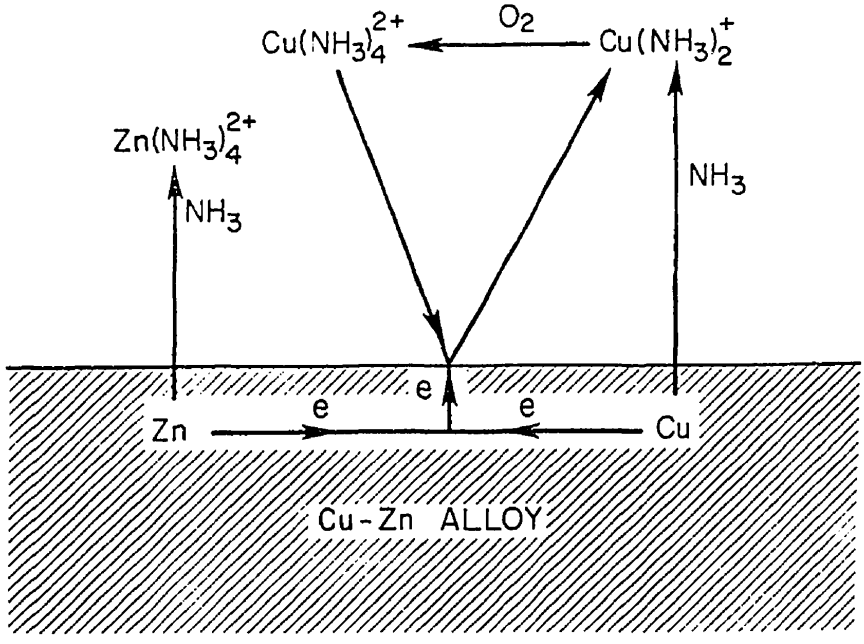

Figure 1.8 Schematic illustration of the electrochemical model for dissolution of brass in non-tarnishing solution.

While the specific reactions responsible for tarnish formation have not been accepted generally, it was suggested [95] that tarnishing involves the adsorption and reaction between cuprous complexes and hydroxyl ions:

$$2Cu(NH_3)_2^+ + 2OH^- \rightarrow Cu_2O + 4NH_3 + H_2O. \qquad (1\text{-}6)$$

Later studies indicated the tarnish film consists mainly of cuprous oxide. Its formation process has three stages [96]: (i) the formation of a thin (<20 nm) protective film of Cu_2O; (ii) local breakdown of the thin film at anodic sites, leading to rapid attack at these sites and the growth by precipitation of a thick porous layer of Cu_2O (the "tarnish film"); and (iii) the formation of an outer layer of CuO. The tarnish film grows faster as the zinc content increases

[97,98], because it forms by the cathodic reduction of Cu in the solution and concomitant anodic dissolution of Zn from the brass [91].

1.2.2.3 SCC of copper alloys in equilibrated cupric/cuprous solution

In solution containing oxygen, cupric complexes are always present and were thought to play a major role in crack propagation [98]. However, a later study found that in the absence of significant concentrations of these complexes, cracking could be produced by applying an anodic current [99]. The anodic reaction (1-2) and cathodic reduction (1-4) in both above conditions produce cuprous complexes which may play a critical role. A series of tests in so-called equilibrium solutions thus has been done to verify this alternative interpretation. The solutions were prepared by adding excess copper powder in aqueous ammonia and allowing it to react in the absence of oxygen until the following reaction reaches equilibrium:

$$Cu^{2+} + Cu \rightarrow 2Cu^{+} \qquad (1\text{-}7)$$

Since copper in alloys is not anodically attacked in these solutions, dissolution based models of SCC would not predict cracking in these conditions. This was supported by the observations of Kaufman *et al* [100] and Dickson *et al* [4]. Other researchers [101,102], however, reported transgranular cracking in such solutions. They explained that because of the relatively fast kinetics of reaction (1-7), the ammonia solution in contact with the bare metal is always close to the equilibrium composition. Such a condition exists inside a crack where a small amount of solution is in contact with a large metal surface. Thus, the cracking will occur in a similar way both in equilibrium and nonequilibrium solutions [96].

1.2.3 Discontinuous propagation

The distinction between intergranular and transgranular SCC had been apparent for many years and was readily observable using conventional metallography. However, as soon as

attempts were made to examine the crack morphology and fractography in greater detail, evidence began to accumulate that transgranular SCC propagation in particular is a discontinuous process.

In 1959 Edeleanu [103], using conventional crack trace analysis, reported the sudden periodic appearance of a "ghost" crack ahead of the main crack tip in brass single crystal exposed to ammonia environment. The crack traces in a side face were observed with an optical microscope. After a period of incubation time, a very faint "ghost" crack appeared suddenly in its length and only widened with time, eventually becoming an obvious crack. If additional stress was introduced soon after the appearance of a new "ghost", the crack yawned but did not grow further. If the additional stress was applied at a stage when a new "ghost" was expected, the crack did grow by an appreciable distance. Therefore, he concluded that SCC cracks can progress by short cleavage periodically in ductile materials.

In this crack trace study, it was argued that surface trace observation did not represent the behavior of subsurface cracks. However, a particular fractographic technique first employed by Bursle and Pugh [21] established that the behavior of the surface trace is representative of subsurface cracks. In their load pulsing test, SCC fracture surfaces were marked by applying small periodic load pulses on an otherwise constant load during crack propagation. The load pulses cause limited plastic blunting at the crack tip and thus mark the position of the crack front on the fracture surface. The crack front showed little bowing and extended continuously to the observation surface. This technique suggests that if the crack propagation is continuous, a one-to-one correspondence would appear between the number of the load pulses and the number of crack front markings (CFMs) observed. If the crack propagation is discontinuous, load pulses in the non-propagating period would not be marked. Therefore, the distance between CFMs, Δx, would attain a limiting value with the pulse frequency increase, approximately equal to the crack advance distance, Δx^*, under constant load.

The results obtained supported the assumption of discontinuous propagation. In earlier load-pulsing tests carried on copper alloys, the crack arrest markings (CAMs) and CFMs were distinguished by the amount of blunting, the latter being more discernible. The CAMs had the spacing Δx^* of 2 μm [18]. Later, Pugh *et al* [22] tested 310 stainless steel in chloride solution by increasing the pulse frequency. They found the CFMs decreased linearly with the decrease in pulse intervals Δt until Δt reached 15s. For Δt below 15s, there were fewer markings than pulses, their spacing remained at 0.4 to 0.7 μm. These results indicated the crack arrest time Δt^* approximately 15s and crack advance distance Δx^* approximately 0.4 to 0.7 μm. Similar results were reported by Desai *et al* [23] that Δt^* is approximately 5s and Δx^* is approximately 0.4 μm in 316 stainless steel tested in chloride solution.

The discontinuous nature of crack propagation is also indicated by the occurrence of discrete acoustic emissions. In Beggs' work on Cu-30Zn [18], each advance of the crack trace was associated with a discrete signal. Each emission preceded the appearance of the fine crack by several seconds, and it was presumed that the crack was not resolvable with the optical microscope until some blunting had occurred. It was reported that the discrete emission lasted 1 ms in admiralty metal [19], including the ringdown time. Thus, the real crack propagation duration may be only 1 μs.

Newman and Sieradzki [20] recorded the anodic current transients during crack propagation and found they could also interpret the discontinuous process as acoustic emissions. They used conventional instrumentation to monitor the electrochemical current together with an analogous signal proportional to the number of acoustic events. The correlation between two showed their simultaneity was within approximately 1 ms. The magnitude of the current transients was consistent with the crack advance distance measured metallographically.

Pugh *et al* was unable to detect the discontinuous propagation on intergranular SCC cracks either by load pulses or the discrete acoustic emissions [18,22]. They did not rule out the possibility of discontinuity on a submicroscopic scale. The crack advance might be very small during intergranular propagation, so that discrete signals are difficult to distinguish from noise, and are also not resolvable by typical microscopy.

1.2.4 Fractography

1.2.4.1 Stainless steels in aqueous chloride solutions

The SCC fracture can be both transgranular and intergranular. Stable austenitic stainless steels, such as 310, tested in boiling $MgCl_2$ aqueous solutions exhibit almost entirely transgranular fracture in a non-sensitized condition. Intergranular fracture was observed in Type 304 stainless steel [104] and in 316 [81]. For a cold-worked metastable austenitic stainless steel [105] and 316 stainless steel [81], increasing K or increasing the negative electrochemical potential increases the tendency towards intergranular cracking. The transgranular fracture resembles that in hydrogen-induced cracking, but detailed differences have been reported on the local cracking path [106] and macroscopic cracking plane relative to the loading axis [107]. When the 300 type stainless steels are sensitized, the precipitation of chromium carbides occurs at the grain boundaries, which causes depletion of chromium in the material near the grain boundaries. The SCC fracture is then mainly intergranular.

1.2.4.2 Copper alloys in aqueous ammonia solutions

The SCC appearance of copper alloys in aqueous ammonia is rather complex. The occurrence of transgranular and intergranular fracture depends on the solution chemistry, the material composition and microstructure, the geometry of the specimens and the crack tip stress intensity factor K. Earlier investigations, employing non-concentrated ammonia solution

with different pH values [108] and concentrated ammonia solution (15N), suggested that the transition from transgranular to intergranular cracking coincided with the onset of tarnishing [93]. Later studies showed that this simple correlation was not totally valid. Failure of Cu-Zn alloys in non-tarnishing solution is intergranular for zinc contents less than 18% and transgranular for zinc contents above this value [96], while cracking in tarnishing solution under good surface protection was found dominantly transgranular [109]. Heavily cold worked brass presents transgranular fracture [93]. Transgranular fracture was also favored under plane stress conditions at high K, while intergranular fracture was favored under plane strain conditions at low K in a 20% cold worked brass [110]. In neutral ammonia solution, a small proportion of transgranular fracture appears in thick (9.51 mm) specimens [111] compared with completely intergranular fracture in thin (0.64 mm) specimens [112]. The intergranular fracture was also observed [113] at areas near the lateral surfaces in thick specimens.

1.2.4.3 Crack crystallography

The fractography of transgranular SCC in fcc materials has been extensively studied [2-5,81,104,105,109,113]. Virtually all transgranular SCC fracture surfaces so far studied are closely similar in their cleavage-like appearance. The microfractography is schematized in Fig.1.9. It is characterized by a series of flat, parallel facets (primary facets) which are separated by steps or secondary facets, and sheet-like facets. In many cases, the primary facets are made up of two or more sets of microfacets. The steps or sheet-like facets, often perpendicular to the primary facets, form river lines and fan patterns, indicating the local propagation directions. Alternating microfacets meet each other along striations normal to the local propagation directions. The opposite fracture surfaces are perfectly matching and interlocking in many alloys. Undercutting is often observed. Some crack-arrest markings are also reported for certain conditions.

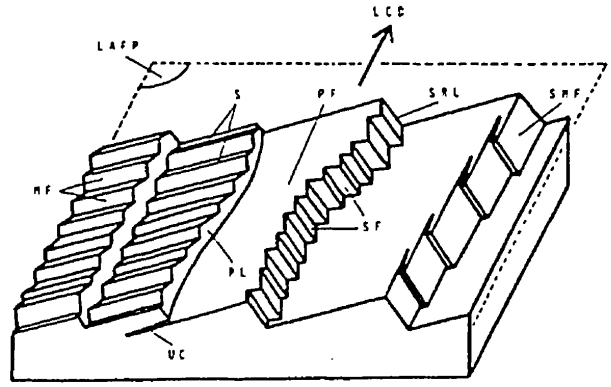

Figure 1.9 Schematic illustration of transgranular SCC microfractographic features. LAFP – local average fracture plane; LCD – local crack propagation direction; MF – microfacets; PF – primary facets; S – striations; SF – serration facets or steps; SMF – sheet-like facets; UC – undercutting.

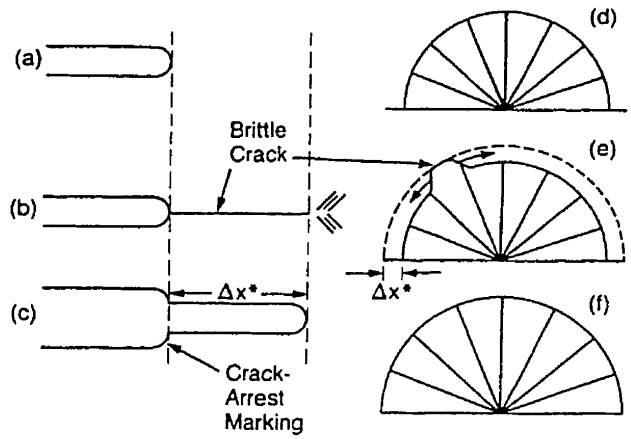

Figure 1.10 Schematic illustration of successive events during transgranular SCC propagation. (a) An arrest stage; (b) Cleavage on {110} planes accompanying with shear on {111} planes which forms steps; (c) Crack arrest caused by shear at the crack tip. A plane view of a semicircular crack is represented by (d) through (f).

Because of the cleavage-like appearance, many efforts have been made to try to determine the orientations of SCC facets and steps in fcc materials. However, the techniques employed are often not ideal for fracture surfaces. The results reported in the literature are often conflicting.

Many authors reported that the primary facets in various copper alloys are {110} planes and secondary facets consisting of serrated river lines are on {111} planes [114–116]. This quite common crystallography led Pugh [117] to propose a discontinuous propagation process in SCC schematically shown in Fig. 1.10. He suggested that the lattice at the crack tip is embrittled by the environment and the crack advances by cleavage on {110} planes for a limited distance. The steps connecting different {110} planes formed by plastic shearing on {111} planes. Because of this shear, the crack tip progressively becomes blunted and then cracking stops.

Compared to the results in copper alloys, the crystallography obtained in stainless steels are more diverse. {100} and {110} primary facets were mostly reported [118–122], but other planes [123-125] such as {210}, {211} and {310} are also indicated as possible. The crack initiation tends to occur on {111} planes, which was supported by the studies of replicas [126] and thin foils [127,128] under TEM. The different results in crystallography should be attributed to the limitations of techniques employed in measurements. It was proposed that [119] SCC initiation is an electrochemical process which takes place preferentially at Lomer-Cottrell barriers. The orientation of the cracking plane depends on the number of dislocation pile-ups on the primary and conjugate {111} slip planes. If equal number of dislocations pile up on each of the two {111} planes, a {110} or {100} fracture appears. If the dislocations pile up on only one {111} plane, then the fracture plane would be 70° from the {111} plane, that is, on another {111} plane.

A particular thorough study of SCC fractography of austenitic stainless steels and of 70Cu-30Zn correlated with K showed [113] that crack path on a sufficiently microscopic scale follows {111} planes. At low K the {100} primary plane in austenitic stainless steels and the {110} primary plane in 70Cu-30Zn can be seen to be made of two pairs of very fine microfacets. As K increased, the size of microfacets increases and could be determined as {111} planes by etch pits. Some primary facets near {110} and {111} appear. The propagation directions indicated by river lines are <110> and sometimes <100>. The <112> propagation direction was often found at low K in 70Cu-30Zn. The orientations of cracking were suggested to be determined by the number of {111} slip planes. Since a {100} and a {110} plane bisect respectively the obtuse and acute angles between a pair of {111} microfacets, the alternating between two {111} microfacets can give rise to a {100} or a {110} fracture plane. If all four sets of {111} slip planes operate, {100}<100> patterns are favored.

1.2.5 The Mechanisms of stress corrosion cracking

Mechanistic studies of SCC have aroused scientific controversy since the very beginning. The history of SCC mechanism research shows an interesting pattern started from diverse suggestions in the 1950s. The various models fell into two groups in the 1960s. One group considered that crack propagation proceeds by anodic dissolution at the crack tip and the other proposed that cracking occurs by mechanical fracture. Some investigators believed that there existed a universal mechanism applied to all systems. This classification had been followed by some mechanism reviews [129–131] in the late 1970s and early 1980s. It was the wide application of scanning electron microscope on fractography that the importance of the local fracture process near crack tips was realized. With the establishment of new techniques which allowed dislocations to be observed near fracture surfaces and *in situ* observations in environment cells under the transmission electron microscope, the plasticity involved in cleavage-like SCC fracture attracted much attention in the 1980s. Although the original suggestion was made by Beachem [51] in

hydrogen embrittlement of steels, localized plasticity has also been observed during SCC [2-5,52,146]. Since then, many new approaches have involved this concept. In this section, some important proposed mechanisms will be briefly described.

1.2.5.1 Anodic dissolution mechanisms

Anodic dissolution was first proposed by Dix [132]. He suggested that galvanic cells are set up between precipitates and adjacent metal at grain boundaries or within grains. The segregated solutes or precipitated phases in these regions result in preferential dissolution in the presence of appropriate environments. The mechanisms related to this concept are stress-assisted intergranular corrosion or tarnish rupture, slip dissolution and corrosion tunneling.

1.2.5.1.1 Tarnish rupture

The tarnish rupture model was initially proposed by Forty and Humble [133] to account for SCC of Cu-Zn alloys in aqueous ammonia. It is also relevant to other systems, notably to the intergranular cracking of low strength ferritic steels and austenitic stainless steels. As shown in Fig. 1.11, the model requires that environments produce a brittle or mechanically weak surface film which grows preferentially along grain boundaries. The growth of the grain boundary film is limited by transport across the film. When stress is applied, the film undergoes brittle fracture to some critical depth. The crack is arrested by plastic deformation encountered in the substrate which destroys the transport barrier and permits continued penetration along the boundaries. This process is then repeated, leading to discontinuous crack propagation. The role of the stress here is simply to eliminate the barrier to transport, and thus the mechanism should be properly described as stress-assisted intergranular corrosion.

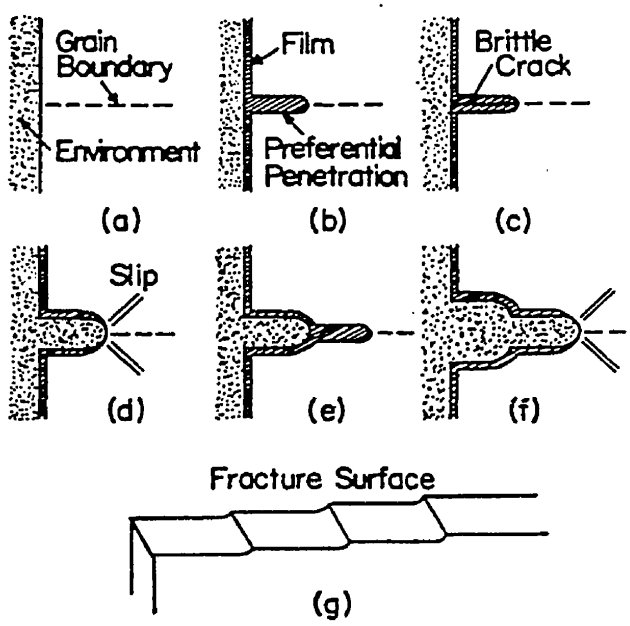

Figure 1.11 Schematic representation of tarnish rupture model: (a) a grain boundary intersected with the surface exposed in an environment; (b) preferential penetration of a film on the grain boundary; (c) a brittle crack formed at a critical length within the film; (d) crack arrest at the ductile substrate; (e) preferential formation of the film again along the grain boundary; and (f) repeated cracking process. (g) Discontinuous propagation observed from the fracture surfaces.

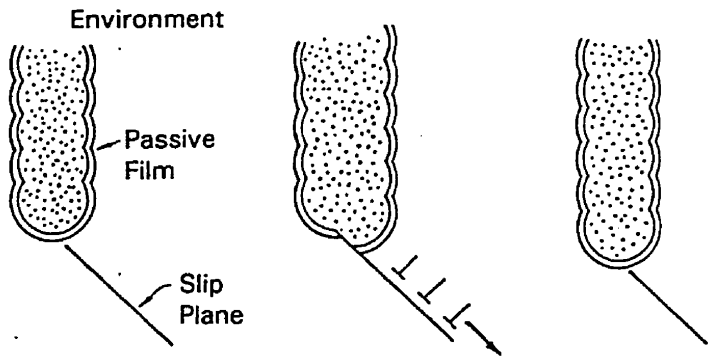

Figure 1.12 Schematic representation of the slip dissolution model.

1.2.5.1.2 Slip dissolution

Slip dissolution, also termed as film rupture, is another dissolution model which had retained great attention in interpreting transgranular SCC before the early 1980s. The basic hypothesis [134,135] is that a protective surface film is disrupted by localized plastic deformation at the crack tip. The exposed substrate is anodically attacked rapidly while the crack walls remain protected by the film. Subsequent formation of the film at the slip step causes the crack growth to cease until further slip destroys the film again and the dissolution is reinitiated (Fig. 1.12).

1.2.5.1.3 Corrosion tunneling

Some investigators reported that preferential attack occurs on planar dislocation arrays in TEM foils [136], especially in fcc alloys having a low stacking fault energy or displaying short range order. Such observations led Swann and Pickering [137] to suggest that this preferential attack resulted in arrays of fine corrosion tunnels, which subsequently interconnected by tearing of the remaining ligaments between the tunnels (Fig. 1.13).

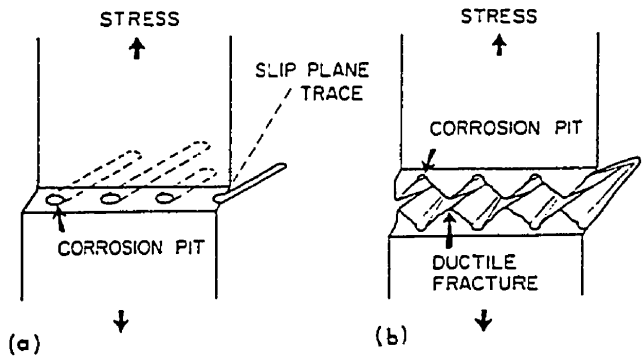

Figure 1.13 Schematic representation of tunnel model.

1.2.5.2. Embrittlement mechanisms

Embrittlement mechanisms are based on the view that the lattice ahead of the crack tip is embrittled by interaction with the environment, and that the crack propagates discontinuously by the repeated formation and brittle fracture of this brittle layer.

1.2.5.2.1 Film-induced cleavage

The film involved in dissolution models is generally regarded to be a passive film or an oxide film. In the film-induced cleavage model, the film can be a dealloyed layer or an oxide, chloride, nitrides or even a porous metallic layer [138,139]. This model differs from earlier film models in that the crack propagation primarily occurs in the substrate, rather than being confined to the film. It is proposed that anodic reactions between a metal and its environment produce a thin film on the metal surface. Due to the elastic modulus mismatch and the lattice parameter misfit with the substrate, this thin film around the crack tip modifies the local deformation and induces cleavage to an intrinsically ductile metal. Atomic modeling studies indicated [139] that a brittle crack can attain a velocity of hundreds of *m/s*, like a cleavage crack, and propagate approximately one micron into the unaffected substrate before arresting.

1.2.5.2.2 Stress sorption

There have been several attempts to explain all instances of environment-assisted cracking, including hydrogen-induced cracking, SCC and liquid metal embrittlement, by some universal mechanism since the 1960's. The adsorption mechanism is one of these. The principal proponent, Uhlig [140], referred to his model as the stress sorption theory. The basic proposal is that adsorption of specific species reduces the surface energy, leading to a reduction in the stress required to produce brittle fracture. Stated more

atomistically [141,142], it suggests that some specific species adsorbs and interacts with strained bonds at the (elastic) crack tip, causing a reduction in bond strength. Later Uhlig [143] claimed that adsorption occurs at dislocations or other mobile imperfections in the vicinity of the crack tip. In order to explain that pure metals are immune to cracking, he pointed out that the role of the environment is to specify the adsorption species on the surface and to determine whether adsorption can or cannot occur. So this model ascribes the same basic environment cause of cracking in stressed metals exposed to damaging electrolytes, hydrogen gas or liquid metals.

1.2.5.2.3 Surface mobility

The most recent universal model is the surface mobility SCC model of Galvele [144,145]. He suggested that high surface mobility is the only common factor to be found in SCC including liquid, gaseous environments and in liquid metal embrittlements. If a sufficiently high surface mobility is induced by the environment, atoms at the crack tip will be transported by surface diffusion from the highly stressed locations at the crack tip to the less stressed crack sides. This process introduces a vacancy at the crack tip and advances the crack by one atom spacing for each such a movement. The coefficient of surface self-diffusion D_s of the metal controls the crack growth rate. The role of the environment is to increase the surface self-diffusivity by forming low melting point surface compounds. If the compounds formed have high melting points, the crack will be protected.

1.2.5.3 Mechanisms related to dislocations

While macroscopic characteristics suggest that SCC is essentially a brittle fracture, there is much evidence indicating that it is associated with some plastic deformation. The latter is not simply related to the yield stress being achieved in the remaining section as

crack growth occurs, because the initiation of cracking can be correlated with the occurrence of microplastic deformation below the yield stress.

1.2.5.3.1 Adsorption-induced localized slip

Beachem [51] observed microvoids and tear ridges existing on cleavage planes and intergranular grain boundaries during hydrogen-induced cracking. That led him to propose a hydrogen-enhanced microplasticity theory. Such fine dimples have subsequently been observed by Lynch [52,146]. Based upon the assumption that cleavage planes should be those associated with minimum slip systems [147], Lynch suggested a unified model for environment-assisted cracking. In this model, adsorption is thought to weaken interatomic bonds at the crack tip thereby facilitating the injection of dislocations from crack tips. As a consequence, crack-tip dislocation sources are now active before extensive dislocation activity occurs ahead of cracks. Dislocations injected from the crack tip on suitable inclined slip planes produce crack advance. Crack opening displacements are accommodated mainly by crack growth. The dislocation nucleation at the crack tip often occurs in roughly equal amounts on either side of the crack, because any imbalance would produce a large back stress from dislocations previously injected on the more active slip plane. This stress prompts subsequent dislocation nucleation on the other slip plane. Thus macroscopic {100} planes are produced by the injection of equal amount of dislocations on two inclined slip planes at the crack tip. If the adsorption occurs preferentially on the grain boundary, intergranular cracking appears. This model is schematically shown in Fig.1.14.

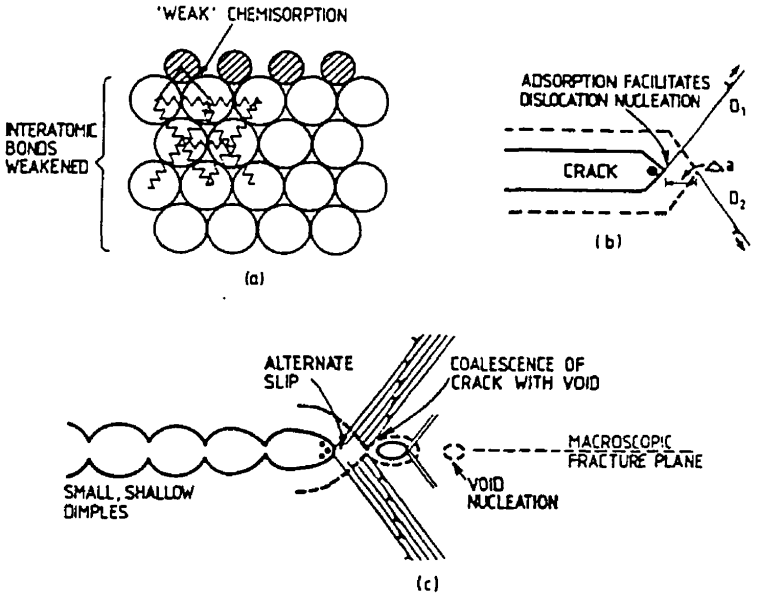

Figure 1.14 Schematic representation of the adsorption-induced localized slip model: (a) adsorbed atoms weaken interatomic bonds; (b) dislocations injected from slip planes D_1 and D_2 produce a crack advance Δa; and (c) crack propagates by microvoid formation and alternating slip coalescing with the voids.

1.2.5.3.2 Corrosion-assisted cleavage

Another microcleavage model is Lichter's corrosion-assisted cleavage model [148,149]. This model was proposed to explain {110}<001> fractographic features in α-brass and in Au-Cu alloys where the hydrogen effect is considered impossible. Employing Stroh's pileup mechanism for opening a Lomer-Cottrell lock [150], the calculation indicates that selective dissolution reduces the critical stress intensity factor K_{IC} needed to open an incipient crack, a Lomer-Cottrell lock induced by the dislocation pileups at the SCC crack tip. Such a stress state could produce cleavage before shear on a plane perpendicular to the Burgers vector of the Lomer-Cottrell lock, *i.e.*, {100} planes. Crack propagation is anisotropic. Discontinuous crack growth near {110}<001> is due to the crack arrest by dislocation blunting on slip planes coincident with the crack front.

Repropagation of an arrested crack involves active dissolution of shear bands at the crack tip, which is assumed to lower the K_{IC} by "breaking" crack tip bonds.

1.2.5.3.3 Corrosion-enhanced plasticity

Magnin *et al* [56,151] also noticed that {111} microfacets often intersect in a zigzag manner to produce average {100} propagation. Thus he proposed a physical model to interpret this cracking feature of austenitic stainless steels in chloride solution. It is based on the interaction between the localized dissolution, the localized adsorption and the dislocation behavior at the crack tip. As shown in Fig. 1.15, a localized anodic dissolution takes place on the {111} slip planes at the very crack tip after depassivation. This localized corrosion and chemisorption enhance localized shearing. Emitted dislocations then interact with obstacles to produce dislocation pileups. If the obstacles are strong enough, K_{IC} will be reached locally. A crack embryo then forms by a kind of Stroh mechanism [150] at the obstacle. Adsorption decreases the decohesion strength of the {111} microfacets leading to cracking along the {111} plane. In mixed I/II mode, dislocations emitted on symmetrical {111} plane *vs.* the main crack shield the new crack tip. This process is expected to lead to regular changes of crack planes. Zigzag microcracking can occur on {111} and/or {100} facets.

Recently, this model was developed and adapted to interpret intergranular SCC. It was suggested that the influence of localized dissolution and adsorption on the local plasticity is qualitatively the same for both transgranular and intergranular SCC. Fracture can occur on grain boundaries because the pileup formation depends on the relative orientations of the grain boundaries and the {111} planes with regard to the main stress axis.

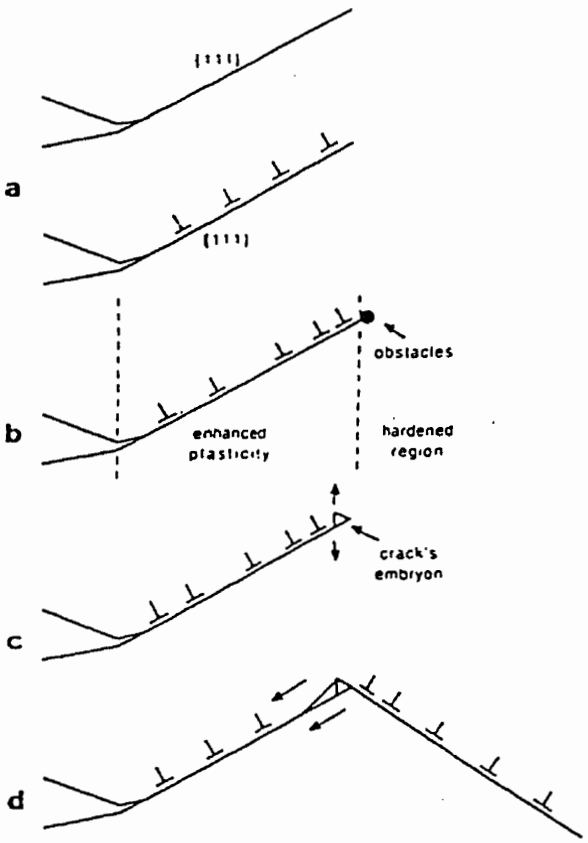

Figure 1.15 Schematization of corrosion-enhanced plasticity model.

1.2.5.4 Hydrogen involved in stress corrosion cracking

SCC may not be as simple as a stress-corrosion problem. In some cases the SCC behavior indeed attributes to pure SCC, but a number of cases are known where hydrogen is involved, such as SCC of high strength steels in aqueous solution. Electrolytic hydrogen can be introduced into materials as a consequence of electrochemical corrosion at crack tip regions. Thus various mechanisms summarized in section 1.1.3 can all be applied to SCC associated with hydrogen.

In many cases the fracture appears to have contributions from both SCC and hydrogen-induced cracking, although they may be difficult to distinguish. The following similarity of both failure process were summed up by Thompson *et al* [152,153]:

1) The material becomes more sensitive to degradation as the strength of an alloy is increased in both failures.
2) Susceptibility to both fractures depends on the slip mode. Alloys which are most sensitive typically exhibit planar slip.
3) Discontinuous crack propagation was observed both in SCC and hydrogen-induced cracking.
4) Both fractures have similar dependency of crack propagation rates on stress intensity (three stage velocity *vs.* K curves).
5) There exists a threshold stress (or stress intensity) below which failure or crack propagation are not observed.

Also, both fractures have similar grain size dependencies and entry processes into metals in hydrogen gas and in aqueous environments. Similar response to metallurgical variables and similar temperature and strain rate dependencies were observed in some systems.

1.3 MICROSCOPIC FRACTURE PROCESS

As already reviewed in previous sections, stress corrosion cracking and hydrogen-induced cracking usually shows macroscopically brittle characteristics in otherwise ductile materials, such as a low or even zero elongation in tensile fracture and cleavage-like fracture surfaces. Microscopic ductility, however, can be increased by species which are detrimental to mechanical properties. Thus, the microscopic cracking process in an environmental media is not represented by its macroscopic aspects. This section will present firstly the microscopic cracking process in an inert environment and then the environmental effects on fracture, with the focus on the microscopic scale.

1.3.1 Crack tip microplasticity in inert environment

1.3.1.1 The emission of dislocations at the crack tip

Some metals such as pure copper normally fail by plastic instability and necking on a macroscopic scale. Some materials like diamond and mica apparently can undergo pure brittle cleavage with no observable plasticity. In between these two extremes, there exists a class of materials where a cleavage crack in the true atomically sharp sense exists, but is surrounded and associated with dislocations. For example, by examining the elastic interaction of a crack tip and a dislocation, Rice and Thomson [154] found that in iron and fcc metals, spontaneous or thermally assisted blunting at a crack tip occurs. Dislocation emission from cracks was observed both in bulk single crystals [155] and in TEM specimens of various materials [11]. In mode I crack, edge dislocations are emitted from the crack tip on two symmetrically inclined slip planes. In mode II and III cracks, edge and screw dislocations are generated on planes that are inclined or slanted respectively to the tensile stress. Emitted dislocations are driven out of the crack tip area, leaving behind a dislocation-free zone which can be as small as 170 nm in ductile materials [12].

A criterion for dislocation emission from the crack tip was first suggested [154] to related to the value of $\mu b/\gamma$, where the γ is the surface energy of the crack plane. Later, Anderson and Rice [156] further suggested that crystallographic parameters, such as the orientation of the crack plane and the direction of crack propagation relative to the available slip system, must be considered in evaluating the cleavage *vs.* dislocation emission competition. The existence of a dislocation-free zone at the crack tip indicates that emitted dislocations are strongly repelled by the stress field of the crack tip. The plastic deformation produced by dislocation emission thus reduces the local stress intensity factor K_{loc}. This phenomenon is referred as the dislocation shielding of the crack tip [157,158]. Thus, a criterion of dislocation emission should be defined as [11,159]:

$$K_{loc} = K + K_{dis} > K_e . \qquad (1\text{-}8)$$

Depending on the sign of K_{dis}, the crack tip K_{loc} can also be increased. This is the condition of anti-shielding, when dislocations from other sources ahead of the crack tip are attracted to the crack tip region.

1.3.1.2 Crack tip dislocations and fracture

Conventionally, fracture of materials will either be ductile or brittle depending on the ratio of theoretical shear strength to theoretical tensile strength σ_{th}. However, with the observation of crack tip dislocation generation in semi-brittle (Mo, Nb, W) or brittle materials (ceramics), it is not clear to what extent crack tip deformation is related to the ductile *vs.* brittle behavior of materials.

It was found that the nonlinear elastic strain and the hydrostatic stress are very high in the dislocation free zone of 310 stainless steel. The microcrack (10 nm long) initiates when stress concentration reaches σ_{th} within this region, and is then blunted by the operation of second slip system [12]. Further, *in situ* TEM observation showed [13] that the crack tip in ductile materials is blunted by emitting an array of edge dislocations on a

plane nearly perpendicular to the crack plane. The propagation resumes abruptly without emitting dislocations when the area ahead of the crack tip is thinned sufficiently by plastic deformation. In semi-brittle materials, the fracture of a long dislocation-free zone occurs by cleavage, which in some instances is accompanied by the emission of dislocations as well. Therefore, both dislocation emission and elastic fracture contribute to the COD. The crack tip deformation makes it easier for the material to fail finally by brittle fracture.

Many materials studied by Ohr *et al* [13] often showed a mixed mode crack propagation, that is, crack tip plastic deformation on two alternating slip planes with superimposed mode I cleavage. After emitting a number of dislocations on the first slip plane, the crack propagates a certain distance (typically less than 1 μm) concurrently by plastic and elastic fracture and stops temporarily. The second slip system is then activated, and the crack changes planes and propagates along the second direction. The two different Burgers vectors are combined to give the resultant COD close to the direction of tensile axis, thus the observed crack geometry is very similar to that produced by cleavage.

Supporting the observation that the pileup of edge dislocations produces a pure mode II crack and the pileup of screw dislocations produces a mode III crack, the calculation of Hirth [160] suggested that these slip or shear would induce subsequent mode I separation on slip planes. The stress concentration produced by the linear elastic field of a pileup of edge dislocations would open a pure mode I crack inclined −70° to the slip plane, while the nonlinear core field produced either by edge or screw dislocations creates a stress concentration σ_{yy} on slip planes. This stress concentration provides the driving force for the decohesion of slip planes, although it makes a smaller contribution to the energy release.

1.3.2 Environmental effects on fracture

1.3.2.1 Adsorption

Adsorption is a phenomenon that allows higher concentration of gas or liquid molecules (the adsorbate) to stay on liquid or solid (the adsorbent) surfaces. This process usually does not accompany chemical reactions between the adsorbate and the adsorbent. The adsorbent remains in its original physical and chemical state throughout the operations. Physical adsorption refers to cases where there is no electronic interaction or relatively weak interactions (similar to condensation) between the adsorbent and the adsorbate; therefore, the surface characteristics of the adsorbent are not significantly changed. Chemisorption is a process involving strong intermolecular forces, similar to chemical reactions, but it only affects the surface monolayer.

1.3.2.1.1 Effect on decohesion strength

Kamdar *et al.* [161,162] proposed that adsorption could reduce the lattice decohesion strength at the crack tip. As shown in Fig. 1.16, adsorbate atom B only affects a few atoms at the crack tip (Fig. 1.16a) because of free electron screening effects. The bond strength a larger distance away from the crack tip will not be affected by adsorption of atom B to cause the dislocation motion in the vicinity of the crack tip. He suggested that the density of the cohesive electron cloud between crack tip atomic bond A-A_0 is reduced by the presence of atom B. The equilibrium distance between A-A_0 is reduced to a_c from a_0 which is the equilibrium distance between atoms across the fracture plane without adsorption. Thus, the stress required to break the A-A_0 bond is reduced from σ_m to $\sigma_{m(B)}$, according to the interatomic stress σ *vs.* bonding distance a curves (Fig. 1.16b) in the absence and presence of adsorption.

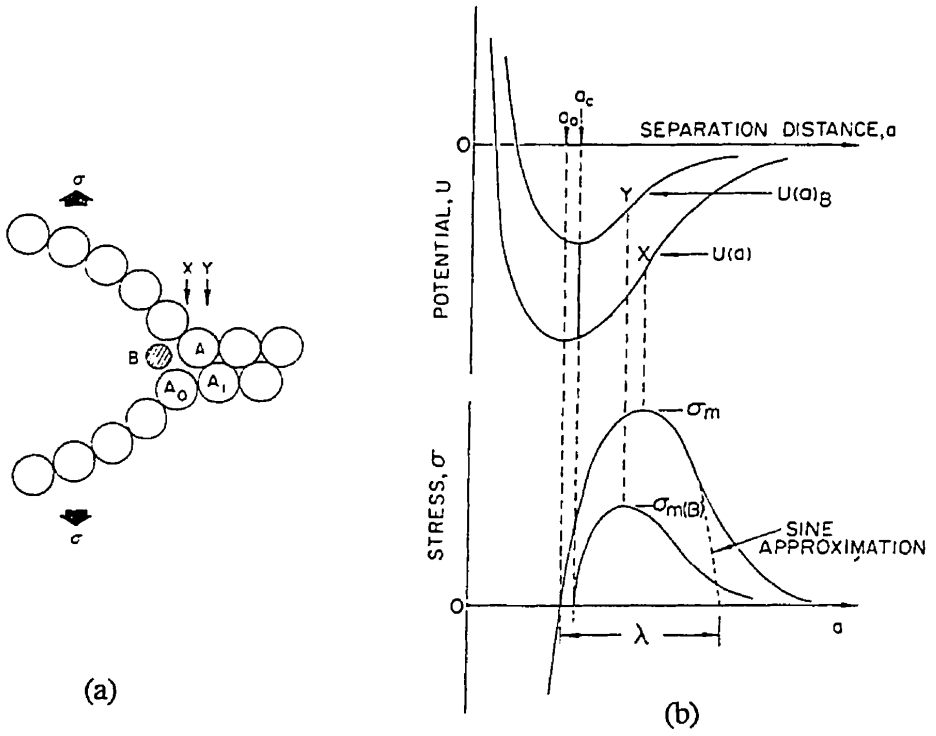

Figure 1.16 Proposal of adsorption-reduced decohesion strength at the crack tip. (a) Displacement of atoms near the crack tip. (b) Schematic potential energy U(a) and $U(a)_B$, and resulting stress σ(a) and $\sigma(a)_B$ *vs.* separation distance for A-A_0 bond in the absence and presence of liquid metal atom B.

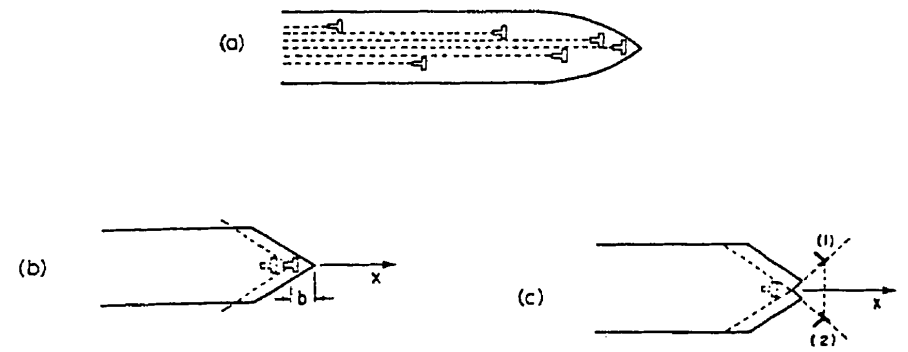

Figure 1.17 Dislocation models of crack tip process: (a) array of dislocations representing crack, (b) cleavage and (c) crack tip blunting by plastic shear.

1.3.2.1.2 Effect on surface energy

Petch [163] first used Gibbs adsorption equation to relate the surface energy reduction of iron to hydrogen adsorption. The uniformed distribution of hydrogen in the crack tip lattice required in his model was then opposed by later studies, thus less attention was paid to this model. However, Tromans [164] who believes that bond energy and surface energy are inter-related, redirected attention back to the surface energy changes. He has recently developed a suitable adsorption isotherm to treat the real situation (high local concentration of hydrogen, impure materials and local stress concentration) of hydrogen-induced cracking. This adsorption isotherm represents the interactions between the surface and a mobile hydrogen atom in the metal lattice, and in a manner similar to Petch, relates the adsorption to the surface energy reduction. Calculated surface energy changes are generally consistent with deleterious effects of hydrogen reported in the literature. It was concluded that a high stress is necessary to produce a sufficient decrease in surface energy to promote cracking.

1.3.2.1.3 Effect on dislocation nucleation

Strong chemisorption, such as oxygen on many metals, often produces incipient formation of compounds (*e.g.* oxide) and adsorbate atoms are often incorporated into the atoms of the topmost layer of the adsorbent. Such disruption of the surface lattice and formation of strong directional bonds between adsorbate and adsorbent atoms will hinder dislocation nucleation. Gilman [165] used a simple crack tip dislocation model (Fig. 1.17) to state this possibility. To create a cleavage plane as shown in Fig. 1.17b, the crack tip tensile stress σ_0 must be equal to or greater than the cohesive strength $2\gamma_c/b$ (γ_c is the surface energy of cleavage planes), however, to blunt the crack tip, the crack tip shear stress τ_0 should satisfy $\tau_0 b > \gamma_g$ (γ_g is the surface energy of slip steps). Since $\sigma_0 \leq 2\tau_0$, the condition for cleavage to occur is $\gamma_c \leq \gamma_g$. Strong chemisorption forms a thin surface

compound and increases the surface energy γ_g by ΔF, but decreases γ_c by the same amount. As a result, cleavage is expected if $\Delta F > (\gamma_c - \gamma_g)b^2/2$. The calculated ΔF is so small, even physical adsorption can have such a value. Therefore, strong chemisorption inhibits dislocation nucleation but favors cleavage at the crack tip.

Atoms at clean surfaces have fewer neighbors than atoms in the interior and hence the lattice spacings in the first few atomic layers are often smaller, probably by approximate 5%, than those in the interior. Such "surface-lattice distortion" could hinder the nucleation and motion of dislocations at surfaces, since dislocation moving in the first few atomic layers would be associated with larger-than-normal lattice distortion. Weak chemisorption, as suggested by Lynch [57], effectively increases the number of neighboring atoms. The "surface-lattice distortion" is reduced and the dislocation nucleation is facilitated at the crack tip. In other words, the transfer of electrons from weakly adsorbed embrittling atoms to solid metal atoms locally increase the electron density, increase the repulsive force between the surface atoms and therefore reduce the shear strength of interatomic bonds at surfaces.

1.3.2.2 Surface films

The importance of surface films on the initiation and propagation of SCC cracks has long been recognized. One of the most durable concepts in SCC research is that crack growth occurs by highly localized anodic dissolution. The model related to this concept (slip dissolution or film rupture) describes film breakdown as a necessary process for SCC to occur. When a plastic strain is applied to a surface with a surface layer, often assumed to be a conventional passive film, transient dissolution and repassivation take place alternatively at the crack tip, allowing SCC to continue. This model has been applied to a wide variety of SCC systems, but fails in systems where no passive film forms. For example, copper alloys immersed in tarnishing ammonia solution form a tarnishing film which is mainly oxide. Shimodaira

suggested [166] that a thick tarnish film could suppress slip while a thin tarnish film favored transgranular cracking. Forty concluded [167], however, for the same system, that dezincification was the most likely surface process involved. The injection of vacancies by chemical dezincification of the brass leads to surface embrittlement, which sufficiently restricts the plastic deformation of the underlying brass, so that a crack forms.

Usually, the proposals [93,166] on film-induced cracking in brass-ammonia system are consistent with the slip dissolution model except for the different properties of the films considered. The dezincification alternative involves the embrittlement effect of the film, but there is no dizincification near the tips of cracks in non-tarnishing solution [168] and it cannot account for a very fast SCC velocity. Therefore, the definition of film must be extended to a wider range. Similar to the dezincification layer in brass, dealloying (selective dissolution) occurs in solid solutions where there is a large difference in reactivity between the components. A dealloyed layer often shows nanoporous morphology which has been found in brass [128], Au-Ag [169] and Au-Cu [170] alloys. A dealloyed layer can initiate brittle fracture that propagates beyond this layer into the substrate. The important parameters determining crack initiation are the film-substrate misfit, the bonding strength across the film-substrate interface, the film thickness and the film ductility [138]. It was also proposed that other forms of reacted film can nucleate cleavage [139,171 ,172]. These can be oxides, nitrides and a carbide or carbon hardened layer. For stainless steels, the possibility of dealloying was suggested [75,172] and spongy layer was observed [173]. However, the presence of a dealloyed layer has not been demonstrated. Newman *et al* [174] reported that the tarnish film (detected by Auger electron spectroscopy) on 304 and 316 stainless steels is evidence for dealloying of stainless steels in chloride solutions. This film contains some oxygen, a very high concentration of iron, some chromium and enriched nickel near the surface. They therefore suggested that SCC of stainless steels in chloride solution also occur by film-induced cleavage.

1.3.2.3 Dissolution

Dissolution is the first step in most cases of SCC. Usually, it provides the possible initiation sites for SCC cracks through pitting or crevice corrosion. Under the applied stress or strain, the stress concentration at these corrosion sites opens a microcrack and helps continue its propagation.

In the past decades, the effect of dissolution has been discussed in the microscopic scale with the relation between dislocation structures in materials and the SCC crack path. Preferential attack of environments happens to structural imperfections, such as strained slip planes [175] or solute segregated stacking faults [176]. It was [177,178] pointed out that alloys with a planar dislocation structure and/or short range order are more susceptible to transgranular SCC because the destruction of short range order by plastic deformation on the slip planes induces localized chemical attack. Latter, the TEM observations found that dislocations are subject to preferential dissolution and are the principal initiation sites for both intergranular and transgranular SCC. In annealed 70Cu-30Zn [128], small (1.5%) prestrain-induced short dislocation pileups against grain boundaries, which resulted in the intergranular cracking and occasional transgranular cracking immediately adjacent to the main grain boundaries. The selective dissolution began in grains at a prestrain of 2%. As the prestrain increased to 5%, mixture of intergranular and transgranular cracking occurred.

Chapter 2

Experimental Procedures

2.1 MATERIALS

The stainless steels employed in this study were 316L and 310. The plates were first hot-rolled, then annealed at 1050°C for one hour followed by water quenching. Their compositions of the main elements analyzed [179] are shown in Table 2.1.

Table 2.1 Analyzed composition of 316L and 310 stainless steels

wt %	C	Cr	Ni	Mo	Mn
316L	0.06	16.42	11.08	0.64	1.55
310	0.05	20.9	21.7	—	2.30

The thickness of the plates was 50 mm for the 316L stainless steel and 20 mm for the 310 stainless steel. Some retained δ-ferrite was present in the 316L stainless steel,

which was concentrated, approximately 5% in volume, in the mid-thickness of the plate [179]. Metallographic examination showed that the δ-ferrite was in the form of platelets and was sandwiched among austenite grains. In the direction perpendicular to the rolling plane, the platelets can be seen composed of a group of small grains with a grain size of approximately 10 μm (Fig. 2.1). The metallographic specimen showed entirely austenite in 310 stainless steel, but linear regions of preferential attack appeared in the direction parallel to the rolling direction on the plane perpendicular to the rolling plane (Fig. 2.2). EDS analysis indicated that Cr was higher in these preferential attack regions (Table 2.2).

Table 2.2 Regional composition difference in 310 stainless steel

at %	Cr	Ni	Mn	Si	Fe
Average	27.40	18.29	1.42	0.55	balance
In region A	38.72	9.36	2.67	0.26	balance

A commercial foil (thinness of 25 μm) of 316 austenitic stainless steel was employed in the slow strain rate tensile tests. The initial metallographic examination showed equiaxed austenite grains with some annealing twins. Then the foil was annealed in a vacuum of approximately 10^{-3} torr for 15 minutes at 1050°C followed by quenching the vacuum tube with foils into water upon removal from the furnace. This process is supposed to relieve most of the residual stresses and prevent chromium carbides from precipitating on the grain boundaries. The final microstructure was austenite with a grain size of approximately 10 μm. No chromium carbides were found by TEM examination.

The α-brass used in this study was from different ingots, all of which had the nominal composition of 70Cu-30Zn. The hot-rolled 70Cu-30Zn plate received in a 10 mm thick plate had approximate equiaxed α grains with a grain size approximately 0.67 mm. After annealing at 650°C for one hour, the grain size remained unchanged with the hardness decreased from HRB 71 to HRB 64. The grain shapes in the received 15 mm

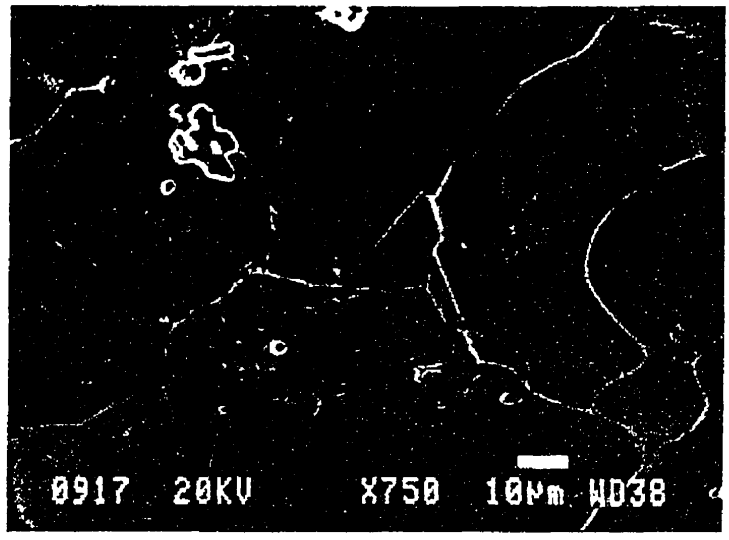

Figure 2.1 The microstructure of δ–ferrite in 316 stainless steel observed from the direction perpendicular to the rolling plane.

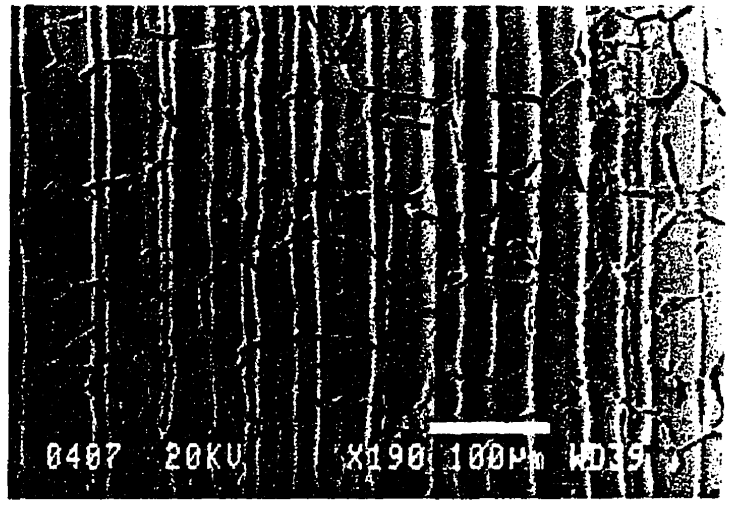

Figure 2.2 The microstructure of 310 stainless steel observed on the plane perpendicular to the rolling plane. The preferential attacked traces appears parallel to the rolling direction.

thick plate were different in three directions (Fig. 2.3). Measured hardness (HRB 83) indicated that it was in a cold worked (hard temper) condition. Annealing was then carried out at 350°C for 1.5 hours in an argon atmosphere, which decreased hardness to HRB 35. The annealing provided well formed equiaxial grains, however, their size varied from 0.01 to 0.08 mm.

This low annealing temperature for 70Cu-30Zn was selected in order to meet the requirement of predominant elastic condition $W-a \geq \frac{4}{\pi}\left(\frac{K}{\sigma_y}\right)^2$ at the crack tip in standard CT specimens [180]. This annealing resulted in a minimum σ_y of 150 MPa$\sqrt{m}$ according to its hardness [181]. Within the calibrated crack length range described in Section 2.3.2.2, elastic requirement was fulfilled under the applied stress intensity factor K during SCC tests on CT specimens. But the plane strain condition was met only for CT specimens in the as-received condition.

2.2 GEOMETRY OF THE SPECIMENS

As shown in Fig. 2.4, T-notched, double cantilever beam (TN-DCB) specimens, reported to be able to minimize macro-crack branching, were employed in SCC tests. Specimens were machined from the as-received plates in different orientations corresponding to the rolling direction L, transverse direction T and short transverse direction S. Their orientations were identified by two letters, the first indicating the normal of the cracking plane and the second indicating the crack propagation direction.

ST orientated specimens were employed in SCC tests of 316L stainless steel. They were machined so that the concentration of the δ-ferrite platelets distributed near the cracking plane was approximately 5%. The distribution of δ-ferrite with regard to the specimen orientations is shown in Fig. 2.5. It is seen that the platelets are parallel to the cracking plane, which minimize the macro-crack branching during SCC, and their

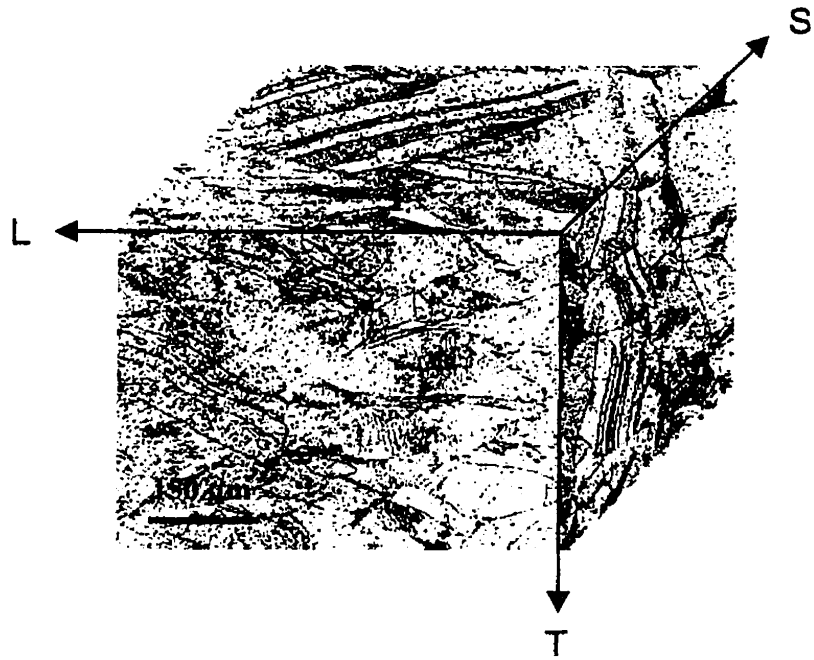

Figure 2.3 A three dimensional illustration of the microstructure of 70Cu-30Zn in the as received condition. The thickness of the plate is 15 mm.

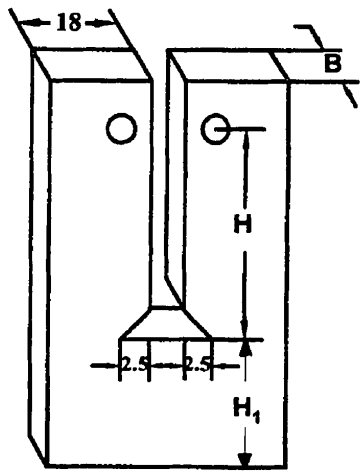

H = 25 mm for stainless steels; B = 4 mm for some of 70Cu-30Zn specimens;

H = 35 mm for 70Cu-30Zn. B = 3 mm for others.

H_1= 20 mm

Figure 2.4 Dimensions of TN-DCB specimens employed

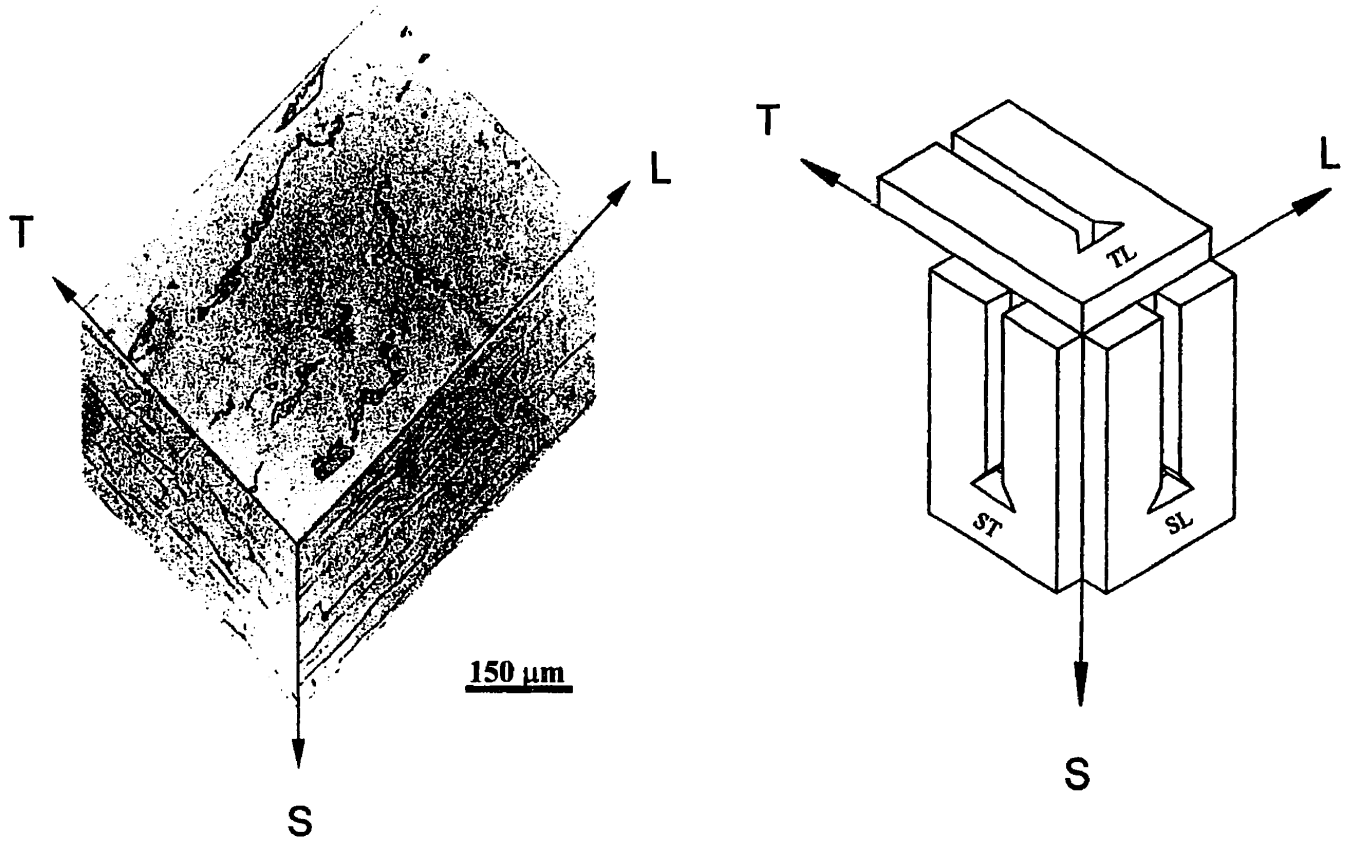

Figure 2.5 The three dimensional distribution of the δ–ferrite platelets in 316L stainless steel with regard to the orientations of TN-DCB specimens.

longitudinal directions are perpendicular to the propagation direction. In SCC tests of 310 stainless steel and 70Cu-30Zn, TL orientated specimens were employed. Standard CT specimens cut from 15 mm 70Cu-30Zn plate were also employed in SCC tests.

Tensile specimens were cut from a 316 stainless steel thin foil. Their dimensions are shown in Fig. 2.6.

Some SCC specimens of 70Cu-30Zn, tested by Maxime Gauthier [226], were employed for fractographic study. These specimens were TL orientated and had the identical dimensions as 70Cu-30Zn specimens employed in the present study. Before SCC tests, the as-received 10 mm plate was reduced in thickness 50 % and 70 % by cold rolling. Then the portion which would be immersed in the ammonia solution underwent slight deformation in tension just past the yield stress of 70Cu-30Zn. This procedure was employed to reduce the residual stress induced by cold rolling.

2.3 SCC TESTS

2.3.1 Testing on TN-DCB specimens

SCC specimens were immersed in testing solutions up to half of their beam length. To prevent the surface corrosion, all the specimens were protected by lacquer except for the notch tips where would be in direct contact with the solution. Then specimens were wrapped with Teflon tape before immersion. Only the lateral sides of the notches were exposed to allow the crack length measurements. Some specimens of 70Cu-30Zn were covered with silicon sealant or glass plates on the lacquer layer to prevent further surface corrosion.

All the SCC tests were performed under freely corroding potentials. The corrosion environment for stainless steels was boiling 44.7% $MgCl_2$ aqueous solution. The boiling temperature (154°C) was controlled by an electric heater placed under the beaker. For 70Cu-30Zn, tests were done under stirring conditions at room temperature. Two solutions were employed. One was a so-called non-tarnishing solution: concentrated 15 N aqueous ammonia with 6 g/l Cu added as $Cu(NO_3)_2$. The other equilibrium solution was used under deoxygenated condition: 15 N aqueous ammonia with 3.6 g/l Cu_2O and 8 g/l Cu powder to give 0.05 N of cuprous copper. To reach the deoxygenated testing condition, the Cu_2O and Cu powder were first added after specimen was mounted in a beaker containing ammonia. A bluish color appeared immediately. The beaker was immediately sealed and nitrogen was introduced. By stirring approximately 3 hours, the solution became transparent, indicating the absence of oxygen in solution [93]. Then the load was applied.

A horizontally mounted tensometer was employed which exerted pin loading on the arms of the SCC specimens with a quite soft spring to reduce the load decrease resulted from cracking. The applied load was maintained manually as approximately constant by periodically readjusting the load. The stress intensity factor K calculated by applied force increased with crack growth. Crack lengths were measured with a traveling microscope in the case of the stainless steels. For the SCC of 70Cu-30Zn in non-tarnishing solution, the blue color of the testing solution did not allow to observe the crack growth. However, the initially applied load tended to decrease 4 to 5 hours after the test had begun. This load decrease indicated that the crack had started to propagate.

Constant displacement was applied on some of the stainless steel specimens which had been tested under constant load. These tests were performed when the specimen remained in the boiling $MgCl_2$ solution and in the same tensometer. The opening cross-head displacement rates employed were approximately 0.05 mm/min and 5 mm/min.

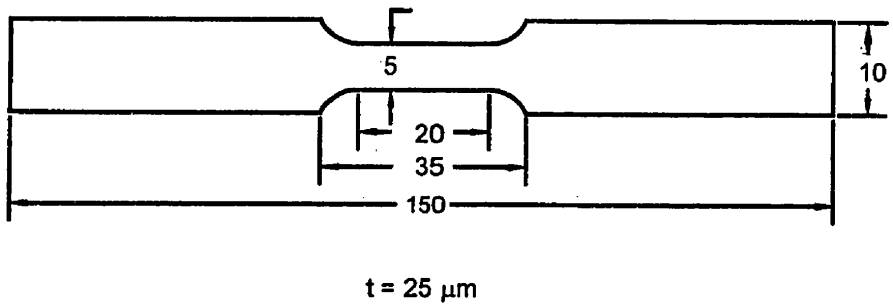

Figure 2.6 Dimensions of 316 stainless steel tensile ribbon specimens.

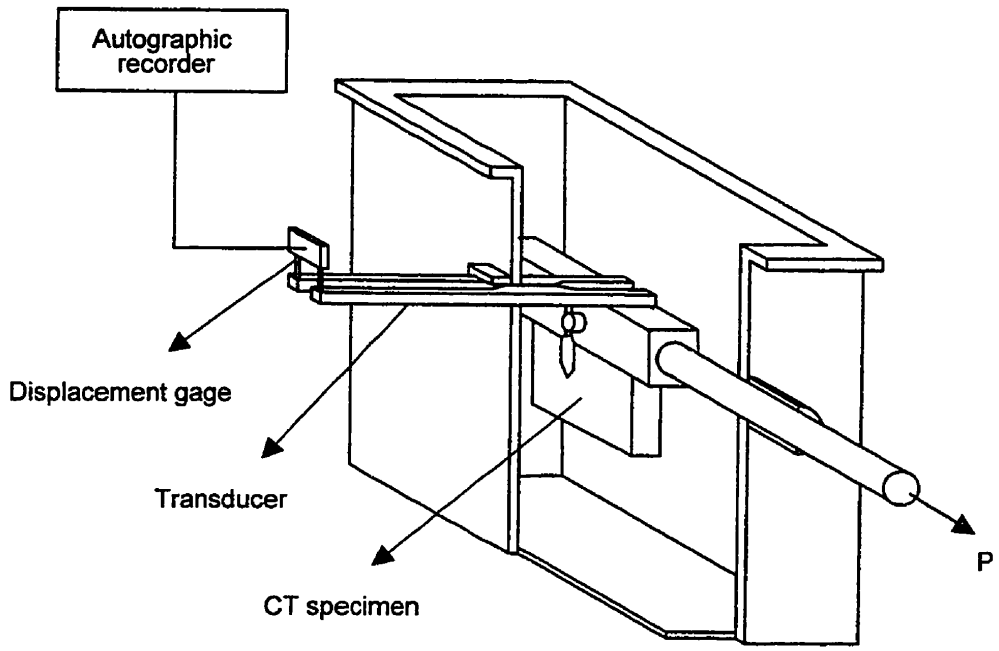

Figure 2.7 Schematic illustration of a SCC testing device employed for CT specimens

2.3.2 Testing of CT specimens

DN-TCB specimens are advantageous in preventing crack branching and shortening the test time. However, they are not suitable for SCC tests of 70Cu-30Zn in ammonia solution. The color of the solution made the simultaneous crack length observation impossible. Thus, the compliance method was employed instead which monitors the crack length growth by measuring the crack opening displacement v. In this method, standard CT specimens are mounted with a displacement gage, for which the relationship between compliance and crack length a has been analytically derived.

A low speed autographic recorder was employed to record the load and the displacement signals which were indicated by the output voltage E of the measuring gage. As shown in Fig. 2.7, a fatigue precracked CT specimen, protected by red lacquer on the surfaces, was immersed in the test solution close to the notch. To avoid the ammonia atmosphere from corroding the measuring gage, a transducer connected the specimen to the gage to transfer and amplify the crack opening displacement to the gage. This system no longer fulfilled the ASTM specification for a single CT specimen [180], because the measuring gage was far away from the positions defined in the analytical equation. Thus, calibration was performed before the SCC test.

2.3.2.1 Linearity of the measuring gage

Before calibration, the linearity of the displacement gage was verified by using an extensometer calibrator within the working range (v from 3.8 to 7.6 mm) of the specimen. A total of 25 displacement readings were taken with each interval of 0.127 mm. At the exciting voltage of 6V DC, the output voltage E of the gage on each reading was recorded by the graphic recorder. This procedure was performed 3 times, by removing and reinstalling the gage in the extensometer calibrator between each run. The maximum

deviation of the reading was ± 0.0025 mm. As shown in Fig. 2.8, the slope of the E *vs.* v curve, $\Delta E/\Delta v$, was determined by a least-squares-best-fit as 5.537 mV/mm.

2.3.2.2 Compliance calibration

The relationship between the normalized compliance $EB\frac{\Delta v}{\Delta P}$ and the normalized crack length $\frac{a}{W}$ for single CT specimens are expressed as [180]:

$$\frac{a}{W} = C_0 + C_1 U_x + C_2 U_x^2 + C_3 U_x^3 + C_4 U_x^4 + C_5 U_x^5 , \tag{2-1}$$

with

$$_x = \left(\sqrt{EB\frac{\Delta v}{\Delta P}} + 1 \right)^{-1} ; \tag{2-2}$$

where E is the Young's modulus; W and B are the dimensions of specimen; P is the load; and a is the crack length. A similar relationship was assumed for a CT specimen mounted with a transducer which was designed to linearly amplify the crack opening displacement signals.

Two CT specimens were employed in this calibration. Different crack lengths were obtained by fatigue precracking. After each run, the specimens were set up on the device shown in Fig.2.7 and the load was applied and relieved in steps within the elastic range. The average slope of the loading and deloading P *vs.* v curves was calculated as the compliance for this crack length. The normalized crack lengths $\frac{a}{W}$ employed were between 0.25 to 0.8 in each specimen. The measured compliance at different crack lengths gave the following fitted equation:

$$\frac{a}{W} = 1.705 - 46.79U_x + 924.36U_x^2 - 9792.51U_x^3 + 49912.53U_x^4 - 97563.88U_x^5 . \tag{2-3}$$

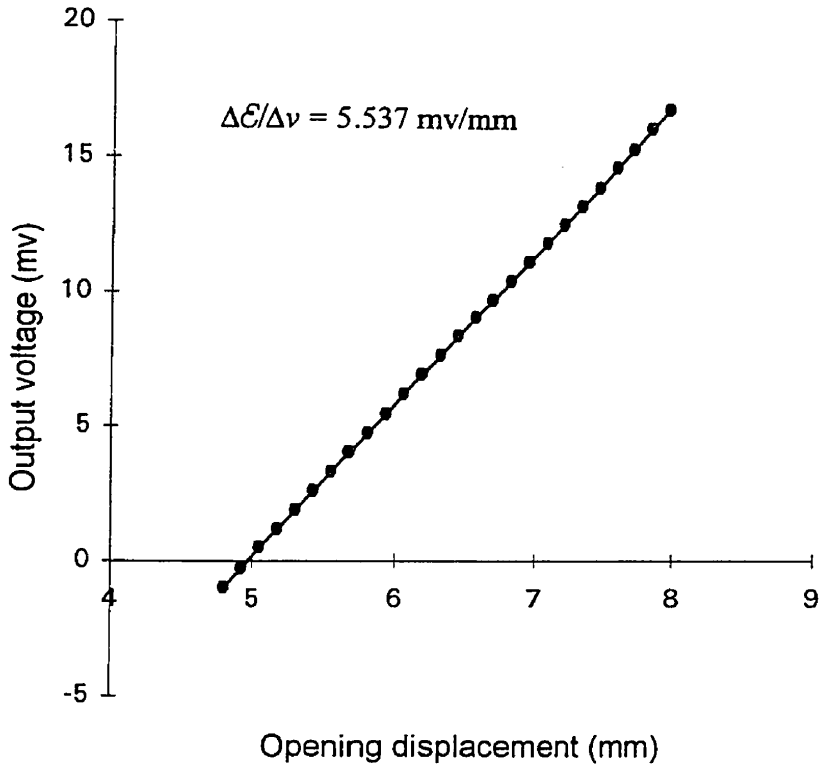

Figure 2.8 The linearity of the displacement gage employed in SCC tests of CT specimens.

Fig. 2.9 shows the comparison of equation (2-3) with equation (2-1) which is for a single CT specimen. The crack length derived from equation (2-3) was used to calculate the crack tip K, according to the following equation [180]:

$$K = \frac{P}{B\sqrt{W}} \frac{(2+\alpha)}{(1-\alpha)^{\frac{3}{2}}} \left(0.886 + 4.64\alpha - 13.32\alpha^2 + 14.72\alpha^3 - 5.6\alpha^4\right). \qquad (2\text{-}4)$$

2.4 LOAD PULSE TESTS

Load pulse tests were employed to investigate the crack propagation process. They were performed during SCC tests on 310 stainless steel and 70Cu-30Zn. After the crack propagated into Stage II of the $\frac{da}{dt}$ *vs.* K curve where the propagation velocity is independent of K, small load pulses were superimposed on an otherwise constant load. The increment ΔP was 10% to 40% of the base load on 310 stainless steel, and 25% to 50% of the base load on 70Cu-30Zn. The duration of a load pulse was approximately 4 seconds, and the time interval between pulses was between 5 and 10 minutes.

2.5 TENSILE TESTS

Tensile tests on SCC specimens of stainless steel were employed to investigate the nature of hydrogen-induced cracking at the SCC crack tip. The SCC tests were usually terminated in stage II, so that a sufficiently large uncracked ligament remained for the post-SCC (PSCC) tensile fracture.

The PSCC tensile tests were performed at room temperature on an Instron tensile machine from one day up to three months after the SCC tests. SCC cracks were opened in air at a cross-head speed of either 0.05 mm/min or >100 mm/min. A few SCC specimens underwent short time fatigue cracking before being opened, until the fatigue crack had

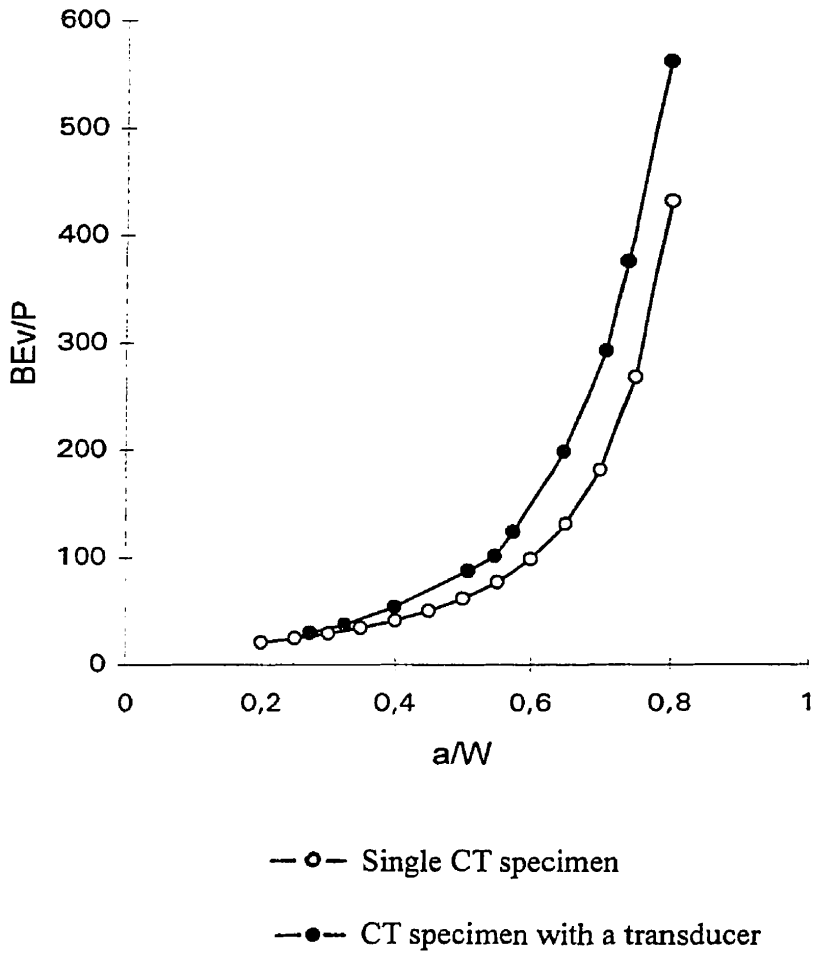

Figure 2.9 The relationship of measured compliance and crack length in the testing device shown in Figure 2.7.

propagated approximately one hundred microns. No superficial plastic deformation was observed after fatigue.

Tensile tests were also carried on 316 thin ribbons schematized in Fig. 2.6. Before tension, specimens were treated according to some of the procedures shown in Fig. 2.10. Some ribbon specimens were annealed in a vacuum of approximately 10^{-3} torr for 15 minutes at 1050°C followed by water quenching. Some were annealed plus strained less than 4% in tension. Others were maintained in the as-received condition. Some specimens were not polished after annealing in order to avoid introducing any possible residual stress.

The ribbons were attached to one end of glass bars and placed in between the bars and the wall of a beaker to prevent their floating in 154°C $MgCl_2$ solution. After immersing for 20 hours and 40 hours respectively, tensile tests were carried out either immediately or after aging a period of time. The ends of the ribbon were wrapped on a customized sample holder and were gripped by screwnails. This customized sample holder was then handed on the standard sample holder on an Instron tensile machine. The tensile tests were performed at a cross-head speed of 0.05 mm/min, which gave an initial strain rate of 4.16×10^{-5} 1/s. Some ribbons were cathodically charged in a solution of 0.5M H_2SO_4 plus 0.25g/l $NaAsO_2$ as well as in 154°C $MgCl_2$ solution at a current of 50 mA/cm^2 before tensile testing at room temperature.

2.6 FRACTOGRAPHIC OBSERVATIONS

When the individual SCC tests was terminated, each specimen was cleaned ultrasonically in warm water and then in acetone and dried with compressed air. Before microfractographic observations in the scanning electron microscope (SEM), usually no special treatment was needed for fractured specimens of stainless steels. The corrosion products on the fracture surfaces of 70Cu-30Zn specimens could be removed partially by

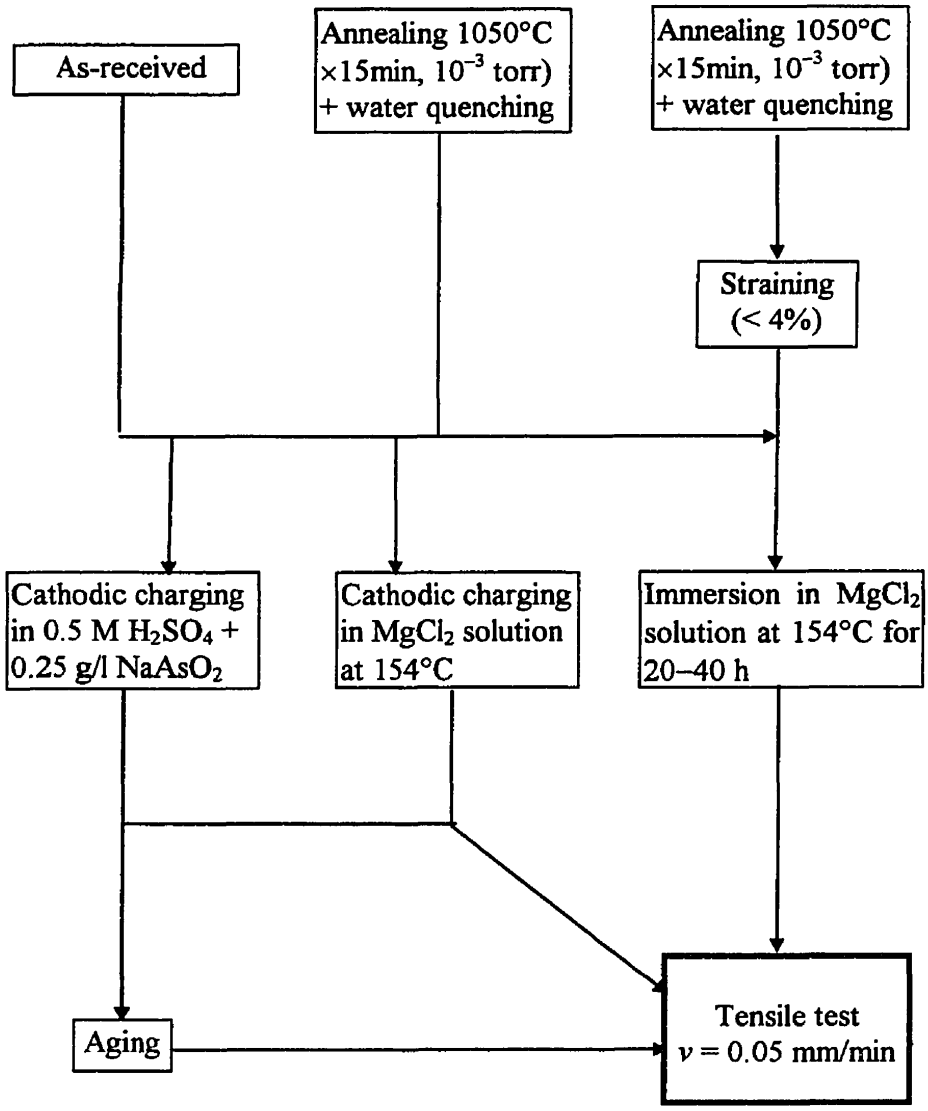

Figure 2.10 Testing procedures employed on 316 ribbon specimens before tension

immersing in solution of 100 ml of alcohol and a drop of Teepol 610. However, this cleaning procedure was only performed on CT specimens, because severely branched TN-DCB brass specimens often lost fragments even during short time cleaning after SCC tests.

All the fracture surfaces were examined employing a JEOL 820 or a JEOL 840 scanning electron microscope.

2.7 DETERMINATION OF THE CRACKING CRYSTALLOGRAPHY OF δ–FERRITE IN 316L STAINLESS STEEL

Investigating the cracking crystallography was a part of the fractographic study performed on transgranular cracking. The etch pitting technique which successfully determined the SCC crystallography of austenitic stainless steel [2,3], did not give satisfactory results on δ-ferrite in 316L stainless steel. Although many suggested etching reagents were tried, good pits in general were not obtained. Probably, the local etching potential deviated from the optimal value in the presence of two phases. In addition, the small amount and tiny grain size of δ-ferrite as well as the roughness of SCC fracture surfaces did not allow the precise cracking crystallography to be obtained. Therefore, the following three methods were employed to make the results more reliable.

2.7.1 Texture measurement

The texture measurement was performed by $(CM)^2$ laboratory of Ecole Polytechnique. It was carried out on a polished surface which was perpendicular to the S direction in ST orientated 316L specimen. The specimen was placed, with the polished surface horizontal, on the sample holder of the Philips X'Pert X-ray diffractometer. The incident X-ray was set, at the angles of Bragg diffraction of {200}, {110} and {211}

planes respectively, to the polished surface. During each diffraction, the specimen was first rotated 360° around the normal of the polished surface, then inclined by steps of 5° and rotated around this normal. This procedure was repeated to the inclination angle of 85°. Data acquisition and pole figure plotting were performed employing commercial software PC-TEXTURE and shearware POPLA.

2.7.2 Photogrammetric analysis

The photogrammetric method was used to determine the crystallography of SCC and of PSCC. Employing the SEM, the principle of this method is to measure the angle between two intersected microfacets or river lines, which allows to determine the possible crystallographic combinations of these two microfacets and/or river lines.

To do this, the intersection line of two facets should be rotated until parallel to the tilting axis of the SEM sample holder. Then, the holder was tilted to minimize or maximize the size of each facet. These two extreme conditions respectively corresponded to the facet's position parallel and normal to the electron beam. The tilting angle between the two extreme positions of the two facets was their intersection angle. In the position where the facet was perpendicular to the electron beam, measuring the angles between serrations or steps was then possible by simply rotating the specimen.

Since the δ–ferrite in the ST orientated specimens was fractured on the plane approximately perpendicular to the tensile axis in PSCC, the angles between river lines within a grain could be simply measured as their intersection angle. Corresponding propagation directions could be then determined. It should be noticed that the δ–ferrite platelets are composed of many subgrains which have a small orientation difference. This small orientation shift might cause some error in measuring. Therefore, the slip markings associated with cracking were also employed to help the crystallographic determination. In order to distinguish

the slip associated with SCC and the slip produced afterwards during the PSCC fracture, only the traces existing on both opposite fracture surfaces and approximately perpendicular to river lines were considered. The indexes of river lines was then determined based on the intersection angle and the possible slip planes which they intersected.

2.7.3 Analysis of electron back scattered patterns

Assistance in the determination of PSCC crystallography was obtained from Mr. Jian Li of the Department of Metallurgical Engineering of Queen's University. In their system for generating electron back scattered patterns (EBSPs), the sample holder was tilted 70° to the electron beam. In addition, assuming the sample surface is flat, each crystallographic orientation in an area of interest is given by nine direction cosines relative to the surface coordinate system of the specimen. If the area of interest is not parallel to the sample surface, it is not possible to determine the crystallography.

For these working conditions, the fracture surface was very difficult to view due to the surface undulations and SCC crystallography could not be analyzed due to the inclination of the SCC facets. In order to analyze the crystallography of PSCC, the specimen was first set in a conventional SEM sample holder to locate the interesting area and photographs were taken at different magnifications. Then the specimen was set in an EBSP sample holder and the area was relocated with the help of those photographs. Often the ductile fracture which was elevated over the crystallographic regions blocked the diffraction patterns. Therefore, not many PSCC regions could be analyzed by this technique.

Chapter 3

Fracture Induced by Hydrogen Evolved from SCC

3.1 INTRODUCTION

Among possible SCC mechanisms of stainless steels, hydrogen-induced cracking is a very attractive one. Many results have shown indirectly that hydrogen is produced near the crack tip by the SCC reactions. For example, the estimated crack tip pH and the active potential E_{corr} with respect to the hydrogen electrode at the testing temperature are all sufficiently low that cathodic reduction of H^+ ions is thermodynamically possible near the crack tip [81,182]. Hydrogen entry promoters such as thiourea added either to steels or to the $MgCl_2$ solution could cause failure of immune ferritic stainless steel and accelerate the cracking of austenitic stainless steel [183]. SCC fractography can be very similar to that of hydrogen-induced cracking although some differences were reported [105,125,184,185].

However, the occurrence of SCC does not need the presence of martensite which is considered by some authors as a prerequisite for hydrogen-induced fracture [125,185]. This casts doubt about the role of hydrogen during SCC. Some authors [86] claimed that hydrogen produced during SCC is insufficient to cause cracking. Uncertainty also comes from how to characterize hydrogen-induced cracking. Cleavage-like fracture is generally accepted as a symbol of brittleness caused by hydrogen. But hydrogen can also influence fracture by facilitating the nucleation or the growth of microvoids [186,187]. In these cases, only the size of dimples is changed.

Restricted by the current experimental techniques, the SCC crack tips are too sharp and the amount of hydrogen generated during SCC is too small to permit hydrogen to be detected directly. The investigations of hydrogen involved in SCC were often done under potential-controlled conditions to maximize the effect of hydrogen, which is different from the SCC conditions. On the other hand, the hydrogen produced by SCC nevertheless can influence the fracture to a certain extent, providing such an influence can be demonstrated by an appropriate method. In this chapter, our systematic fractographic observations of post-SCC (PSCC) tensile fracture in 316L and 310 stainless steels will be presented. The fracture performed in air isolated the effect of absorbed hydrogen on cracking from other electrochemical influences during SCC, and therefore should aid in the interpretation of the fracture surfaces. The bcc δ–ferrite present in 316L stainless steel might help to reveal the hydrogen effect, while in stable 310 stainless steel the possibility of deformation-induced martensite being embrittled by hydrogen can be ruled out. Thus the cracking behavior of austenite could be clarified. The results of the tensile tests performed in this study on thin ribbons of austenitic 316 stainless steel and their fractography in conditions of cathodic charging and immersion in $MgCl_2$ solution will also be presented.

3.2 GENERAL DESCRIPTION OF SCC FRACTURE SURFACES

For the 316L stainless steel employed, approximately 5% of δ–ferrite was distributed near the cracking plane of ST orientated specimens. The δ–ferrite was present in form of platelets parallel to the cracking plane, which generally resulted in the main SCC cracks perpendicular to the tensile axis. Near notches, transgranular fracture dominated with small areas of interfacial fracture. The amount of interfacial fracture increased as increasing K and became dominant at high K. Fig. 3.1 shows the SCC features in low magnification. The macroscopic propagation direction is from the bottom to the top in all photographs presented in this thesis, unless otherwise indicated. In Fig.3.1, the interfacial fracture was quite flat and δ–ferrite (indicated by F) was flattened and sandwiched between austenite grains (indicated by A). Fig. 3.2 is a matching photographic pair on two opposite fracture surfaces of interfacial fracture. White traces on the austenite (A) side correspond to impressions of small δ–ferrite grains on the opposite interface, while impressions of large austenite grains are shown on the δ–ferrite side (F). The SCC crack preferred to propagate along the interface between δ–ferrite and austenite, resulting in a flat and interlocked interfacial fracture surface.

The change from interfacial cracking to transgranular cracking occurred when the crack propagated into the austenite phase. However, for K greater than 12MPa$\sqrt{m}$, the δ–ferrite platelets on the fracture surface were always surrounded by intergranular fracture in the austenite (Fig. 3.1). The amount of intergranular fracture in the austenite appeared more frequently in high K regions.

Transgranular cracking was often found in the δ–ferrite phase both in the high K and low K regions of SCC (Fig. 3.3). The crack generally propagated across the thickness of the δ–ferrite at approximately 45° to the tensile axis and then changed its direction at the interface and propagated in the other direction at approximately –45° to the tensile axis. The facets resulted from such transgranular propagation formed regular hills and valleys, generally

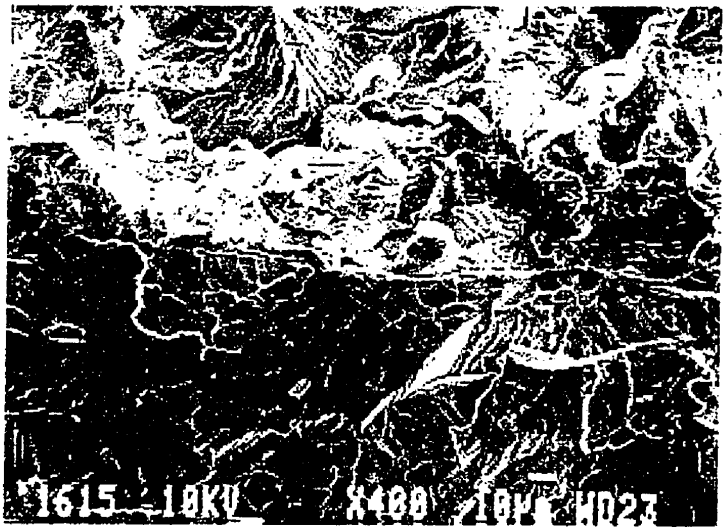

Figure 3.1 Interfacial SCC fracture between the austenite (A) and the δ–ferrite (F) phases in ST orientated specimens of 316L stainless steel. Intergranular fracture in the austenite beside the δ–ferrite phase is also present.

Figure 3.3 Transgranular SCC fracture in the δ–ferrite is present among interfacial cracking in ST orientated specimens of 316L stainless steel. The transgranular fracture often shows such regular hills and valleys between the ferrite-austenite interfaces.

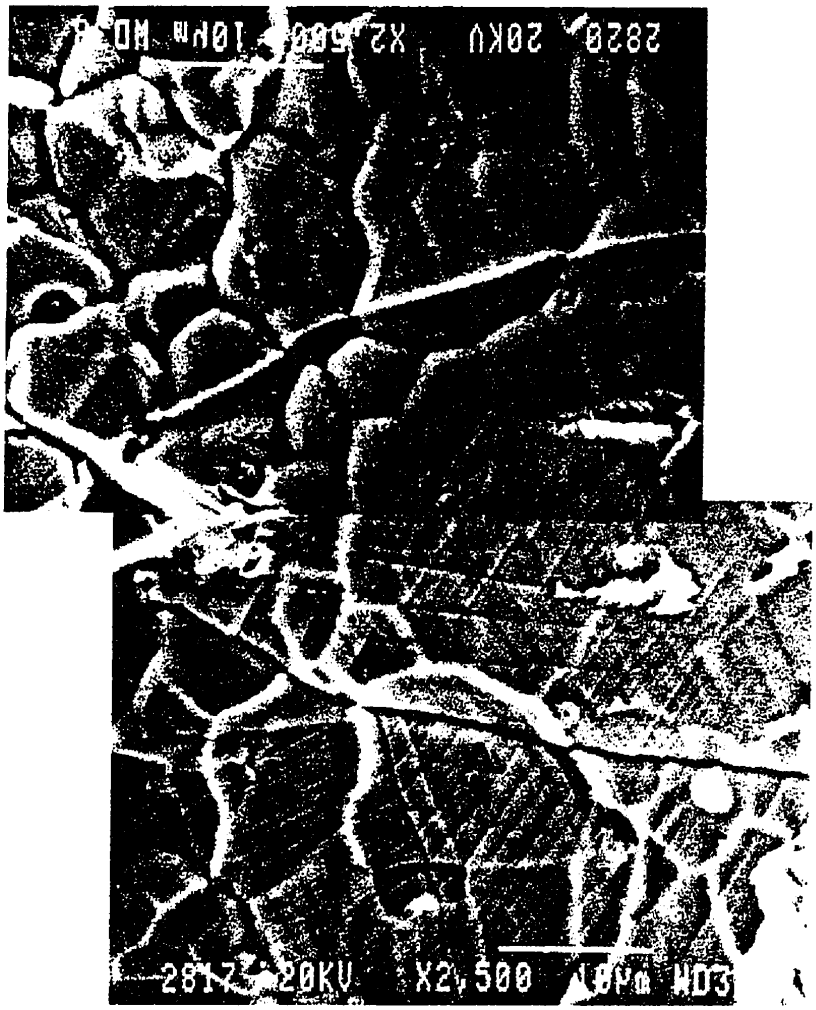

Figure 3.2 Matching fractographs of interfacial SCC fracture in a ST orientated specimen of 316L stainless steel. White traces are the impressions of small δ–ferrite grains on the austenite (A) grain boundary and of large austenite grains on the δ–ferrite (F) grain boundary.

somewhat curved, between the ferrite-austenite (δ–γ) interfaces. Occasionally, a small amount of interfacial cracking occurred before the crack propagated in the δ–ferrite in the other direction. Such cracking was initiated on a number of small facets at the interface and propagated across the δ–ferrite. River lines resulted from the coarsening of those small cracks on each inclined facets were often perpendicular to the intersections of two inclined facets.

The SCC fracture in 310 was transgranular and was described in detail by Dickson *et al* [2].

3.3 PSCC MICROFRACTOGRAPHY

3.3.1 PSCC crystallographic cracking in 316L stainless steel

In ST orientated 316L specimens, PSCC crystallographic cracking was found in the stretch zone regions which had been fractured in air at room temperature. Crystallographic fracture could occur in δ-ferrite and in austenite. It was present within the ductile fracture of the austenite phase in this region (Fig. 3.4). Inclusions were easily found in these regions. In the specimens in which the SCC crack front was outlined by a small amount of fatigue cracking, the same mixture of fracture regions still existed ahead of the fatigue zone. This confirms that these inclined regions were fractured out of the solution.

Intergranular cracking generally was absent in the PSCC regions. Transgranular PSCC were observed either starting at the previous SCC crack tip or ahead of the previous SCC crack tip. The features of transgranular PSCC were different from those of SCC in both phases, but particularly in the δ-ferrite. Fig. 3.5 shows interfaces between SCC and PSCC fracture. In PSCC, the facets in the δ-ferrite were approximately perpendicular to the tensile axis, which was in the short transverse direction. The transgranular river lines in δ-ferrite were long and straight, and often initiated either at inclusions or at γ–δ interfaces. Occasionally, river

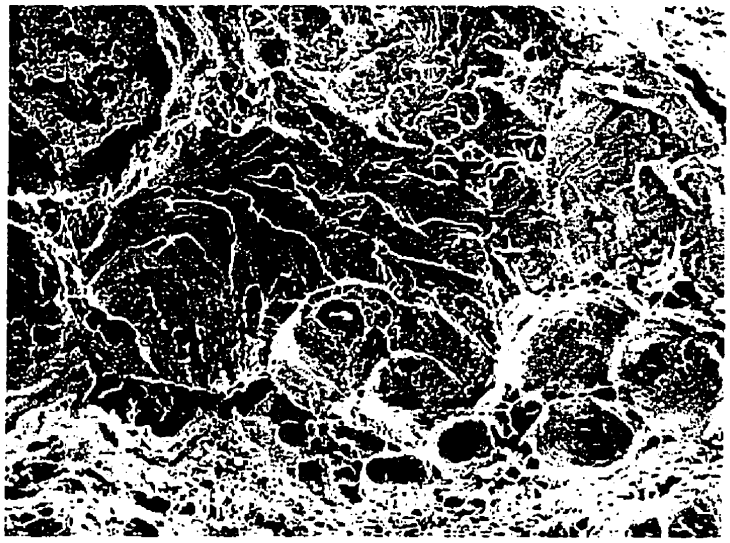

Figure 3.4 Mixture of cracking patterns in PSCC fracture ahead of the SCC crack tip in 316L stainless steel. Dimples and crystallographic fracture appear in the austenite (A) and in the δ–ferrite (F) respectively.

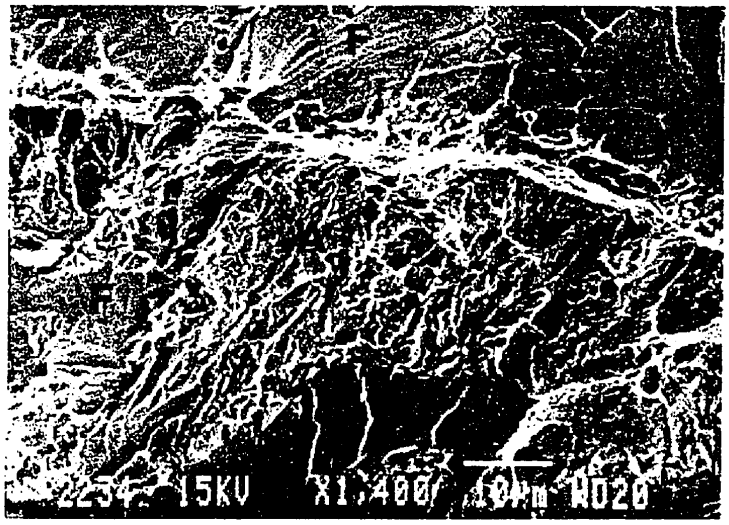

Figure 3.6 Crystallographic PSCC cracking in austenite (A) which initiated following cracking in the δ–ferrite (F).

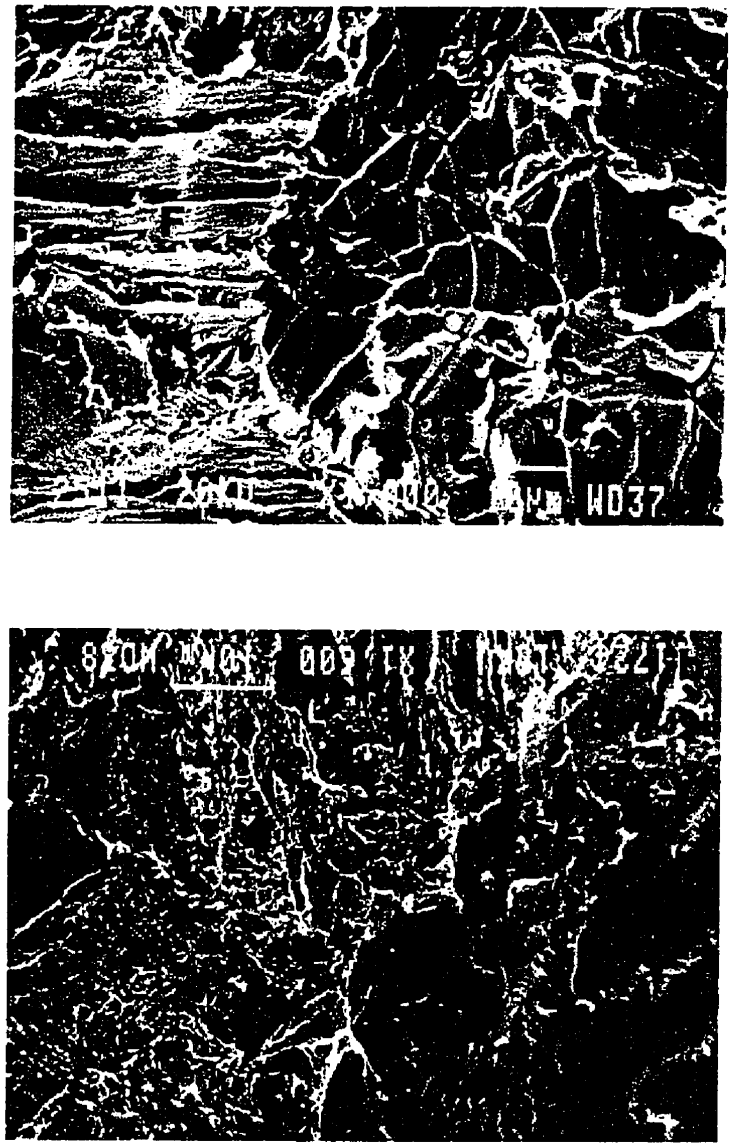

Figure 3.5 Interfaces between interfacial SCC fracture (right portions of the photographs) and PSCC crystallographic cracking in the (a) δ–ferrite and (b) austenite.

lines propagated back to meet the main PSCC crack. Pronounced striations were essentially perpendicular to the river lines and interlocked with each other on opposite surfaces. Comparing Fig. 3.5a with Fig. 3.3, it can be seen that transgranular PSCC fracture is considerably different from transgranular SCC in the δ-ferrite, which occurs along planes inclined approximately 45° to the tensile axis and goes back and forth between the γ-δ interfaces in ST orientated specimens.

Transgranular fracture of the austenite phase in PSCC were often found at the start of PSCC (Fig. 3.5b) and beside the δ-ferrite ahead of SCC crack tips (Fig. 3.6). Compared with those in SCC, numerous closely spaced microfacets were often present, complicating the identification of the cracking crystallography. At high magnification, the two opposite fracture surfaces were observed not to be exactly matching and a few microvoids were present in some regions (Fig. 3.7), indicating a quite strong amount of deformation was involved during cracking. The microfacets gradually became less crystallographic with increasing distance from the δ-ferrite. Ductile fracture appeared far away from the δ-ferrite and near inclusions, which are the strong traps to hydrogen.

3.3.2 PSCC crystallographic cracking in 310 stainless steel

The fractography of the stretch zone regions in TL orientated 310 specimens showed features very similar to normal ductile fracture. However, flattish facets appeared in some individual grains among shallow dimples, especially on the planes close to the maximum shear stress in the plane strain regions. The features on these facets can be classified as being one of the following three types:

I) Nearly equally spaced, quite crystallographic striations.

As shown in Fig. 3.8, these crystallographic lines appear to be made up of fine steps. They are approximately perpendicular to the macroscopic propagation direction, and

Figure 3.7 Matching fractographs of PSCC crystallographic cracking in austenite. Note some of the features do not match exactly on both sides.

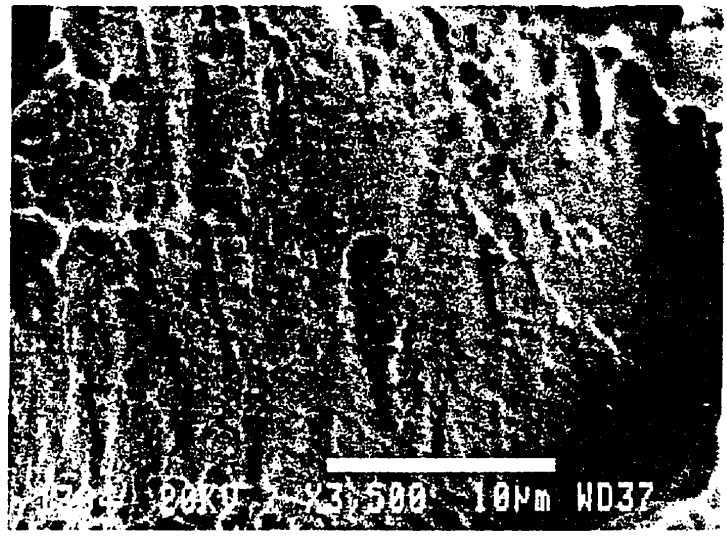

Figure 3.8 A region of PSCC in 310 stainless steel, which is typical of Type I PSCC fracture. The cracking is highly crystallographic, although some very fine microvoids can be observed at the horizontal crystallographic lines.

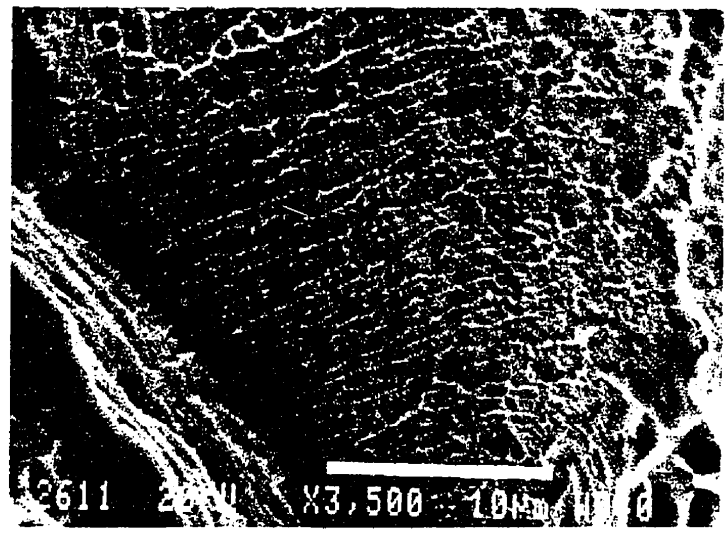

Figure 3.9 A region of PSCC in 310 stainless steel, which is typical of Type II PSCC fracture. More microvoids are present at horizontal striations which are approximately perpendicular to the propagation direction.

generally interlock on the two opposite fracture surface. At high magnifications, some very fine microvoids (< 0.5 μm), which was more clearly presented on one fracture surface, formed by stretching.

II) Aligned small dimples at intersections of two slip systems.

Fig. 3.9 shows this type of feature at relatively low magnification. The matching photographs at higher magnification (Fig. 3.10) reveal that the striations perpendicular to the propagation direction match peak to peak on the two opposite fracture surfaces. Uncracked ligaments between crystallographic facets were stretched, producing these striations and aligned microvoids at both sides of the striation.

III) Fine shear dimples.

Compared with above two, this feature appears to be more ductile. The dimples, however, are present on a flattish plane. Their size is of the order of a micron and are considerably smaller than those in the surrounding grains (Fig. 3.11).

Type II features appeared more often than others. All three types of features were situated on facets inclined 30 to 60° from the tensile axis. These facets were approximately as large as the grain size, and appeared to be more or less crystallographic. Because of the slip after fracture, these facets were quite deformed. The matching of opposite surfaces was not perfect, and the angles between slip traces were generally not good enough to determine the plane index. Quantitative X-ray analyses (ZAF) showed that Cr and Mn were often 2 to 3 at% higher in these regions or next to these regions, which agrees with the metallographic examination (see Table 2.2). Moreover, these features were not found in an annealed specimen. This suggests that alloying segregation acted as hydrogen traps. Therefore, the influence of hydrogen on the fracture in these particular regions becomes more evident.

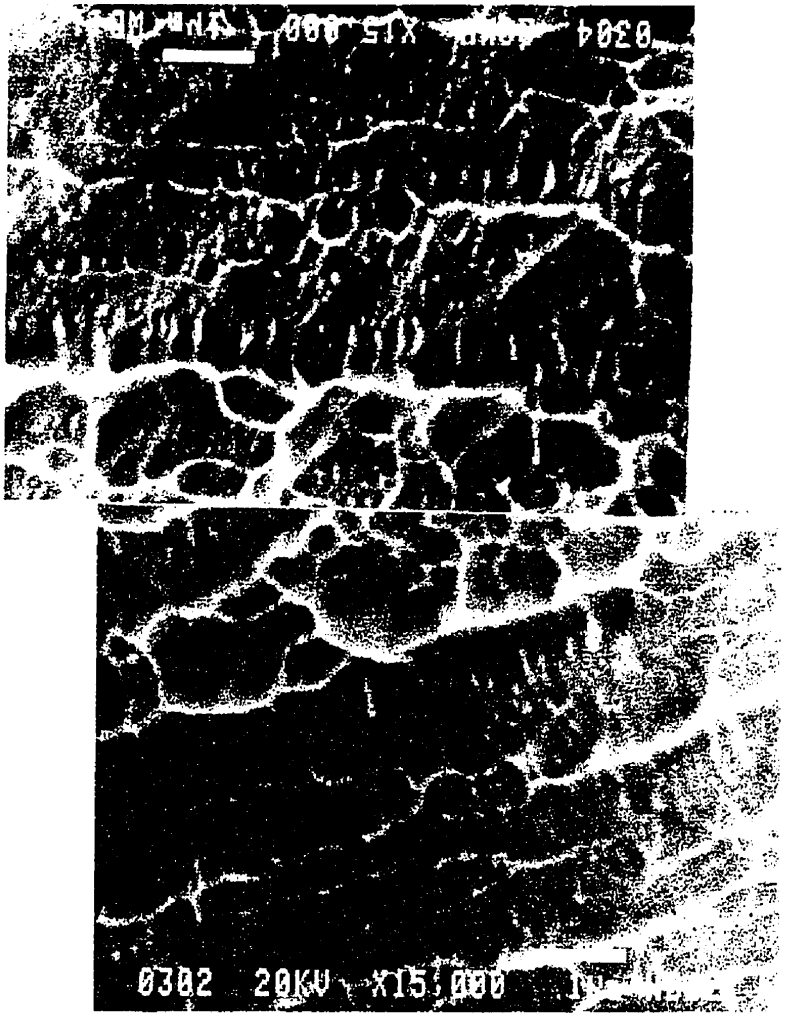

Figure 3.10 Matching fractographs of Type II PSCC fracture in 310 stainless steel at higher magnification. Aligned microvoids were produced by the stretching on an almost crystallographic plane.

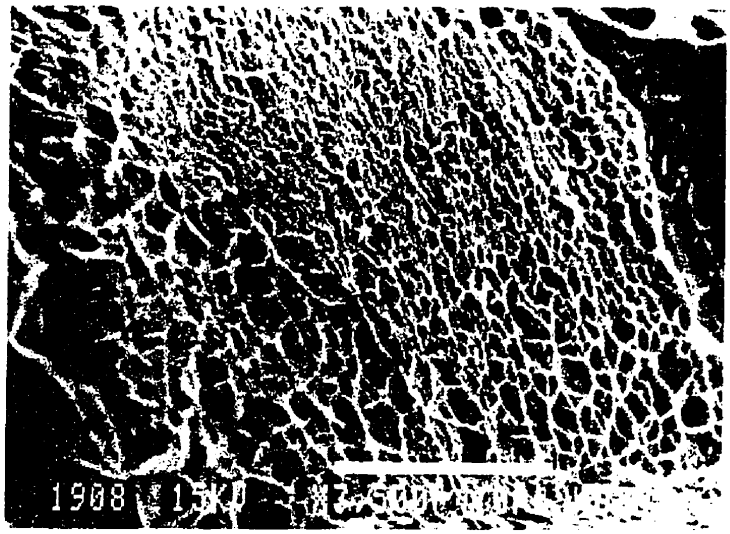

Figure 3.11 A region of PSCC in 310 stainless steel, which is typical of Type III PSCC fracture. Fine shear dimples are grouped together on a flat plane close to the plane of maximum shear stress. The dimples were produced by an off-center tensile stress.

Figure 3.12 A large {100} facet with microvoids formed during fatigue in 316L stainless steel.

3.3.3 The size of PSCC crystallographic cracking zones

The unusual crystallographic fracture features produced by room temperature tension were always found within a few hundreds microns of the SCC crack tip in all ST orientated 316L stainless steel specimens, and in six out of nine 310 stainless steel specimens. In a few specimens of 316L stainless steel, these features were observed up to 2 mm ahead of the SCC crack tip. Therefore, this kind of fracture cannot be explained by anodic dissolution or by other surface layer effects. Hydrogen absorbed from SCC reactions appears to be the only reasonable explanation. As shown in Table 3.1 and Table 3.2, the size of PSCC crystallographic cracking zones tend to increase with increasing K and with the time interval, up to 3 months between SCC tests and PSCC tensile fracture.

Table 3.1 The size of crystallographic cracking zones (μm) in 316L

Final K of SCC tests (MPa√m)	Slow COD, opened soon	Slow COD, opened in three months	Fast COD, opened soon	Plastic zone d** (μm)
10	~100	~400	Not tested	140
15	Not tested	~600(→1.8 mm)	Not tested	315
20	~500, ~700*	~300 (→2 mm)	~200	560
>30	Not tested	Not tested	~300	1260

Table 3.2 The size of crystallographic cracking zones (μm) in 310

Final K of SCC tests (MPa√m)	Slow COD, opened soon	Slow COD, opened in three months	Fast COD, opened soon	Plastic zone d** (μm)
15	~300*	~300 (→1 mm)	Not tested	351
20	~300	~300	~100	624
25	~150 (→300)	Not tested	Not tested	975

* Specimen was fatigued after SCC.

** $d = \frac{1}{3\pi}\left(\frac{K}{\sigma_y}\right)^2$

3.3.4 Fatigue fractography in PSCC regions

Short time fatigue cracking was employed in some SCC specimens to outline the SCC crack front and to distinguish between SCC and PSCC. The fatigue cracking features are also interesting since this fracture occurred between SCC and PSCC. In order to compare the fatigue fractography after SCC with the normal fatigue fractography, a 316L stainless steel specimen with the same orientation and geometry as the SCC specimens was fatigued under the same nominal conditions employed for the fatigue of SCC precracked specimens. For this specimen not precracked by SCC, fatigue crack propagation began effectively at a nominal ΔK value of approximately 8 MPa$\sqrt{m}$. At this near-threshold value, fracture surface presented crystallographic cracking as reported previously [113]. Some large and flat facets which had been determined [113] as {100} were observed. With increasing ΔK, the {100} facets became rougher. Some microvoids appeared on them (Fig. 3.12) and disappeared when the nominal ΔK was over 10 MPa$\sqrt{m}$. No δ-ferrite was distinguished except for one small interfacial fracture zone. Inclusions were also not detected on the fracture surface.

The fatigue propagation after SCC tests in 316L stainless steel started at a nominal ΔK value of approximately 15 MPa$\sqrt{m}$. Fine, more crystallographic cracking features appeared on a plane inclined from the SCC cracking plane. Flat facets, as large as 50 to 80 μm, were often found in the austenite. There was no microvoids on such facets, but often evident slip lines produced after fatigue fracture. In Fig. 3.13, such slip lines indicate that this facets is a {111} slip plane. Transgranular fractured δ-ferrite very similar to that of PSCC crystallographic cracking was also observed (Fig. 3.14). These observations indicate that hydrogen absorbed during SCC influenced the fatigue fracture produced after SCC tests.

Similar fractographic observations were also carried out on 310 stainless steel specimens fatigue cracked under nominally similar conditions without SCC and after SCC.

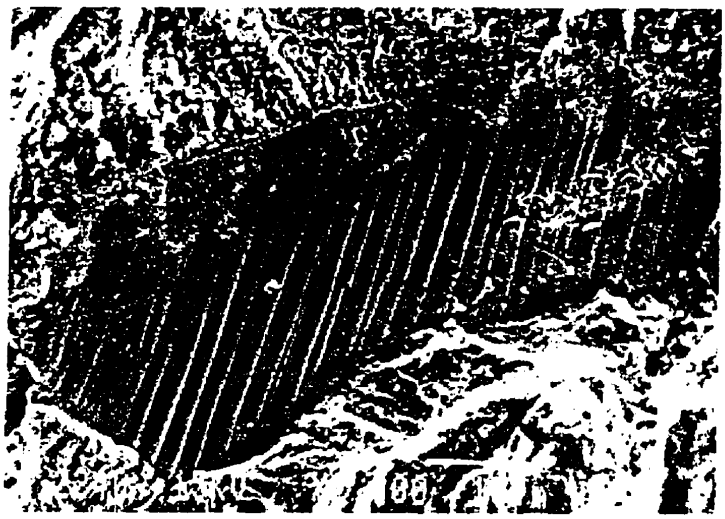

Figure 3.13 A large facet formed during fatigue after SCC in 316L stainless steel. The slip lines indicate that this is a {111} slip plane.

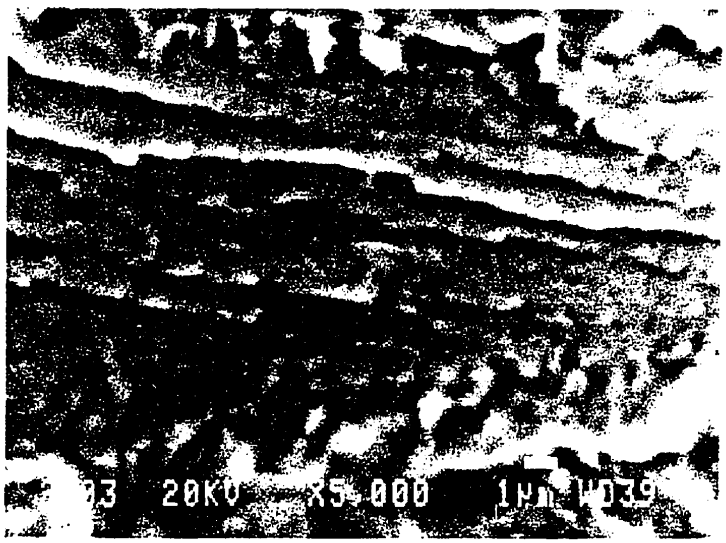

Figure 3.14 A transgranular feature of fatigue after SCC in the δ-ferrite. It is very similar to PSCC crystallographic cracking in the δ-ferrite, with the interaction between the striations and the river lines stronger than during the PSCC fracture.

Near the stress corrosion crack tip, fatigue fracture tended to be more crystallographic and more complex, again indicating an influence of absorbed hydrogen on the subsequent cracking.

3.4 SCC FRACTOGRAPHY UNDER A CONSTANT COD RATE

Since the observations of PSCC crystallographic cracking indicate that absorbed hydrogen is responsible for this type of fracture and the fracture features in the δ–ferrite are very similar to hydrogen-induced cracking in a ferrite phase, it is interesting to study the fractographic features when a SCC crack is opened at a similar displacement rate in boiling $MgCl_2$ aqueous solution as in PSCC fracture in air. In this condition, the solution remains in touch with the crack tip while the crack passes through the hydrogen diffusion zone at the crack tip. This could show which factor, the solution or the hydrogen, determines the crystallographic fracture.

3.4.1 Fractography of 316L stainless steel

For a ST orientated specimen of 316L stainless steel opened at a crack opening displacement (COD) rate of 0.05 mm/min, the fracture surface remained on the same plane of SCC, i.e., normal to the tensile axis. The cracking features were almost identical to that of SCC at high K. Only slip lines at the lateral surfaces indicated that this portion was fractured under constant COD rate.

Faster opening at a COD rate of 5 mm/min in solution resulted in a hydrogen-induced cracking zone ahead of the interfacial SCC fracture in the specimen. This zone extended on an inclined plane about 200 μm ahead of the previous SCC crack and then was followed by a stretch zone (Fig. 3.15). The fracture of δ-ferrite in this zone was very similar to that of PSCC in air, but corrosion pits on the facets indicated that it fractured in $MgCl_2$ solution (Fig. 3.16).

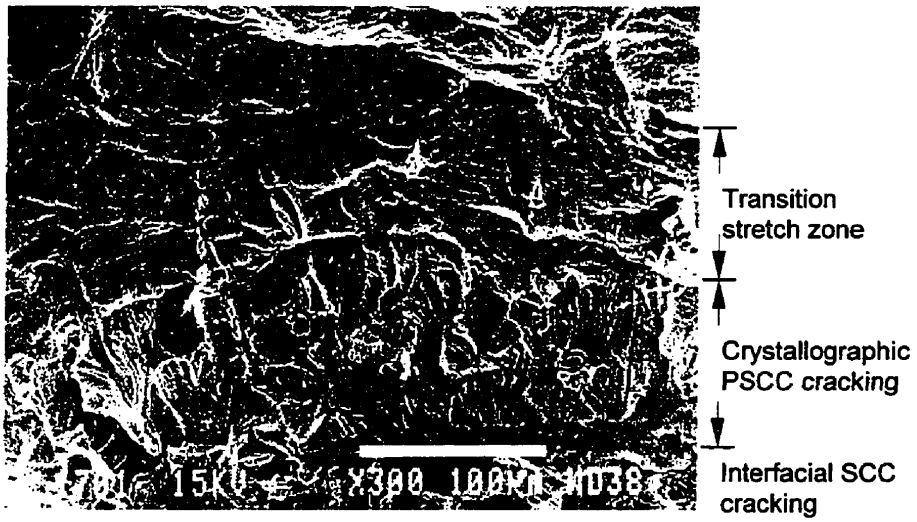

Figure 3.15 A inclined hydrogen-induced cracking zone, followed by a stretch zone at the SCC crack tip in a 316L stainless steel specimen opened in solution at a COD rate of 5 mm/min.

Figure 3.16 Transgranular fracture in δ-ferrite in the hydrogen-induced cracking zone, from the same specimen as Fig. 3.15.

Sometimes the crystallographic fracture in δ-ferrite was separated from the SCC fracture by an austenite strip which had partial crystallographic features (Fig. 3.17).

In the first 50 μm of this 200 μm large zone, the austenite also presented crystallographic features which looked like that of SCC at high K and matched quite well on the opposite fracture surface. Then the matching became partial with an increasing amount of crack tip stretching combined with the PSCC crystallographic fracture in the δ-ferrite. The last 100 μm region showed neither crystallographic facets nor dimples but a transition stretch zone: regularly arranged shear bands which resembled the shear bands on large dimple wall but which were aligned more regularly. This change in fracture features is illustrated in Fig. 3.18. It indicates the transition from crystallographic fracture to ductile fracture associated with a gradually decreasing hydrogen concentration.

3.4.2 Fractography of 310 stainless steel

Two 310 SCC specimens were also opened in $MgCl_2$ solution at a COD rate of 0.05 mm/min. The opening process performed on the first specimen lasted 30 minutes in solution, and was later continued in air at room temperature until the specimen was fractured. Fractographic examination indicated a few small areas ahead of the SCC fracture which appeared slightly different. It was believed that the SCC crack tip was very irregular at high K (~20 MPa$\sqrt{m}$) when the slow opening started. A higher applied load or longer test duration was needed. The second specimen was opened when K reached 17 MPa$\sqrt{m}$. The opening lasted 2 hours and 30 minutes and was terminated because the capacity of the beaker could not offer more space for crack tip opening.

On the fracture surface of this specimen, the slowly opened region appeared ahead of SCC crack. As shown in Fig. 3.19, this region is inclined from the former SCC crack, and resembles SCC fracture at high K. These aspects agree with the feature of the

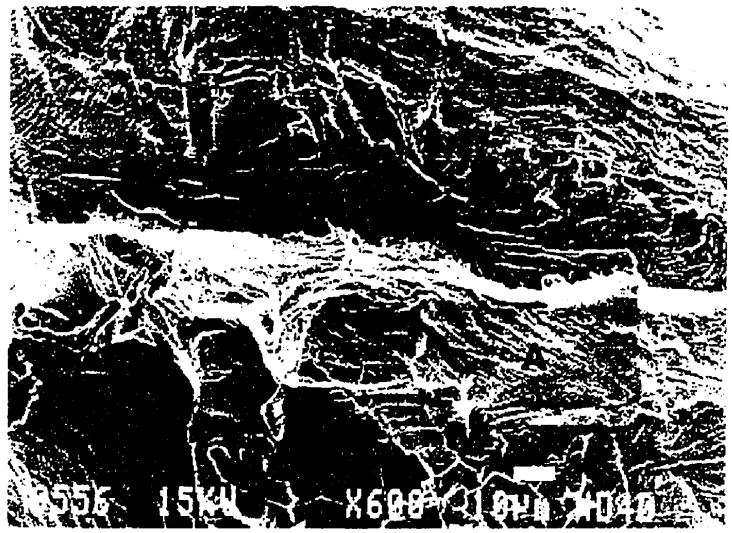

Figure 3.17 Transgranular fractured δ-ferrite (F) is separated by a transition stretch zone in austenite (A) in the hydrogen-induced cracking zone, in the same specimen as Fig. 3.15.

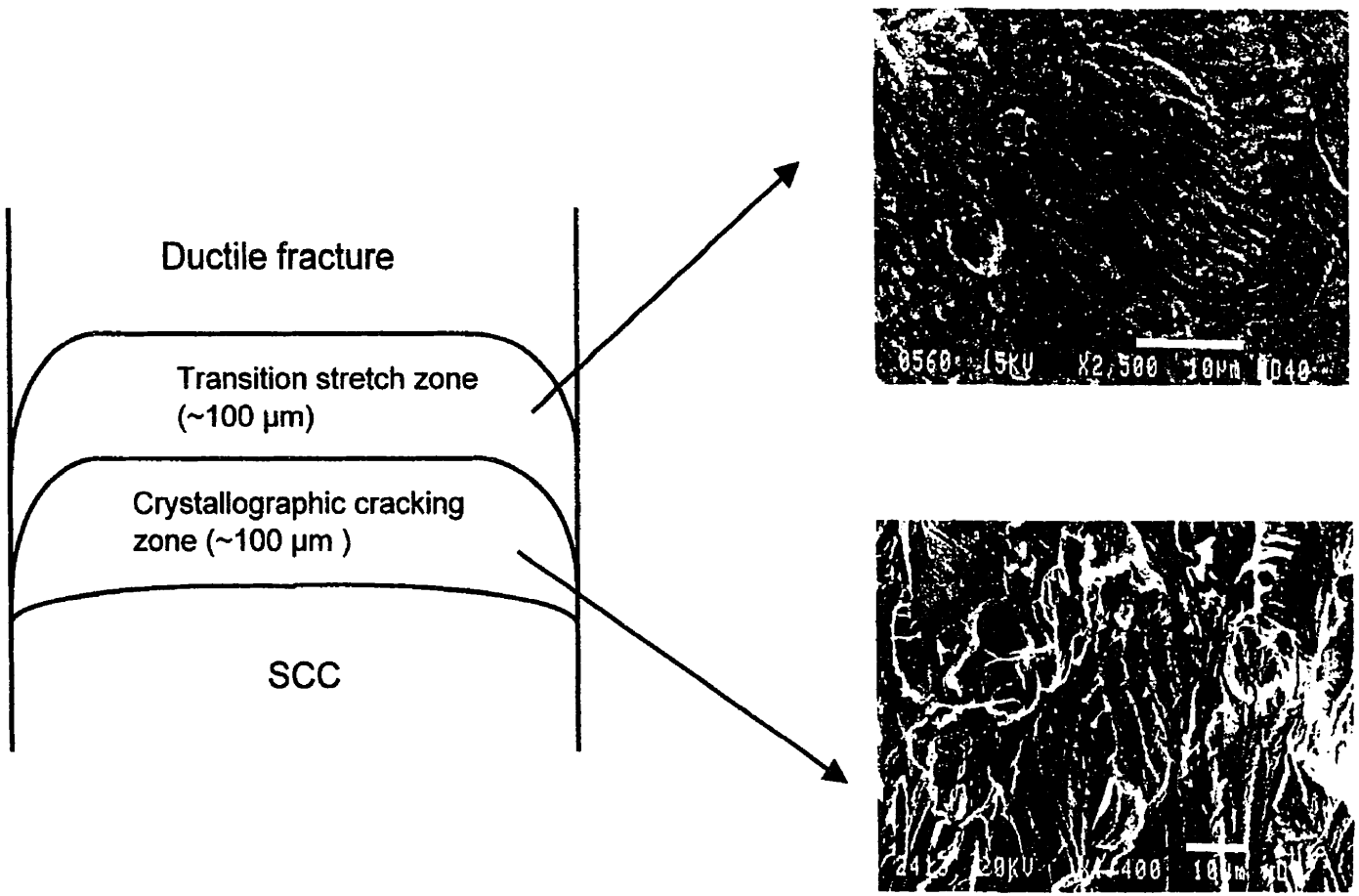

Figure 3.18 A schematic illustration of the fracture features in austenite in the hydrogen-induced cracking zone, from the same specimen as Fig.3.15. (a) Crystallographic cracking at the beginning of this zone. (b) The transition stretch zone features.

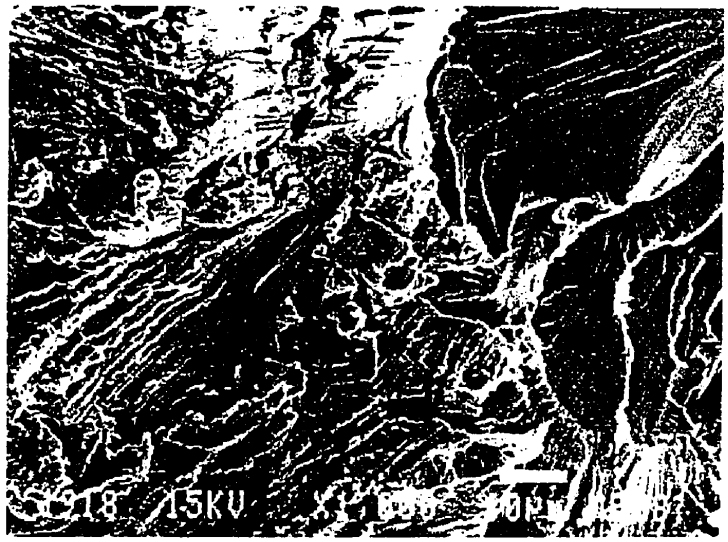

Figure 3.19 The fracture features produced by the constant load SCC (at the right) and by opening at a slow COD rate in $MgCl_2$ solution (at the left) in a 310 stainless steel specimen. The latter shows features of higher *K*.

austenite in slowly opened 316L specimen in solution (section 3.4.1). However, the opposite fracture surfaces were not easily matched because secondary cracks were opened and uncracked ligaments were pulled out. On the matching fracture surfaces shown in Fig.3.20, not all the striations match on the opposite fracture surface. Such pronounced striations shown in Fig. 3.20 were claimed [18,22,23,129] as evidence of propagation discontinuity in slow strain rate SCC tests. The present observations show, however, that these non-matching striations are produced by slip after fracture, most probably due to the high strain at the crack tip during crack opening.

The change of cracking features from the fan-shape pattern to the dense serrated river lines occurred suddenly on the fracture surfaces, which indicated that the latter was produced during slow COD opening. Although the opening time was 5 times longer than the first specimen, the size of this region, varying somewhat from location to location, was nearly 100 μm, which was approximately the same as in the first specimen. This indicates that crystallographic cracking occurs only over a certain distance at the SCC crack tip, within which the absorbed hydrogen was sufficiently high to produce crystallographic cracking. Afterwards, some ductile fracture was produced when the specimen was still fractured in solution.

3.5 TENSILE TESTS ON THIN RIBBONS

Since the cathodic reduction of H^+ is thermodynamically possible near the crack tip and it influence the fracture afterwards, supplementary tests were performed to provide additional information of hydrogen involvement during SCC in $MgCl_2$ solution. Thin foils of 316 stainless steel were selected because they were relatively easier to be saturated with hydrogen.

Figure 3.20 Striations on matching fracture surfaces produced at a slow COD opening rate in $MgCl_2$ solution in a 310 stainless steel specimen. Not all the striations, such as in regions A and A', are matching on the opposite fracture surfaces.

3.5.1 Tensile data

After immersion in the $MgCl_2$ solution for 3 to 4 hours, the surfaces of ribbon specimens lost their shininess and became dark. Pitting occurred randomly at many sites on the surfaces. The amount of pits appeared independent of the immersion time and pretreatment described in Chapter 2. Some specimens were severely corroded after a short immersion time, with some pits piercing the foil thickness.

The pitting greatly influenced the tensile behavior of these thin ribbon specimens. Therefore, the σ *vs.* ε curves obtained may not represent the true conditions of specimens. The set up of tensile tests described in Section 2.5 may also prevent precise data from being obtained. The following tables present the yield stress (σ_y) and elongation at failure $(\Delta l/l)_F$ in different conditions which came from specimens not severely corroded.

Table 3.3 Tensile data (after charging 6 hours in H_2SO_4 at 25°C)

Treatment	σ_y (MPa$\sqrt{m}$)	$(\Delta l/l)_F$ (%)	Aging time (h)
annealed	274	12	0
as received	274	12	0
as received	274	15	18

Table 3.4 Tensile data (after charging 6 hours in $MgCl_2$ at 154°C)

Treatment	σ_y (MPa$\sqrt{m}$)	$(\Delta l/l)_F$ (%)	Aging time (h)
annealed	235	17.5	0
as received	274	10	0
as received	266	13	0
as received	298	18	24
as received	353	14	45

Table 3.5 Tensile data (after immersing 40 hours in $MgCl_2$ at 154°C without stress)

Treatment	σ_y (MPa$\sqrt{m}$)	$(\Delta l/l)_F$ (%)	Aging time (h)
as received	274	8	0
as received	314	11.5	78
annealed	274	12.2	0
annealed, non polished	235	14.5	0

Table 3.6 Tensile data (after straining and immersing without an applied stress 24 hours in $MgCl_2$ at 154°C)

Treatment	σ_y (MPa$\sqrt{m}$)	$(\Delta l/l)_F$ (%)	Prestrain (%)
annealed	235	8.2	1.5
annealed	188	8.5	2
annealed	220	5	2.1
annealed	172	2.5	4

A qualitative comparison can be made from these results which show that the hydrogen absorbed in ribbon specimens influences the tensile properties:

1) The elongation $(\Delta l/l)_F$ increases with the increasing aging time after specimens were cathodically charged (Table 3.4) or simply immersed in boiling $MgCl_2$ solution (Table 3.5). This tendency agrees with that obtained for ribbons charged in H_2SO_4 (Table 3.3), and indicates that outgassing of absorbed hydrogen during aging improves the ductility of the specimens.

2) Annealing increases the elongation of specimens charged and immersed in $MgCl_2$ solution (Table 3.4 and 3.5) because annealing relieved most of the residual stress produced in specimen preparation. The density of hydrogen traps (dislocations) and thus the hydrogen concentration in specimens were reduced. The elongation was further increased if the annealed specimens were not polished.

3) Generally, the prestrain increases the dislocation density, resulting in a decrease of elongation although its influence on the yield load is not evident.

3.5.2 Fractographic observations

In this section, the fractography observed on ribbons tensile fractured after cathodically charged or immersed in $MgCl_2$ solution will be described.

3.5.2.1 Cathodically charged specimens

The fracture surfaces of specimens cathodically charged in $MgCl_2$ solution were very similar to those charged in H_2SO_4. From the edge to the center on the fracture surfaces, cracking facets gradually decreased in size and were finally replaced by ductile fracture (Fig. 3.21). The large facets at the edges were often crystallographic, approximately perpendicular to the tensile axis and were of the typical grain size, approximately 10 μm in length and 2 μm in width. Some small triangular pits, protrusions and slip lines on these facets indicated that they were often on {111} slip planes, although it is difficult to exclude the possibility of intergranular cracking due to the size of those facets. Some secondary cracks, which are the typical feature of hydrogen-induced cracking, were observed on these large facets. The portion of the fracture surfaces beside large facets was inclined approximately 45° to the tensile axis. Crystallographic facets were then much smaller and a little deformed, similar to the fracture of austenite produced during PSCC crystallographic cracking of bulk specimens.

With increasing aging time before tensile testing, the number of secondary cracks and the size of large facets decreased. Some slip traces appeared on large facets. Crystallographic facets in inclined regions became smaller and more deformed.

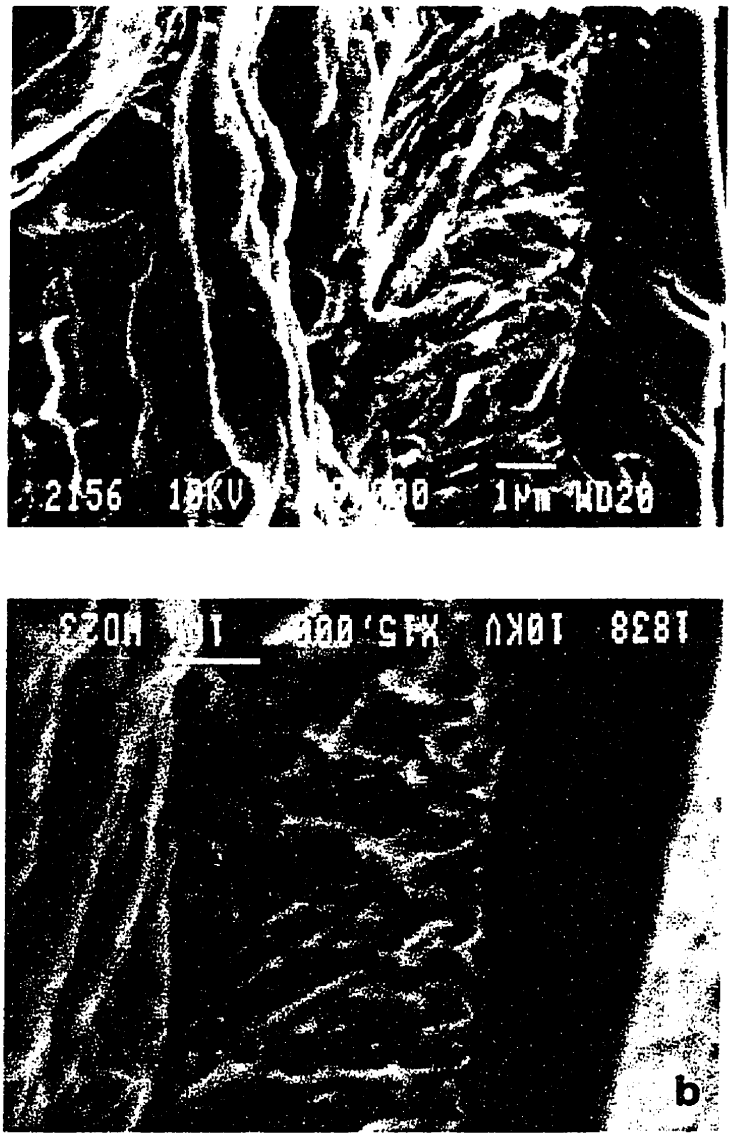

Figure 3.21 Similar tensile fracture features of 316 stainless steel ribbons after cathodic charging (a) in 154°C $MgCl_2$ solution and (b) in H_2SO_4 solution.

The similarity in fractography of cathodically charged specimens in H_2SO_4 and in $MgCl_2$ solution suggests that hydrogen produced in the cathodic reactions of SCC resulted in the crystallographic fracture in austenite.

3.5.2.2 Immersed specimens without stress in $MgCl_2$ solution

The fracture surfaces of non-annealed specimens immersed in $MgCl_2$ solution without an applied stress showed a portion of transgranular cracking. This type of fracture covered about 90% of the thickness (Fig. 3.22), and all fractures initiated linearly from the lateral sides of specimens. The initiation sites corresponded to corrosion pits and slots on ribbon surfaces. This indicates the transgranular fracture is a SCC crack. The SCC may be caused by the residual stress of specimen preparation during immersion or by the residual solution in pits during tension. However, in a small region near the final ductile fracture, a crystallographic cracking zone was found to have initiated in the interior of the specimen (Fig. 3.23). The facets in this region are very small and deformed but interlock on two opposite surfaces. This is the characteristic of PSCC crystallographic cracking in bulk specimens. EDS analysis showed that Fe/Cr ratio was normal and no evidence was found for Cl in this region. Again the fracture in this region indicates it was induced by the hydrogen from the SCC reactions.

Prestrain before immersion induced higher residual stresses on specimens. Both SCC and hydrogen-induced cracking between SCC and ductile fracture were observed. However, annealed specimens did not show clearly the region of hydrogen-induced cracking between SCC and ductile fracture. Annealed specimens without surface polishing only presented ductile fracture, although there were some pits on the surface of the specimens.

In summary, the above results demonstrate that hydrogen can evolve from boiling $MgCl_2$ solution either during pitting or during SCC at the free corrosion potential. For cathodic charging conditions, high hydrogen content near the ribbon surfaces produced large

Figure 3.22 Transgranular SCC fracture found in the non-annealed ribbons immersed in 154°C $MgCl_2$ solution without stress.

Figure 3.23 Crystallographic cracking in a non-annealed ribbons immersed in 154°C $MgCl_2$ solution without stress. The cracking is initiated at A between the surface SCC fracture and final ductile fracture. The microfacets in this region are very small and interlock (such as those indicated by arrows) on opposite fracture surfaces.

crystallographic facets or intergranular cracking. Lower hydrogen content beneath the surface region produced small deformed facets similar to those observed for PSCC crystallographic cracking in bulk specimens, as well as those in-between SCC and ductile fracture in immersed ribbons. In non-polished ribbons, no crystallographic fracture was observed even near corrosion pits. Probably there were not sufficient dislocations to trap absorbed hydrogen. The same {111} cracking crystallography in SCC and hydrogen-induced cracking suggests that hydrogen-dislocation interaction is essential for both fracture.

3.6 DISCUSSION

3.6.1 The influence of hydrogen to the PSCC fracture

The fractography of PSCC crystallographic cracking zones observed in the present study clearly shows their difference from normal ductile fracture. Since their size are usually hundreds of microns in length, the PSCC crystallographic cracking zones cannot be explained by superficial effects resulting from SCC. Particularly, the presence of crystallographic cracking zones ahead of SCC crack tips strongly suggests that absorbed hydrogen from SCC is responsible for this type of fracture.

It has been reported that hydrogen can be generated from SCC tests in chloride aqueous solution [81,182]. Hydrogen evolved from SCC reactions adsorbs on crack walls, and enters into the crack very quickly by absorption [188]. The absorption of hydrogen through transportation and accumulation either during or after SCC influences the PSCC tensile fracture.

3.6.1.1 Diffusion of hydrogen ahead of SCC crack tips

Fick's diffusion law ($x = \sqrt{2Dt}$) gives the depth that hydrogen diffuses ahead of the SCC crack tip in a certain time t. The diffusivity D of austenitic stainless steels are quite low at room temperature, usually in the order of 10^{-12} cm^2/s [25]. The calculated depths are much smaller than the size of observed PSCC crystallographic cracking zones if t is the time interval between SCC and PSCC tests. Thus, random diffusion after SCC cannot account for PSCC crystallographic cracking. In addition, Fick's equation does not relate the depth of hydrogen diffusion to the crack tip K. Diffusion at room temperature is mainly associated with the outgassing of hydrogen near the lateral surfaces of specimens, indicated by the disappearance of the PSCC crystallographic cracking zone in the plane stress regions.

However, the diffusion at 154°C in $MgCl_2$ solution is faster, especially under the stress gradient of the SCC crack tip [60,189,190]. The moving velocity of hydrogen atoms in the stress field of a crack can be estimated by the Einstein-Stokes equation:

$$v = \frac{D}{kT} F; \tag{3-1}$$

where F is the stress gradient at the crack tip which is proportional to $\frac{K}{r^{3/2}}$ along the crack propagation direction. In the K range employed in SCC tests (10 to 30 MPa$\sqrt{m}$) and within a few millimeters at the crack tip, the velocity v from equation (3-1) is at least in the order of 10^{19} m/s, which is much larger than the SCC velocity in stage II (10^{-8} m/s). This suggests that a hydrogen diffusion zone should always exist ahead of the crack tip during SCC tests.

3.6.1.2 Hydrogen concentration at the triaxial stress region

It was proposed that hydrogen-induced cleavage occurs by the enhanced hydrogen concentration C_H in the triaxial tension region of the crack tip [59,60]. The relation of C_H with the equilibrium concentration in the unstressed lattice C_0 was given by Ritchie [191] as:

$$C_H = C_0 \exp\left(\frac{\bar{\sigma}V}{RT}\right); \tag{3-2}$$

with

$$\bar{\sigma} = \sigma_y + 2\alpha_2 K; \tag{3-3}$$

where $\bar{\sigma}$ is the hydrostatic tension and V is the partial molar volume of hydrogen, which is 2×10^{-6} m^3 [30] in iron; α_2 is a constant of 5.08 $cm^{-1/2}$ [191].

Since the stress intensity factors K employed in our tests were less than 30 MPa$\sqrt{m}$ and were well below the yield strength σ_y which is approximately 200 MPa$\sqrt{m}$, the calculated C_H/C_0 according to equations (3-2) and (3-3) was 1.1 for all specimens. The crack tip K does not influence the C_H which is supposed to change the size of PSCC crystallographic cracking zones. On the other hand, the site of maximum hydrostatic tension is not determined by the loading process except for the final fracture stage, but by the geometry of the specimen [192]. The sharper the notch, the closer this site is to the crack tip. Since the SCC crack tip remains sharp during the tests, a similar hydrogen distribution is expected for specimens of the same material. Therefore, the hydrogen accumulation at the hydrostatic tension site is not the main or, at least, the only factor controlling the PSCC fracture.

3.6.1.3 Hydrogen trapped by dislocations and the size of crystallographic cracking zones

A more realistic elastic-plastic treatment shows that most of the hydrogen in steels is trapped by dislocations in the plastic zone of a crack tip [38,193]. When they glide, these dislocations can drag an hydrogen atmosphere. The distance that hydrogen can penetrate into a specimen by dislocation dragging is much greater than by random diffusion. The critical dislocation velocity below which an atmosphere can move with dislocations is given by [67]:

$$v_c = \frac{D}{kT}\left(\frac{E_B}{30b}\right); \tag{3-4}$$

where E_B is the binding energy of a hydrogen atom to a dislocation. The corresponding critical strain rate can be calculated from the Taylor equation:

$$\dot{\varepsilon}_c = \rho b \upsilon_c. \tag{3-5}$$

Assuming a mobile dislocation density in hot rolled steel of 10^{-9} cm^{-2}, the critical strain rate is estimated to be 10^{-3} s^{-1} from equation (3-5). This value is larger than the strain rate associated with the slow crack opening velocity employed (3.3×10^{-4} s^{-1}). Therefore, hydrogen atoms can be carried by mobile dislocations during slow opening.

After SCC tests, the diameter of plastic zone ahead of the crack tip can be estimated by:

$$d = \frac{1}{3\pi}\left(\frac{K}{\sigma_y}\right)^2. \tag{3-6}$$

The calculated d values are listed in Table 3.1 and Table 3.2 for different final K conditions. As mentioned previously, there is always a hydrogen diffusion zone ahead of the crack tip during SCC, which results from the competition between hydrogen diffusion velocity and SCC propagation rate. The size of the hydrogen diffusion zone was not measured in our tests, but it is reported to be approximately 600 μm after 24 hours of SCC [86]. This is larger than the plastic zone calculated from equation (3-6) at K below 20 MPa$\sqrt{m}$ (see Table 3.1 and Table 3.2). Therefore, every dislocation generated during SCC could attract solute hydrogen atoms and, during the subsequent tensile test after SCC, move them beyond the plastic zone of SCC. The larger the plastic zone and the more dislocations present, the more hydrogen would be moved. This explains why the PSCC zone appeared to increase with the final K during SCC in slowly opened specimens of 316L stainless steel. The atmospheres around dislocations would gradually dump hydrogen atoms during their glide to other strong traps, such as inclusions or phase boundaries. Hydrogen-induced cracking can also be initiated in these regions when the local hydrogen amount reaches a critical value.

In the fast opening condition, hydrogen cannot move with mobile dislocations. The critical concentration of hydrogen within the hydrogen diffusion zone at the SCC crack tip determines the size of PSCC crystallographic cracking zone. Due to the similar hydrogen distributions at the SCC crack tip, all of the PSCC crystallographic cracking zones are of the range 200 to 300 μm and are independent of K in 316L, including for the crack opened in solution.

Another important influence on the size of PSCC crystallographic cracking zones is the presence of δ-ferrite. Cracking in this phase is more sensitive to hydrogen than cracking in austenite. Its presence increases the hydrogen concentration in neighboring austenite because its hydrogen solubility is lower. This has been shown by the spatial distribution of deuterium (hydrogen) in austenite phase along crack path of SCC in a duplex stainless steel [194]. Thus crystallographic fracture can appear in both phases. Compared with 310 stainless steel, the PSCC crystallographic cracking zone in 316L stainless steel is enlarged by the presence of the δ-ferrite for the same testing conditions.

PSCC fracture in 310 stainless steel is also attributed to hydrogen-dislocation interactions. Without the presence of δ-ferrite, PSCC crystallographic fracture in 310 stainless steel occurs only at regions of higher hydrogen concentration within the crack tip hydrogen diffusion zone. These PSCC regions are close to planes of maximum shear. Because austenite has low hydrogen diffusivity at room temperature, the hydrogen discharged from dislocations in the previous SCC crack tip plastic zone remains in the vicinity of slip planes. On the slip planes close to the maximum shear stress, many dislocations activated by the overload tensile stress re-trap hydrogen and enable these shear planes fracture at low local strain. The small individual crystallographic cracks within a grain later join together when the local strain is large enough to form dimples. This explains the similar size of PSCC crystallographic cracking zones in 310 stainless steel for all test conditions.

Due to the hydrogen concentration, the unit of crystallographic cracking may be very small (< 1 μm), as indicated by the interstriation spacing in Fig. 3.10b. Very fine dimples formed by stretching effectively reduced the local strain, which allows the subsequent step of crystallographic cracking to occur. Fig. 3.10b also shows the crystallographic cracking appears to be initiated 0.3 to 0.5 μm ahead of the crack tip. This distance agrees with the size of fine dimples formed by stretching in Type I features shown in Fig. 3.8.

Usually, the composition of elements in the Type II features was similar to the macroscopic composition of 310 stainless steel. Because this feature frequently appeared, especially in the specimen undergoing fatigue after SCC, it is more likely produced by a mechanism involving hydrogen-dislocation interactions. Type I and III features represent two extreme conditions of local hydrogen concentrations. Type I features often corresponded to the local segregation of Cr and/or Ni. It has been found in nickel based alloys [195] that segregation of Cr and Ni may form interstitial-substitutional complex with hydrogen. Hydrogen atoms are reoriented under stress around solute atoms. Thus the local hydrogen concentration is increased which should favor more crystallographic fracture. In areas presenting Type III features, higher Si content was found. Because Si atoms are moderate traps for hydrogen [29], fine dimples may be formed at Si-H bonds at relatively low strain. The ends of dimples being toward the same directions on matching fracture surfaces coincides with this assumption in that relatively low hydrogen only helps dimple initiation by an off-center tensile stress.

The above discussion shows that PSCC crystallographic cracking is produced by hydrogen, absorbed from the previous SCC process, interacting with dislocations activated during the early stage of tensile fracture at room temperature. The critical hydrogen concentration C_{pscc} required to produce crystallographic PSCC fracture may not be attained in the entire SCC crack tip plastic zone, the size of which depends on the crack tip K. Meanwhile, the region having C_{pscc} is certainly within the hydrogen diffusion zone. When the SCC crack tip K is lower than 20 MPa$\sqrt{m}$, all dislocations generated in the SCC plastic zone can carry a

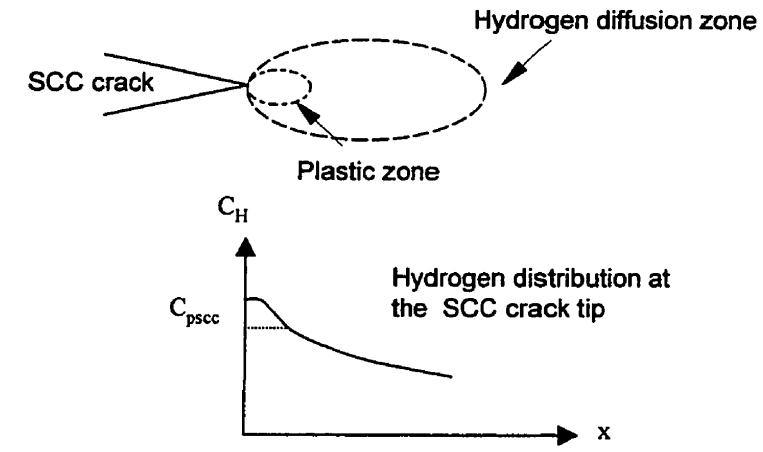

(a) Before PSCC fracture

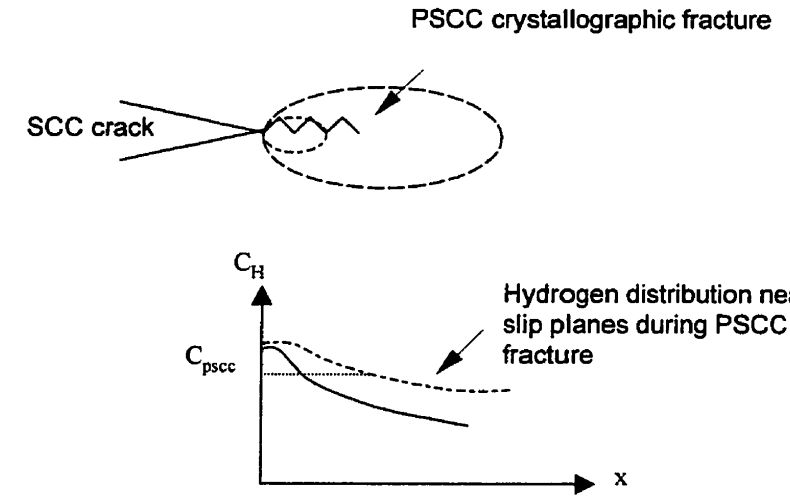

(b) After PSCC fracture

Figure 3.24 A schematic illustration of hydrogen at the SCC crack tip and its influence on PSCC crystallographic fracture

hydrogen atmosphere. During the PSCC tensile fracture, these dislocations move with other newly generated dislocations and with their hydrogen atmospheres, if the crack opening displacement rate is sufficiently slow. This will increase the local hydrogen concentration near the slip planes. Crystallographic cracking could thus occur in a region larger than the former plastic zone, provided that in this region the C_{pscc} is locally reached in the cracking phase. This fracture process is schematically shown in Fig.3.24.

3.6.2 Hydrogen contribution to SCC of austenitic stainless steels

The role of hydrogen in SCC of austenitic stainless steels has been debated, although it is generally accepted that hydrogen is often generated near the tip of SCC cracks. Detailed fractographic and crystallographic studies of SCC, especially in fcc metals [2-5] has already cast doubt on the mechanisms based on crack tip dissolution and cleavage. The present study of PSCC crystallographic fracture strongly indicates that absorbed hydrogen produced during SCC induces the PSCC crystallographic fracture both in austenite and in δ-ferrite. Since the appearance of the fracture surfaces also gives important information about fracture processes, the fractographic study of PSCC suggests that hydrogen is involved in producing SCC fracture as well.

Firstly, both SCC and PSCC crystallographic fracture present similar crystallographic features in austenite in 316L stainless steel. In PSCC, the facets are usually smaller and more deformed because of the higher K generated in the constant opening rate tensile test. Lower hydrogen content in PSCC also contributes to its less crystallographic appearance. The fractography of cathodically charged ribbons has also shown that higher hydrogen concentration produces large crystallographic facets. Compared with PSCC, the hydrogen content very near the crack tip during SCC is higher because the hydrogen supply is constant through the cathodic reactions. The hydrogen permeability and solubility are also higher at 154°C, and there is no outgassing. Hence, the

fracture surface appears to be more crystallographic. In the low K SCC region where the hydrogen-dislocation interaction is weak, the appearance of very fine {111} microfacets on {100} primary planes resembles those in the PSCC areas of 316 ribbons which has also low hydrogen accumulation. In addition, etch-pitting showed a {111} PSCC crystallography in austenite in the 316L stainless steel [196], which is the same as in SCC. Therefore, the remarkable fractographic similarity between SCC and PSCC crystallographic cracking in austenite clearly indicates the close relationship in their fracture mechanisms.

Secondly, for the specimens opened up in solution, the cracking did not always remain crystallographic for the entire fracture produced in $MgCl_2$ solution. In the rapidly-opened 316L stainless steel specimen, the crystallographic fracture surface gradually became ductile ahead of the SCC crack tip (Fig. 3.18). In 310 stainless steel, the occurrence of crystallographic fracture ahead of the SCC crack tip was restricted to a certain distance (~100 μm). If the cracking speed employed allowed dissolution or other time dependent processes to happen, the crystallographic fracture should have been continuous until the environment was no longer available. However, the crystallographic cracking stopped in the solution. The explanation very probably concerns the hydrogen gradient at the SCC crack tip. The critical hydrogen amount C_{pscc} needed for crystallographic cracking in 310 stainless steel, in which δ–ferrite is not present, cannot be reached far away from the crack tip. When the cracking surpasses the region with a hydrogen content of C_{pscc}, ductile fracture appears as the cracking proceeds. This further indicates that hydrogen generated from solution, not the solution itself, is necessary for SCC.

Chapter 4

SCC Behavior of δ–ferrite in 316L Stainless Steel

4.1 INTRODUCTION

It has been shown that both wrought and cast duplex stainless steels are resistant to cracking in chloride solutions and that their increase in resistance to SCC is related to the amount of retained ferrite [73,197-199]. Shimodaira *et al* [88] demonstrated that the SCC resistivity increased with increasing ferrite content in the range of austeno-ferritic structures, but this phenomenon was reversed in the range of ferro-austenitic structures. Crack propagation of 26-8 steel containing 50% ferrite and 50% austenite was extremely slow in $MgCl_2$ solution [199]. Ferrite in the austeno-ferritic alloys acts as a crack arrester mechanically and electrochemically to the crack propagation in austenite [88].

However, the superiority to SCC of duplex steels over austenitic stainless steels is not always clear-cut. Denhard [200] mentioned that the austeno-ferritic steel (AISI 312 stainless steel) cracked almost as quickly as austenitic steels, because the SCC crack propagated preferentially in austenite and bypassed the ferrite. In stainless steel weldments containing 5 to 10% δ–ferrite dendrites, the two-phase interface was a preferential SCC cracking path due to solute segregation. It was [201-203] suggested that the presence of δ–ferrite provides effective cathodic protection of the austenite against SCC. However, the presence of approximately 5% δ–ferrite in 316L stainless steel can strongly accelerate the Stage II SCC propagation in some orientations [179]. If the amount of retained δ–ferrite was reduced to 0.5%, 316L stainless steel had a similar cracking velocity to that of austenitic 310 stainless steel [179].

Similarly, the role of ferrite to resist hydrogen embrittlement in stainless steels is also not simple. In a gaseous hydrogen environment, it was found that the sensitivity to hydrogen increased in the following order: duplex stainless steels, highly-alloyed ferritic stainless steels and unstable austenitic stainless steels [204,205]. The presence of δ–ferrite did not affect the ductility loss in 309 stainless steel [206], and the fracture surface was entirely ductile. It was suggested that δ–ferrite is important as a crack arrester in aqueous solution, possibly by affecting the crack tip electrochemistry through a complex electrochemical coupling between two phases, but it is not important in controlling the void growth and hydrogen accumulation processes accompanying hydrogen induced ductility losses [207]. It should be pointed out, however, that the orientation of the ferrite phase with respect to the loading direction can greatly influence the propagation of SCC in aqueous solution. Mandziej [208] reported that in a duplex stainless steel, SCC initiated exclusively on the surface parallel to the rolling plane and pits and microcracks on the plane perpendicular to the rolling plane never developed into macrocracks, when the specimens were tested under a constant load in the rolling direction. The SCC propagation velocity in stage II was measured to be more rapid

on the rolling plane in the longitudinal direction of the δ–ferrite platelets than on the plane perpendicular to the rolling plane in the same direction [179] in 316L stainless steel.

Obviously, it is not very clear how the presence of ferrite influences the SCC of austenitic stainless steels, especially when hydrogen is involved in assisting this cracking. There has been little work reported concerning the detailed SCC fractography of the ferrite phase in stainless steels. In this chapter, the SCC fracture features in the δ–ferrite of 316L stainless steel will be reported in detail. The objective of this work in the present study was to correlate the SCC fractography with the microplasticity at the crack tip. Based on the obtained fractography, a SCC mechanism in δ–ferrite is proposed, which is described by the effect of hydrogen on dislocations in the bcc lattice.

4.2 MICROFRACTOGRAPHIC OBSERVATIONS

Some surface cracks were observed during the present SCC tests, in spite of the lacquer protecting the lateral surfaces of the specimens. These surface cracks are small, detached from the main crack, and approximately perpendicular to the tensile axis (Fig.4.1a). The formation of surface cracks is believed due to the preferential SCC of δ–ferrite on the surface because δ–ferrite acts as a microanode [179,201,203] with regard to austenite. The electrochemical cell coupled between the two phases makes the δ–ferrite a preferential corrosion site. Actually, many indications on the fracture surfaces showed a crack propagation direction from the lateral sides towards the central region. All the fractographs presented in this chapter have a vertical macroscopic propagation direction from the bottom to the top. The river lines, slip steps and arrest lines indicated, however, that the local propagation direction deviated, in some regions by approximately 90°, to the macroscopic propagation direction (Fig. 4.2 and Fig. 4.7).

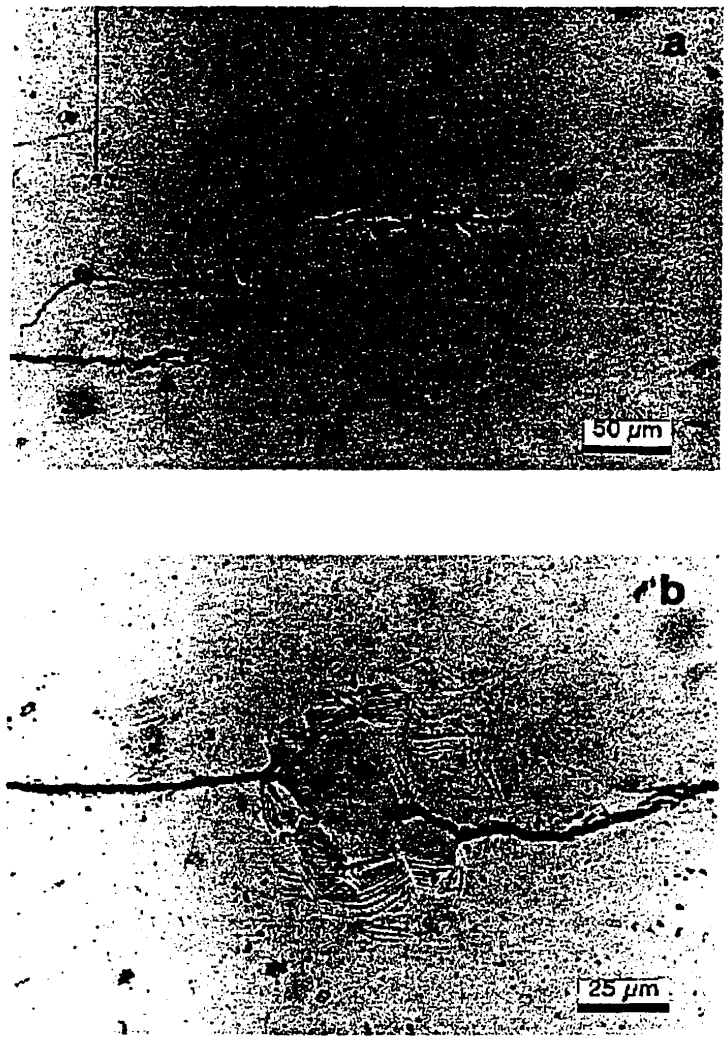

Figure 4.1 Lateral surface observation in a 316L stainless steel specimen show (a) several detached small SCC cracks ahead of the main crack (indicated by an arrow) and (b) a plastic zone between two detached SCC cracks.

Fig. 4.1b reveals a plastic zone between two detached surface cracks. These active slip planes may provide the preferential path to the following cracking. In fact, SCC spreading from δ–ferrite to austenite was found along slip planes. Shown at the top of Fig. 4.2, the crack propagates from right to left in the δ–ferrite, while the transgranular cracking in the austenite, seen in the middle of this figure, initiates at the boundary of the δ–ferrite. It propagates from top right to bottom left, then meets the main crack at a tearing ridge below the middle of Fig.4.2. Cracks propagating from regions of interfacial fracture to the surrounding austenite were also observed.

The transgranular fracture in δ–ferrite usually showed that crack propagated on inclined facets in the direction approximately perpendicular to the macroscopic propagation direction (Fig. 4.3). The cracking facets were inclined to the tensile axis and to the macroscopic SCC crack front, in both cases by an angle of approximately 45°, and formed regular hills and valleys. The river line patterns on these inclined facets indicated that the crack initiated at the interfaces between the δ–ferrite and the austenite. Occasionally a small amount of interfacial cracking was seen between two transgranular regions. The observations of crack propagation along the interfaces (Fig. 3.2) and from the boundaries to the interior in both phases (Fig. 4.2 and Fig. 4.3) suggest that interfacial cracking occurs prior to the transgranular cracking in the δ–ferrite.

Slip steps were observed frequently on the δ–ferrite side of the interface but only occasionally on the austenite side. Generally, these slip steps were wavy, had a similar trend and were less than 1 μm in height. Fig. 4.4 presents such slip steps at high magnification in the δ–ferrite. Stereomicrographs showed that the slip occurred upwards on the right and downwards on the left. The wavy and irregular slip traces indicate the occurrence of cross slip within δ–ferrite grains. This picture also clearly demonstrates the correspondence between these slip traces and the transgranular cracking: fine river lines corresponded to propagation suddenly changing on slip planes, and coarse river lines resulted from decohesion, probably

Figure 4.2 SCC fracture in austenite (A) was initiated from the δ–ferrite (F) ahead of the main crack and linked up with the main crack at the tearing ridge. The macroscopic propagation direction is from the bottom to the top.

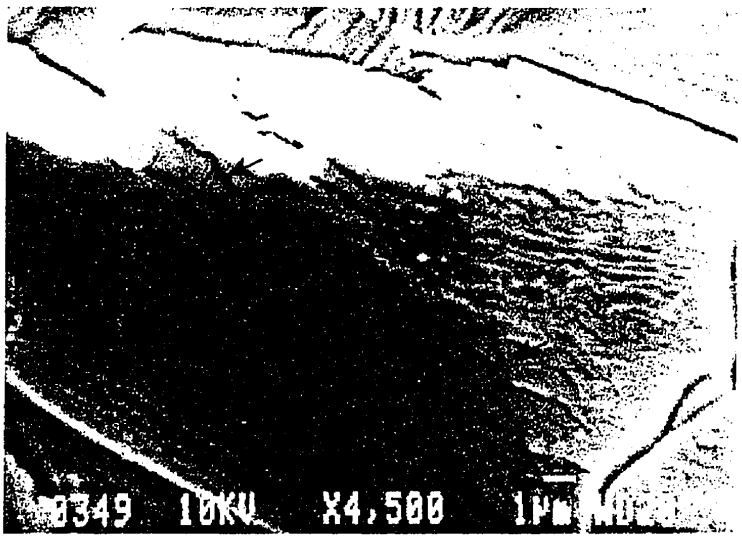

Figure 4.4 Slip steps on the δ–ferrite side of the δ–γ interfacial boundary. The facets of transgranular fracture initiate following the wavy slip steps.

Figure 4.3 Matching fractographs of transgranular fracture in δ–ferrite. Cracks initiate at the interface between δ–ferrite and austenite and propagate on inclined facets.

following cross slip planes, between relatively large slip bands. There are some traces (indicated by arrows) that do not follow the major trend of the slip steps. This may be caused by slip involving another Burgers vector which is responsible for the serrations on river lines. Some slip steps can be seen as opened microcracks on the interface boundary (Fig. 4.5).

The terms used to describe the transgranular SCC features of austenite, such as serrated river lines, serration facets, sheet-like microfacets, undercutting, can also be employed to describe the transgranular fracture of δ–ferrite. However, *crystallographic* striations were rarely observed on the δ–ferrite facets. At high magnification, no striations or any other markings perpendicular to the river lines were found in Fig. 4.3 and Fig. 4.6. On the contrary, very fine "striation-like" markings appear parallel to the river lines in Fig.4.6. This is an indication that very local and fine cross slip occurred on the primary facets, since the Burgers vector should be approximately parallel to the river lines to allow cross slip to occur.

In some regions, crack arrest lines were observed on the δ–ferrite side of the interfacial boundaries. These arrest lines indicate temporary positions of the crack front and imply that the interfacial crack propagation occurred by a series of discrete crack advances (Fig. 4.7). Arrest lines were at first noticed near the boundaries of δ–ferrite platelets, but at low working distance on the SEM which improves considerably the resolution, they were found in various regions. This may be attributed to the resistance of austenite grains against more rapid propagation in the δ–ferrite, which results in a higher local stress to form more pronounced yielding. In a few cases, the pronounced propagation discontinuity extended into transgranular regions of the δ–ferrite (Fig. 4.8), where arrest lines are perpendicular to the river lines and match peak to peak. This mirror matching is completely different from the interlocking matching of the striation-like features found in austenite.

Slip steps on boundaries, another important feature of the interfacial fracture seen on the δ–ferrite side, coexisted at times with arrest lines (see Fig. 4.7). Both types of markings

Figure 4.5 Some opened slip steps on the δ–ferrite side of an interfacial boundary.

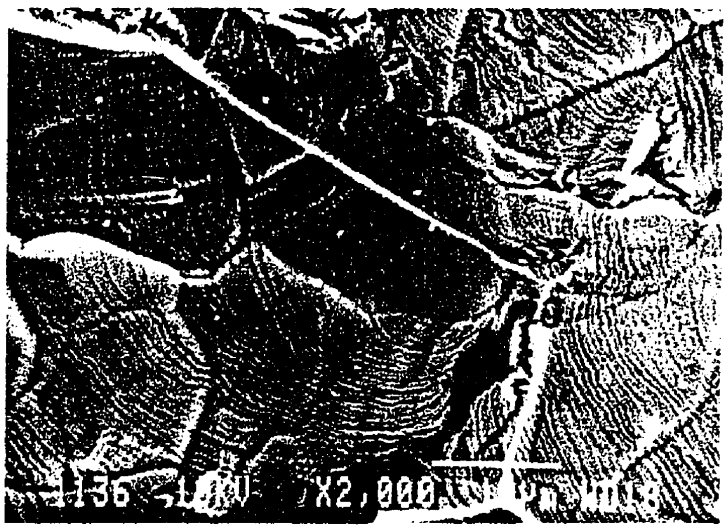

Figure 4.7 Arrest lines and slip steps on the δ–ferrite side of the δ–γ interfacial boundary.

Figure 4.6 Matching fractographs of transgranular fracture in the δ–ferrite. Fine river lines are parallel to coarse river lines.

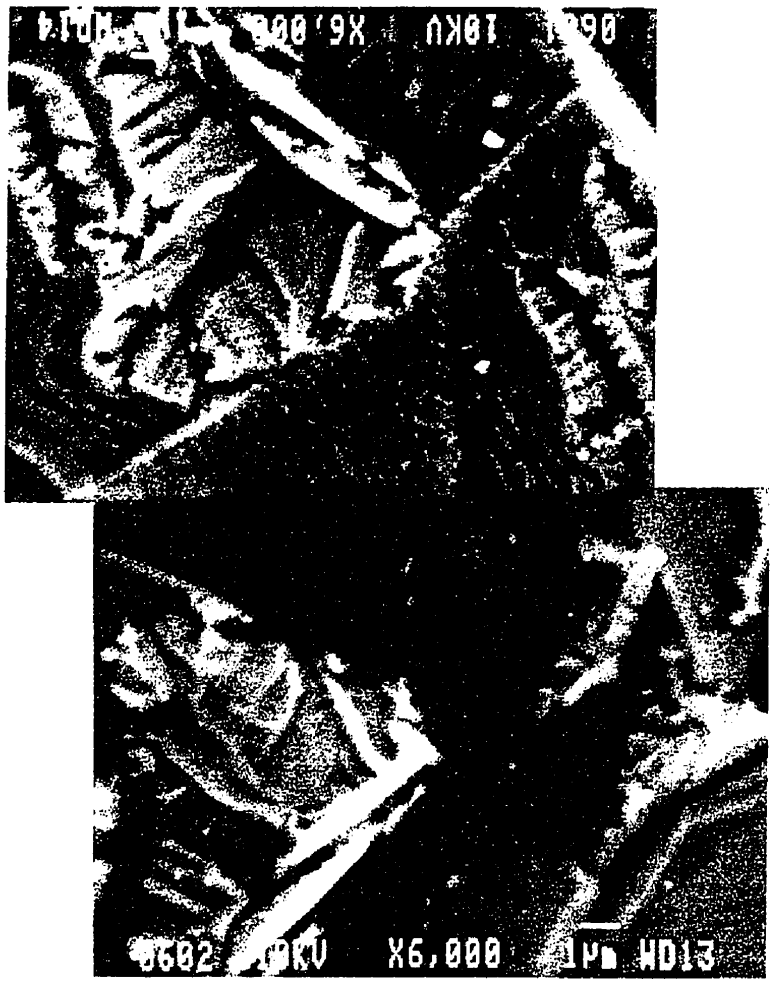

Figure 4.8 Matching fractographs of SCC fracture surfaces. Arrest lines appear on the interfacial boundary of the δ–ferrite side and match on the transgranular facets on both sides in the δ–ferrite.

were often parallel to one another locally, suggesting that slip steps are also crack front markings during the SCC. The curvature of the arrest lines was often consistent with the beginning of the transgranular fracture in the δ–ferrite, illustrating again that this transgranular fracture was incited by the interfacial propagation (Fig. 3.3 and Fig. 4.8). In addition, arrest lines were rarely found on the corresponding austenite boundaries (Fig. 4.8 and Fig. 4.9) or disappeared during propagation into the austenite (Fig. 4.9). This indicates that the dislocations are more active in the δ–ferrite than in the austenite during SCC. In addition, the transgranular fracture in the δ–ferrite shown in Fig. 4.9b demonstrates again its correspondence to the slip traces.

One exception was found in Fig. 4.10 where arrest lines surround initiation sites on both sides of interfacial fracture surfaces. However, these arrest lines matched in an interlocking manner. This unique evidence of interfacial initiation ahead of the SCC crack tip strongly indicates that absorbed hydrogen from cathodic reactions is involved in the SCC fracture. A crack initiation site ahead of the crack tip is also shown in Fig. 4.11 near a triple point on δ–ferrite boundaries.

4.3 DISCUSSION

4.3.1 Hydrogen enhanced dislocation activity in δ–ferrite

Previous studies [14-16,54,209] by *in situ* TEM observations have revealed that dissolved hydrogen can either promote the injection of dislocations nearby the surface cracks, or increase the mobility in particular of the screw dislocations in pure iron. Dilute hydrogen entering dislocation cores enhances the double kink nucleation along screw dislocations [41,210]. As a result, the yield stress is reduced at room temperature. In duplex stainless steels, a decreased yield stress resulting from hydrogen charging was reported [211] with a simultaneous increase of the dislocation density, most of which are $\frac{1}{2}$<111>

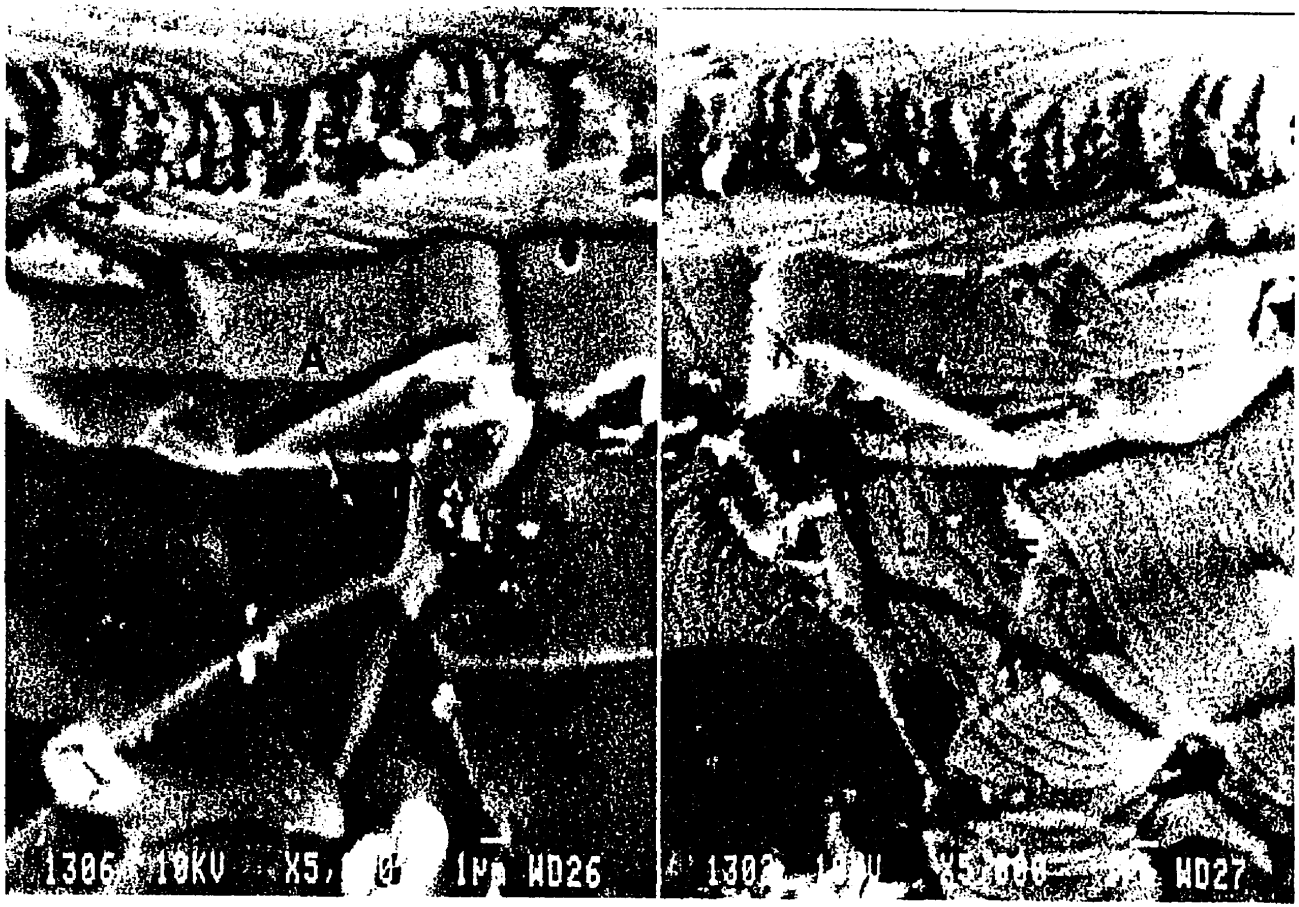

Figure 4.9 Matching fractographs of SCC fracture surfaces indicate that arrest lines appear on the δ–ferrite side (F) of the interfacial boundary, but not on the austenite side (A).

Figure 4.10 Matching fractographs of an interfacial SCC fracture. Several initiation sites ahead of the SCC crack tip are indicated by crack arrest lines which interlock on opposite fracture surfaces.

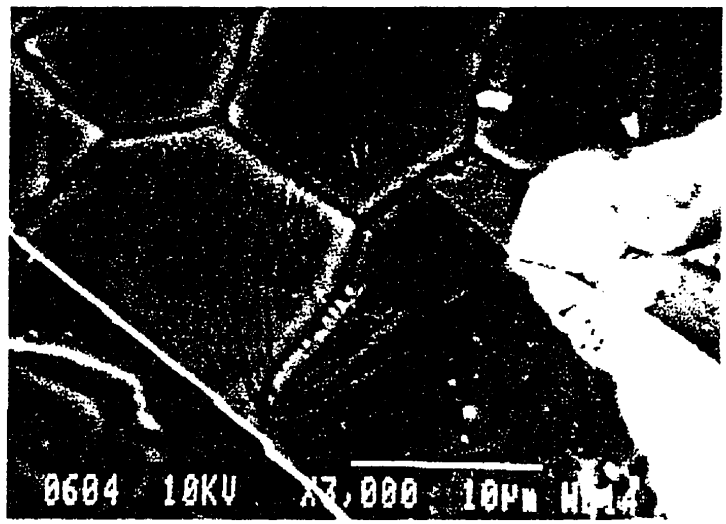

Figure 4.11 A crack initiation site at a triple point of δ–ferrite grain boundaries.

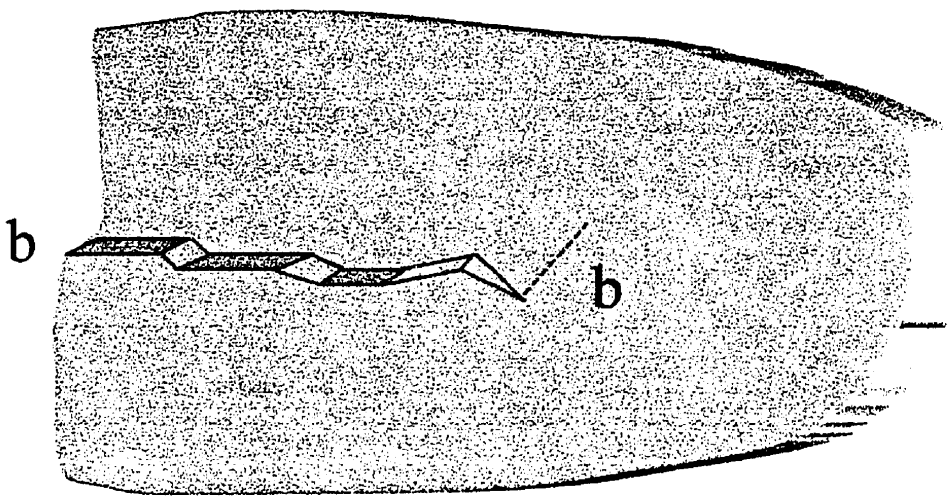

Figure 4.12 Schematic illustration of crack initiation and propagation by the slip and cross slip of screw dislocations in the δ–ferrite.

screw dislocations, in ferrite. The decrease in yield stress is due to the hydrogen-induced ferrite softening. The phenomenon of hydrogen-induced ferrite softening was also observed in the present study. Slip traces and crack arrest lines often appeared on the δ–ferrite side of interfacial boundaries, but rarely on the austenite side of interfacial boundaries. The δ–ferrite, which would normally have a higher yield strength than the austenite, is softened by the absorbed hydrogen during SCC.

Hardening produced by hydrogen charging occurs at low temperatures by hydrogen atoms pinning dislocations [41], and at high hydrogen content by shear localization resulted from hydrogen-trapped edge dislocations [212] in austenite. But this is not the case during SCC at 154°C. The hydrogen concentration at the crack tip produced in SCC reactions is very low compared with that in an hydrogen environment. Hydrogen absorbed by the δ–ferrite during SCC could be even lower. A few kinks generated by the dilute hydrogen in δ–ferrite could move a considerable distance along the screw dislocation before being pinned by hydrogen in the matrix. Also, the kinks generated would drag more movable hydrogen atoms at 154°C. Therefore the motion of a screw dislocations can be facilitated as a whole. Even if shear localization occurs on some slip planes, it would be relieved easily by thermally activated cross slip in this bcc phase. In addition, mainly primary dislocations are injected under the applied stress in SCC which was well below yield strength in the present study. There are few forest dislocations to cause rapid work hardening. Hence, hydrogen activates screw dislocations in the δ–ferrite and causes the consequential softening of the δ–ferrite during SCC. The SCC fractography of the δ–ferrite described in section 4.2 can be well explained by such a contribution of hydrogen to the SCC fracture.

4.3.2 Cracks initiation at δ-γ interfaces in δ–ferrite

In the present study, both the lateral surface and the fracture surface observations showed preferential crack propagation along interfacial boundaries and from the interfacial boundaries to the interior, because the δ–ferrite is more anodic to austenite, which promotes corrosion near the interface. Once this corrosion starts, hydrogen adsorption and absorption follow. Since hydrogen diffuses more quickly along grain boundaries, dislocations are injected near the interfacial boundaries then move into the interior of grains. Slip steps are produced first on the interfacial boundaries and microcracks are then nucleated. In some cases, crack arrest markings produced by more pronounced localized slip occurred on the grain boundaries of δ–ferrite but were rarely found on the corresponding austenite boundaries. This indicates that dislocations in the austenite are less active than in the δ–ferrite and agrees with the general knowledge that the critical amount of hydrogen required for "embrittlement" is lower in δ–ferrite. Actually this critical amount should be that required to increase the number of mobile screw dislocations or to increase the mobility of the screw dislocations.

Crack initiation at the interfacial boundaries is also attributed to the incompatible deformation between two phases at the SCC crack tip. In the same time period, hydrogen diffuses almost 200 times more quickly in the δ–ferrite than in the austenite at 154°C. When hydrogen diffuses through the whole thickness of δ–ferrite platelet, it only reaches less than 0.1 μm deep in the neighbouring austenite. Dislocations activated by this amount of hydrogen in austenite might not be sufficient to form many visible slip steps on grain boundaries in this phase, although slip steps was observed occasionally (Fig. 3.2). Also the stress concentration produced by the dislocation pileups in δ–ferrite could not initiate many dislocations within the austenite due to the limited length of pileups in thin δ–ferrite platelets. Without compatible deformation in austenite, stress concentration produced by enhanced dislocation movement in the δ–ferrite could only be relieved through interfacial cracking. On the other hand, emitted dislocations pile up on slip planes at the crack tip. Once the pileup is sufficient long and leads to

decohesion on those slip planes, the crack can change its path from the grain boundary to the slip planes. Thus, transgranular cracking initiates after interfacial cracking which is the result of enhanced dislocation motion as well.

It can be argued that the dislocation motion could be enhanced by the dissolution-induced stress concentration [6,151]. This effect is hardly ruled out since the δ–ferrite has an anodic potential to the austenite. However, Fig. 4.10 and Fig. 4.11 suggest that the crack can sometimes initiate ahead of the main SCC crack without the access to solution. This is a strong indication that the hydrogen is absorbed ahead of the crack tip which induces dislocation motion and crack initiation. In the case of Fig. 4.10, where the initiation sites are located among SCC tongues and surrounded by many small inclusions, the hydrogen amount is relatively higher in the austenite than it usually is as a result of absorbing hydrogen from its surroundings. Thus dislocations are also activated in the austenite and softening in this phase possibly follows, which is suggested by the interlocked arrest lines in both phases along this interfacial boundary.

4.3.3 Contributions of screw dislocation movement

It was reported [211] that most dislocations observed in the ferrite phase of hydrogen charged duplex stainless steels were screw dislocations. In the present study, no effort was made to observe and identify dislocations, however, the fractography indicated that slip and cross slip of screw dislocations in the δ–ferrite make a large contribution to the fracture process.

Firstly, slip and cross slip of screw dislocations initiates SCC cracks on interfaces, as demonstrated by the wavy but nearly parallel slip steps on grain boundaries of δ–ferrite phase (Fig. 4.4). These slip traces alternate randomly due to the multiple slip planes in bcc δ–ferrite and the cross slip of screw dislocations. Such a slip behavior would not lead to the quite

symmetric microfacets alternating between slip planes, as observed in transgranular SCC cracking of austenite, if decohesion occurred on these planes. Schematically shown in Fig.4.12, the slip and cross slip of screw dislocations facilitated by absorbed hydrogen in the δ–ferrite could produce slip steps on the interfacial boundary, which was often observed in the fractographic study (Fig. 4.4, 4.5 and 4.7). The presence of those slip steps reduces the strength of the interfacial boundary and initiates microcracks. The interfacial crack propagates by repeatedly initiating slip steps near the crack tip region on the δ–ferrite boundaries and by linking of those slip steps.

Secondly, slip and cross slip of screw dislocations are also able to produce transgranular cracks through decohesion on the slip planes. It has been proposed [213] that either screw or edge dislocations have a nonlinear core field. In a dislocation pileup, these core fields generate a stress concentration on the plane of the pileup that favors the formation of an opening mode I crack. Such microcracks opening up on the slip planes were found on δ–ferrite grain boundaries (Fig. 4.5). Dislocations emitted from interfacial boundaries pile up on slip planes when they meet an obstacle such as other grain boundary or the unfavorable local condition to the cross slip. Once the pileup is sufficiently long and the stress concentration is high, decohesion occurs.

The frequently appearing transgranular features in δ–ferrite correspond to facets inclined both to the tensile axis and to the macroscopic crack front by an angle of approximately 45°. These features were always found away from the lateral surface regions, consistent with the regions subjected to a maximum shear stress in the plane strain condition. Dislocations are readily active on these facets, therefore decohesion occurs more easily. Fig.4.4 shows a rare case where the major Burgers vector is nearly perpendicular to the grain boundary. It can be seen, at the top of the picture, that decohesion occurs on very fine cross slip planes, on sessile edge segments and between two bands of cross slip planes where they cannot link together, provided that the critical decohesion strength of the lattice is exceeded by

the local stress concentration. Hence, typical transgranular cracking features, such as serrated river lines and sheet-like microfacets (Fig. 4.4 and Fig. 4.6) were observed.

Decohesion may also occur by the pileup of edge dislocations. However, many fine river lines were observed (Fig. 4.6) nearly parallel to the coarse rivers instead of striations perpendicular to the coarse rivers. This suggests that the microfacets of transgranular cracking in the δ–ferrite are composed mainly of fine cross slip planes.

4.3.4 Discontinuous propagation

The crack arrest lines and slip steps observed in the present study, especially the former, imply that the interfacial crack propagation is discontinuous. Depending on the orientation and local chemical and mechanical conditions, one or more slip systems may be activated, leading to slip steps or homogeneous yielding at the crack tip. The interface is weakened by microcracks or work hardening, thus the crack advances a small distance. A further crack jump does not occur until the absorbed hydrogen approaches the critical amount to produce sufficient slip, which is a time dependence process.

A similar procedure could happen during transgranular cracking in the δ–ferrite. Repeated dislocation shielding, piling up and decohesion occur on slip planes. Since this procedure takes place on crystallographic planes, arrest lines were rarely detected. One example is shown in Fig. 4.8 where arrest lines are observed throughout the intergranular and transgranular cracking. This region is close to the boundary of δ–ferrite, where the SCC resistance may be larger because of the surrounding austenite. A higher local stress is required to continue propagation, which produces general yielding on slip planes. Another example is shown in Fig. 4.9 which demonstrates a correlation between arrest lines and microfacets and shows discontinuous transgranular propagation in the δ–ferrite.

4.4 PROPOSED SCC MECHANISM

The fractographic observations and the identification of the cracking crystallography (presented in the next chapter) during SCC of the δ–ferrite contained in 316L stainless steel in $MgCl_2$ solution indicate that there is a close correlation between dislocation activity and transgranular SCC. This is strikingly similar to transgranular SCC in fcc materials. In addition, the fractographic observations show that intergranular fracture is also the result of dislocation movement within grains. The hydrogen produced during SCC and absorbed near the crack tip promotes the dislocation activity. The SCC mechanism in δ–ferrite is therefore suggested to be as follows:

1. Hydrogen generated from cathodic reactions is produced near preferential corrosion sites, close to the interface between δ–ferrite and austenite. Some of this hydrogen is adsorbed and then absorbed.

2. Because of the low solubility of hydrogen in the δ–ferrite, dilute hydrogen enhances the dislocation nucleation and motion. This effect is especially evident for screw dislocations, which have relatively low mobility.

3. Activated dislocations emanate from the crack tip, producing slip steps or arrest lines at the crack front in the δ–ferrite. Decohesion of the interfaces between the two phases is easily produced by the enhanced dislocation movement at the crack front in the δ–ferrite and by the incompatible deformation between the austenite and the δ–ferrite. Further propagation occurs when slip steps or arrest lines produce decohesion again on the interfaces.

4. In a suitable orientation, long pileups of shielded dislocations makes decohesion possible on slip planes. Transgranular cracking then occurs.

Chapter 5

Crystallography of δ-ferrite in SCC and PSCC

5.1 INTRODUCTION

In contrast to the large body of crystallographic studies of SCC in austenitic stainless steels, SCC crystallography of ferritic stainless steels has been paid considerably less attention. This may be attributed to the historical view that SCC fracture in ferritic steels corresponds either to intergranular cracking or to cleavage. Fracture surfaces of transgranular SCC in ferritic stainless steels were described as cleavage [183,214], and little effort was made to verify if the cleavage appearance is really a cracking occurred along {100} planes, the typical cleavage planes in bcc metals. To date, there have not been any publications found in our search of the literature reporting the SCC crystallography of ferritic steels.

On the other hand, the crystallographic nature of hydrogen-induced cracking has been studied in a number of ferrous alloys. Both {100} cleavage planes [215-219] and slip planes [220-222] were reported as cracking planes in hydrogen-induced cracking. The {100} cracking, in some cases [215-219], were accompanied by many dislocation arrays or slip bands. Slip planes also appeared in near threshold fatigue of Fe-Si alloy and mild steels [113]. Therefore slip planes cannot be ruled out from SCC crystallography of ferritic steels, especially when fracture involves hydrogen, such as the SCC cracking of δ–ferrite in 316L stainless steel in $MgCl_2$ solution.

An attempt was therefore made to determine the cracking crystallography of the δ–ferrite in 316L stainless steel during SCC and PSCC fracture. This attempt complements the fractographic study of SCC and PSCC in the δ–ferrite reported in Chapter 3 and Chapter 4. The purpose of this work was to establish a correlation of the fracture process between SCC and PSCC, and therefore to cast further light on the SCC mechanism of austenitic stainless steels in boiling $MgCl_2$ solution.

5.2 CRYSTALLOGRAPHY OF SCC

In the present study the crystallography of SCC in the δ–ferrite was determined from the analyses of the hot rolling texture and the fracture surface photogrammetry.

The typical transgranular SCC fracture (shown in Fig. 3.3) often presented similar cracking orientations in different grains, within a δ-ferrite platelet as well as in different δ-ferrite platelets. This led to a texture measurement in the δ-ferrite. Indeed, the pole figures obtained by X-ray diffraction in the δ-ferrite (Fig. 5.1) show the presence of two textures: {100}<110> and {100}<100>. These textures indicate that the {100} plane in the δ-ferrite tends to be parallel to the cracking plane of ST orientated specimens, and that

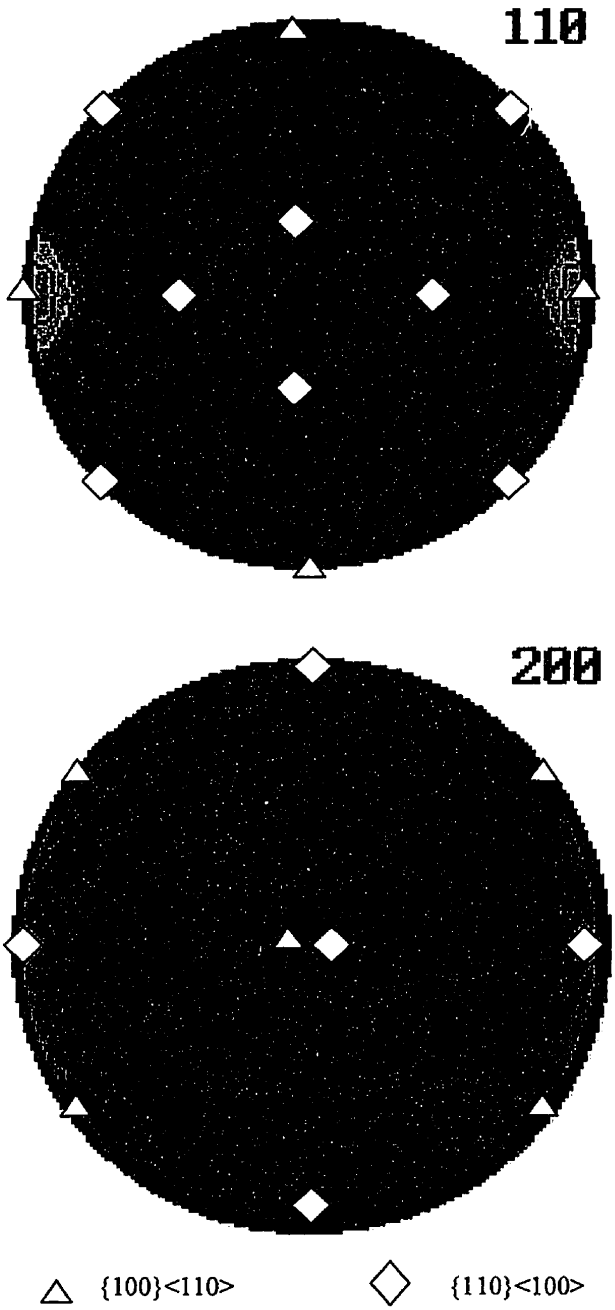

Figure 5.1 The {110} and {200} pole figures obtained by X-ray diffraction from the δ–ferrite in 316L stainless steel.

either <110> or <100> direction in the δ-ferrite tends to be perpendicular to the macroscopic crack propagation direction in ST orientated specimens.

Because of the small volume percentage of the δ-ferrite in 316L, the distribution and intensities of poles were not as typical as ideal {100}<110> and {100}<100> texture. As well, no information was available on exactly how this 316L stainless steel had been processed, which could considerably influence the texture development during hot rolling. However, it is known [223] that recrystallization textures are essentially the same as the previous deformation textures in bcc metals. Therefore, the presence of {100}<110> texture is very reasonable since it is the major component of the deformation texture in iron. The cube texture {100}<100> usually occurs during recrystallization when the grain growth is restricted by the specimen thickness [224]. This meets the grain growth condition of the δ-ferrite platelets which are sandwiched between austenite grains.

With the help of this texture measurement, the SCC crystallography could be determined reasonably by photogrammetric analysis. The typical transgranular SCC fracture in δ–ferrite is shown again in Fig. 5.2. The angles between two inclined primary facets was measured as 90° by tilting the specimen in the SEM. This indicated that these primary facets are close to {110} in the δ-ferrite, because they are also inclined approximately 45° to the cracking plane which is parallel to the {100} planes in the δ-ferrite. Smooth river lines often initiated from the interface with an angle of approximately 30° to the intersection of two {110} planes, while serrated river lines often appear perpendicular to the intersections (Fig. 5.2). The angles between serrations or steps on river lines were measured to be approximately 70°, which corresponded to the angles between two {112} planes perpendicular to a {110} plane. Because two {110} planes perpendicular to each other intersect along a <100>, the local propagation direction indicated by smooth and serrated river lines can be <111> or <110>, respectively. The former is parallel to the Burgers vectors of screw dislocations in the δ–ferrite, suggesting that cross slip is involved in producing these

Figure 5.2 The typical transgranular SCC fracture in the δ–ferrite.

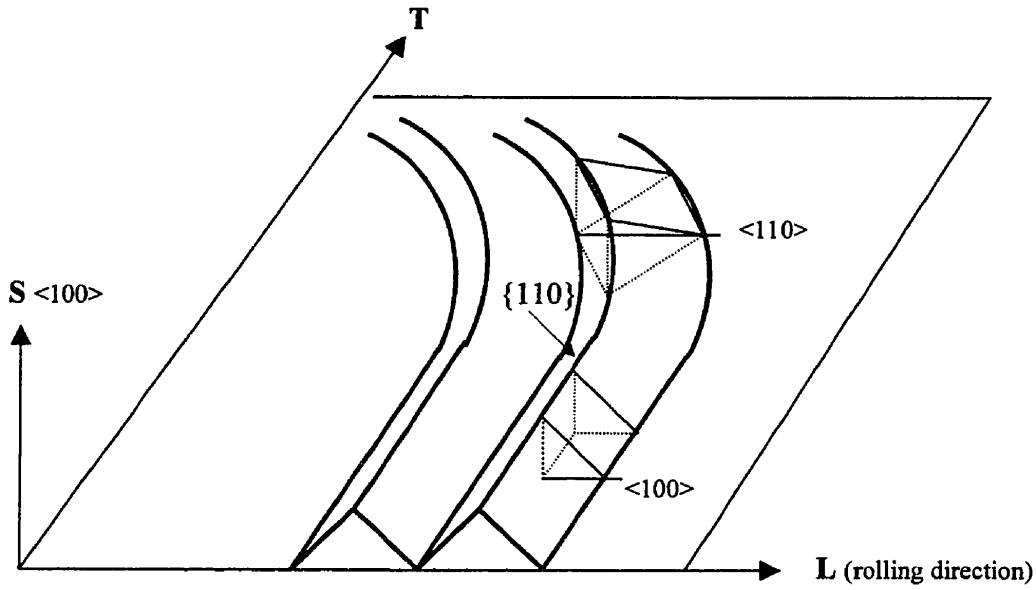

Figure 5.3 Schematic illustration of the SCC crystallography in the δ–ferrite contained in 316L stainless steel. The δ–ferrite has textures of {100}<100> and {100}<110>. Transgranular SCC occurs on {110} planes which inclined ~ 45° to the {100} planes. River lines on these {110} planes are along <110> and <111> directions. The curvature of the hills and valleys is produced by the alternative arrangement of two textured grains in the δ–ferrite.

river lines. The <110> river lines may be produced by more complex dislocation movement, such as the small scale slip on different {112} planes, or the combination of slip on closely parallel slip planes and decohesion between them. Fig. 5.3 schematically illustrates the SCC crystallography in the δ-ferrite. Two textured grains alternatively arranged in the δ-ferrite produced the feature of curved hills and valleys shown in Fig. 3.3.

Although the δ-ferrite is a bcc phase, its transgranular SCC occurs on {110} and {112} slip planes, and clearly not on {100} cleavage planes. This suggests that SCC cracking in the δ-ferrite is associated with microplasticity at the crack tip, which agrees with the fractographic observations presented in Chapter 4 and with the fractography in austenite [2,3].

5.3 CRYSTALLOGRAPHY OF PSCC

The PSCC crystallography in the δ-ferrite was determined by studying the electron back scattered patterns (EBSPs) obtained from PSCC microfacets and by photogrammetric analysis.

Most of the PSCC crystallographic cracking occurred on a plane approximately perpendicular to the tensile axis. The texture measurement showed that this cracking plane was close to the {100} plane in the δ-ferrite. Therefore, the primary facets of PSCC crystallographic cracking in the δ-ferrite should be {100}. This orientation was then confirmed by the analysis of EBSPs.

Theoretically, EBSPs obtained in the SEM give crystallographic information for a small area (diameter of 0.2 μm and depth of 0.05 μm) at the specimen surface. When this technique was employed to study PSCC crystallographic fracture surfaces, the diffraction patterns were often blocked by the surface undulations. Not many PSCC crystallographic cracking regions could generate good patterns available for analyzing. In the regions where good patterns were

obtained, both the normals of PSCC primary facets and the directions of river lines were shown to be close to <100>. This result indicates that the PSCC crystallographic cracking occurred in the δ-ferrite on the {100} planes and in the <100> propagation directions.

The {100} planes were quite serrated at high magnification (Fig. 5.4). Many striations were perpendicular to the river lines and interlocked on opposite fracture surfaces. Microfacets appeared and were obviously inclined to the {100} planes. In the δ-ferrite, the real cleavage facets produced in liquid nitrogen, at the same COD rate as PSCC fracture, presented {100} cleavage facets (Fig. 5.5). Some inclined facets can be seen in Fig. 5.5, but they are parallel to river lines and correspond to deformation twins. At high magnification, the cleavage facets are perpendicular to each other and no inclined microfacets are present except for the "tongues" of deformation twins (Fig. 5.5b). The difference between the two cases suggests that the microfacets inclined to the primary {100} planes in PSCC (Fig. 5.4) are very probably the {110} or {112} slip planes which can make acute angles with the {100} planes.

The river lines in PSCC crystallographic cracking regions in δ-ferrite often radiated from the initiation sites. The angles measured between river lines by the photogrammetric method often gave more than one possible combination of propagation directions. Table 5.1 presents the results of photogrammetric analysis from 20 photos representing 7 regions of crystallographic PSCC. Concerning the subgrains in the δ-ferrite, a measurement error of 6° was possible.

Figure 5.4 Matching fractographs of the PSCC crystallographic fracture in the δ–ferrite.

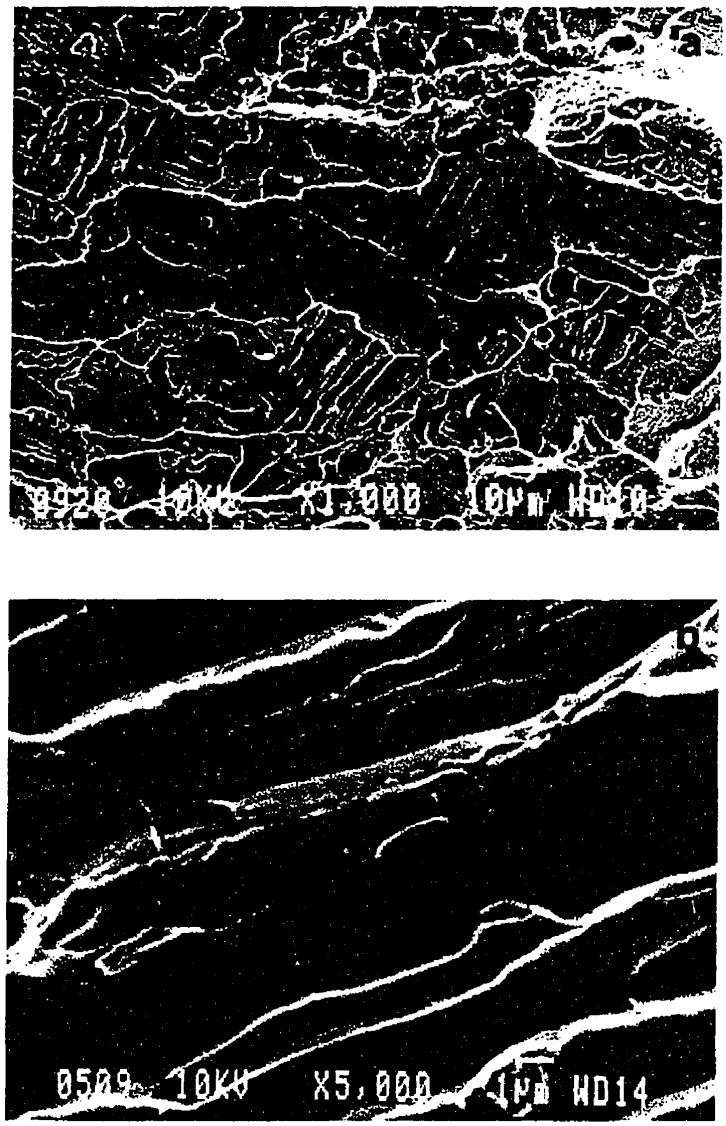

Figure 5.5 Cleavage features in the δ–ferrite by cracking in liquid nitrogen. (a) The {100} cleavage and deformation twins. (b) The {100} cleavage facets are mutually perpendicular and parallel to river lines.

Table 5.1 Results of photogrammetric analysis of the PSCC crystallographic cracking in the δ-ferrite

No.	Measured angle	Suggested directions	Real angle	Intersected slip planes
1	90°	<110>, <110>	90°	{110} or {112}
2	90°	<100>, <100>	90°	{110}
3	22°	<110>, <210>	18.43°	{110}, {112}
4	22°	<100>, <210>	26.56°	{110}, {112}
5	45°	<100>, <110>	45°	{110}, {110}or {112}
6	30°	<100>, <210>	26.57°	{110}, {112}
7	78°	<110>, <210>	71.57°	{112}

Besides the <100> propagation directions already determined by EBSPs analysis, the results of the photogrammetric analysis also suggested <110> and <210> propagation directions. Since there are two texture orientations in the δ-ferrite and EBSPs were only obtained in a few regions, the {100}<110> and {100}<210> should be also considered as probable cracking crystallographies of the PSCC in δ-ferrite.

5.4 DISCUSSION

As already pointed out in Chapter 3, the similarity of the fractography in austenite between SCC and PSCC hydrogen-induced cracking infers that hydrogen is involved in the SCC. In contrast, the differences in fractography are very obvious between the SCC and the PSCC crystallographic cracking in the δ-ferrite retained in 316L stainless steels. However, these differences do not necessarily mean that a different mechanism operates during SCC compared to that operates during PSCC. The fractography presented in Chapter 4 demonstrates that the SCC fracture of the δ-ferrite is also produced by absorbed hydrogen facilitating dislocation movement. The cracking crystallography, although different in SCC and PSCC, are essentially made up of slip planes. As schematically shown in Fig. 5.6, the differences in the crystallographic cracking features can be attributed to the different residual stresses caused by hydrogen distribution in austenite and in the δ-ferrite.

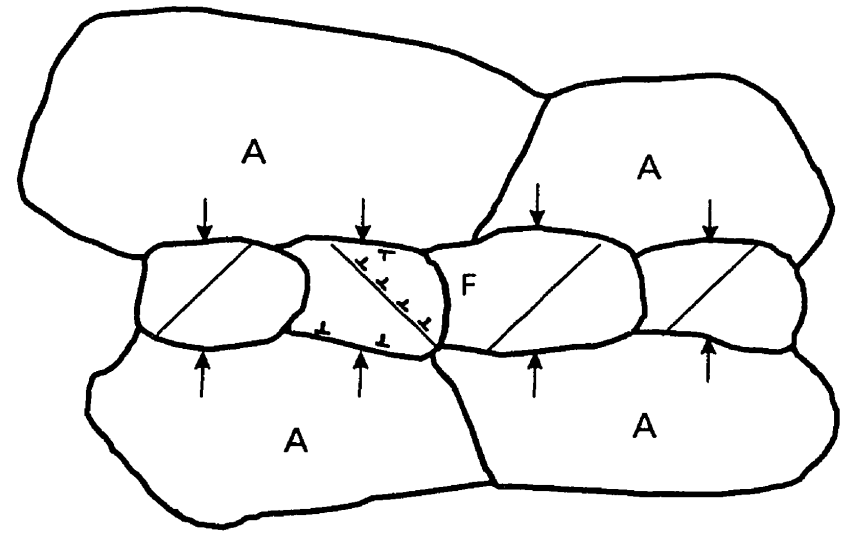

(a)

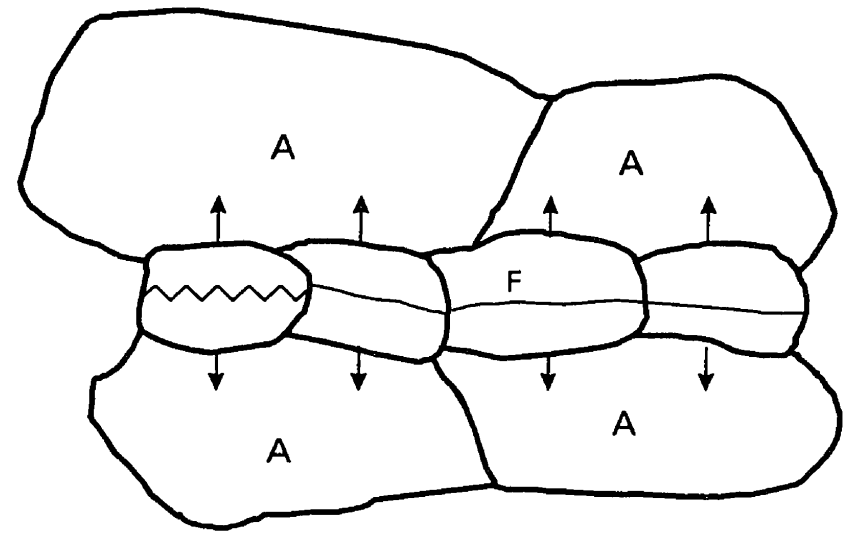

(b)

Figure 5.6 Schematic illustration of residual stresses generated by the hydrogen absorption and diffusion in the δ–ferrite and in austenite (a) in SCC and (b) in PSCC.

Cohen *et al.* [225] reported that dissolved hydrogen can change the lattice parameters of austenite and ferrite quickly during hydrogen charging. Accordingly, during SCC tests, both austenite and ferrite at the crack tip absorbed hydrogen and both phases expand. The higher solubility and lower diffusivity of hydrogen cause the austenite to expand more than the δ-ferrite. In ST orientated specimens, the resulting compressive acting on the δ-ferrite platelets (Fig. 5.6a) disfavors the cracking on the plane perpendicular to the tensile axis in this phase. At the mean time, dislocation sources near the δ-γ interface in the δ-ferrite are activated by the boundary diffusion of hydrogen, thus interfacial cracking becomes predominant. When transgranular cracking occurs, it propagates along the planes inclined at approximately 45° to the tensile axis and to the macroscopic SCC crack front in ST orientated specimens. These planes are determined as {110} planes and in the position close to the planes of maximum shear stress in the plane stress region. Therefore, dislocations are very active due to the effects of hydrogen and the maximum shear stress. The slip and cross slip, the piling up of dislocations and the consequent decohesion lead to transgranular cracking on those {110} planes and on {112} microfacets, all of which are the slip planes in the bcc phase.

When the SCC specimens are cooled to room temperature, supersaturated hydrogen in the δ-ferrite effuses quickly to the surrounding austenite, although the amount is limited because of low diffusivity in austenite. The lattice of the δ-ferrite contracts due to the outgassing and the austenite is expanded by the absorption. A residual tensile stress is produced in the δ-ferrite, or at least the residual compressive stress in this phase is reduced. Also, the applied stress during PSCC is higher than during SCC. Both effects result in a tensile stress in the δ-ferrite which favors the transgranular cracking on the plane perpendicular to the tensile axis (Fig. 5.6b). In ST orientated specimens, this plane is {100} in the δ-ferrite due to the texture developed during hot rolling. However, the {100} cracking in PSCC was seen at high magnification to be composed of many microfacets (Fig. 5.4). Inclined microfacets met each other to form striations which interlocked on opposite fracture surfaces. This suggests that the minimum cracking unit, analogous to that in the austenite, occurs on {110} or {112} slip

planes by hydrogen-enhanced dislocation movement. At room temperature, the hydrogen absorbed in the δ-ferrite is very low and not many dislocations are activated to form long pileups on the slip planes. Therefore the slip occurred on such a short distance.

Chapter 6

Fractographic Observation of SCC in 70Cu-30Zn

6.1 INTRODUCTION

As summarized in Chapter 1, a large number of studies on SCC of copper alloys in ammonia solution have given controversial results. Concerning the fractography, both intergranular and transgranular fracture were reported, depending on the solution chemistry, the material composition, the microstructures and the loading methods. There are several mechanisms proposed to interpret the fracture phenomena, but each is restricted to a certain environment or to just one fracture pattern. For example, intergranular fracture is thought to be produced by tarnish film rupture [133], because it often occurs in tarnishing solution, while this film-rupture mechanism cannot account for the intergranular fracture obtained in non-tarnishing solution for copper alloys with Zn less

than 18% [93]. The film-induced cleavage mechanism characterizes the transgranular fracture as cleavage [138,139], despite the fact that transgranular SCC occurs microscopically on slip planes in 70Cu-30Zn [4]. There is also no proper explanation why intergranular fracture was observed at the same time with such "cleavage" [110]. The corresponding mechanisms for intergranular fracture and transgranular fracture, controlled by electrochemistry and by local mechanics respectively, are difficult to apply for the same specimen and in the same solution.

Obviously, diverse results indicate that our knowledge about SCC of copper alloys in ammonia solution is far from complete. Other than the SCC of stainless steels, the test solution chemistry and the material composition play important roles on the fracture. Since the literature on the SCC mechanisms of copper alloys deals overwhelmingly with the α-brass containing 30% zinc, and the results in highly concentrated (15N) non-tarnishing ammonia solution are the most controversial, this system was selected in the present study. Deoxygenated solution was also employed since it should help specify what are the crucial species during SCC. Both annealed and cold-worked specimens with different thickness were tested. The goal of this study was to examine the details of the SCC fractography of 70Cu-30Zn and its variation with the environment, with the microstructure and with the local stress intensity K, and thus to provide more information on understanding the SCC mechanism in this system.

6.2 FRACTOGRAPHY OF SPECIMENS TESTED IN NON-TARNISHING SOLUTION

The fractographic characteristics of SCC in 70Cu-30Zn have been widely reported, especially for transgranular fracture. Still, controversy remains on the relationship of cracking patterns to the microstructural and environmental conditions. The present fractographic study focused on the variation of the cracking patterns and on the details of

the intergranular fracture. All the fracture surfaces of specimens tested in non-tarnishing solution were examined in order to determine the influence of material and mechanical conditions on the fractography.

6.2.1 Fractography in as-received and annealed conditions

6.2.1.1 TN-DCB specimens

The fracture features were very similar for specimens in the as-received and in the annealed conditions although the hardness has been reduced from HRB 71 to HRB 64 after annealing at 650°C. The metallographic investigation showed little change in the microstructure. Thus we will not differentiate between the annealed and the as-received conditions in describing the results.

The fracture surfaces were dominated by intergranular fracture. Cracking usually started as a transgranular fracture near the notch, then changed to cracking along grain boundaries. In a narrow central region on the fracture surface and near the final overload ductile fracture, transgranular fracture also appeared. The river lines in the transgranular regions indicated that the crack often propagated from both lateral surfaces towards the center of the specimens.

The surface protection could influence the distribution of the fracture patterns. If the specimen surfaces were further protected by glass plates or silicon sealant in addition to the lacquer coating and Teflon tapes (see Chapter 2), larger transgranular regions were found near the notch roots which propagated away from the notch roots and spread to the lateral surfaces. Occasionally, transgranular fracture could be initiated from the lateral surfaces and propagated towards the central regions. As the crack propagated away from the notch, intergranular fracture occurred at some distance from the notch root and

became dominant again. Then transgranular fracture appeared in the central regions and near the final ductile fracture, with the similar propagation tendency to those protected only by a lacquer layer. Similar variation of cracking patterns was also found in the thicker (B = 4 mm) specimens. This suggests that, despite the better surface protection, intergranular fracture occurs preferentially if the specimens are exposed for a long time to the environment.

The intergranular fracture generally presented smooth grain boundaries, but some small protrusions appeared, especially near the transgranular regions and for those specimens further protected by glass and silicon sealant on the surfaces. Fig. 6.1 is an example of such quasi-intergranular fractures. The slip lines and corrosion pits on the grain boundary indicate this boundary is almost parallel to {100} in one grain. Dissolution slots were observed along slip lines on grain boundaries. These preferential sites coincided with the slip system where the local transgranular cracking formed (Fig. 6.2).

The intergranular crack front appeared to follow crystallographic orientations on grain boundaries. This was observed at visible annealing twins on the grain boundaries. Intergranular crack propagation was not always along grain boundaries, but often deviated from its original path to form transgranular (Fig. 6.3) or quasi-intergranular fracture (Fig.6.4) at twins due to the orientation difference. Some quasi-intergranular fracture was actually a transgranular fracture near the grain boundaries. As shown in Fig. 6.4b, the crack propagation started from the both sides of the twins. It followed the crystallographic steps in the twin, and some fine steps merged together in the center. In Fig. 6.4c, the coarsening is not apparent because the steps are very regular. But it is clear in Fig. 6.4c that the crack grew first in the twin then spread to the surrounding area in a transgranular manner. The two opposite fracture surfaces were matched and interlocked both in Fig.6.4b and Fig. 6.4c.

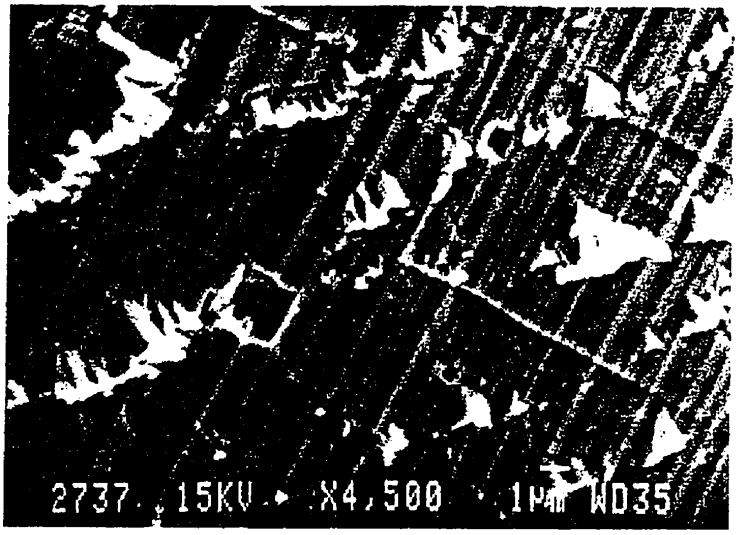

Figure 6.1 Quasi-intergranular SCC fracture in annealed 70Cu-30Zn. The corrosion pits and slip traces indicate this grain boundary is locally close to {100} plane.

Figure 6.2 Preferential dissolution occurs on grain boundaries along slip lines during SCC in annealed 70Cu-30Zn, which also corresponds to the regions of transgranular SCC cracking.

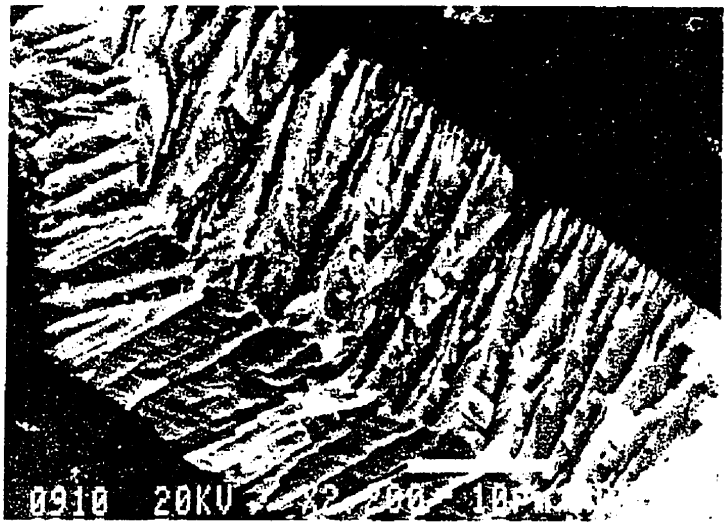

Figure 6.3 Intergranular SCC fracture changes to transgranular fracture at the twin boundary and then switches back to intergranular fracture, from an annealed specimen.

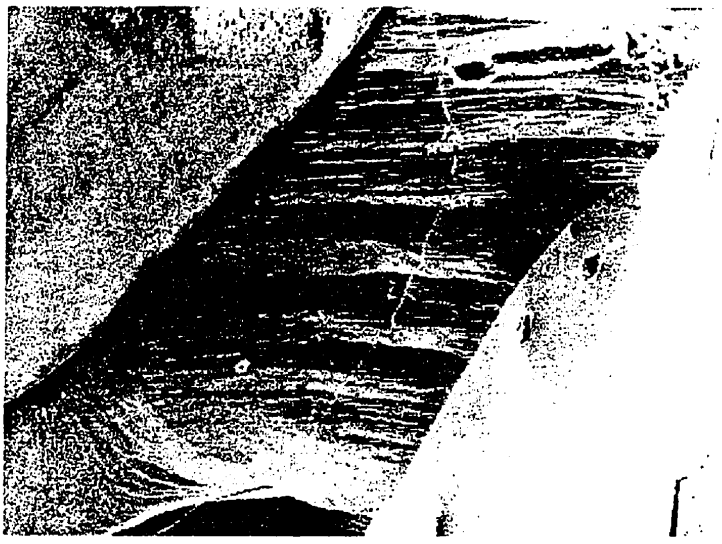

Figure 6.5 A zigzagged grain boundary in the intergranular SCC region of annealed 70Cu-30Zn.

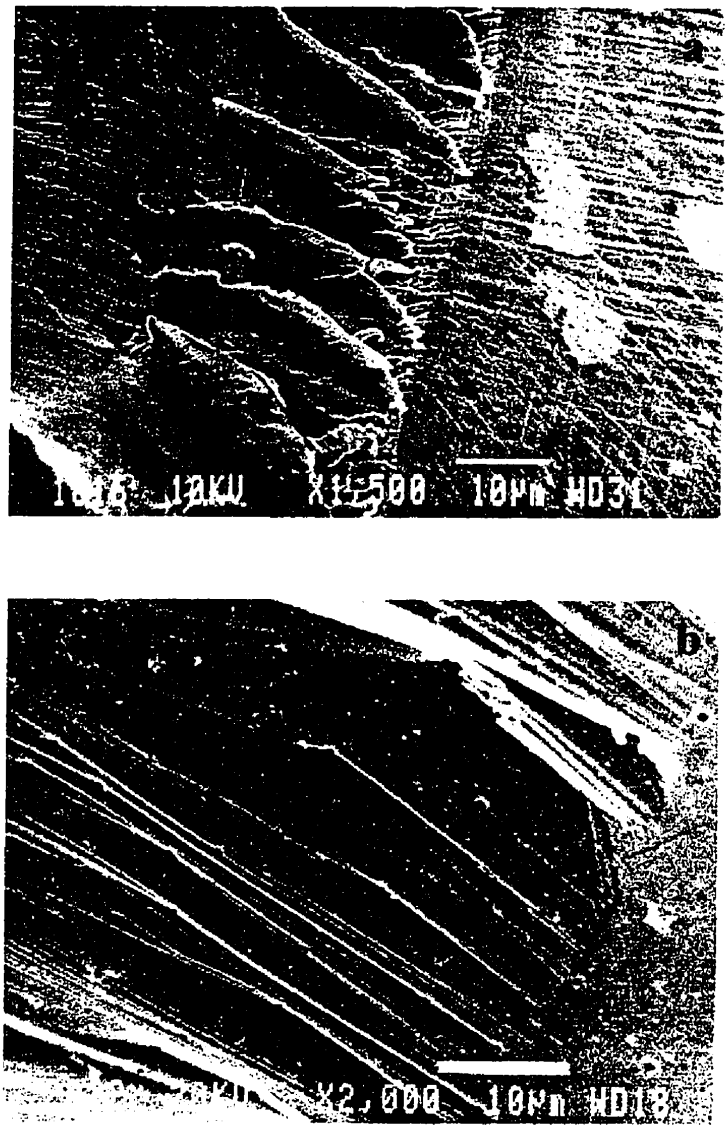

Figure 6.4 Annealing twins are observed on the grain boundaries in intergranular SCC fracture regions by: (a) a combination of quasi-intergranular and intergranular fracture; (b) crack initiating from both sides of twin boundaries and propagating along crystallographic facets within a twin.

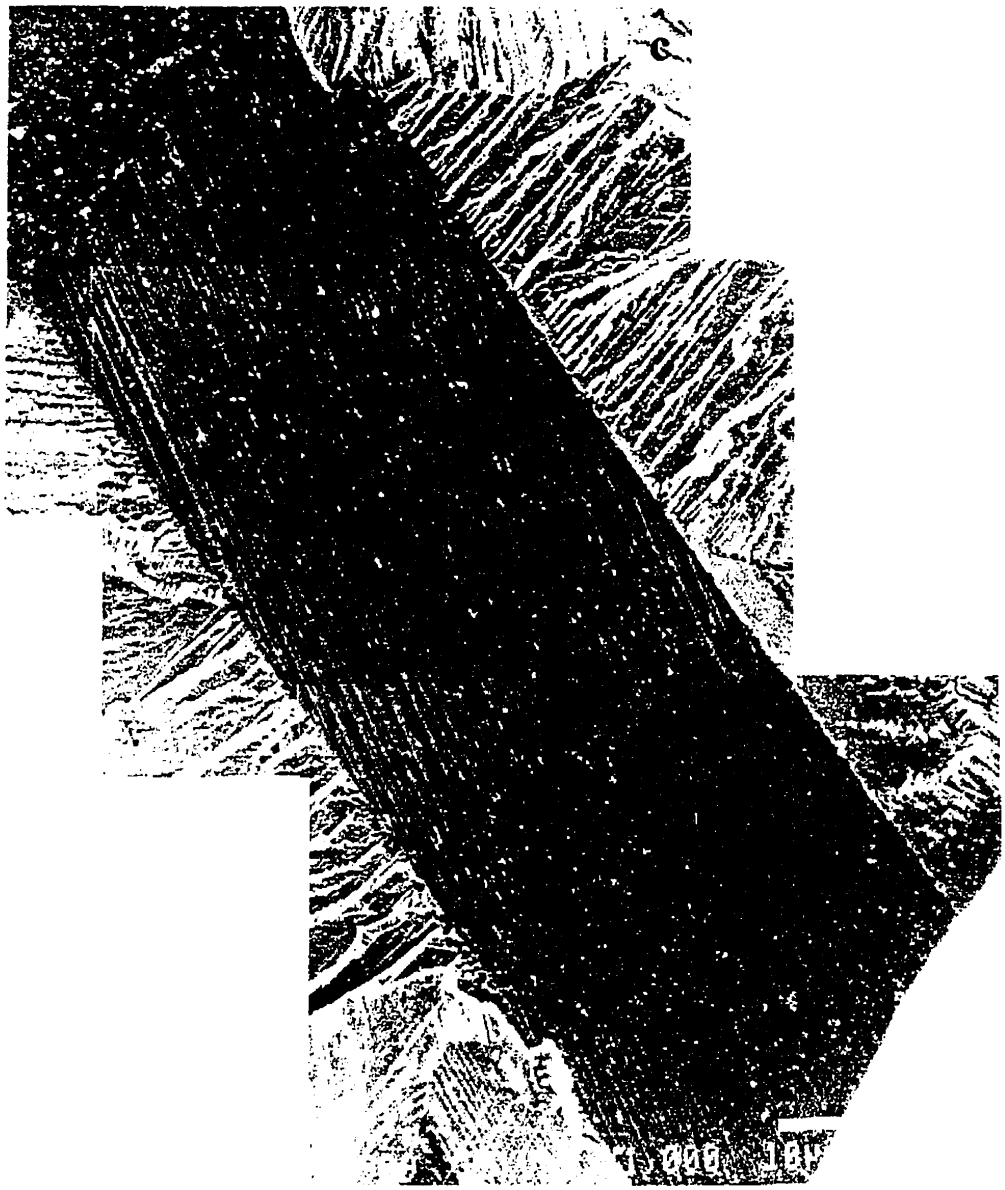

Figure 6.4 (c) Annealing twins are observed on the grain boundaries in intergranular SCC fracture regions by crystallographic steps in a twin.

Because of the large grain size, grain boundaries were relatively flat. That increased the opportunity of being close to a crystallographic plane for those boundaries. The crystallographic orientation of grain boundaries could be determined by the corrosion pits or the slip systems which appeared on the boundaries, as shown in Fig. 6.1. The formation of quasi-intergranular fracture is the manner that the crack adjusts its path near the grain boundary in order to follow a specific crystallographic orientation. For example, in Fig. 6.5, the boundary zigzagged along two sets of planes. One set with many fine steps is revealed by corrosion pits to have an average orientation of {100}. At high magnification, the other set of large facets was found by steromicroscopy to be approximately parallel to the pyramidal planes of the pits. Therefore, these larger facets are {111}. It was also seen at high magnification that many fine steps in the {100} set have the similar orientations as those pyramidal planes in corrosion pits. The above observations suggest that the intergranular fracture, at least locally, is actually following some crystallographic orientations in the vicinity of the grain boundary, and that it occurs before the transgranular fracture.

Occasionally, large crystallographic planes approximately perpendicular to the tensile axis were found in some isolated grains. These facets were quite large and layered together in one grain. The orientation of the large facets shown in Fig. 6.6 was determined as {111} with the help of corrosion pits in this region by stereomicroscopy. There were some transgranular regions attached on those large facets. The steps linking parallel {111} planes were perpendicular to {111} planes. These steps often initiated from grain boundaries and coarsened towards the center of the grain, resembling those steps in the twin of Fig. 6.4b. Very probably, the facets connected by crystallographic steps in the twin of Fig. 6.4b are also {111}.

Figure 6.6 Large crystallographic facets observed in SCC of annealed 70Cu-30Zn. These facets are approximately perpendicular to the tensile axis and are linked by steps initiated from grain boundaries. Corrosion pits on the facets indicate the {111} orientation of the facets.

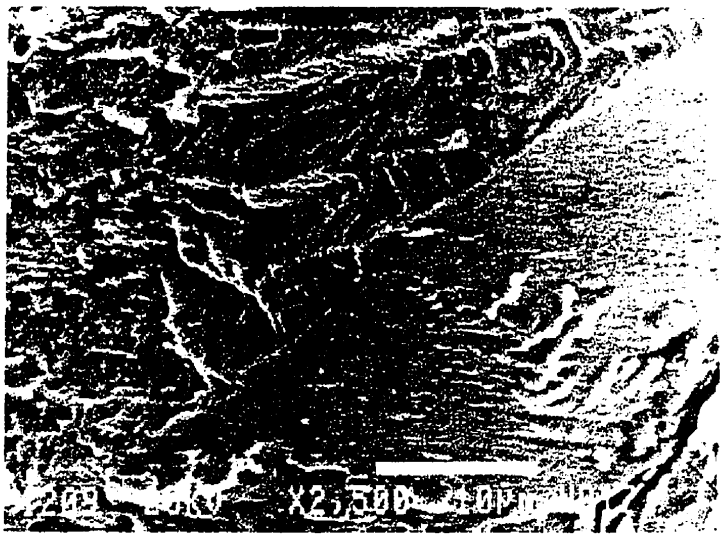

Figure 6.7 Quasi-intergranular SCC fracture and transgranular SCC fracture in the same grain at $K \approx 14$ MPa$\sqrt{m}$ in an annealed CT specimen. Striations are present both on the grain boundary and on the transgranular facets.

6.2.1.2 CT specimen

The CT specimens employed had almost three times the thickness of TN-DCB specimens. The large thickness reduced the influence of near-surface intergranular fracture in the overall propagation process; that is, it reduced the portion of sideways propagation. Therefore, the cracking aspects are more relevant to the crack tip stress intensity factor K.

The fracture surface of the annealed CT specimen became slightly inclined at the crack branch. Optical microscopic observation found that, before this branching occurred, there was a considerable amount of intergranular cracking. Macroscopic characteristics of intergranular cracking, the shininess of the fracture surface, disappeared beyond the crack branch.

Under SEM, a mixture of intergranular and transgranular fracture was found in the region of $K < 14$ MPa$\sqrt{m}$. Intergranular fracture appeared more often in regions near the lateral surface, but disappeared at higher K in the central region. When K was over 14 MPa$\sqrt{m}$, intergranular or quasi-intergranular fracture could be still found in a few individual grains. The grain boundaries were smooth at lower K, but quasi-intergranular fracture appeared at higher K. Fig. 6.7 shows a quasi-intergranular fracture observed at $K \approx 14$ MPa$\sqrt{m}$. Some striation-like markings are present on the grain boundary besides small protrusions. It can be seen that these markings join up with the striations of transgranular fracture, indicating that they result from the same slip system(s).

The transgranular fracture features appeared to be more complicated than those reported [113] at the same K level. Relatively large and flat primary facets with less serrated river lines and fine striations, the character reported at low K region (from 10 to 15 MPa$\sqrt{m}$), presented only at K lower than 12 MPa$\sqrt{m}$ by a certain amount in the present study (Fig. 6.8). More often, the transgranular cracking showed thick river lines associated

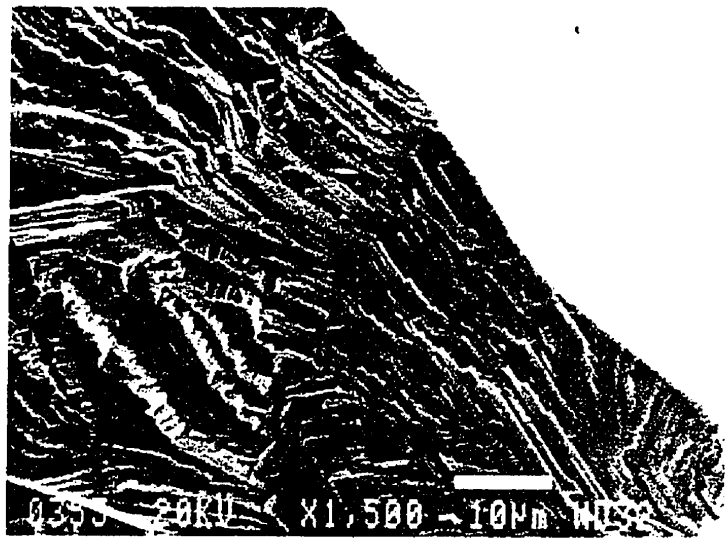

Figure 6.8 Relatively low K features of transgranular SCC fracture in annealed CT specimens.

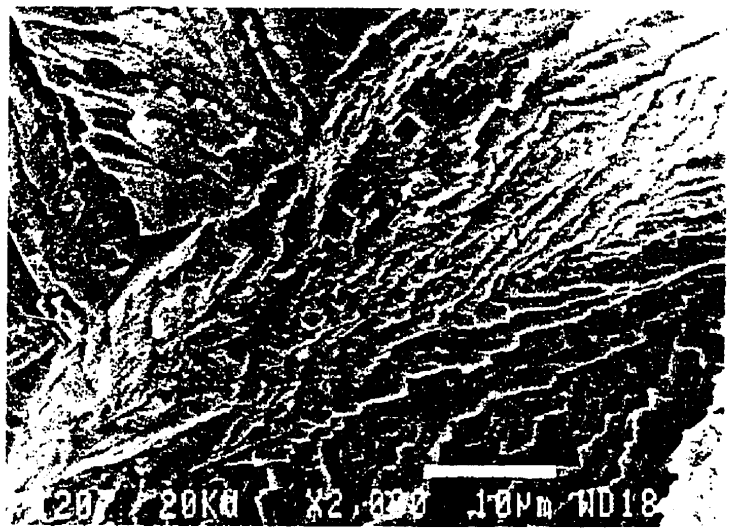

Figure 6.9 Features of transgranular SCC fracture at $K \approx 14$ MPa$\sqrt{m}$ in an annealed CT specimen.

with many serrations as those in the twin of Fig. 6.8. With increasing K, the number of serrations and the size of microfacets increased. Fig. 6.9 is an area found at $K \approx 14$ MPa$\sqrt{m}$ which shows the complexity of the fracture surface. There are pronounced microfacets in the bottom area of the photo which is approximately perpendicular to the tensile axis. The region with corrosion pits is inclined with the striation density so high that it makes this region, as well as Fig. 6.7, have an appearance quite similar to a fatigue fracture. In the high K region, microfacets increased in size so that river lines disappeared in some areas, and only large microfacets were present (Fig. 6.10). On the two opposite fracture surfaces, complicated sets of microfacets still match and interlock, although the steps formed by microfacets intersecting are not sharp.

6.2.2 Fractography in cold-worked condition

6.2.2.1 Cold-worked TN-DCB specimens

The fracture surfaces of three TN-DCB specimens which had been cold rolled prior to machining were examined in the present study. The machining orientation of these specimens was selected so that the SCC cracking plane would be perpendicular to the rolling plane and the crack propagation direction would be parallel to the rolling direction, i.e., the TL orientation. One specimen (50% reduction in thickness) underwent SCC in the same non-tarnishing solution as annealed specimens. The other two specimens were tested in 5 M ammonia solution with 8 g/l Cu added as $Cu(NO_3)_2$ by Maxime Gauthier [226].

At relatively low magnification, the fracture surfaces of cold-worked specimens also presented mixed fracture patterns. Compared with annealed specimens described in 6.2.1.1, the portion of transgranular fracture was greatly increased and was no longer restricted to the mid-thickness regions or near the notch and final ductile fracture. The amount of intergranular fracture was inversely proportional to the amount of prestrain. At

Figure 6.10 Matching fractographs shows complicated transgranular features at high K in an annealed CT specimen. Microfacets match and interlock on opposite fracture surfaces.

the same prestrain, the specimen tested in 15 N ammonia solution showed less intergranular fracture than that tested in 5 M solution. Many intergranular regions appeared parallel to the cracking plane in the latter specimen. Contrary to the annealed specimens, there was little intergranular fracture near the lateral surfaces.

At high magnification, the grain boundaries were not as smooth as in annealed specimens. There were small protrusions such as those shown in Fig. 6.1, and many dense slip lines or steps on the grain boundaries (Fig. 6.11). These slip lines in some regions are very fine which allows their presence to little disturb the contour of grain boundaries. However, matching in an interlocking manner could be found on opposite fracture surfaces, especially in the area parallel to the cracking plane where the slip lines became more pronounced (Fig. 6.11). Fig. 6.12 is an enlargement of an area in Fig. 6.11. The opposite fracture surfaces match and interlock, exactly as for typical transgranular features. Therefore, the apparently rough grain boundary actually corresponds to a transgranular fracture near the grain boundary. The amount of slip near the boundary increases with the increase of prestrain. In the specimen reduced in thickness 70% by rolling, the fracture features presented mainly such rough grain boundaries and transgranular fracture.

The SCC crack front in the specimen with 70% reduction in thickness was very irregular. The crack propagation was fast near the lateral surfaces and along elongated grain boundaries (Fig. 6.13). Most of these leading intergranular cracks were secondary cracks which presented rough grain boundaries. The whole fracture surface was separated vertically by these secondary cracks into several portions which were not coplanar but all were perpendicular to the tensile axis. Such a fracture surface indicates that the transgranular propagation was relatively independent in each portion after initiating from the intergranular fracture. The crack front was quite straight in the specimen reduced 50%

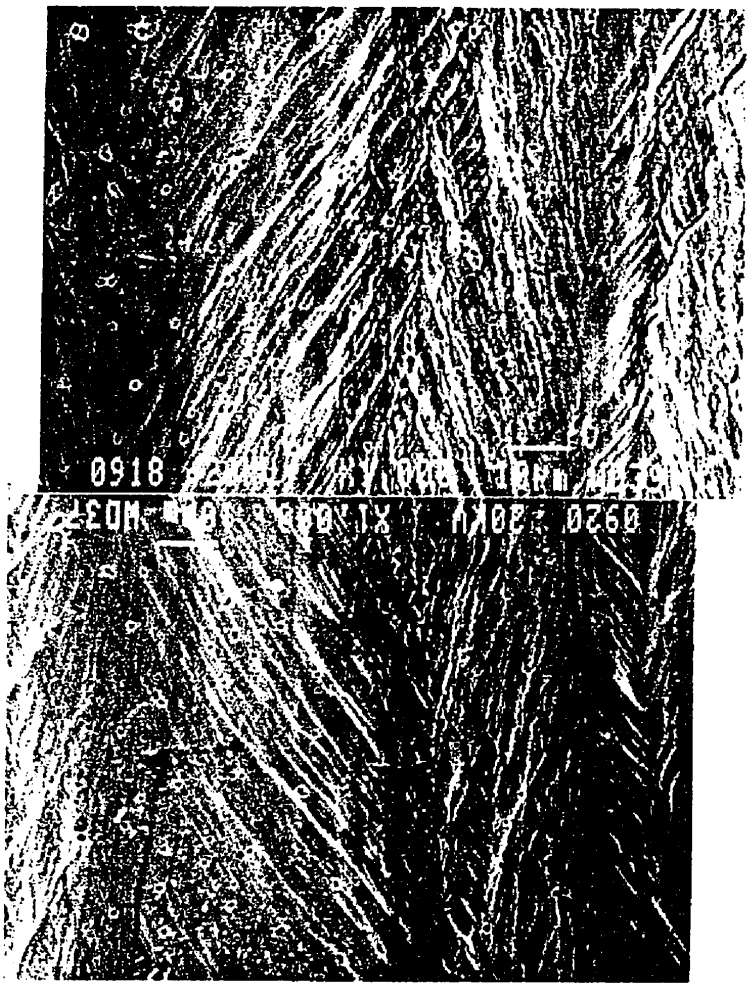

Figure 6.11 Matching SCC fractures in a cold worked specimen. Dense slip lines and steps are present on the grain boundary.

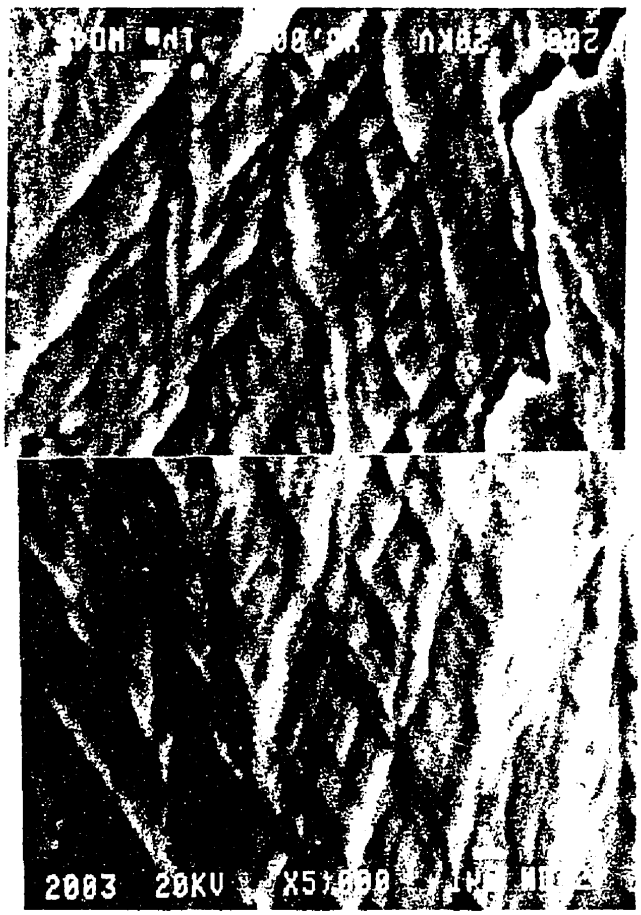

Figure 6.12 Matching fractographs of enlarged "A" region in Figure 6.11. Microfacets match and interlock on the two fracture surfaces.

in thickness. Still, there were some secondary intergranular cracks. But those secondary cracks did not lead the average crack front and they presented less slip traces.

Transgranular fracture in all cold-worked specimens showed high K features although the initial K was around 10 MPa$\sqrt{m}$. Very serrated river lines and sheet-like facets were the typical features. Because of the large prestrain, texture was formed therefore the local propagation directions were usually approximately 45° or 90° to the macroscopic propagation direction (Fig. 6.14). It is also seen in Fig. 6.14 that cracking initiated from secondary intergranular cracks. Again, this indicates that the intergranular fracture is more rapid.

The transgranular cracking features also reveal the amount of local prestrain. A large prestrain produced smaller or narrower grains on the cracking plane of TL orientated specimens. Therefore, relatively low K features appeared in relatively large grains. In Fig.6.15, the larger primary facets appear in the large central grain, while in other small grains, there are only dense river lines. It was noticed that transgranular fracture only appeared on the plane approximately parallel to the macroscopic cracking plane. Regarding the roughness of the grain boundaries, the intergranular fracture presented on the cracking plane was more rough than those presented in secondary cracks. This is because the cracking plane in TL orientated specimens contains the biggest deformation directions which are the rolling direction and short transverse direction. Therefore, the crack patterns are associated with the amount of prestrain. With an increase of pre-existing dislocations, the cracking pattern changed from mainly intergranular fracture to mainly transgranular fracture.

Figure 6.13 Intergranular SCC crack front in a cold rolled specimen with 70% reduction in thickness. Second cracks perpendicular to the average cracking plane lead the average crack front near the lateral surfaces and in the central region.

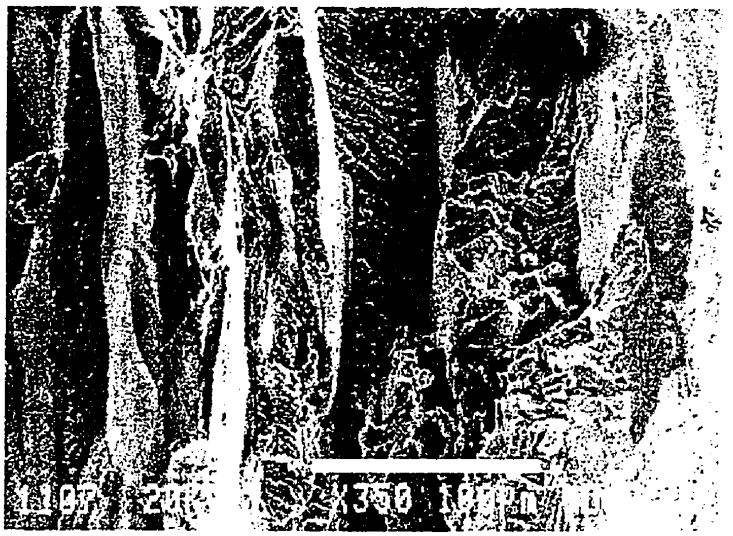

Figure 6.14 Transgranular fracture initiates at the grain boundaries which are parallel to the rolling plane in cold worked specimens. The local propagation directions in the transgranular region make angles either ~ 45° or ~ 90° to the macroscopic propagation direction.

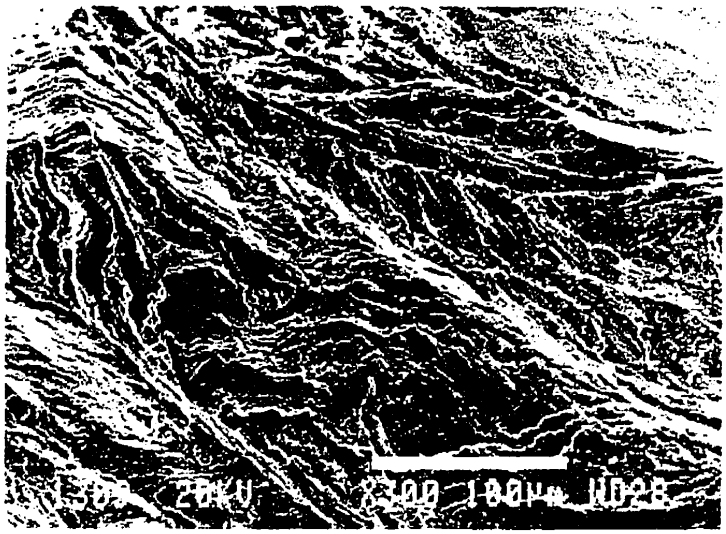

Figure 6.15 A transgranular region presents different local prestrains which are indicated by the different features. Large primary facets in the large central grain represent a relatively low local prestrain, while dense river lines in small grains indicate the local high prestrain.

6.2.2.2 Cold-worked CT specimen

The CT specimen in the as-received condition was in a cold-worked condition (37% reduction in thickness) according to its hardness. This material has a high yield strength which enables the specimen to be tested to a high K value. The orientation selected for testing was also the TL orientation.

Like other specimens, the fracture surface presented a mixture of intergranular and transgranular fracture. Similar to the annealed specimen, the intergranular portion was slightly larger in the low K region than at high K. The amount of intergranular fracture did not appear to vary across the thickness.

The SCC test was interrupted once at $K \approx 18$ MPa$\sqrt{m}$. The specimen was washed in water and in methanol, then dried with compressed air. When the test was resumed one week later, the crack propagation velocity was much higher than before (See next chapter). This more rapid propagation produced a fracture region under high K, which reached the maximum value of ~ 80 MPa$\sqrt{m}$ when the test was stopped. Most of this fast fracture was covered by a black layer. In both lateral regions, shown in Fig. 6.16a as shadowed areas, intergranular fracture dominated. The rapid propagation might result from the surface corrosion. When it remained in air between two tests, the specimen could have been corroded by moisture and residual ammonia solution in regions of surface roughness. This could have reduced the effective thickness and produced dominant intergranular fracture in the near surface region. Fig. 6.16b shows that the continuous SCC crack front (crack front 1) before final ductile fracture is led in the lateral regions. But there are several secondary cracks which propagated as far as several millimeters ahead of crack front 1. These secondary cracks are separated by ductile fracture beyond crack front 1 and they outline crack front 2 which is led in the center.

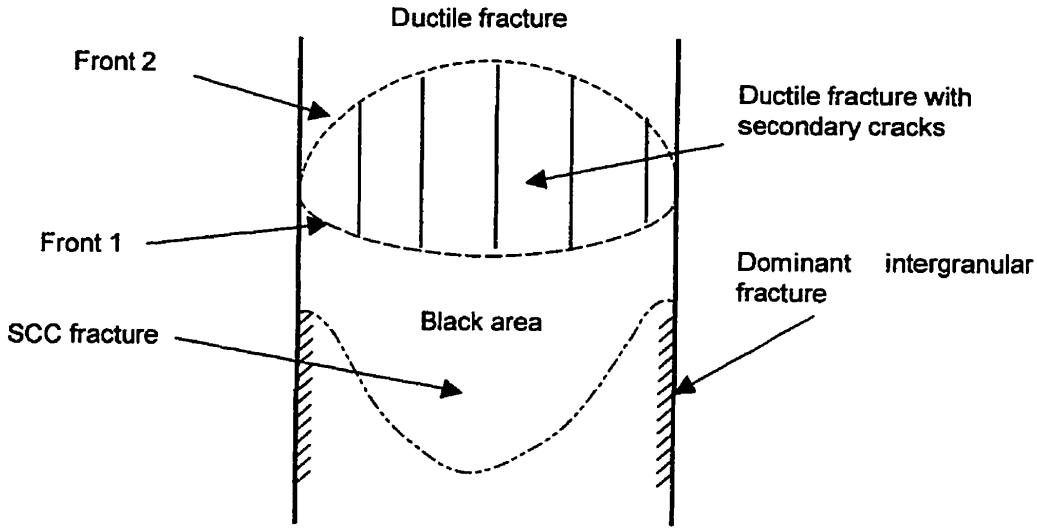

(a)

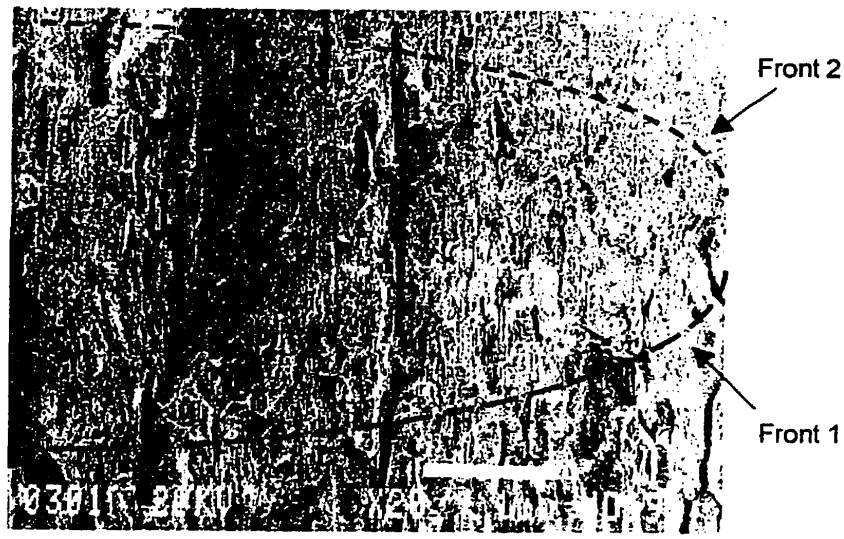

(b)

Figure 6.16 The SCC crack front in a cold worked CT specimen. (a) Schematic illustration of the final part of SCC fracture. (b) The corresponding fracture surface.

The secondary cracks appeared to have smoother grain boundaries than those in cold-worked TN-DCB specimens. But compared to the leading secondary cracks in cold-worked TN-DCB specimens, SCC fracture was not restricted inside the leading secondary cracks between Front 1 and 2. There was a narrow SCC region around each leading secondary crack. Short secondary cracks near the lateral surfaces tended to be surrounded by an intergranular region, while long secondary cracks in the center were surrounded by a transgranular region. Fig. 6.17 shows a transgranular region which initiated from the longest secondary crack.

Because of its moderate prestrain, most of the intergranular fracture appeared on the cracking plane. It contained approximately 30% to 40% area of the cracking plane. The grain boundaries were essentially smooth. Some protrusions and slip steps were observed on grain boundaries. Compared to the highly prestrained TN-DCB specimens (Fig. 6.11), the slip steps tend to be fewer in number (Fig. 6.18) and smaller in height. The intergranular features did not appear to change with K.

Transgranular fracture was also always present on the plane perpendicular to the tensile axis. Low K fracture had less river lines and larger primary facets. Fig. 6.19 shows cracking features found at $K < 20$ MPa$\sqrt{m}$ which resembles that in annealed specimens, but the texture tendency of river lines remains the same as at high K. The low K features were also occasionally found in high K regions. In high K regions, the number of both river lines and serrations on river lines increased. Compared to the high K features in the annealed CT specimen, the coarse river lines were still present despite the pronounced multiple microfacets in most of the area. Fig. 6.20 shows such an example found near the final ductile fracture. Four different sets of {111} facets can be discerned from the river lines. Two sets form horizontal zigzag river lines, in area A. The other two sets met in the direction parallel to the zigzag river lines in area B. Most of the river lines in Fig. 6.20 generally propagated from left to right. The observations indicate that this complicated

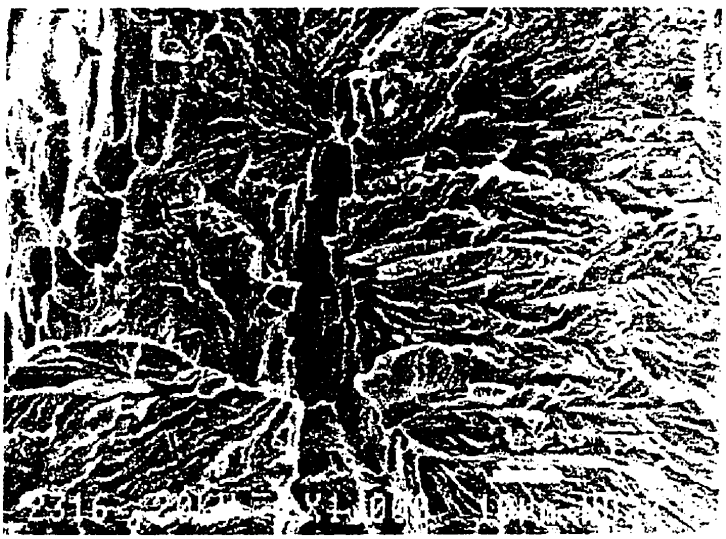

Figure 6.17 A transgranular region surrounding the tip of the longest secondary crack in the same specimen as Figure 6.16.

Figure 6.18 Slip steps on the grain boundary of cold worked CT specimen.

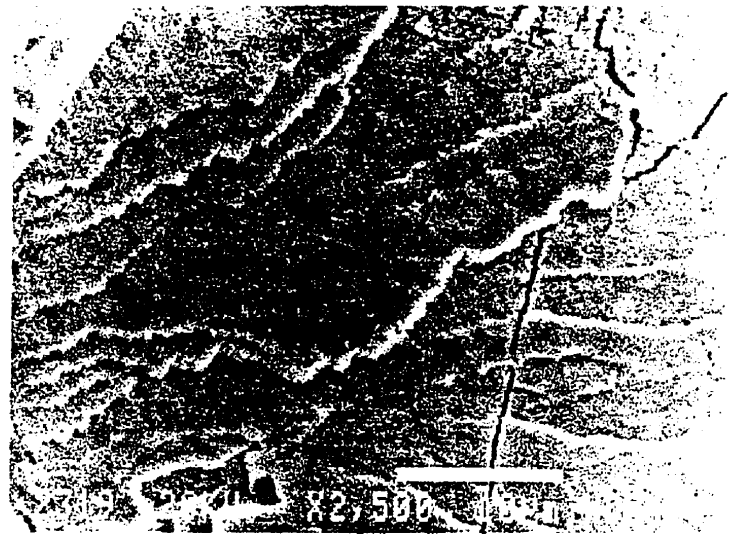

Figure 6.19 Transgranular fracture observed at K ≈ 20 MPa√m in a cold worked CT specimen.

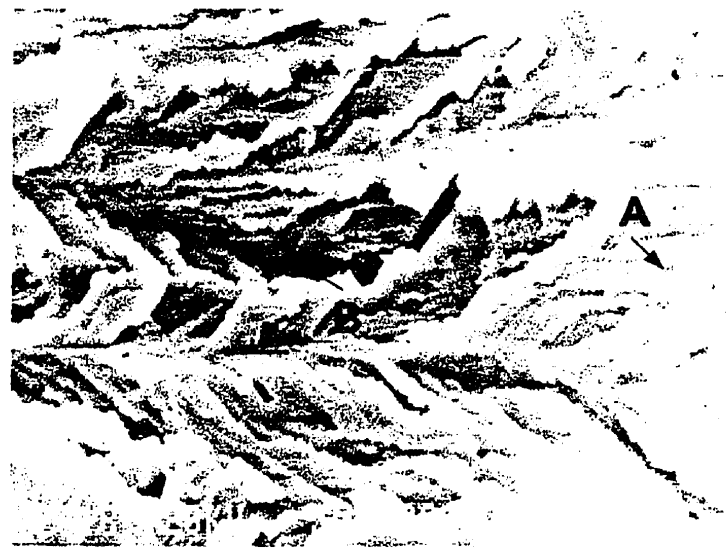

Figure 6.20 Complicated transgranular fracture at high *K* present four different sets of {111} facets in a cold worked CT specimen: two sets form horizontal zigzag river lines, in area A; and other two sets meet in the direction parallel to the zigzag river lines in area B. Despite many microfacets present, river lines generally propagate from left to right.

morphology reflects the local high K condition and the influence of pre-existing dislocations.

6.3 SCC TESTS IN EQUILIBRIUM SOLUTION

SCC tests in equilibrium solution (15 N aqueous ammonia with 3.6 g/l Cu_2O and 8 g/l Cu powder under deoxygenated condition) were performed on TN-DCB specimens in the as-received condition. At first, a notched specimen was tested in this solution for a total of 210 hours. A short crack was observed at one side of the notch approximately one hour after load had been applied. At that time, the solution still had a slight blue color, but it became colorless soon afterwards. As no sign of further propagation was observed, the stress intensity factor K was increased every other day during a total test period of 9 days. The K was increased by steps from 6 to 12.6 MPa$\sqrt{m}$, but this short crack did not propagate. This short crack was verified to be a surface crack after the test terminated (Fig. 6.21a). There were also some surface cracks along grain boundaries and slip traces associated with these cracks. Apparently, they were due to the initial dissolved oxygen in the solution. Some slip traces were found at another uncracked notch tip. This result indicates that SCC cracks have difficulty to initiate in this deoxygenated solution.

After examining the surfaces, this specimen was tested again in the same solution, but the nitrogen supply was stopped. The initial K was only 10 MPa$\sqrt{m}$. This specimen then fractured completely within 24 hours (Fig. 6.21b). The fracture surface was dominated by intergranular cracking, as in the case of annealed specimens tested in non-tarnishing solution. Transgranular fracture appeared only near the notch as well as near the final ductile fracture. Due to the fast cracking, only a few regions of corrosion deposit were observed on the fracture surface.

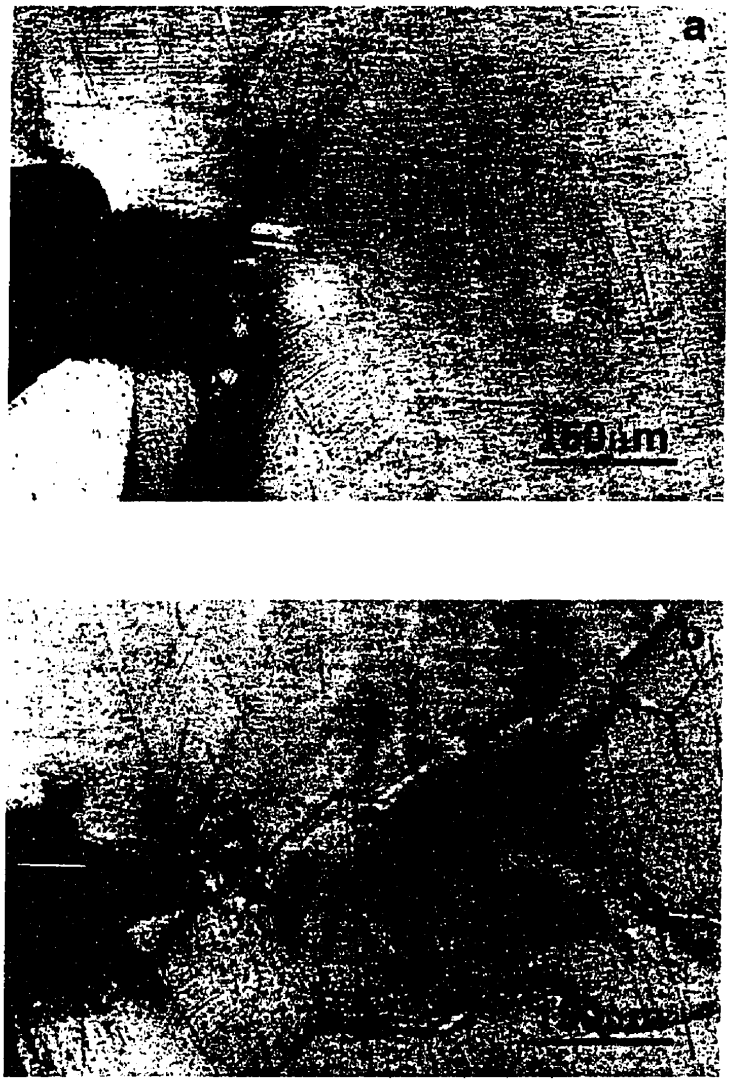

Figure 6.21 Surface observation after a specimen being SCC tested (a) in a deoxygenated ammonia solution for 210 hours; (b) in an oxygenated ammonia solution for 24 hours.

The first test confirms that SCC initiation needs the presence of dissolved oxygen [4]. It implies that the SCC crack propagation very probably needs the presence of oxygen as well, because the surface crack did not continue propagating in deoxygenated solution but propagated rapidly in oxygenated solution. In order to verify this phenomenon, two precracked specimens were tested in the same deoxygenated condition. One specimen already had a SCC crack, which presented an intergranular path from the lateral surfaces. The initial K was set slightly higher than in the previous test. The other specimen was fatigue precracked. The initial K applied in the tests were approximately 10 MPa$\sqrt{m}$, higher than those applied initially in the oxygenated non-tarnishing solution. After testing for 150 and 300 hours respectively, no apparent crack propagation was observed from the surfaces although the crack tip was slightly opened and many slip traces appeared at the fatigue precrack tip (Fig. 6.22). This confirms that SCC propagation in deoxygenated solution either does not occur or, at most, occurs very slowly.

6.4 CORROSION DEPOSITS ON THE FRACTURE SURFACES

The SCC fracture surfaces of TN-DCB specimens tested in 15 N oxygenated ammonia solution showed different colors in different regions. With increasing exposure time to the solution, i.e., going from the final ductile fracture to the notch root, the color changed from yellow, to brown, to black and then to green-blue at different areas of the fracture surfaces. This indicates the growth of copper oxides on the surfaces to form first Cu_2O (red) and then CuO (black). This trend agrees with that in tarnishing solution [227] and suggests that the copper oxides deposit after the SCC fracture. For CT specimens, the testing time was quite long so the early portion of SCC fracture surfaces were severely attacked. In the as-received condition, the black area appeared at high K until the region of final ductile fracture (Fig. 6.16). Black areas were also found at a depressed area near the final ductile fracture and at other isolated areas in the annealed specimen, indicating

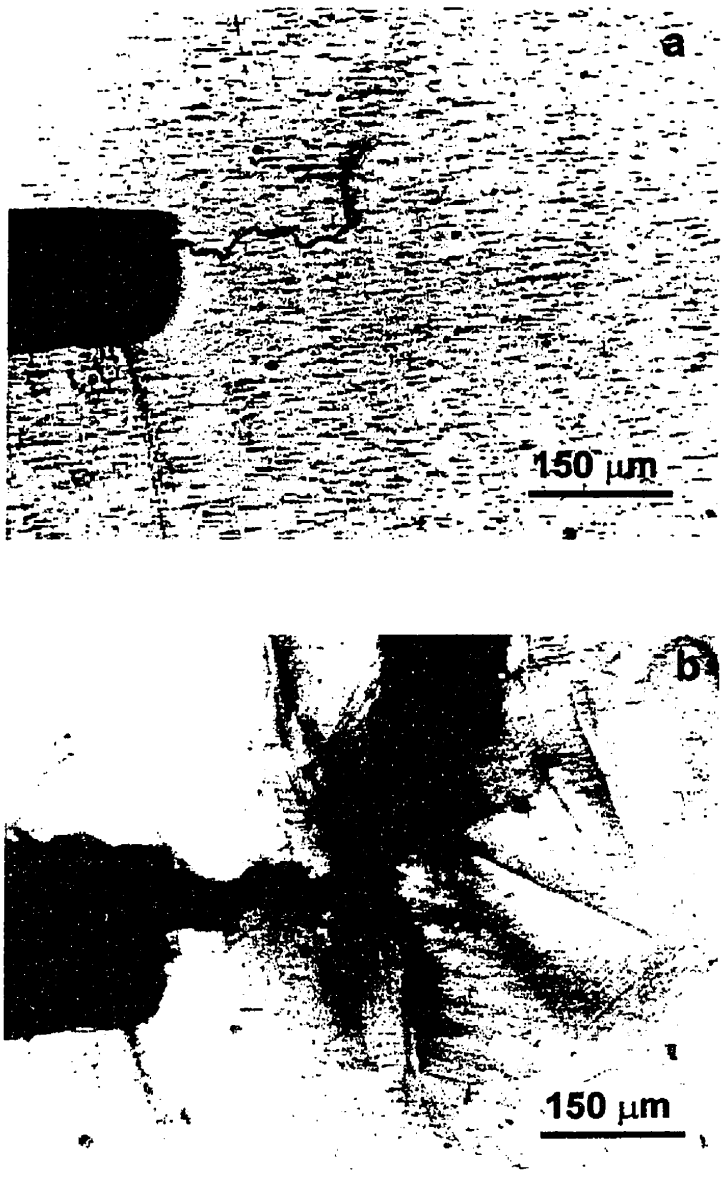

Figure 6.22 Surface observation of (a) a fatigue precrack; and (b) after the specimen was SCC tested in a deoxygenated ammonia solution for 300 hours.

the variation of local chemical conditions. Otherwise, the fracture surfaces presented the typical color for yellow brass.

Deposits were very often observed on fracture surfaces. The transgranular regions near notch roots were covered by a thick layer containing particles where the color was often green-blue (Fig. 6.23), while the transgranular fracture produced later was relatively clean. No particular effort was made to identify these particles, but the EDS analysis performed at low voltage showed that high oxygen peaks always appeared in regions with such depositions, indicating that they are probably oxides.

The copper oxides are believed to have formed after the SCC cracking because they gradually grew on the fracture surfaces from isolated particles to a particulate layer (Fig. 6.24). There might be a protective Cu_2O layer [96] formed in the early stage of oxide growth, since a smooth layer broken by the slip underneath near the final ductile fracture was observed (Fig. 6.25). It can be seen from Fig. 6.25 that the thickness of this layer is less than 1 μm, which is consistent with the thickness of early Cu_2O film formed in tarnishing solution [96].

6.5 DISCUSSION

6.5.1 The cracking patterns of SCC in 70Cu-30Zn

The systematic fractographic observations made on a series of annealed and cold-worked specimens of different thickness showed that both intergranular and transgranular fracture occurred in non-tarnishing solution. The intergranular fracture tended to appear in the lower K regions and near the lateral surfaces in annealed specimens, while for cold-worked specimens, it appeared more often in regions with local low prestrain.

Figure 6.23 A thick corrosion deposition layer near the notch observed in a specimen tested in an oxygenated ammonia solution.

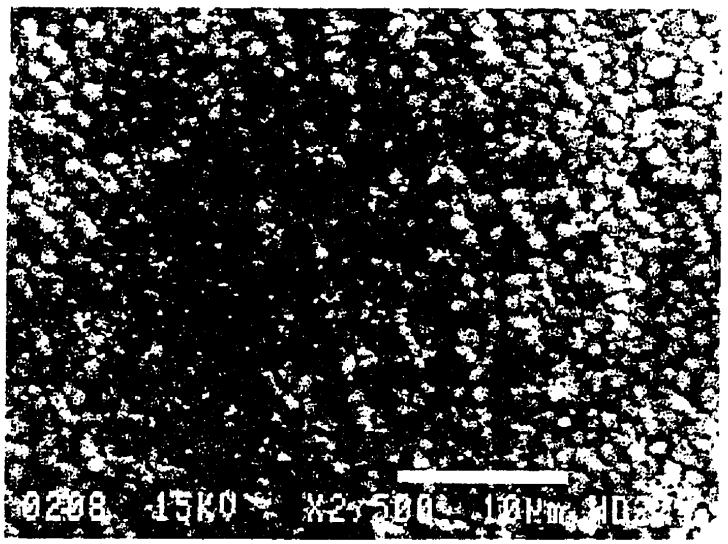

Figure 6.24 Particulate deposits on SCC grain boundaries.

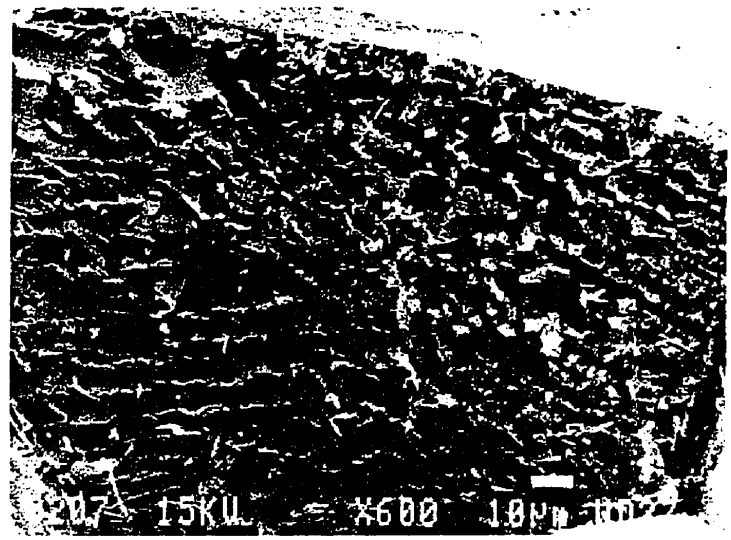

Figure 6.25 A thin deposit layer was broken by slip underneath this layer near the final ductile fracture.

Few studies have reported intergranular fracture in non-tarnishing solution, and most of the research on 70Cu-30Zn focused on transgranular fracture. It has been generally accepted that the tarnish film preferentially formed on grain boundaries causes intergranular fracture. However, Pugh *et al* [93,96] have suggested that tarnishing conditions can occur in non-tarnishing solution. Oxygen dissolves copper forming cupric ions and producing OH^- at the same time, which increases the pH value and makes tarnish film formation possible [164]. Poor circulation at the crack tip facilitates this process. Does the tarnishing induce intergranular fracture? The tarnish film consists of a thin and protective Cu_2O film, covered by a thick porous layer of Cu_2O and an outer layer of CuO [96]. The colors of the fracture surfaces in the present study indicate the presence of a CuO (black) layer and a porous or particulate Cu_2O layer (isolated red Cu_2O particles can give a brown color on brass surface). However, these oxides formed probably after the SCC fracture, since particles gradually growing to particulate layer was observed. This film appears fragile and it can be fractured by slip (Fig. 6.25). In addition, the transgranular fracture was usually in areas where the circulation of oxygen was difficult (in the center of the specimen). The tarnishing condition should be reached quickly in these regions. There appears to be no reason for the crack to avoid "brittle" grain boundaries and instead to propagate within the ductile grains. Therefore, it appears improbable that the tarnish film induces the intergranular fracture.

The frequent appearance of intergranular fracture and its locations in annealed TN-DCB specimens suggest surface dissolution as an alternative explanation for the intergranular fracture. Because of the presence of high oxygen [228], the grain boundaries are anodic to the grain interiors. With the exposure time increasing in oxygenated solution, the lateral surfaces are more susceptible to anodic intergranular dissolution. Intergranular SCC cracking thus initiates from these surfaces, as observed. Thicker specimens and improved surface protection partially block the transportation of oxygen to the interior and reduce the surface corrosion. Transgranular fracture thus increases in amount and can even start right at the surface.

Cracking in TN-DCB specimens started from many sites at the surfaces because of the surface dissolution and the thin specimen thickness. The relationship between K and the cracking patterns could not be established. In CT specimens, although somewhat more intergranular fracture appeared in the near-surface regions, the surface dissolution did not significantly reduce the effective section of the specimen. So the local K could be better determined from the crack length on the fracture surfaces. The fractography of the annealed specimen showed that most of the intergranular fracture appeared at low K (< 14 MPa$\sqrt{m}$) where plain strain conditions was favored. Transgranular fracture preferentially appeared in the higher K region. This agrees with the previous reports that intergranular fracture appears at low stress [96] and in plain strain conditions [110]. It therefore appears that the mechanics determines the propagation patterns in the annealed specimen. However, such a correspondence is much less clear in the cold-worked specimens. Superficial intergranular fracture was not observed on thin TN-DCB specimens. In contrast, intergranular fracture, present mostly in the form of secondary cracks, occurred preferentially in the mid-thickness region. The features of the transgranular fracture appear not to be related to K but to the local prestrain. The dislocation configuration therefore has an intrinsic influence on the cracking patterns.

The fractography obtained in the present study suggests that the cracking patterns during SCC are determined by the dislocations locally present through their interactions with the environment. In annealed materials, the dislocations initially move easily within the grains. Very low strain (< 1%) can lead them to pile up against grain boundaries in brass [229]. As the strain increases, the length and the number of dislocation pileups on the slip planes increase. The planar distribution of dislocations still remains until a high strain for this low stacking fault energy material. Since many dislocations are pile up against grain boundaries at low strain, intergranular fracture tends to appear at low K (low strain). This intergranular fracture is orientation driven, as dislocations are situated on individual crystallographic planes. While at high K, more dislocations are emitted from the

crack tip which move away and form long pileups in the grains. Grain boundaries are no longer the preferential interaction sites. So the transgranular fracture is induced by dislocations within grains reacting with the environment. For cold-worked materials, the crack tip dislocation emission does not change strongly the pre-existing dislocation distribution. Accordingly, no clear correspondence between K and the cracking patterns was observed. This was very evident for the heavily cold-worked specimens, as textured river lines and sheet like facets were seen everywhere on the fracture surfaces. The variation of the cracking patterns represents the local extent of prestrain rather than the crack tip mechanics. Transgranular fracture tends to appear on the plane where the grains were stretched and compressed. The locally larger deformation near the lateral surface by the previous rolling also greatly reduces the intergranular fracture in these regions. For the same reason, the cold-worked microstructure might not be completely reversed to its original status in the annealed CT specimen because of the low annealing temperature (350°C). The retained dislocations made transgranular fracture more complex than usual. Of course, the environment, i.e., oxygen and resulting dissolution in brass-ammonia system, also played a role on determining the cracking patterns. Cracking occurred first where the oxygen arrived, such as near the lateral surfaces and along the grain boundaries.

This dislocation-cracking pattern hypothesis touches the root cause of cracking pattern variation of SCC in 70Cu-30Zn, in that it generalizes the interpretation of both intergranular fracture and transgranular fracture. It is applicable to other materials with low stacking fault energy. This hypothesis is consistent with the previous results concerning the K and cracking features in transgranular fracture of annealed material [3]. It also predicts that intergranular fracture is a crystallographic fracture, as well. This has been proved partially by the morphology of grain boundaries in intergranular fracture. A good example is the secondary cracks in cold-worked specimens. These secondary cracks usually propagated faster, reflecting the preferential interaction between grain boundaries and environments. They also tended to be parallel to the rolling plane, which is close to {110} in heavily

deformed condition [230]. Furthermore {110} is the usual average cracking plane for transgranular SCC in 70Cu-30Zn [113]. More direct evidence will be presented in the next chapter.

6.5.2 A possible mechanism involved in the SCC of brass-ammonia system

Once the correspondence of fractography to the dislocation substructures has been established for SCC of 70Cu-30Zn, it is necessary to investigate how the environment interacts with dislocations to produce the observed characteristics. For the current experimental facilities, the real events occurring at the crack tip are difficult to identify directly. Therefore, we will try to draw relevant information from indirect experimental evidence and by evaluating the proposed mechanisms.

Embrittlement mechanisms, especially that of film-induced cleavage, have received considerable attention in recent years for SCC in Cu-Zn alloys because of the possibility of forming tarnishing or dealloyed layers. It is proposed that film formed on surface could initiate cleavage cracking in the ductile substrate. This mechanism was supported by the results of Newman *et al* [102] and Bertocci *et al* [101]. They reported that crystallographic cracking was observed in equilibrium solution on Cu-Zn alloys and suggested that crystallographic cracking could only be nucleated by the dealloying of zinc, since oxygen was excluded from the solution.

It is known [93] that, in aqueous ammonia solution, copper in brass is anodically attacked by ammonia:

$$Cu + 2NH_3 \rightarrow Cu(NH_3)_2^+ + e^- . \qquad (6\text{-}1)$$

The $Cu(NH_3)_2^+$ produced on brass surface is unstable in the presence of oxygen which oxidizes $Cu(NH_3)_2^+$ to $Cu(NH_3)_5^{2+}$:

$$2Cu(NH_3)_2^+ + \tfrac{1}{2}O_2 + H_2O + 6NH_3 \rightarrow 2Cu(NH_3)_5^{2+} + 2OH^- . \qquad (6\text{-}2)$$

At the beginning of the SCC test, there is insufficient $Cu(NH_3)_5^{2+}$ complex provided as cathodic reactant in solution, the oxygen is first reduced as follows:

$$\tfrac{1}{2}O_2 + H_2O + 2e^- \rightarrow 2OH^- . \qquad (6\text{-}3)$$

As reaction (6-2) proceeds, the cathodic reaction will become

$$Cu(NH_3)_5^{2+} + Cu \rightarrow 2Cu(NH_3)_2^+ + NH_3 . \qquad (6\text{-}4)$$

The presence of oxygen allows the coupous complex $Cu(NH_3)_2^+$ to form $Cu(NH_3)_5^{2+}$ by reaction (6-2), which in turn dissolves Cu from brass by reaction (6-4).

Reaction (6-1) also occurs in the equilibrium ammonia solution. But it is the copper powder dissolved in the solution before the SCC test that is oxidized instead of the copper in the specimens. If there is a little dissolved oxygen in the solution, it will be eliminated by reaction (6-2). The resulting cupric complexes can be reduced by copper powder through the cathodic reaction (6-4), if there always is excess Cu powder in solution. Finally, the solution will contain negligible $Cu(NH_3)_5^{2+}$ and oxygen. This was the condition reported by Kaufman & Fink [100] and Dickson *et al* [4]. They took great caution during their tests to scavenge oxygen as much as possible, and failed to obtain crystallographic cracking or any cracking.

More interestingly, Dickson *et al* [4] repeated SCC tests on thin films of 65Cu-35Zn brass in a manner similar (including solution and specimens) to that described by Newman *et al* [102], although the conditions may not have been exactly identical. They found that crystallographic cracking always started from corrosion pits or slots on the surfaces, produced when insufficient precautions were taken. For this testing procedure, the pitting may have happened very quickly when oxygen contacted the wet specimens, due to the fast kinetics [96] of reaction (6-1) and (6-2). This strongly suggested that anodic dissolution of copper was required, at least for the initiation of SCC. The present study agrees with this assumption, because the initial oxygen leakage and cupric complex ions (indicated by their slightly blue color) in the solution also quickly produced surface intergranular cracks (Fig. 6.21). After oxygen and cupric complex ions were eliminated, no new crack was initiated and the surface

cracks stopped growing, even though K was more than double that in oxygen containing solution.

Film-induced cleavage mechanism emphasizes the role of the surface film in *initiating cleavage* in the ductile substrate. For the propagation to continue by further dealloying and cleavage, this mechanism requires the dynamic plastic strain to destroy any protective action of the local electrochemistry at the crack tip [102,231] to allow further dealloying to continue. Despite the fact that transgranular SCC actually occurs along slip planes, the supportive experiments carried out at dynamic strain rates do not correspond to the real SCC failures, in which cracks propagate a considerable distance under stress. Precracked specimens should therefore be better to study the propagation behavior.

In the present study, precracked specimens came in contact with the ammonia solution at the very start of the testing procedure when the equilibrium condition was not yet reached for the solution. Although at that time, a load was not applied, corrosion could not be precluded. The fracture surfaces of precracked specimens produced by tension after the SCC tests showed some indications of this corrosion in the precrack tips. For the SCC precracked, the fracture near the final ductile region was intergranular, which is difficult to distinguish the intergranular corrosion in solution from the previous SCC. For the fatigue precracked, the inert environment was not very good during the first 48 hours because of the low nitrogen pressure in the cylinder. A periodic slight color was observed in the solution and the initial applied force decreased approximately 10%, although a soft spring was connected with the specimen in attempt to keep the constant load. After nitrogen pressure was maintained stable, the force stopped to decrease until the tests terminated. On the fracture surface, intergranular and quasi-intergranular fracture was found after the transgranular fatigue fracture in the center, while near the lateral surface, there is a transgranular region (~ 150 μm) developed after a full stop of the

fatigue propagation. Again, it is uncertain if the precrack propagated under poor deoxygenated condition 48 hours after the test was started.

Supposing the propagation occurred within the first 48 hours, the average propagation velocity in the intergranular region was approximately 9.26×10^{-6} mm/s, and in the transgranular region it was approximately 8.68×10^{-7} mm/s, both of which were lower than the average propagation velocity of well protected TN-DCB specimens in oxygenated solution (see next chapter). But the average propagation velocity of the transgranular region agrees with the annealed CT specimens at lower K in which the surface dissolution effect was minimized by its large thickness. Load drop phenomenon and the mainly intergranular fracture surface were also observed on TN-DCB specimens in oxygenated solution. Therefore, the observed intergranular and transgranular fractures very probably occurred under the poorly deoxygenated condition of the first 48 hours of testing.

Because of the low oxygen and cupric complex ions in solution, the amount necessary for cracking was concentrated to the central plain strain region by the triaxial stresses. Grain boundaries became anodic in this region, favoring intergranular fracture and faster propagation in center. The propagation near the lateral surface thus became too small to be noticed by optical microscope. Once the oxygen had been eliminated, the crack propagation stopped. At that time, the superficial dealloyed layer existed on the precrack tip wall. If it had nucleated a cleavage crack, the cracking would not exceed the distance of its original thickness, as reported by Cassagne *et al* [232]. Under constant load, the formation of cleavage microcrack releases the local strain, which prevents the next cleavage. Another possibility is that the continuing dealloying along this fresh cleavage crack may cause another cleavage events intersecting the first one, which would effectively blunt the crack tip and block further cleavage in this direction. In other words, this superficial event is not responsible for the

SCC propagation. This explains the immunity of the precracks to the deoxygenated solution and the ductile failure observed during strain rate tests in this solution [4,100].

The SCC tests in equilibrium solution also show that the amount of oxygen or cupric complex ions required for propagation may be very low. A quantitative figure can be drawn from the result of Bertocci *et al* [101]. They measured "copper in solution" when crystallographic cracking was observed and did not specify whether the ions present were Cu^{+} or Cu^{2+}. But in their "copper free" solution, reaction (6-1) should happen. Thus, the copper in solution should be Cu^{2+}. The lowest concentration when the crystallographic propagation occurred was 0.05 mol/l in solution.

On the other hand, the dealloyed layer on brass is a copper sponge, analogous to the tarnish film which was shown [96] to consist of thick porous layer of Cu_2O. The thin protective Cu_2O film (< 20 nm in brass) should be the strongest region within the tarnish film. For specimens tested in the oxygenated non-tarnishing solution in the present study, a thin smooth film observed on the grain boundaries was broken by slip underneath (Fig. 6.25). This indicates that this thin film is too weak for the slip. Thus, it is difficult to imagine that a thicker, porous CuO or dealloyed layer (> 30 to 40 nm) would not be broken by slip before they could initiate cleavage in the ductile substrate.

Among proposed SCC mechanisms, hydrogen-induced cracking is ruled out by the thermodynamic conditions in brass-ammonia system which should not result in the formation of hydrogen. Anodic dissolution has been shown to be incompatible with the transgranular crystallography [4], because independent dissolution events would not always produce interlocked crystallographic facets. The importance of the environment, namely oxygen and/or cupric complex ions, has been demonstrated previously [4,100] as well as in the present study. These studies indicate that other mechanical mechanisms are also incomplete without considering the environmental effects on the propagation. From

the experimental results and the above discussion, we suggest that the adsorption of oxygen or cupric complex ions promotes crack propagation in brass-ammonia system. The nature of adsorption can account for the fast crystallographic fracture propagation in preimmersed ribbon tests [4]. It is also consistent with the condition of cracking pattern variation in this system, which has been discussed in the previous section. One feature which adsorption-induced propagation cannot easily explain is the discontinuous propagation character. However, there are some counter arguments to this issue, such as the fractographic definition of crack arrest markings. In addition, the acoustic emission technique failed to detect crack arrest in this system [18,22]. The detailed propagation study will be presented in the next chapter.

Chapter 7

SCC Crack Propagation

7.1 INTRODUCTION

The detailed crystallographic study of transgranular SCC in austenitic stainless steels and in 70Cu-30Zn [2-4] has shown that the SCC propagation occurs along alternative {111} slip planes. The fractographic results presented in chapters 3 to 6 related both transgranular and intergranular SCC fracture to the activity of crack tip dislocations. However, as the measurement of crack propagation velocity only represents the kinetic aspects of crack propagation without showing any details of how the crack propagates physically, fractography also only reveals the paths of propagation and does not give complete information on the process. The instant crack growth moment can be represented by the positions of the crack front, but these positions must be marked by a proper method.

Different techniques have been employed to investigate [18-23] the transgranular propagation process. The results favor a discontinuous propagation behavior. One important fractographic evidence concerning discontinuous propagation is the presence of crack arrest markings. The similarity of crack arrest markings to crack front markings produced by load pulses and the loss of one to one correspondence of crack front markings for short time intervals between load pulses led Pugh [117] to propose a discontinuous cleavage model.

Despite additional results [5] supporting the involvement of crack tip slip during SCC, some arguments remain against the experimental evidence of discontinuous cleavage. First, no matching photos were demonstrated to identify that crack arrest markings were not slip traces produced behind the SCC crack tip. Second, the crack front markings did not fractographically show, even at high magnifications, that the propagation occurs by leading tips on the primary facets separated by uncracked ligaments behind as described by Pugh's discontinuous cleavage model [117]. Third, it is improper to equalize the crack arrest time Δt^* with the minimum time interval Δt in which each load pulse produces a crack front mark, since the plastic deformation induced by load pulses is greater than that produced during propagation. The resulting arrest time should probably not be the same.

This chapter will report the fractography of the crack front markings produced by load pulses and will compare their features with observed crack arrest markings. The objective of repeating load pulse tests in single-phase 310 stainless steel and 70Cu-30Zn is to have a close look at the crack front and crack arrest markings, to verify how these markings form and how the crack stops and repropagates. The tentative measurement of crack propagation velocity in 70Cu-30Zn will also be presented here in order to obtain more information about crack propagation.

7.2 CRACK PROPAGATION VELOCITY IN SCC OF 70CU-30ZN

7.2.1 Average crack propagation velocities of TN-DCB specimens

Similar to their fractography presented in section 6.2.1.1, the SCC propagation velocity of TN-DCB specimens cut from 10 mm plate did not show any difference in the as-received and in the annealed (650°C × 1 h) conditions when tested in 15 N non-tarnishing ammonia solution. This solution had a royal blue color at room atmosphere, which prevented simultaneous crack propagation observation. For specimens protected only by a layer of lacquer on the surface, the initial applied load started to decrease very soon after the tests begin. About 15 to 26 hours after the tests started, the initial applied loads were often close to zero, indicating the final failure of specimens. Because the total failure time was relatively short in this solution, the average propagation velocity could be estimated by the total crack length and the total testing time. It was approximately 1 to 3×10^{-4} mm/s for 4 specimens both in the as-received and in the annealed conditions. One specimen, cut from 15 mm plate and annealed at 650°C, had a smaller grain size (0.1 mm, compared to 0.6 mm for those cut from 10 mm plate). The total failure time for this specimen was more than 48 hours for the same test conditions, which gave an average propagation velocity of 6.65×10^{-5} mm/s.

Some specimens were further protected from surface attack by covering with glass plates or with silicon sealant on the immersed areas which had been already coated with lacquer and Teflon tape. This procedure considerably increased the total failure times, up to 72 to 76 hours. The average propagation velocity calculated was then 2×10^{-5} to 6×10^{-5} mm/s.

Thicker specimens (B = 4 mm) were also tested in single or double protection conditions. For one specimen only protected by lacquer, the load decrease was noticed 24

hours after the beginning of the test. It failed another 24 hours later, which gave an average propagation velocity of 6.9×10^{-5} mm/s. For another specimen protected by lacquer and glass plates, the applied load did not decrease in 24 hours, but a surface crack was noticed at that time. The test was interrupted after 83 hours when the total crack propagation was barely 1 mm. Supposing a crack initiation time of 24 hours, the average propagation velocity in this specimen was 1.35×10^{-7} mm/s. This specimen was later fractured without glass plates at an average propagation velocity of 5×10^{-5} mm/s.

In summary, a larger thickness, a smaller grain size and better surface protection all increased the total failure time and decreased the average propagation velocity of TN-DCB specimens tested in the non-tarnishing solution. Good surface protection was especially important for thin TN-DCB specimens and decreased the average propagation velocity by a factor of 5. Combined with the thickness effect, the average propagation velocity could be decreased further.

7.2.2 $\frac{da}{dt}$ *vs.* K curves of CT specimens

SCC crack propagation was directly monitored in the non-tarnishing solution by a compliance method on two CT specimens, one in the as received cold-worked condition and another after annealing at 350°C. The crack length a was calculated from equation (2-2) and (2-3) by the measurement of crack opening displacement. The crack tip stress intensity factor K was given by equation (2-4). Specimen surfaces were coated with a layer of lacquer. Because the total testing times were quite long compared to the TN-DCB specimens, surface corrosion occurred on both specimens, but was especially severe for the annealed one. One crack branch was observed in the annealed specimen at $K \approx 13$ MPa$\sqrt{m}$. There was no macroscopic crack branching observed either on the lateral surfaces or on the fracture surfaces of cold-worked specimen. Relatively straight SCC cracks propagated on the plane perpendicular to the tensile axis in both specimens.

Fig. 7.1 shows the $\frac{da}{dt}$ *vs.* K curve for the annealed specimen. In the K range of approximately 9 to 15 MPa$\sqrt{m}$, propagation velocity increases with increasing K. Load pulses were applied between K values of 11 to 13 MPa$\sqrt{m}$ which probably caused some retardation of propagation. However, the curve shows no clear tendency to present a plateau region where the propagation velocity is independent of K. The lowest K in this curve is larger than most of the initial K for the SCC tests performed on TN-DCB specimens. But the propagation velocity is at least one order lower than in those thin specimens, because the surface corrosion had a smaller influence on crack propagation. SCC tests were not continued to higher K values due to the limitation of applied load available on the tensometer employed and the concern of increasing damage to the fracture surfaces in a long time test.

For the specimen in the as-received (cold-worked) condition, its $\frac{da}{dt}$ *vs.* K curve shows a tendency to form a plateau at a K of approximately 10 MPa$\sqrt{m}$ (Fig. 7.2). The propagation velocity is approximately 2×10^{-5} mm/s in the plateau region. Load pulses were also performed in the plateau region which induced a large propagation retardation when K was approximately larger than 15 MPa$\sqrt{m}$, but had little effect in the lower K region. This suggests that the increase of load at low K does not produce significantly additional crack tip work hardening in this already hardened material. The SCC test was interrupted when $K \approx 18$ MPa$\sqrt{m}$, because the crack length a was close to its maximum value of 38 mm calibrated by Eq.(2-3). One week later, the test was resumed and the crack propagated more than 7 mm during 5 hours, which gave an average velocity of ~ 4×10^{-4} mm/s, more than 10 times to the plateau value. The final K calculated from the maximum SCC crack length measured on the surface was close to 80 MPa$\sqrt{m}$. The reason for such rapid propagation is not clear. It may due to the effective thickness reduction, as already stated in section 6.2.2.2. It may also be an indication of Stage III. Since no more data was available for Stage III in this test, this value is not presented in Fig. 7.2.

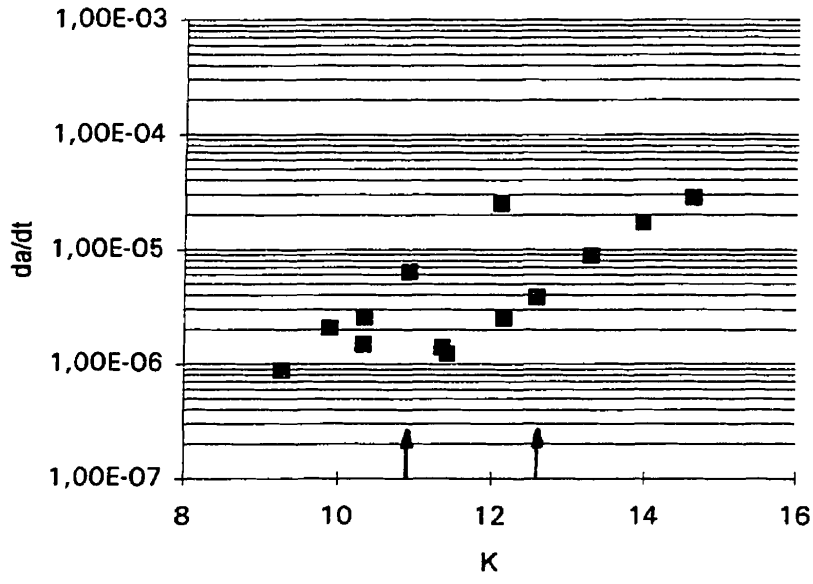

Figure 7.1 $\frac{da}{dt}$ *vs. K* curve of annealed 70Cu-30Zn. Arrows indicate the region applying load pulses.

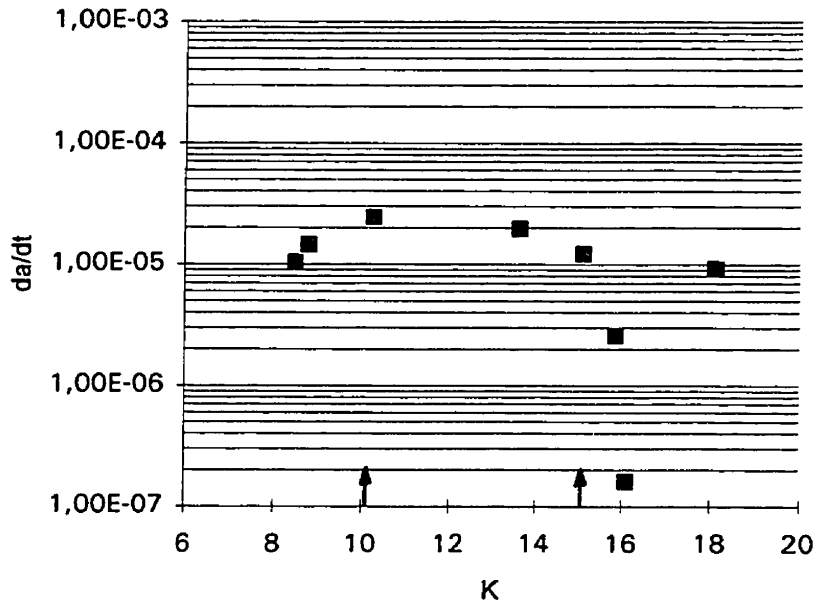

Figure 7.2 $\frac{da}{dt}$ *vs.* K curve of cold worked 70Cu-30Zn. Arrows indicate the region applying load pulses.

7.3 FRACTOGRAPHY OF SCC PROPAGATION

Although the specific SCC processes are different, the propagation behavior is similar in 310 stainless steel and 70Cu-30Zn, independently of whether the crack propagates within grains or along grain boundaries. To simplify the interpretation, the two materials will be considered together in the following description.

7.3.1 General morphology of load pulse traces

The traces of load pulses were not easy to be found on the fracture surfaces. They were not curved across the whole fracture surface. Instead, they were discontinuous, appearing only in a few grains, suggesting the irregularity of the SCC crack tip. Because of the irregularity of the crack tip, the effective K can be quite different at individually local portions, which in turn results in the different local propagation velocities of each portion and increases the crack tip irregularity. When the load pulses were applied, only some leading portions had sufficiently high K to mark the crack front. The observed pulse traces outlined the curved or straight crack front within one grain, depending on the orientation of that grain. The orientation difference between two grains often made the traces invisible at grain boundaries.

The magnitude of the load pulses influenced their appearance. Small load pulses did not produce blunting at the crack tip. However, it was observed that the appearance of crack front markings was also more likely determined by the local mechanics. As shown in Fig. 7.3a, the first load pulse introduced a secondary crack and made the cracking facet inclined. Later similar load pulses disturbed the propagation less. The crack kept going in the same direction after smaller crack tip blunting. This suggests that some load pulses might not make any markings on the fracture surface. Another reason for missing pulse traces was that load pulses often resulted in secondary cracks. Later propagation might go

Figure 7.3 Matching fractographs show crack front markings in 310. The inclination is interlocked on opposite fracture surfaces but slightly in (b).

along the secondary crack, since pulse traces were some times observed inside secondary cracks. Some of the secondary cracks could be pulled out during final fracture, hiding the nearby set of pulse traces. This may explain why the least pulse traces were observed on specimens which underwent the largest load pulses.

Matching fracture surfaces were investigated in the regions of pulse traces, but the matching pulse traces were not always found. Often the matching pulse traces showed a small blunting corresponding to a step (Fig. 7.4). Pulse traces corresponding secondary cracks occurred at high K. Other features of matching pulse traces included interlocked inclined facets with fine traces as shown in Fig. 7.3 and interlocking fine steps which indicate only slight blunting produced by load pulses.

7.3.2 Crystallographic crack front

The crack front defined by the load pulse traces is crystallographic. In 70Cu-30Zn, the large grain size allowed the crack front to be straight and parallel to striations along a certain distance (Fig. 7.5). Straight crack fronts were also found in 310 stainless steel when the crack propagated along {100}<110> (Fig. 7.4). The crack front was then parallel to striations and curved to link straight segments, where the two cracking planes were joined by forming larger rivers. This indicates that the crack propagation follows {111} planes because the striations during SCC of fcc materials are the intersection of two {111} planes [2].

The matching crack fronts on opposite fracture surfaces also showed crystallographic aspects. The interlocked facets with fine markings shown in Fig. 7.3 and interlocked fine steps indicate that load pulses produce very limited yielding at the crack tip. The interlocked steps were very small and their inclination could not be examined. They may be larger {111} microfacets induced by load pulses, because they were parallel

Figure 7.4 A matching pulse trace in 310 stainless steel on a {100} primary facet. Arrows indicate the local corresponding step and blunting produced by the load pulse. The straight crack fronts are perpendicular to <110>. The step in (b) indicated by an arrow is identified as {110} since it is perpendicular to {100} and to <110>.

Figure 7.5 A crack front marking composed of two straight segments in 70Cu-30Zn.

Figure 7.6 A large step, composed of several tiny steps, produced by a load pulse in 310 stainless steel.

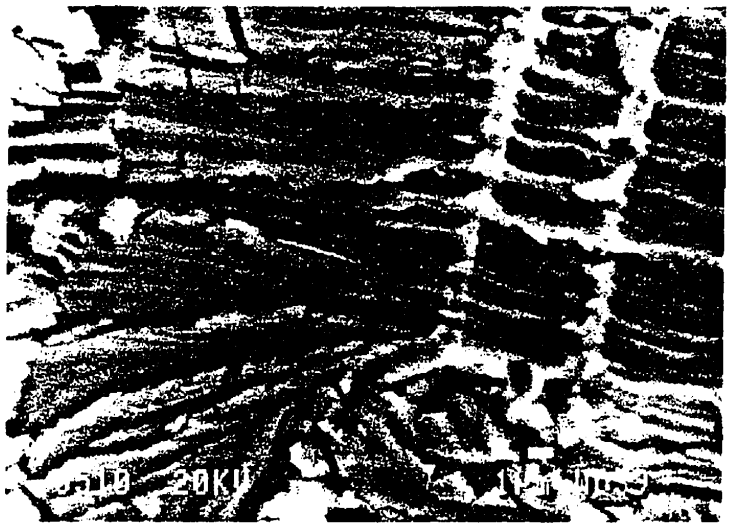

Figure 7.7 Two crack front markings produced by load pulses in 310 stainless steel. The blunting appears to be made up of tiny steps.

to striations. In the easy propagation direction <110>, load pulse deviated the {100} plane from its original orientation to form a {110} step on one side (Fig. 7.4). The following propagation occurred on an inclined {100} plane on the other side after a very small blunting. When the steps became larger, it made up of several tiny steps (Fig. 7.6). The observed blunting at the pulse traces actually corresponded to several tiny steps at the corner (Fig. 7.7).

The crack front observed in intergranular regions had straight segments, more or less parallel to the slip traces in one or the other of the grains (Fig. 7.8). This implies that the slip near the grain boundaries is involved in cracking. The region in Fig. 7.8 was found near the final ductile fracture which often induced many slip traces on the SCC fracture surfaces. The slip lines are very useful to determine the crystallography of grain boundaries. As shown in Fig. 7.9 at a higher magnification, the slip lines A_1 are convex and interlocked to slip lines B_1. Slip lines B_1 are the depression of A_1 on the opposite surface. Similarly, slip traces $\underline{B_4}$ correspond to traces A_4 on the opposite surface. The rest two sets of normal slip lines indicate that grain boundary B has an orientation close to {100}. In grain A, slip lines A_1 and A_4 make an angle of approximately 50° to slip lines A_2 (the pulse trace). This suggests that grain boundary A has an orientation close to {110}, since the intersections of two {111} planes with a {110} plane are bisected by a <110> direction approximately at 54°. Slip traces A_3 correspond to slip traces $\underline{B_3}$ on the opposite surface although the matching appears less than perfect. The crack front markings are both parallel to the intersection of one of the {111} planes with grain boundaries. The SCC propagation crystallography for grain A is close to {110}<100>, for grain B it is close to {100}<110>, and both were observed in transgranular fracture of 70Cu-30Zn [113]. The impression of slip after SCC on both grain boundaries may be due to the softness of annealed brass and the large deformation of final overload fracture. It also indicates that SCC crack tips remain very sharp during SCC.

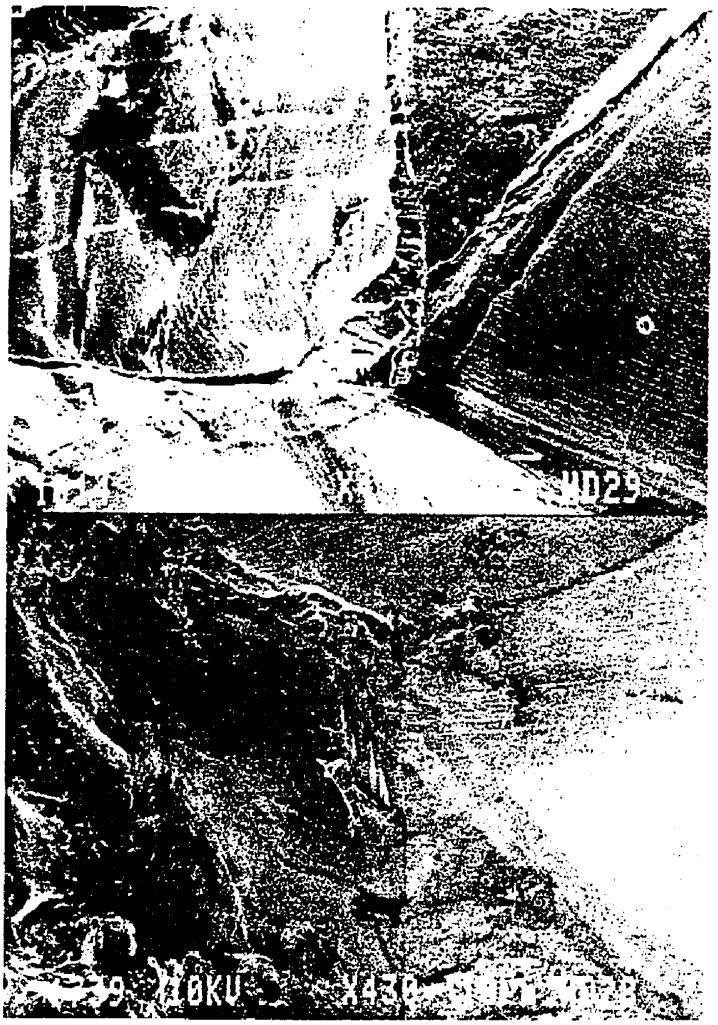

Figure 7.8 Matching fractographs of crack front markings in 70Cu-30Zn near the final overload fracture. The crack front markings appear parallel to slip traces on the grain boundary.

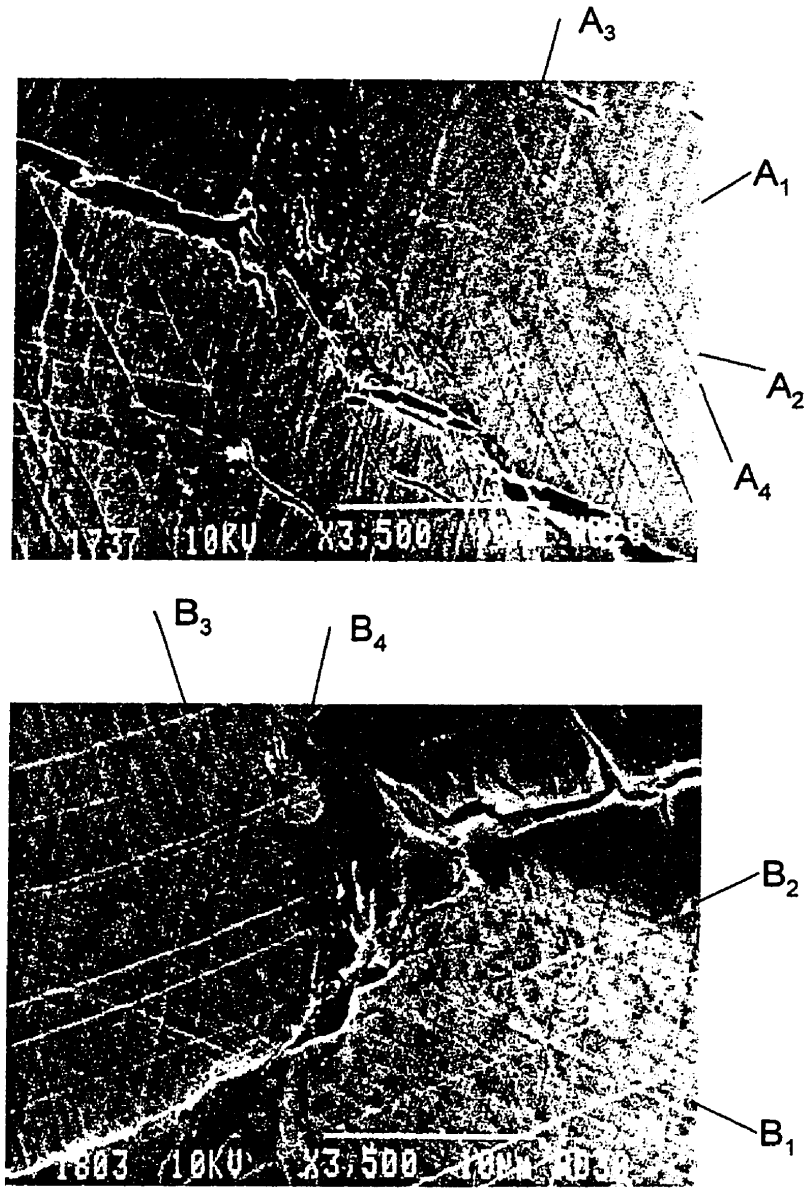

Figure 7.9 An enlargement of a region of Figure 7.8. A_i and B_i indicate the matching slip traces on both surfaces. Grain boundary A has an orientation close to {110} and grain boundary B has an orientation close to {100}, which are determined by the intersection angles of slip traces on grain boundaries.

Very similar to the transgranular fracture, the crack fronts in intergranular regions curve when the local propagation direction changes (Fig. 7.10). The crack front seen in Fig. 7.11 is a step pulled out of the grain boundary and follows two sets of slip planes. Some fine and detached steps appear between two markings. Figure 7.12 shows that the intergranular crack front follows facets in twin and slip steps induced by load pulses on nearby smooth grain boundary. The matching markings on one side of grain boundary are steps, on the opposite grain boundary they are often secondary cracks.

7.3.3 Crack propagation after the load pulses

Since the crack "blunting" made by load pulses were very small and crystallographic, the crack reinitiation sites were all very close to the crack front markings. The closest position in 70Cu-30Zn was just at the markings (Fig. 7.13). In 310 stainless steel, the crack front markings were usually not as sharp as those in 70Cu-30Zn. Some reinitiation sites were observed approximately 1 μm ahead of markings (Fig. 7.14). In these cases, however, no inverse propagation was observed. The position of reinitiation site agrees with the mechanisms proposed here for SCC: adsorption is very important in the SCC of 70Cu-30Zn while absorbed hydrogen is involved in that of austenitic stainless steels.

Transgranular SCC propagation after the load pulses tended to present complex features. The higher load resulted in larger microfacets produced ahead of crack front markings. As shown in Fig. 7.15, two {111} planes which compose the {100} primary facet become approximately 2 μm in width and another set of {111} facets appears ahead of the crack front markings. A little further the crack front marking, four sets of {111} planes are all operating. The high K features were more evident in 70Cu-30Zn where the primary facets were usually larger than in 310 stainless steel. The complexity appears for about 30 μm ahead of the crack front markings in Fig. 7.16, then the propagation returns

Figure 7.10 Crack front markings on a grain boundary of 70Cu-30Zn.

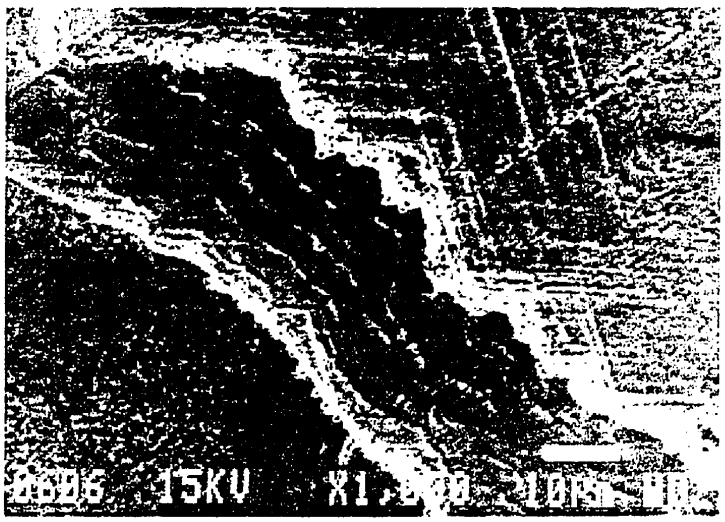

Figure 7.11 Curved crack front markings on a grain boundary of 70Cu-30Zn, which locally follow two sets of slip lines.

Figure 7.12 Two intergranular crack front markings are parallel to crystallographic orientations in twins and slip steps on the grain boundary.

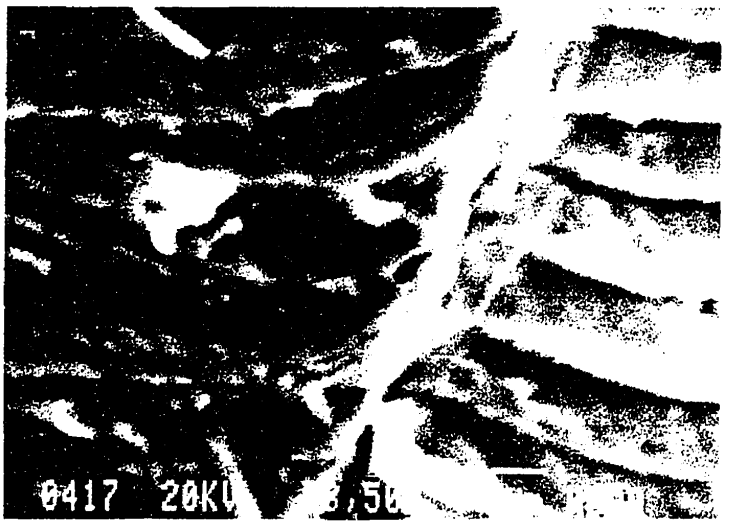

Figure 7.13 Cracking reinitiates at the crack tip after a load pulse in 70Cu-30Zn.

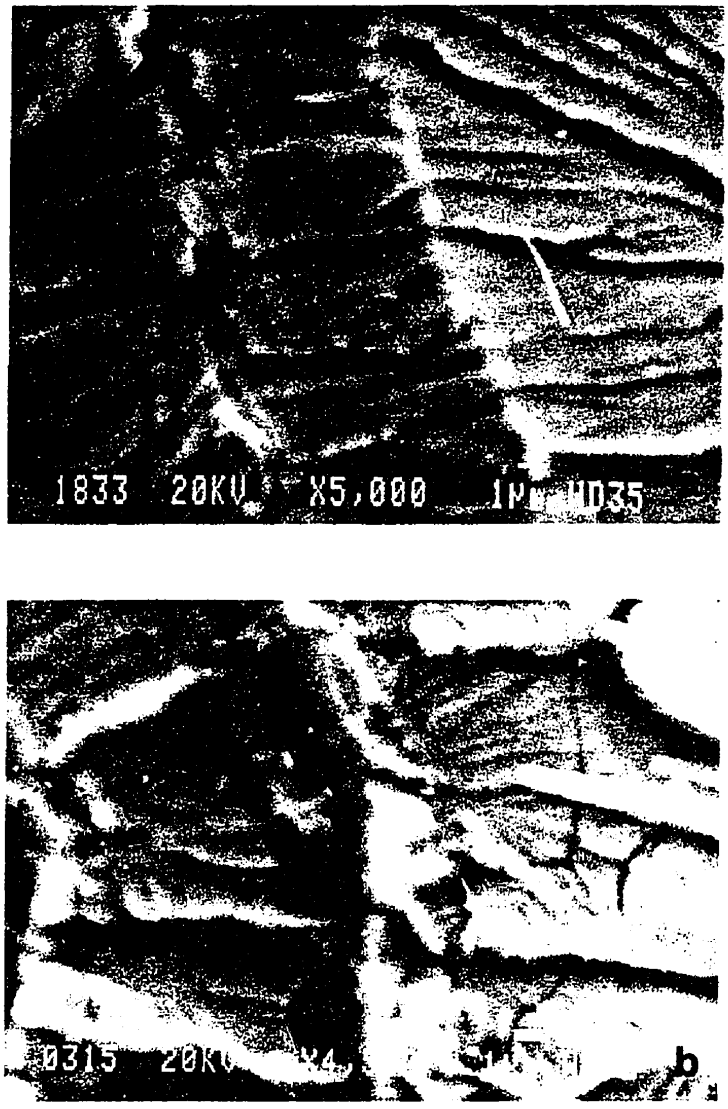

Figure 7.14 Crack reinitiation sites after a load pulse in 310 stainless steel. (a) Crack reinitiated at the crack front marking. (b) Crack reinitiated slightly ahead of the crack front marking.

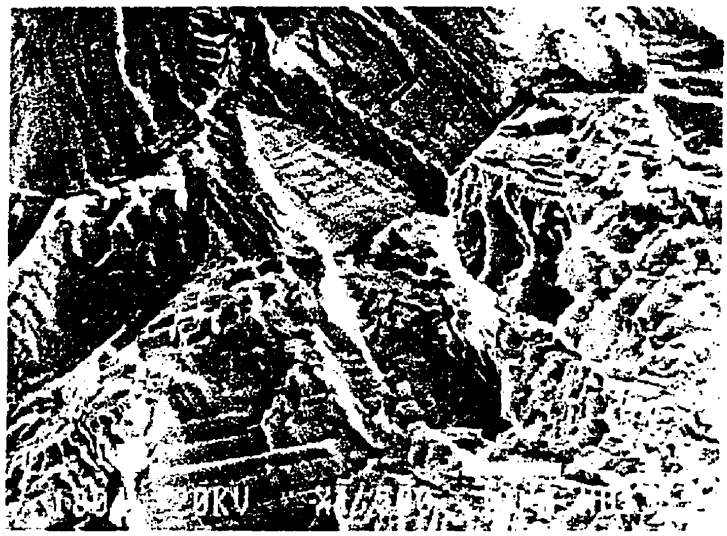

Figure 7.15 Large microfacets ahead of a crack front marking in 310 stainless steel. Two sets of {111} facets meet along a <110> and the third set intersects these as striation markings. In the lower right corner of the photograph, four sets of {111} facets are present.

Figure 7.16 High *K* features ahead of a crack front marking in 70Cu-30Zn.

to its previous orientation. Some times, the first load pulse induced only a simple step, while the second load pulse (same ΔP but a little high ΔK) significantly changed the cracking aspect. This feature indicates that the cracking is very sensitive to the local deformation in 70Cu-30Zn.

The cracking patterns at times changed from intergranular fracture to either quasi-intergranular or transgranular fracture in the load pulse regions. It may then return to intergranular fracture as the crack propagated. Sometimes in the load pulse region, a thin layer of material was pulled out (Fig. 7.17) or lost, permitting the transgranular fracture to be observed in the vicinity of the grain boundaries. The quasi-intergranular fracture appeared as small protrusions or tongue-like facets near the pulse traces on the grain boundaries, such observations also indicate near boundary transgranular fracture (Fig.7.18).

7.3.4 Crack arrest markings

In a 70Cu-30Zn specimen tested under constant load, arrest lines were sometimes observed. Usually these arrest lines were in the transgranular regions and near the final ductile fracture, or along the line where two crack branches met. In areas where the correspondent lines could be found, crack arrest markings on both fracture surfaces showed mirror matching. In contrast to the crack front markings produced by applied load pulses, the crack arrest markings are produced by spontaneously momentary crack arrest. The manner in which they match on opposite fracture surfaces agrees with Pugh's model for discontinuous propagation [117]. Compared to Fig. 7.6, the observed steps are very fine on both fracture surfaces (Fig. 7.19). Almost all the river lines transverse the crack arrest markings. No inclination of cracking planes were found. However, in many cases, the correspondence of crack arrest markings was not observed. The two opposite fracture surfaces often showed different fracture aspects (Fig. 7.20). One possibility is that the

Figure 7.17 The quasi-intergranular fracture in a load pulse region of 70Cu-30Zn. It produced by the local crack branching into the grain boundary.

Figure 7.18 Tongue-like facets appear near a crack front marking in 70Cu-30Zn. The shape of these facets indicates that they lie on {111} slip plane and grow perpendicular to <110>.

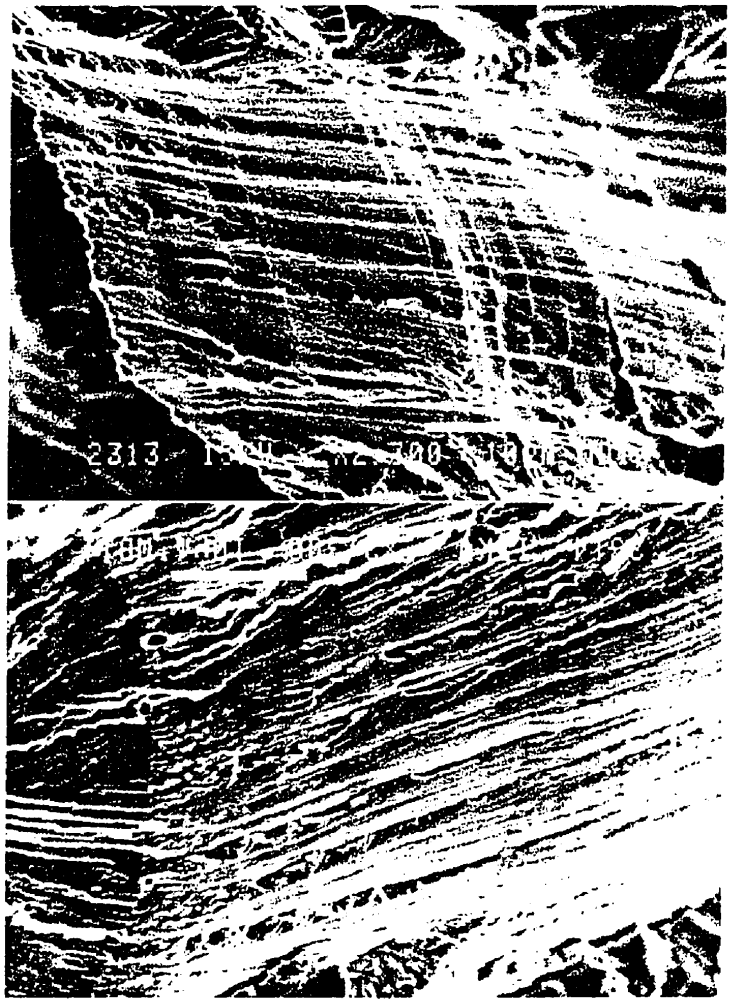

Figure 7.19 Matching fractographs of crack arrest markings found in a crack branch of 70Cu-30Zn specimen tested under constant load.

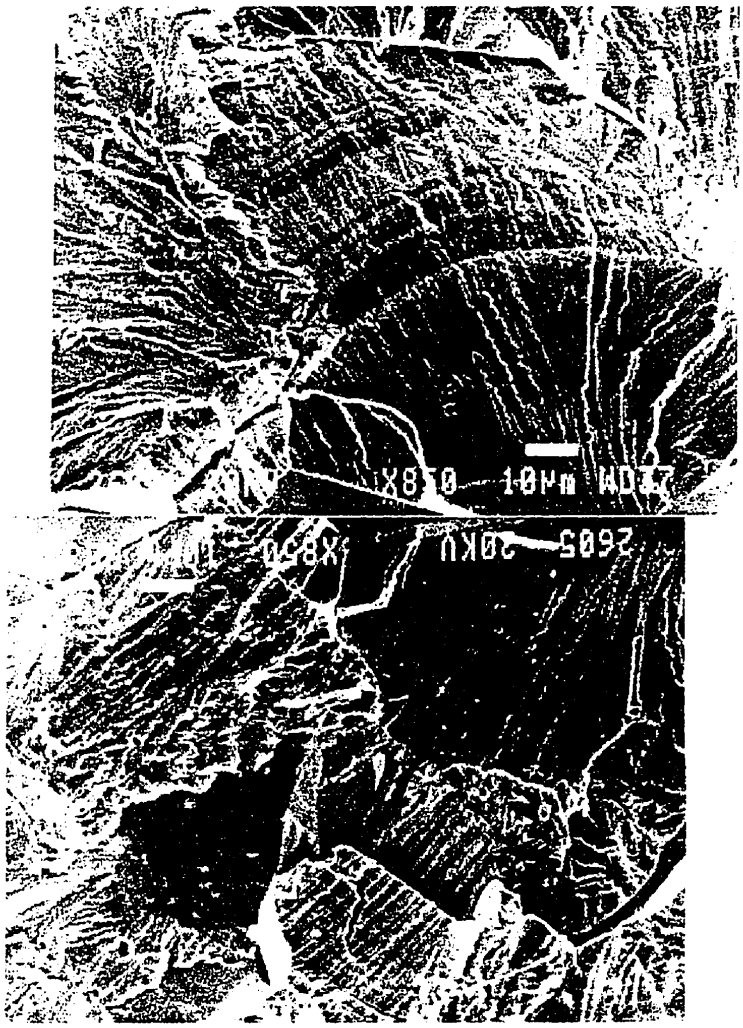

Figure 7.20 Matching fractographs of a region with crack arrest markings on both surfaces of a 70Cu-30Zn specimen tested under constant load. The corresponding areas indicated by arrows show different features.

markings were produced by slip after fracture. This has been shown by matching fracture surfaces of SCC in 310 (Fig. 3.20). For the marked areas shown in Fig. 7.20, the fracture aspects on both sides are different. The indication here is that the two fracture surfaces represent two crack branches opened during the final overload fracture. The walls of multiple branches at the crack tip were easily pulled out and lost during the final crack opening.

7.4 DISCUSSION

7.4.1 The mechanistic indications from $\frac{da}{dt}$ *vs.* K curves

A quantitative relationship between propagation velocity and crack tip stress intensity factor has become an important part of SCC mechanistic studies since the technique of fracture mechanics was applied to high strength steels [233]. Such an approach encounters difficulty to keep predominantly elastic conditions at the crack tip when applied to soft materials. Only a few studies applied the approach of fracture mechanics on 70Cu-30Zn. Among those studies, the tests performed by Kermani and Scully are the most comparable to the present study [234]. They employed a 15 N ammonia solution with 6 g/l of dissolved copper powder and specimens with a similar thickness (9.71 mm) as in the present study. A plateau region where the propagation velocity was independent of K was observed in the low K region ($K < 10.72$ Mpa$\sqrt{m}$) both for annealed and as-received conditions. Because our tests were done mainly at K higher than 10 MPa$\sqrt{m}$, the low K plateau region is not clearly present. However, the K dependent propagation at $K > 10$ MPa$\sqrt{m}$ in the present study should not be due to general yielding, the explanation given by Kermani and Scully in their study. In contrast to their tests, the predominant elastic condition was always maintained in our tests in annealed material. No sign of yielding was observed on the fracture surface. Even the load pulses only produced a limited amount of blunting. Although further work on the rate controlling

process during SCC of brass-ammonia system is required, a direct explanation to the different shape of $\frac{da}{dt}$ *vs.* K curves in annealed and cold-worked conditions can be related to crack tip dislocations and their interaction with environments. For almost dislocation-free annealed 70Cu-30Zn, the amount of dislocations required for propagation should be provided by the applied stress. Obviously, a higher stress intensity K provides more dislocations and results in quicker propagation. For cold-worked material, the dislocation density at the crack tip is almost indifferent to the small increase of load, especially in the low K region. The propagation velocity in the plateau region may be determined by the interactions between the environment and the pre-existing dislocations which do not increase significantly at the crack tip in a certain K range.

The importance of dislocation-environment interactions on the propagation is also revealed by these curves. Compared to the cold-worked material, it can be proposed that the relatively lower velocity in the corresponding K range of annealed material is caused by the number of available dislocations for the interaction. Concerning the environmental effect of interactions, the important role of cupric-ammonia complexes has been shown by previous work [93,100,110]. The exact role of $Cu(NH_3)_5^{2+}$ is not clear without further investigation. It was reported [96] that in more alkaline solution prepared by dissolving copper powder, the $Cu(NH_3)_2^{+}$ complexes are lower than that prepared by dissolving neutral cupric salt at the same copper content in solution. This calculation suggests that with low $Cu(NH_3)_2^{+}$ in the same concentrated ammonia solution, reaction (6-4) $Cu(NH_3)_5^{2+} + Cu \rightarrow 2Cu(NH_3)_2^{+} + NH_3$ occurs more readily. More $Cu(NH_3)_5^{2+}$ and Cu from brass are involved. Thus, the propagation in tarnishing solution is faster than in non-tarnishing solution. The difference of propagation velocity in the same K level between Kermani and Scully's tarnishing solution and our non-tarnishing solution coincides with this explanation. In addition, the similar shape of $\frac{da}{dt}$ *vs.* K curves in both tarnishing and non-tarnishing solution suggests that the cracking mechanisms are not distinct.

7.4.2 Crack front markings and crack arrest markings

The technique of using periodic overload pulses on an otherwise constant load to delineate the crack front is not new. It was employed to investigate the discontinuity of crack propagation and the cleavage features of transgranular SCC [18,19,21,22]. The general morphology of crack front markings produced by load pulses in the present study agrees with the previous descriptions. However, the detailed fractography of crack front markings in the present study showed that the crack front markings were parallel to the striations on the primary facets. These striations were not always the crack arrest markings, but more precisely, the intersections of {111} secondary facets to make up the primary facets in fcc metals. In other words, the transgranular SCC propagation follows slip planes, at least in fcc materials. The crack front markings were also found on grain boundaries. At low magnification, they did not appear crystallographic, but at high magnification, they locally followed the slip traces on the grain boundaries (Fig. 7.10 and Fig. 7.11). This means that such intergranular SCC propagation also has crystallographic features. The other observations supporting this statement are the linear transitions of intergranular to transgranular fracture (Fig. 7.10) and the occurrence of quasi-intergranular fracture (Fig. 6.5).

The appearance of crack arrest markings are very similar to crack front markings on one surface. However, mirror matching was found for crack arrest markings on both fracture surfaces. This one-to-one correspondence and mirror matching differentiate them from the slip produced after fracture (not one-to-one matching) and striations (interlocked and crystallographic). The crack arrest markings in the present study were often observed in high K regions and in crack branches, thus they may not be a general feature of propagation. It was proposed that the crack tip plastic zones increase where two cracks are approaching each other [235]. The crack arrest markings in Fig. 7.20 was found in a region where another surface crack was approaching in the opposite microscopic

propagation direction. The partial non-matching fracture surfaces indicates that this region also contained crack branches. Thus a full stop occurred in the branches by the increasing crack tip plastic zones or by the further propagation of the other branches which effectively decreased the crack tip K of the former branches. The crack repropagated when K was further increased.

The crack arrest markings were reported in SCC tests performed under constant strain rate conditions and in the regions near final ductile fracture. For the same material and in the same solution, however, the crack arrest markings were absent if the test was conducted at a constant load lower than the yield strength [149]. The load *vs.* time curve and the current signal record did not show signs of discontinuity. This result suggests that the crack arrest markings often result from the imposed plastic deformation. The imposed strain rate cannot be the same as the SCC propagation velocity. If the imposed strain rate is lower than the propagation velocity, the propagation will be stopped by the reduction of crack tip strain due to the crack growth. A load drop thus occurs, as observed by Zhong *et al* [24]. On the other hand, if the imposed strain rate is higher, the large plastic deformation at the crack tip has the same effect as the load pulse. Thus, for either an imposed strain rate higher or lower than that associated with the SCC propagation velocity, similar crack arrest markings are produced. The propagation velocity should be anisotropic in anisotropic crystals. In some orientations, for example, in the {110}<110> single crystal of Cu-25Au, the crack arrest markings disappeared [236], probably due to the better matching of the imposed strain rate with the propagation velocity. Therefore, the appearance of crack arrest markings does not mean that the SCC crack propagation is necessarily discontinous. Their appearance may only demonstrate the adjustment of the crack propagation to the exterior mechanical restraint.

Because of the reasons mentioned in Section 7.3.1, the entire set of pulse traces were rarely observable on the fracture surface. Only a few regions were available to

calculate the crack propagation velocity v_m based on the crack front markings. Nevertheless, such a calculation was made, mainly in transgranular regions. The macroscopically measured velocity v_M in an annealed CT specimen of 70Cu-30Zn was 10 times larger than v_m, while in TN-DCB specimens, v_M could be 10^3 times larger than v_m. In 310 stainless steel v_M was similar to v_m. The smaller v_m in 70Cu-30Zn accounts for the time necessary for reinitiation. That suggests the SCC crack in 70Cu-30Zn either does not stop during normal propagation, or does not stop as long as the stoppage induced by load pulses, because adsorption is involved in cracking process. The similar v_m and v_M in 310 stainless steel implies the same time needed for hydrogen diffusion ahead of crack tip to induce the next cracking event in conditions with and without load pulses. The round corners of crack front markings and a little further crack reinitiation sites in 310 may be caused by this volume effect. On the other hand, the similar v_m and v_M suggests the reinitiation time after load pulses is quite short, since no inverse propagation was observed at the crack tip even though reinitiation was ahead of the crack front markings. This further indicates that adsorbed hydrogen is involved in the SCC of 310 stainless steel.

The general absence of crack arrest markings in the present study indicates that the process of transgranular SCC under constant load does not include crack tip blunting, although in some specific conditions, such as in δ–ferrite, crack arrest markings were found on transgranular facets (Fig. 4.8). It is the environmental effect involved in SCC that facilitates and localizes the crack tip slip on a few slip planes, thus prevents the general blunting. Transgranular SCC propagation may arrest for a while, probably at the point where the crack switches from one of {111} plane to another {111} plane, although the duration of such a stop can be very short. For intergranular SCC, the crack jump is probable, which is indicated by observed arrest lines in δ–ferrite and the apparent crystallographic propagation in 70Cu-30Zn. The jumping distance may be the interspacing between active slip planes. It is not clear from the observation carried out how far the crack jumps each time in 70Cu-30Zn, and how long it waits for the next jump.

Chapter 8

General Discussion

The crack tip SCC process on the atomic scale is probably impossible to observe directly. The SCC mechanisms, containing the crack tip environment-lattice interactions, therefore have to be deduced from the cracking kinetics and from the fractographic features, as well as from the environmental and metallurgical variables. Detailed discussions have been given in the previous chapters regarding the important experimental results in each chapter. Based on these discussions and the fractographic observations, this chapter will focus on the general SCC process, that is, the environmental effects on the crack tip dislocations, and how these interactions lead to SCC fractures which appear macroscopically brittle but are produced by microscopically localized slip.

8.1 THE ROLE OF HYDROGEN

As already discussed in Chapter 3 and Chapter 4, absorbed hydrogen from cathodic reactions at the SCC crack tip is involved in SCC fracture of austenitic stainless steels. Hydrogen-enhanced dislocation motion at the vicinity of the crack tip has been demonstrated by *in situ* TEM dislocation observations in austenitic stainless steels [54]. Such motion is also indicated in the present study by the SEM fractographic observations on the δ–ferrite phase in 316L stainless steel. The slip traces were observed on the δ–ferrite side of interfacial boundaries but were rarely present on the austenite side. It is the absorbed hydrogen that causes the ferrite phase, usually with a higher yield strength than the austenite, to become softer than the austenite. The slip traces on δ–ferrite grain boundaries and the transgranular cracking along slip planes both in the δ–ferrite and in the austenite suggest that localized slip plays a decisive role in the cracking.

8.1.1 Localized and planar slip caused by hydrogen

The presence of hydrogen in materials increases the dislocation mobility by decreasing the barriers to dislocation motion and causes a localized deformation region at the crack tip. This then results in a highly localized plastic fracture process which appears brittle due to the lack of general yielding. The localized plastic process is refined at the crack tip on a few slip planes. For fcc materials sensitive to transgranular SCC, the localized and planar slip behavior is expected, because most of these materials have a low stack fault energy. Hydrogen increases this planar slip tendency, since fewer slip traces [212] and a more planar dislocation distribution near the fracture surfaces [9] were observed in 304 stainless steel in hydrogen environment and during SCC fracture respectively. It was suggested [212] that the stronger bonding of hydrogen atoms with edge dislocations would tend to maintain dislocations in the edge configuration, making

cross slip of screw dislocation less likely and slip localized on a fewer slip planes in hydrogen-containing materials.

The above hypothesis may be appropriate for fcc materials, but it is not applicable to the SCC of δ–ferrite in 316L stainless steel. Cross slip at 154°C is not inhibited by hydrogen since it was observed in δ–ferrite during SCC. However, cross slip may occur in a shorter distance relative to the hydrogen-free ferrite. Mandziej [211] observed that hydrogen inhibits the annihilation (probably by cross slip) of different families of $\frac{1}{2}$<111> screw dislocation in the ferrite phase of a duplex stainless steel. Two screw dislocations, with different Burgers vectors on two close and parallel {110} planes, would interact to form a <100> edge jog at the intersection of cross slip planes of former $\frac{1}{2}$<111> screw dislocations. Because the jogging plane is not the cross slip plane of both screw dislocations, this jog is glissile on its slip plane but has sessile segments on two close and parallel {110} planes intersected by its slip plane. Such a dislocation structure would reduce the ability of cross slip and thus strain relief would be favored through the decohesion along slip planes in hydrogen-bearing ferrite.

8.1.2 Hydrogen-induced decohesion

The evidence of hydrogen-enhanced dislocation mobility and the SCC crystallography in stainless steels suggest that slip is a prerequisite for SCC fracture, which causes the dislocations piling up on slip planes and the fracture of slip planes by decohesion. The decohesion of slip planes needs a mechanical driving force to separate the atomic bonding, which will be discussed later. The separation may also be facilitated when the bond strength is reduced by hydrogen. This is the suggestion of hydrogen-induced decohesion theory which emphasizes that hydrogen reduces bond strengths and produces cleavage without slip. However, the well known {100} cleavage plane was not found in the crystallographic fracture in δ–ferrite by SCC. Instead the SCC crystallographic facets

were determined as slip planes in both fcc austenite and bcc δ–ferrite. As well, the fracture by PSCC had an average {100} plane but did not occur by a typical cleavage mechanism, since the microfacets appeared to correspond to slip planes. Since slip precedes fracture in SCC and slip is a structure conserving process, it would easily be missed unless a detailed microscopic investigation is performed. Due to the difficulty of direct measurement, there is no experimental result indicating that hydrogen decreases atomic bond strength or lattice potential. A theoretical calculation [237] indicated that locally inducing hydrogen atoms on {111} planes would reduce the bond strength of {111} planes and lead to fracture on those planes. Besides absorption at the SCC crack tip, the hydrogen concentration near slip planes is further increased by the movement of hydrogen-bearing dislocations, and the bonding of slip planes is very probably decreased. Such decohesion on slip planes was observed, even in the δ–ferrite with low hydrogen solubility (Fig. 4.13).

Furthermore, the extent of enhanced dislocation mobility and reduced bond strength by hydrogen should depend on the local hydrogen concentration at the crack tip. With lower hydrogen involved in PSCC of austenite, less dislocations are activated and carry hydrogen. The extent of the bond strength reduced by absorbed hydrogen probably is lower. Decohesion could only occur on a small scale and a higher stress needed to separate slip planes favors the formation of small, deformed microfacets. This is more evident in 310 stainless steel specimens, in which no δ-ferrite was present to help concentrate hydrogen in certain regions of austenite. The local hydrogen content at the crack tip should be lower than in the austenite near δ-ferrite in 316L stainless steel, so the PSCC fracture appeared less crystallographic. In the least crystallographic regions (Type III), microvoids formed by hydrogen-facilitated the nucleation of tearing dimples under a tensile stress. In such a case, the reduction of the bond strength by hydrogen is still possible.

Observed association of slip with the intergranular fracture in the δ–ferrite is another reason to say that hydrogen-induced decohesion is involved during SCC. The dislocation activity enhanced by hydrogen in the δ–ferrite grains often produced interfacial cracking instead of fracture along slip planes. This interfacial cracking could be initiated by the microcracks or slip steps on the δ–ferrite side of the interfacial boundary. Alternatively, interfacial boundary strength could also be reduced by the concentrated hydrogen due to the annihilation of dislocations at the interface and the easier hydrogen diffusion along the interface.

8.1.3 Hydrogen adsorption

That hydrogen is absorbed during SCC has been shown unambiguously by crack initiation sites ahead of the SCC crack tip in 316L stainless steel (Fig. 4.10). However, there is no experimental evidence indicating clearly whether adsorbed hydrogen plays a role during SCC. Since adsorption is the prerequisite for absorption [188], adsorbed hydrogen may also be involved in SCC. Very probably, adsorption helps the crack initiation on the slip planes by reducing the cohesive strength of interatomic bonds [237] exactly at the crack tip. This effect is consistent with the observation that transgranular SCC cracks propagate away from the crack tip both in the austenite and within the δ–ferrite. Compared with absorption, the influence of adsorption is less important during SCC. It was shown in Chapter 3 that the crystallographic cracking could occur in PSCC without adsorption, but the crystallographic cracking did not always appear in SCC specimens opened in solution. When the cracking was beyond the region with high hydrogen concentration C_{pscc}, ductile fracture occurred while adsorption was still expected.

8.2 ADSORPTION IN THE SCC CRACK TIP OF 70CU-30ZN

Mechanisms proposed to account for the SCC in Cu-Zn alloys are those associated with hydrogen embrittlement, surface film-induced cleavage, localized dissolution and adsorption. It is almost certain that hydrogen can be precluded from SCC of Cu-Zn alloys in a concentrated ammonia solution. The film-induced cleavage and the dissolution models which emphasize dissolution causing propagation cannot account well for the detailed SCC fractography. Hence, a mechanism of adsorption inducing fracture should be considered as an alternative. It is difficult, however, either to measure directly the effect of adsorption during SCC or to isolate adsorption from other related processes, such as dissolution and absorption. The understanding of the role of adsorption on SCC propagation of 70Cu-30Zn thus comes from theoretical calculations, deductions and simulations more than from experimental observations.

8.2.1 The adsorbate

Previous studies [4,100] as well as the present work have shown that the presence of oxygen is crucial to the SCC of 70Cu-30Zn in a concentrated ammonia solution. The adsorption of oxygen on many metal surfaces produces an incipient oxide film, which may prevent crack initiation. It was found [110] that the diffusion of cupric ammonia complex to the crack tip controls the stage II propagation in oxygenated ammonia solution. Thus the dissolution product in the presence of oxygen, cupric ammonia complex, is the probable adsorbate. However, studies of adsorption were focused at gas / solid or liquid / solid interfaces. Information on how an ionic adsorbate behaves at a metal interface has not been found in our literature research. In proposed adsorption mechanisms for Cu-Zn alloys [238,239], the critical damaging species was not identified.

To solve this problem, it is worthwhile to consider Hintz's thermodynamic approach [240]. He suggested that the ionic forms of the dissolution product in SCC could be discharged and subsequently interact with the crack tip as metal atoms. In this condition, the adsorption process at interfaces between ions and metals would be treated analogously to liquid or solid metal embrittlement. Chemisorption of these ions to the crack tip substrate will reduce the propagation energy. This work throws some light on the problem that the dissolution of copper is necessary to cause SCC, but dissolution alone does not explain the phenomenon of SCC. Although his work did not provide detailed information on the process of adsorption or of other requirements for an adsorbate, it did point out that for binary alloys immersed in a solution containing ions of a more noble component, the deposition of the more noble component is highly favored. Therefore, copper, or more precisely, a cupric complex in the SCC of 70Cu-30Zn in an oxygenated ammonia solution should be the adsorbate. The necessary presence of oxygen during SCC helps the formation of the cupric complex, but does not have a direct effect on cracking. Thermodynamically, similar adsorption of cuprous complex should have occurred during SCC in deoxygenated ammonia solution. It is not clear why such an adsorption does not cause apparent crack propagation. It is possible that without oxygen, the desorption process overwhelms the adsorption process and therefore no or very little cracking is obtained.

8.2.2 The effects of adsorption on the crack propagation of 70Cu-30Zn

The effects of adsorption on SCC were proposed [52,53,140] as either reducing the atomic bond strength or facilitating dislocation emission at the crack tip. In the following discussion, the synergistic effect of the two will be considered.

The crack propagation energy or surface energy is related to the bond strength by a simplified Griffith criterion for crack formation. It has been known [237] that {111}

planes have the lowest surface energy in Ni. If the adsorption occurs on {111} planes, the surface energy or the bond strength of these planes will be further lowered and preferential cracking will be favored. This crystallographically orientated adsorption is possible since the adsorption of sulfur atoms on nickel surface forms the strongest bonding on {111} planes compared with those on {100} and {110} planes [241].

Similar to the hydrogen-induced decohesion theory, the weakness of the traditional adsorption mechanisms is that they neglect the localized slip accompanying SCC. When employed on the {111} planes to agree with the observed microfractography, there remains the question of how the damaging species preferentially adsorbs on the intersections of {111} planes with the initially non-crystallographic crack tip. Uhlig [143] later suggested that the chemisorption may take place only on mobile dislocations. The interstitial or impurity atoms are attracted to dislocations and increase the chemical affinity of adsorbates to the dislocations. Being available for adsorption, dislocations should be emitted from the crack tip, which may be, as Lynch suggested [52,53], also facilitated by adsorption. Because of the dislocation movement on {111} planes, emerged steps are covered with adsorbates. The material in the vicinity of the step fractures due to the reduction of the bond strength, which provides an access for adsorbate to more dislocations. This further increases dislocation egress on these planes. Consequently, the influence range of adsorption is not limited to a few atomic layers from the surface, and the length of pileups as well as the number of dislocations involved in a pileup increase. This speculation is supported by the thermodynamic calculation of Oriani [242]. His theoretical analysis pointed out that adsorption can enhance both bond breakage and slip at the SCC crack tip.

For transgranular SCC, adsorption weakening the bond strength has an indirect but necessary effect on cracking. It allows more dislocations to be emitted from the crack tip, so that there are sufficient dislocations to form a pileup and decohesion on the slip plane.

Without decohesion, the alternating {111} microfacets should not form, which will be discussed later. For intergranular cracking, adsorption can induce grain boundary decohesion directly. Grain boundaries are often the preferential adsorption sites due to impurity segregation and preferential dissolution. At low K, not many dislocations are available at the crack tip to interact with the adsorbate. Without the stress concentration, the dislocation emission is much less on the surface, but the surface dissolution still allows adsorption to occur at grain boundary areas. Both of the situations favor intergranular fracture produced by adsorption-induced grain boundary decohesion. This is the reason that in annealed 70Cu-30Zn, intergranular and quasi-intergranular fracture (fracture locally follows slip planes in the vicinity of grain boundaries) appear at low K and in regions near the external surface.

8.3 LOCALIZED SLIP AND DECOHESION ON SLIP PLANES

The microfacets of transgranular SCC fracture in austenitic stainless steels (316 and 310) and in 70Cu-30Zn were identified as corresponding to {111} slip planes [2-5]. The crystallographic analysis of transgranular SCC in δ–ferrite in Chapter 5 also shows the cracking along {110} or {112} slip planes in this bcc phase. The variations of cracking patterns with crack tip K and with the dislocation density in 70Cu-30Zn demonstrate a close relationship between crack tip dislocations and cracking appearance. Moreover, interfacial and intergranular SCC was found associated with slip near grain boundaries in both fcc 70Cu-30Zn and bcc δ–ferrite restrained in austenitic stainless steel. All this evidence suggests that the crack tip slip makes a very important contribution to the SCC fracture, although the fracture surfaces appear brittle. How the localized slip acts to favor the cracking, however, is still not clear.

The contribution of crack tip slip to transgranular SCC fracture has been noticed by many investigators [9,52,53,56,148,149,151]. Different causes of crack tip slip were

proposed, but the result of this slip was quite similar in most of the interpretations, i.e., cleavage. Because the macroscopic crack plane is often {100} or {110}, the emission of dislocations on two symmetric slip planes intersecting the crack tip was considered to induce Lomar-Cottrell locks which block further slip and produce cleavage on a plane bisecting these two slip planes. Such an interpretation cannot account for the alternating slip planes observed during transgranular SCC. It has already been pointed out that the environment effects (absorption and adsorption of hydrogen in stainless steels and adsorption of cuprous complex in 70Cu-30Zn) facilitate localized slip, induce dislocation pileups and then cause decohesion along slip planes.

The linear elastic stress field of a dislocation pileup does not provide a sufficient driving force to "cleave" the slip plane. However, the dilatational core field of either edge or screw dislocations contains a normal stress component, which acts on the slip plane and helps fracture along this slip plane [160]. Combined with the weakening effect of the environment, the slip planes are separated, at least partially by this normal stress component because the SCC microfacets are generally consistent with the characteristics of cleavage except for being situated along slip planes. Also, large {111} slip planes were occasionally observed perpendicular to the tensile axis in SCC of annealed Cu-Zn alloys both at the initiation site [4] and during propagation (Fig. 6.6). The cleavage plane in fcc materials has not been clearly identified till now. There is evidence, however, that the cleavage of austenitic stainless steel containing high N at low temperature is associated with slip [1]. In the case of SCC, the dislocation sources are activated by the crack tip stress concentration, and more importantly, by the environmental effects which are unique to each specific system. To distinguish it from traditional cleavage which occurs in the orientation associated with minimum slip [147], the separation of slip planes by enhanced dislocation activity during SCC should be better termed as environment-induced decohesion, since the environment-enhanced localized slip and a stress normal to the slip plane are both involved in crack initiation and propagation.

According to Stroh's [150] calculation, a dislocation pileup will initiate a maximum normal stress on a plane approximately −70° to the pileup plane. This plane happens to be another {111} in fcc metals. Therefore, the environment-induced decohesion occurs in pair, by the non-linear dislocation core field on the pileup plane and by the linear elastic stress field on the plane with the maximum normal stress from the pileup. The crack propagates by repeating this process to form an alternating path along a pair of {111} planes in fcc materials. This is exactly the case of cracking in 70Cu-30Zn (Fig.8.1a). Dislocations on a {111} plane intersecting at the crack tip are activated by the adsorption of cupric complex. They pile up, inducing decohesion on the pileup plane and another {111} plane inclined with 109°. The two {111} planes intersecting with 109° forms a primary {110} plane which often appears at low K of SCC in 70Cu-30Zn. In stainless steels, absorbed hydrogen in lattice tends to occupy the larger tetrahedral interstitial sites centered on {100} planes (Fig. 8.1b). This tendency would favor the activation of dislocations on {111} planes closest to these sites and produce macroscopic {100} planes by alternating along the pyramid {111} facets of the tetrahedral interstitial sites. Moreover, the volume effect of hydrogen absorption could activate dislocations on a few slip planes further to the crack tip, Stroh's type stress concentration may not be a necessity to open the second slip planes during SCC in stainless steels. When the K increases, more slip planes operate at the crack tip, and the dislocation pileups become longer. As a result, four sets of {111} are observed on fracture surfaces and the primary facets become larger {111} microfacets in the high K regions. Because the two decohesion events follow different rules, the length of cracking on two alternating planes can be different. This explains the different propagation directions which are composed of {111} microfacets of different sizes.

The interstriation spacing is often of the order of one micron or less in fcc materials. This suggests that the slip at the crack tip enhanced by environment is very localized near the crack tip. This also indicates that the occurrence of decohesion on slip

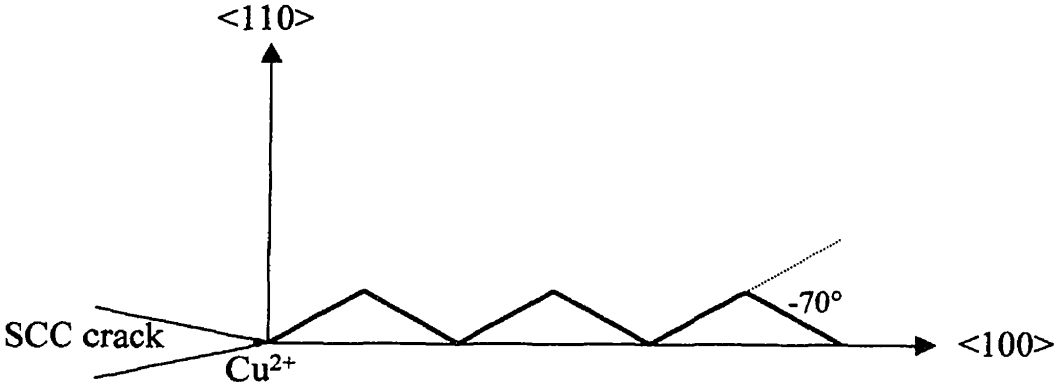

(a) Adsorption facilitates slip on a {111} plane at the SCC crack tip, resulting a {110} primary facet by decohesion on this {111} plane and on the {111} plane inclined -70°.

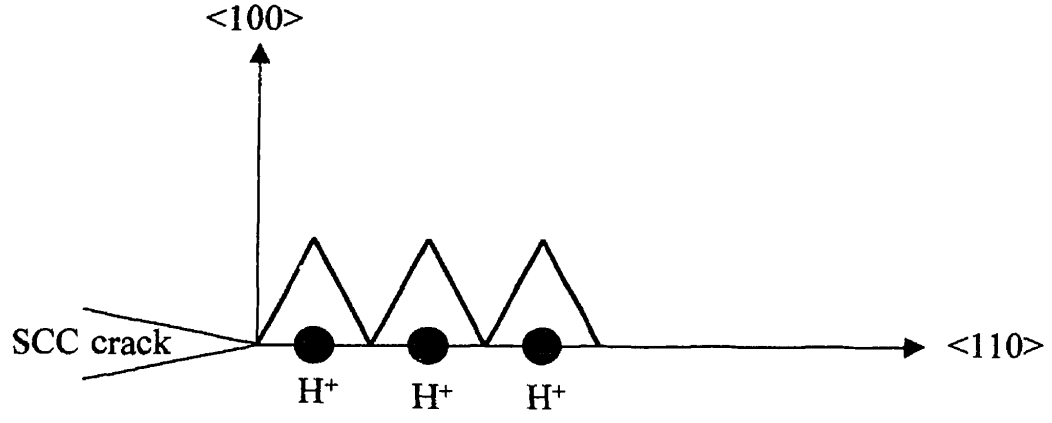

(b) Absorbed hydrogen in tetrahedral interstitial sites on {100} planes facilitates slip ahead of the SCC crack tip, resulting in a {100} primary facet by decohesion on {111} planes surrounding these tetrahedral interstitial sites.

Figure 8.1 Schematic illustration of the SCC crystallography in (a) 70Cu-30Zn and (b) stainless steels.

planes needs a certain number of dislocations to form a certain length of pileup and a certain amount of stress concentration on the slip planes. Without decohesion, the cracking along alternating slip planes cannot be interpreted. Shear stress is possible to cause fracture on slip planes, but the alternation between the two slip planes is not predicted by the shear. Some mechanisms based on environment-enhanced shear at the SCC crack tip considered [52,53,56,151] that the Stroh pileup model [150] might be involved with shear. It is very unlikely, however, that the fracture is completed through a shear-decohesion combination under monotonic loading.

Cracking along alternating slip planes requires only *one set* of slip planes activated at one time instead of two symmetric ones. This requirement can be achieved by the interaction of dislocations with the environment. For example, adsorption can cause an anisotropic change of surface stress in crystallographic materials [242], which would allow only one slip plane to reach the cracking criteria at one moment. If cracking occurs simultaneously on two symmetric slip planes at the crack tip, the crack opening displacement will become large. Blunting is unavoidable, as described in Gerberich [217,218] and Lichter's models [148,149]. This is not the case for transgranular SCC fracture in fcc materials. The crack alternating along two different slip planes prevents the crack tip from blunting. Therefore, crack arrest marks are generally absent in constant load tests. It is also impossible that two symmetric slip planes alternate their orientations independently along slip planes to keep the crack tip sharp. If so, the fracture surfaces will not interlock but rather be mirror matching.

For bcc δ–ferrite, the microfacets of transgranular fracture are not as symmetric as in austenite. Their size and orientations are more random. In Chapter 4, it was suggested that such an aspect is due to the slip and cross slip of screw dislocations at the crack tip. The correspondence of slip and cross slip and transgranular microfacets was well shown in Fig. 4.4. The frequently appeared transgranular feature, cracking along primary {110}

planes inclined approximately 45° to the tensile axis (Fig. 3.3), is also in agreement with the slip and cross slip of screw dislocations on these primary planes. Because the primary {110} planes make an angle of approximately 45° to the tensile axis and to the macroscopic SCC crack front in δ–ferrite, they are situated in the most favored position for dislocation movement under the maximum shear stress in the plane strain region. The screw dislocations emitted from the crack tip on those planes create a Mode III deformation at the macroscopic crack front. Therefore, the local propagation directions observed often make a large angle the macroscopic crack propagation direction. Cross slip combined with decohesion on the primary {110} planes produce both microfacets and incompatible deformation on interfaces. The latter may induce interfacial cracking (Fig.3.3) to relieve the strain before new transgranular crack is initiated on another primary {110} plane. It is also possible that several primary {110} planes form simultaneously at the main crack front then link together by short interfacial cracking. In either case, cross slip occurs separately on each primary plane and interfaces act as sinks to absorb dislocations. Since hydrogen inhibits the annihilation of screw dislocations with different Burger vectors [211], serrations on river lines could be formed by cross slip and by decohesion of dislocations with Burgers vectors different from those which produce the larger microfacets.

This environment-induced decohesion model can explain very well the microfractography of transgranular SCC either in fcc materials and in bcc δ–ferrite. As well, no inconsistencies are encountered when applying it to intergranular SCC. The observations of interfacial fracture in the δ–ferrite in 316L stainless steel suggest that it was produced by microcrack initiation and by interfacial decohesion though enhanced dislocation movement primarily on the δ–ferrite side of the interfaces. In 70Cu-30Zn, some of the intergranular SCC fracture were observed by locally following slip planes in the vicinity of grain boundaries. In areas of *true* intergranular fracture, grain boundaries may undergo decohesion at the intersections of slip planes with the grain boundaries,

which are the sites of strong adsorption. This process is difficult to verify, but is suggested as probable by the crystallographic intergranular crack front (Fig. 7.9). The intergranular SCC in 70Cu-30Zn essentially occurs at low K and in the near-surface regions. These are the conditions not favorable for long distance slip but the grain boundary decohesion could be induced by the environment-enhanced dislocation mobility in the vicinity of the grains. It is the environment that enhances dislocation movement on the localized slip planes. This localized slip induces decohesion of slip planes, resulting in transgranular fracture on alternative slip planes and intergranular fracture initiated by the slip close to the grain boundary. Therefore, environment-enhanced dislocation mobility and the consequent decohesion is the intrinsic driving force for SCC.

Conclusions

1. Crystallographic cracking was obtained in PSCC overload tensile fracture of 316L and 310 stainless steels. This crystallographic cracking started at times at the previous SCC crack tips and at times ahead of the previous SCC crack tips. Within a certain distance from the previous SCC crack tip, the crystallographic cracking initiated in the δ–ferrite contained in 316L stainless steel ahead of the previous SCC crack tip. But in the austenite, it only appeared at the previous SCC crack tip, or in areas surrounding fractured δ–ferrite platelets. In austenitic 310 stainless steel, the crystallographic cracking presented in isolated regions ahead of the previous SCC crack tip. Most of these regions were on a plane making an angle of approximately 45° to the tensile stress and near the composition inhomogeneity. PSCC crystallographic cracking also occurred ahead of the fatigue crack tip which was used to distinguish the PSCC fracture from SCC crystallographic cracking. It is the absorbed hydrogen from the SCC tests that produces crystallographic fracture during PSCC in ductile stainless steels at room temperature.

2. In 316L stainless steel, the PSCC crystallographic cracking in δ–ferrite appeared on the plane perpendicular to the tensile axis. Its cleavage-like appearance is very similar to the crystallographic cracking produced by hydrogen. The microfacets in the PSCC of austenite were smaller and more deformed than those in SCC. Otherwise, both fracture have very similar cracking aspects. The PSCC in 310 stainless steel was not a very typical crystallographic cracking. The microfacets were either accompanied by much plastic deformation or were linked by microvoids. In some regions the microvoids were smaller than the neighboring dimples. These microfractographic variations apparently result from different local hydrogen concentrations in different regions. Higher hydrogen concentration produces more crystallographic features.

3. Slow displacement rate tensile tests in the 154°C $MgCl_2$ aqueous solution did not always produce crystallographic cracking. Ductile fracture in solution was observed at some distance ahead of the previous SCC crack produced under constant load. The size of the PSCC crystallographic cracking in 316L stainless steel increased with increasing K at which SCC was stopped, with increasing time interval between the SCC tests and the overload tensile fracture and with decreasing tensile displacement rates. The size of PSCC cracking in 310 stainless steel was approximately the same for all the test conditions, but generally smaller than that in 316L stainless steel. Absorbed hydrogen at the SCC crack tip can be transported by the gliding of dislocations during overload tensile tests. The presence of δ–ferrite phase in 316L stainless steel increases the size of PSCC crystallographic cracking zones.

4. The change of tensile properties of 316 stainless steel ribbons, after cathodic charging or after immersion in boiling $MgCl_2$ solution, showed the same tendencies as for ribbons cathodically charged in H_2SO_4 solution. The elongation increased with increasing aging time before the tensile fracture in air at room temperature. Annealing of the ribbons before they came in contact with $MgCl_2$ solution also increased the elongation, while prestrain

decreased the elongation. These results demonstrate that hydrogen can evolve from $MgCl_2$ solution either during pitting or during SCC at the free corrosion potential.

5. High hydrogen content near surfaces of ribbons cathodically charged in boiling $MgCl_2$ solution produced large crystallographic facets or intergranular cracking. Small deformed facets, like those obtained in PSCC crystallographic cracking in bulk specimens, were produced by lower hydrogen contents beneath the surface regions of cathodically charged ribbons, as well as in the areas between the SCC and the ductile fracture in ribbons immersed in boiling $MgCl_2$ solution. Some {111} facets were found in hydrogen-charged ribbons. The similar fractographic features and the similar cracking crystallography in ribbons of both hydrogen-charged and immersed in the $MgCl_2$ solution confirm that hydrogen is involved during SCC of stainless steels in boiling $MgCl_2$ solution. It also suggests that hydrogen-dislocation interaction is essential both for SCC and for hydrogen-induced cracking

6. The SCC cracking of the δ–ferrite phase in 316L stainless steel presented interfacial fracture along the δ–γ interfaces and transgranular fracture within the δ–ferrite. Many wavy slip traces often appeared on the grain boundaries of the δ–ferrite, which corresponded to the path of the transgranular fracture. Very often, the transgranular fracture occurred on an average plane approximately 45° to the tensile axis. Usually the serrations on river lines were very small. Striations perpendicular to the river lines were generally absent during transgranular SCC in δ–ferrite. These characteristics indicate the contribution of screw dislocations to this transgranular SCC.

7. Besides the wavy slip traces, many crack arrest lines were also found on the grain boundaries of the δ–ferrite. These crack arrest lines showed similar trends with the wavy slip traces, indicating that both correspond to instantaneous crack fronts during interfacial SCC propagation. The interfacial SCC propagation appears discontinuous.

The crack arrest lines and the wavy slip traces existed almost everywhere on the δ–ferrite grain boundaries, but rarely appeared on the corresponding austenite grain boundaries at the δ–γ interfaces. This indicates that the δ–ferrite is softened by the hydrogen absorbed from the SCC reactions. Crack initiation ahead of the crack front was occasionally observed on the δ–ferrite grain boundaries.

8. The crystallography of transgranular SCC and PSCC in δ–ferrite was determined by the measurement of the texture of the δ–ferrite phase, by the photogrammetric analysis of the fracture surfaces and by the EBSPs obtained from the PSCC regions. The average cracking planes in δ–ferrite during SCC is {110} with a macroscopic propagation direction of <110>. The microfacets composed of the average cracking planes and the serrations on river lines were determined as {110} and {112}. The crystallography of PSCC in δ-ferrite were determined as {100}<100>, {100}<110> and (100}<210>, but the {100}planes are made up of many microfacets which should correspond to slip planes.

9. The SCC of 70Cu-30Zn in concentrated non-tarnishing ammonia solution showed both intergranular and transgranular fracture in the annealed condition. The intergranular fracture tended to occur in lower K regions, while the transgranular fracture tended to occur in higher K regions. The intergranular fracture was also favored in the near surface regions where the presence of dissolved oxygen is plentiful. Better surface protection and a large specimen thickness reduced the amount of intergranular fracture, particularly in the near-surface regions. Temporarily increasing the crack tip K by superimposed load pulses can induce local transgranular fracture. In the prestrained condition, the extent of deformation prior to the SCC tests influences the fracture patterns. Heavy cold work increased greatly the amount of transgranular fracture and changes the intergranular fracture to quasi-intergranular fracture. Also, the textured river line patterns were apparently not influenced by the increase of crack tip K.

10. The intergranular propagation was more rapid than the transgranular propagation during SCC in 70Cu-30Zn in the concentrated ammonia solution employed. The transition in cracking patterns, from intergranular fracture to quasi-intergranular fracture or to transgranular fracture, occurred following the slip traces on the grain boundaries. The intergranular crack front, indicated by the load pulse traces on grain boundaries, showed in some locations it at least locally coincided with slip traces on the grain boundaries. Similar to the transgranular SCC, the intergranular propagation also appears associated with localized slip.

11. The relationship of SCC crack propagation velocities with the crack tip K was tentatively measured by inducing a compliance measurement method on CT specimens during constant load SCC tests. The crack propagation velocity appeared to increase with increasing K up to ~ 20 MPa$\sqrt{m}$ in the annealed condition, while the plateau region where the crack propagation velocity independent of K was more clear in the cold worked condition. This is consistent with the fractographic observations that the SCC propagation is closely associated with the dislocation configuration at the crack tip.

12. The SCC of 70Cu-30Zn cannot occur in deoxygenated ammonia solution dissolved with 3.6 g/l Cu_2O and 8 g/l Cu powder. The cracking did not initiate in the notched specimen and did not have any apparent propagation in precracked specimens. The presence of oxygen and the anodic dissolution of Cu to Cu^{2+} appear necessary for SCC in this system. The propagation reinitiations after a short time stop imposed by small load pulses in the non-tarnishing solution were observed at the crack front lines under the resolution of the SEM employed. The most probable effect of oxygen and therefore of Cu^{2+} ions on the SCC cracking is adsorption.

13. The crack front marks produced by the superimposed load pulses in 310 stainless steel and in 70Cu-30Zn differed from the crack arrest marks spontaneously produced during constant load SCC. But both of them were quite crystallographic on appearance. The occurrence of the crack arrest marks is accompanied with higher plastic deformation at the crack tip, such as in regions with crack branches and at high K. It is not a general phenomenon during SCC propagation under constant load.

14. The environment-dislocation interactions and their effects on the SCC fracture were considered. The present study indicates that the absorption of hydrogen in the system of stainless steels / $MgCl_2$ solution and the adsorption of Cu^{2+} ions in the system of 70Cu-30Zn / ammonia solution are very important in producing these SCC fractures. Although the environment-dislocation interaction is specific in each system, macroscopically brittle SCC fracture is produced by a localized slip process at the crack tip. The mobility of dislocations is enhanced by the specific environment, leading to the piling up of dislocations at the SCC crack tip. Combined with the weakening effect of the environment to the bond strength, localized slip will induce decohesion, either by the core field or by the elastic stress field of dislocation pileups, on alternating slip planes. Intergranular SCC fracture is also produced by the environmentally enhanced dislocation movement near the grain boundary and the resultant decohesion very near the grain boundary.

References

1. DICKSON, J. I., VOGT, J.-B., MESSAI, A. H. and FOCT, J., A fractographic study of the low temperature fracture of a high Mn, high N austenitic stainless steel. George R. Irwin Symposium on Cleavage Fracture, Kwai S. Chan ed., TMS, 277-284, 1997.

2. DICKSON, J.I., GROULX, D. and LI, SHIQIONG, The fractography of stress corrosion cracking of 310 stainless steel: Crystallographic aspects and the influence of the stress intensity factor. Mat. Sci. Eng., 94, 155-173, 1987.

3. LI, SHIQIONG, DICKSON, J.I and BAILON, J. P., The influence of the stress intensity factore on the fractography of stress corrosion cracking of 316 stainless steel. Mat. Sci. Eng., A119, 59-72, 1989.

4. DICKSON, J. I., LI, SHIQIONG, BAILON, J. P. and TROMANS, D., The fractography of transgranular SCC in f.c.c. metals. Parkins Symposium on Fundamental Aspects of Stress Corrosion Cracking, S. M. Bruemmer, E. I. Meletis, R. H. Jones, W. W. Gerberich, F. P. Ford and R. W. Staehle eds., TMS, 303-322, 1992.

5. CHAMBREUIL-PARET, A., CHATEAU, J. P. and MAGNIN, T., Influence of the slip conditions on the stress corrosion cracking microprocesses in fcc materials. Scripta Mater., 37, 1337-1343, 1997.

6. KAUFMAN, M. J. and FINK, J. L., Evidence for localized ductile fracture in the "brittle" transgranular stress corrosion cracking of ductile f.c.c. alloys. Acta Metall., 36, 2213-2228, 1988.

7. KASUL, B., WHITE, C. L. and HELDT, L. A., Relationship between plasticity and stress corrosion cracking. Environmental-Induced Cracking of Metals, R. P. Gangloff and M. B. Ives eds., Houston, TX, NACE, 219-222, 1990

8. KRAMER, I. R., WU, B. and FENG, C. R., Dislocation distribution in transgranular stress corrosion cracking of naval brass. Mat. Sci. Eng., 82, 141-150, 1982.

9. JAIN, S., MAREK, M., HOCHMAN, R. F. and MELETIS, E. I., A mechanistic study of transgranular stress corrosion cracking of Type 304 stainless steel. Met. Trans., 22A, 1453-1461, 1991.

10. MELETIS, E. I., LIAN, K. and HUANG, W., Vacancy-dislocation interactions and transgranular stress corrosion cracking. Corrosion--Deformation Interactions CDI 92, T. Magnin and J. M. Gras eds., 69-81, 1992.

11. OHR, S. M., Electron microscope studies of dislocation emission from cracks. Scripta Metall., 20, 1501-1505, 1986.

12. CHEN, Q., CHU, W-Y., and HSIAO, C-M., The *in-situ* observations of microcrack nucleation and bluntness in ductile fracture. Scripta Metall. Mater., 30, 1355-1357, 1994.

13. OHR, S. M., An electron microscope study of crack tip deformation and its impact on the dislocation theory of fracture. Mat. Sci. Eng., 72, 1-35, 1985.

14. ROBERTSON, I. M. and BIRNBAUM, H. K., An HVEM study of hydrogen effects on the deformation and fracture of nickel. Acta Metall., 34, 353-366, 1986.

15. TABATA, T. and BIRNBAUM, H. K., Direct observations of hydrogen enhanced crack propagation in iron. Scripta Metall., 18, 231-236, 1984.

16. SHIH, D., ROBERTSON, I. M. and BIRNBAUM, H. K., Hydrogen embrittlement of alpha titanium alloys — *in situ* TEM studies. Acta Metall., 36, 111-124, 1988.

17. BOND, G., ROBERTSON, I. M. and H. K. Birnbaum, The influence of hydrogen on deformation and fracture processes in high strength aluminum alloys. Acta Metall., 35, 2289-2296, 1987.

18. BEGGS, D. V., HAHN, M. T. and PUGH, E. N., Recent observations on the propagation of stress-corrosion cracks and their relevance to proposed mechanisms of SCC. Hydrogen Embrittlement and Stress Corrosion Cracking, R. Gibala and R. F. Hehemann eds., Metals Park, ASM, p.181, 1984.

19. BEAVERS, J. A. and PUGH, E. N., The propagation of transgranular stress corrosion cracks in admiralty metal. Met. Trans., 11A, 809-820, 1980.

20. NEWMAN, R. C. and SIERADZKI, K., Correlation of acoustic and electrochemical noise in the stress corrosion cracking of α-brass. Scripta Metall., 17, 621-624, 1983.

21. BURSLE, A. J. and PUGH, E. N., Mechanisms of Environment Sensitive Cracking of Materials, The Metals Society, London, p.471, 1977.

22. HAHN, M. T. and PUGH, E. N., Application of load pulsing to the fractographic study of stress corrosion cracking of austenitic stainless steels. Fractography and Materials Science, ASTM STP 733, L. N. Gilbertson and R. D. Zipp eds., ASTM, 413-427, 1981.

23. DESAI, V., FRIEDERSDORF, F. and SHAW, T., Study of transgranular stress corrosion cracking propagation in austenitic steels by load-pulsing method. Environmental-Induced Cracking of Metals, R. P. Gangloff and M. B. Ives eds., Houston, TX, NACE, 549-553, 1990.

24. ZHONG, L., FLANAGAN, W. F. and LICHTER, B. D., The competitive role of slip and dissolution in transgranular stress corrosion cracking. Corrosion–Deformation Interactions CDI 92, T. Magnin and J. M. Gras eds., 309-322, 1992.

25. CASKEY, Jr, G. R., Hydrogen effects in stainless steels. Hydrogen Degradation of Ferrous Alloys, R. A. Oriani, J. P. Hirth and M. Smialowski eds., Noyes Publications, N.J.07656, 822-862, 1985.

26. STAFFORD, S. W. and MCLELLAN, R. B., The thermodynamic properties of the Fe-Ni-H ternary system. Acta Metall. 24, 553-558, 1976.

27. COLDWELL, D. M. and MCLELLAN, R. B., Thermodynamic properties of Fe-Cr-H ternary solutions. Acta Metall. 23, 57-61, 1975.

28. BIRNBAUM, H. K., Mechanisms of hydrogen-related fracture of metals. Environmental-Induced Cracking of Metals, R. P. Gangloff and M. B. Ives eds., Houston, TX, NACE, 21-29, 1990.

29. GIBALA, R. and KUMNICK, A. J., Hydrogen trapping in iron and steels. Hydrogen Embrittlement and Stress Corrosion Cracking, R. Gibala and R. F. Hehemann eds., ASM, Metal Park, Ohio, 65-77, 1984.

30. HIRTH, J. P., Effects of hydrogen on the properties of iron and steels. Met. Trans., 11A, 861-890, 1980.

31. BUCHHOLZ, J., VOLKL, J. and ALEFEL, G., Anomalonsly small elastic curie constant of hydrogen in tantalum. Phys. Rev. Lett., 30, 318-321, 1973.

32. HIRTH, J. P., Hydrogen-defect interactions. Hydrogen Degradation of Ferrous Alloys, R. A. Oriani, J. P. Hirth and M. Smialowski eds., Noyes Publications, N.J.07656, 131-139, 1985.

33. BASTIEN, P. and AZOU, P., C. R. Acad. Sci. Paris, 232, p.1845, 1951.

34. KURKELA, M. K. and LATANISION, R. M., The effect of plastic deformation on the transport of hydrogen in nickel. Scripta. Metall., 13, 927-932, 1979.

35. DONOVAN, J. A., Sorption of trituim by nickel during plastic deformation. Met. Trans., 7A, 145-149, 1976.

36. HIRTH, J. P. and JOHNSON, H. H., On the transport of hydrogen by dislocations. Atomistics of Fracture, R. M. Latanision and J.R.Pickins eds., 771-787, 1981.

37. KITAGAWA, H. and KOJIMA, Y., Diffusion of hydrogen near an elasto-plastically deformed crack tip. AtomisticS of Fracture, R. M. Latanision and J.R.Pickins eds., 799-811, 1981.

38. SOFRONIS, P. and MCMEEKING, R. M., Numerical analysis of hydrogen transport near a blunting crack tip. J. Mech. Phys. Solids, 37, 317-350, 1989.

39. WU, S., CHEN, L. and LIU, M., Acta Metallurgica Sinica, 26, p.A86, 1990.

40. TURNBULL, A., FERRISS, D. H. and ANZAI, H., presented in the conference of CDI 1996.

41. MATSUI, H., KIMURA, H. and MORIYA, S., The effect of hydrogen on the mechanical properties of high purity iron: I. Softening and hardening of high purity iron by hydrogen charging during tensile deformation. Mater. Sci. Eng., 40, 207-216, 1979.

42. ORIANI, R. A. and JOSEPHIC, P. H., Hydrogen-enhanced local relaxation in a deformed medium-carbon steel. Acta Met., 27, 997-1005, 1979.

43. LEE, T. D., GOLDENBERG, T. and HIRTH, J. P., Hydrogen and plastic instability in deformed, spheroidized 1090 steel. Fracture 1977, 2, D. M. R. Taplin ed., Pergamon, Oxford, 243-247, 1977.

44. MORIYA, S., MATSUI, H. and KIMURA, H., The effect of hydrogen on the mechanical properties of high purity iron: II. Effect of quenched-in hydrogen below room temperature. Mater. Sci. Eng., 40, 217-225, 1979.

45. LUNARSKA, E., Effects of hydrogen on the plastic properties of iron single crystals, whisers and polycrystals. Hydrogen Degradation of Ferrous Alloys, R. A. Oriani, J. P. Hirth and M. Smialowski eds., Noyes Publications, N.J.07656, 321-352, 1985.

46. BIRNBAUM, H. K., Hydrogen effects on deformation – Relation between dislocation behavior and the macroscopic stress-strain behavior. Scripta Metall. Met., 31, 149-153, 1994.

47. WESTLAKE, D. G., A generalized model for hydrogen embrittlement. Trans. ASM, 62, 1000-1006, 1969.

48. GAHR, S., GROSSBECK, M. L., and BIRNBAUM, H. K., Low temperature hydrogen embrittlement of niobium II — microscopic observations. Acta Metall., 25, 135-147, 1977.

49. NARITA, N., ALTSTETTER, C. J. and BIRNBAUM, H. K., Hydrogen related phase transitions in austenitic stainless steels. Met. Trans., 13A, 1355-1365, 1982.

50. LOUTHAN, Jr, M. R., DONOVAN, J. A. and RAWL, Jr, D. E., Effect of high dislocation density on stress corrosion cracking and hydrogen embrittlement of Type 304L stainless steel. Corrosion, 29, 108-111, 1973.

51. BEACHEM, C. D., A new model for hydrogen-assisted cracking (hydrogen embrittlement). Met. Trans., 3, 437-451, 1972.

52. LYNCH, S. P., Environmentally assisted cracking: Overview of evidence for an adsorption-induced localised-slip process. Acta Metall., 36, 2639-2661, 1988.

53. LYNCH, S. P., A fractographic study of hydrogen assisted cracking and liquid-metal embrittlement in pure magnesium. J. Mater. Sci., 21, 692-704, 1986.

54. ROZENAK, P., ROBERTSON, I. M. and BIRNBAUM, H. K., HVEM studies of the effects of hydrogen on the deformation of AISI Type 316 austenitic stainless steel. Acta Metall. Mater., 38, 2031-2040, 1990.

55. BIRNBAUM, H. K., Hydrogen related fracture of metals. Atomistics of Fracture, R. M. Latanision and J.R.Pickins eds., 733-769, 1981.

56. MAGNIG, T., A unified model for trans and intergranular stress corrosion cracking. Corrosion–Deformation Interactions CDI92, T. Magnin and J. M. Gras eds, 27-41, 1992.

57. LYNCH, S. P., Liquid-metal embrittlement in an Al 6% Zn 3% Mg alloy. Acta Metall., 29, 325-340, 1981.

58. PFEIL, L. B., Proc. Roy. Soc., London, A112, p.182, 1926.

59. HOHMBERG, R. P., BARNETT, W. J., and TROIANO, A. R., Delayed failure in hydrogen embrittlement. Trans. ASM, 47, 892-923, 1955.

60. TROIANO, A. R., The role of hydrogen and other interstitials in the mechanical behavior of metals. Trans. ASM, 52, 54-80, 1960.

61. ORIANI, R. A., Hydrogen embrittlement of steels. Ann. Rev. Mater. Sci., 8, 327-357, 1978.

62. ORIANI, R. A., A decohesion theory for hydrogen-induced crack propagation. Stress Corrosion Cracking and Hydrogen Embrittlement of Iron-base Alloys, R. W. Staehle, J. Hochmann, R. D. McCright and J. E. Slater eds., NACE, Houston, TX, 351-357, 1977.

63. ZAPFFE, C. A. and SIMS, C. E., Hydrogen embrittlement, internal stress and defects in steel. Hydrogen Damage, C. D. Beachem ed., ASTM, Metals Park, OH, 13-59, 1977.

64. TETELMAN, A. S., Recent development in classical (internal) hydrogen embrittlement. Hydrogen in Metals, I. M. Bernstein and A. W. Thompson eds, ASM, Metal Park, OH, 17-34, 1974.

65. TETELMAN, A. S., The mechanism of hydrogen embrittlement in steel. Fundamental Aspects of Stress Corrosion Cracking, R. W. Staehle, A. J. Forty and D. Van Rooyen eds., Houston, TX, NACE, 446-460, 1969.

66. TIEN, J. K., THOMPSON, A. W., BERNSTEIN, I. M., and RICHARDS, R. J., Hydrogen transport by dislocation. Met. Trans., 7A, 821-829,1976.

67. TIEN, J. K., Diffusion and the dislocation sweeping mechanism for hydrogen transport. Effect of Hydrogen on Behavior of Matetials, I. M. Bernstein and A. W. Thompson eds., TMS-AIME, Warrendale, PA, 309-325, 1981.

68. JOHNSON, H. H. and HIRTH, J. P., Internal hydrogen supersaturation produced by dislocation transport. Met. Trans., 7A, 1543-1548, 1976.

69. BERNSTEIN, I. M. and THOMPSON, A. W., The importance of transient effects resulting from dislocation transport of hydrogen. Atomistics of Fracture, R. M. Latanision and J. R. Pickins eds., 813-821, 1981.

70. PAES DE OLIVEIRA, C., AUCOUTURIER, M. and LACOMBE, P., Hydrogen trapping in b.c.c. Fe-Cr alloys as studied by microautoradiography. Corrosion, 36, 53-59, 1980.

71. BAKER, H. R., BLOOM, M. C., BOLSTER, R. N. and SINGLETERRY, C. R., Corrosion, 26, p.420, 1970.

72. GREENE, N. D. and JUDD, G., Relation between anodic dissolution and resistance to pitting corrosion. Corrosion, 21, 15-18, 1965.

73. EDELEANU, C., JISI, 173, p.140, 1953.

74. NEWMAN, R. C. and MEHTA, A., Stress corrosion cracking of austenitic steels. Environmental-Induced Cracking of Metals, R. P. Gangloff and M. B. Ives eds., Houston, TX, NACE, 489-509, 1990.

75. LATANISION, R. M. and STAEHLE, R. W., Stress corrosion cracking of iron-nickel-chromium alloys. Fundamental Aspects of Stress Corrosion Cracking, R. W. Staehle, A. J. Forty and D. Van Rooyen eds., NACE, Houston, TX, 214-295, 1969.

76. TSUJIKAWA, S., SHINOHARA, T. and HISAMATSU, Y., Corrosion Cracking, V. S. Goel ed., ASTM, Philadelphia, PA., p.35, 1985.

77. JONES, R. L., Potential and chloride effects in the stress corrosion cracking of Type 304 stainless steel in 290°C water. Corrosion, 31, 424-431, 1975.

78. ANDRESEN, P. L. and DUQUETTE, D. J., The effects of dissloved oxygen, chloride ion and applied potential on the stress corrosion cracking behavior of Type 304 stainless steel in 290°C water. Corrosion, 36, 409-415, 1980.

79. UHLIG, H. H. and LINCOLN, Jr, J., Chemical factors affects stress corrosion cracking of 18-8 stainless steels. J. Electrochem. Soc., 105, 325-332, 1958.

80. SMIALOWSKI, M. and RYCHICK, M., Corrosion, 16, p.359t, 1960.

81. RUSSELL, A. J. and TROMANS, D., A fracture mechanics study of stress corrosion cracking of Type-316 austenitic steel. Met. Trans., 10A, 1229-1238, 1979.

82. BARNARTT, S. and VAN ROOYEN, D., Anodic behavior of austenitic stainless steels and susceptibility to stress corrosion cracking. J. Electrochem Soc., 108, 222-229, 1961.

83. KOHL, H., Corrosion, 23, p.39, 1967.

84. SMITH, J. A., PETERSON, M. H. and BROWN, B. F., Electrochemical conditions at the tip of an advancing stress corrosion crack in AISI 4340 steel. Hydrogen Damage, C. D. Beachem ed., ASTM, Metals Park, OH, 255-258, 1977.

85. NIELSEN, N. A., Observations and thoughts on stress corrosion mechanisms. Hydrogen Damage, C. D. Beachem ed., ASTM, Metals Park, OH, 219-224, 1977.

86. QIAO, L., MAO, X. and CHU, W., The role of hydrogen in stress corrosion cracking of austenitic stainless steel in hot $MgCl_2$ solution. Met. Trans., 26A, 1777-1784, 1995.

87. HOCHMANN, J., DESESTRET, A., JOLLY, P. and MAYOUD, R., Properties of high-chromium ferritic stainless steels and austeno-ferritic stainless steels. Stress Corrosion Cracking and Hydrogen Embrittlement of Iron-Base Alloys, R. W. Staehle, J. Hochmann, R. D. McWright and J. E. Slater eds., NACE, Houston, TX, 956-1002, 1977.

88. SHIMODAORA, S., TAKANO, M., TAKIZAWA, Y. and KAMIDE, H., Mechanisms of transgranular stress corrosion cracking of duplex and ferritic stainless steel. Stress Corrosion Cracking and Hydrogen Embrittlement of Iron-Base Alloys, R. W. Staehle, J. Hochmann, R. D. McWright and J. E. Slater eds., NACE, Houston, TX, 1003-1015, 1977.

89. BARTERI, M., MANCIA, F., TAMBA, A. and MONTAGNA, G., Engineering diagrams and sulphide stress corrosion cracking of duplex stainless steels in deep sour well environment. Corr. Sci., 27, 1239-1250, 1987.

90. OLTRA, R. and DESESTRET, A., Anodic dissolution and hydrogen embrittlement during mechanical depassivation of the ferritic phase of a duplex stainless steel in chloride solution containing H_2S. Environmental-Induced Cracking of Metals, R. P. Gangloff and M. B. Ives eds., Houston, TX, NACE, 207-211, 1990.

91. HOAR, T. P. and BOOKER, C. J. L., The electrochemistry of the stress-corrosion cracking of alpha brass. Corr.Sci., 5, 821-840, 1965.

92. JOHNSON, H. E. and LEJA, J., Corrosion, 22, p.178, 1966.

93. PUGH, E. N., CRAIG, J. V. and SEDRIKS, A. J., Stress-corrosion cracking of copper, sliver and gold alloys. Fundamental Aspects of Stress Corrosion Cracking, R. W. Staehle, A. J. Forty and D. Van Rooyen eds., NACE, Houston, TX, 118-150, 1969.

94. BERTOCCI, U., Mass transfer phenomena and equilibria in the corrosion of copper and brass in ammonia solution. Electrochimica Metallorum, 3, 275-280, 1968.

95. PUGH, E. N., The mechanism of stress corrosion cracking of alpha-brass in aqueous ammonia. The Theory of Stress Corrosion Cracking in Alloys, J. C. Scully ed., NATO, Brussel, 418-440, 1971.

96. BERTOCCI, U., PUGH, E. N. and RICKER, R. E., Environment-induced cracking of copper alloys. Environmental-Induced Cracking of Metals, R. P. Gangloff and M. B. Ives eds., Houston, TX, NACE, 273-283, 1990.

97. GREEN, J. A. S., MENGELBERG, H. D. and YOLKEN, H. T., The mechanism of stress corrosion cracking of alpha-brass in aqueous ammonia. J. Electrochem. Soc., 117, 433-440, 1970.

98. PUGH, E. N. and WESTWOOD, A. R. C., Complex ions and stress-corrosion cracking in α-brass. Phil. Mag., 13, 167-183, 1966.

99. PUGH, E. N. and GREEN, J. A. S., The role of cupric complex ions in the dissolution and stress-corrosion cracking of α-brass in non-tarnishing aqueous ammonia. Met. Trans., 2, 3129-3144, 1971.

100. KAUFMAN, M. J. and FINK, J. L., A closer look at the transgranular stress corrosion cracking of Cu-30Zn in cuprous ammonia. Met. Trans., 18, 1539-1542, 1987.

101. BERTOCCI, U., THIMAS, F. I. and PUGH, E. N., Stress corrosion cracking of brass in aqueous ammonia in the absence of detectable anodic dissolution. Corrosion, 40, 439-440, 1984.

102. SIERADZKI, K., KIM. J. S., COLE, A. T. and NEWMAN, R. C., The relationship between dealloying and transgranular stress-corrosion cracking of Cu-Zn and Cu-Al alloys. J. Electrochem. Soc., 134, 1635-1639, 1987.

103. EDELEANU, C., Crack propagation during stress corrosion. Physical Metallurgy of Stress-Corrosion Cracking, T. N. Rhodin ed., New York, Interscience, 79-90, 1959.

104. NEILSEN, N. A., Electron microscopy of stress corrosion cracking. Fundamental Aspects of Stress Corrosion Cracking, R. W. Staehle, A. J. Forty and D.Van Rooyen eds., NACE, Houston, 308313, 1969.

105. RUSSELL, A. J. and TROMANS, D., Stress corrosion cracking of austenitic steels — Region II behavior. Met. Trans., 12A, 613-621, 1981.

106. NAKAYAMA, T. and TAKANO, M., HVEM observations of crack tip produced in Type 304 stainless steel by SCC and hydrogen embrittlement. Corrosion, 38, 1-8, 1982.

107. QIAO, L. J., Hydrogen-induced cracking and stress corrosion cracking of austenitic stainless steel under Mode III loading. Corrosion, 43, 479-482, 1987.

108. MATTSSON, M., Electrochim. Acta, 3, p.279, 1961.

109. KERMANI, M. and SCULLY, J. C., Fractographic aspects of the stress corrosion cracking of α-brass in 15N ammonia solutions. Corr.Sci., 19, 489-506, 1979.

110. LEE, L. P. and TROMANS, D., A fracture mechanics study of stress corrosion cracking of leaded alpha-brass. Environment Sensitive Fracture of Engineering Materials, Z. A. Foroulis ed., AIME, Warrendale, 232-249, 1979.

111. KERMANI, M. and SCULLY, J. C., The effect of strain-rate upon stress corrosion crack velocity in α-brass in ammoniacal solutions. Corr.Sci., 19, 89-110, 1979.

112. KERMANI, M. and SCULLY, J. C., The role of the tarnish film in the stress corrosion crack propagation process in α-brass in neutral ammoniacal solutions. Corr.Sci., 19, 111-122, 1979.

113. LI, S. Q., Study of the Fractography and Micromechanisms of Near-Threshold Fatigue Cracking and Transgranular Stress Corrosion Cracking, Ph.D thesis, Ecole Polytechnique de Montreal, 1991.

114. BAKISK, R., Trans. AIME, 9, p.494, 1957.

115. LICHTER, B. D., CASSAGNE, T. B., FLANAGAN, W. F. and PUGH, E. N., Microstructural Science, 13, p.361, 1985.

116. MELETIS, E. I. and HOCHMAN, R. F., The crystallography of stress corrosion cracking in face centred cubic single crystals. Corr. Sci., 24, 843-862, 1984.

117. PUGH, E. N., Progress toward understanding the stress corrosion problem. Corrosion, 41, 517-526, 1985.

118. REED, R. E. and PAXTON, H. W., First International Congress on Metallic Corrosion, Butterworths, London, p.301, 1962.

119. ROBERTSON, W. D. and TELELMAN, A. S., A unified structural mechanism for intergranular and transgranular corrosion cracking. Strengthening Mechanisms in Solids, ASM, Metals Park, OH, 217-252, 1962.

120. HARSTON, J. D. and SCULLY, J. C., Corrosion, 26, p.387, 1970.

121. MUKAI, Y., WATANABE, M. and MURATA, M., Fractographic observation of stress-corrosion cracking of AISI 304 stainless steel in boiling 42 percent magnesium-chloride solution. Fractography in Failure Analysis, ASTM STP 645, 164-175, 1978.

122. AHLERS, M. and RIECKE, E., Stress corrosion cracking in single crystals of Fe-25Cr-20Ni. Corr. Sci., 18, 21-38, 1978.

123. MAREK, M. and HOCHMAN, R. F., Crystallography and kinetics of SCC in Type 316 stainless steel single crystal. Corrosion, 27, 361-370, 1971.

124. ASARO, R. J., WEST, A. J. and TILLER, W. A., Hydrogen induced phase transformation of austenite to martensite. Stress Corrosion Cracking and Hydrogen Embrittlement of Iron-base Alloys, R. W. Staehle, J. Hochmann, R. D. McCright and J. E. Slater eds., NACE, Houston, TX, 1115-1124, 1977.

125. LIU, R., NARITA, N., ALTSTETTER, C. J., BIRNBAUM, H. and PUGH, E. N., Studies of the orientation of fractures produced in austenitic stainless steels by stress-corrosion cracking and hydrogen embrittlement. Met.Trans., 11A, 1563-74, 1980.

126. NIELSEN, N. A., Corrosion, 20, p.104, 1964.

127. LOUTHAN, M., Corrosion, 21, p.104, 1965.

128. TROMANS, D. and NUTTING, J., Stress corrosion cracking of face-centered-cubic alloys. Corrosion, 21, 143-159, 1965.

129. BURSLE, A. J. and PUGH, E. N., An evaluation of current models for the propagation of stress-corrosion cracks. Environment-Sensitive Fracture of Engineering Materials, Z. A. Foroulis ed., AIME, Warrendale, Pa, 18-47, 1978.

130. PARKINS, R. N., Mechanistic aspects of stress corrosion cracking. Parkins Symposium on Fundamental Aspects of Stress Corrosion Cracking, S. M. Bruemmer, E. I. Meletis, R. H. Jones, W. W. Gerberich, F. P. Ford and R. W. Staehle eds., TMS, 3-40, 1992.

131. LATANISION, R. M., General overview: Atomistics of environmentally-induced fracture. Atomistics of Fracture, R. M. Latanision and J. R. Pickins eds., 3-37, 1981.

132. DIX, E., Jr, Trans. Am. Inst. Min. Met. Engrs., 137, p.11, 1940.

133. FORTY, A. J. and HUMBLE, P., The influence of surface tarnish on the stress-corrosion of α-brass. Phil. Mag., 8, 247-264, 1963.

134. NEWMAN, R. C. Newman, PROCTER, R. P. M., Stress corrosion cracking: 1965 –1990. Br.Corr.J, 25, 259-269, 1990.

135. VERMILYEA, D.A., A film rupture model for SCC. Stress Corrosion Cracking and Hydrogen Embrittlement of Iron-base Alloys, R. W. Staehle, J. Hochmann, R. D. McCright and J. E. Slater eds., Houston, NACE, 208-217, 1977.

136. SCAMANS, G. M. and SWANN, P. R., Stress corrosion crack tip morphology. Stress Corrosion Cracking and Hydrogen Embrittlement of Iron-base Alloys, R. W. Staehle, J. Hochmann, R. D. McCright and J. E. Slater eds., Houston, NACE, 166-173, 1977.

137. SWANN, P. R. and PICKERING, H. W., Corrosion, 19, p.369, 1963.

138. SIERADZKI, K. and NEWMAN, R. C., Brittle behavior of ductile metals during stress corrosion cracking. Phil. Mag.A, 51, 95-132, 1985.

139. SIERADZKI, K. and NEWMAN, R. C., Stress corrosion cracking. J. Phys. Chem. Solids., 48, 1101-1113, 1987.

140. UHLIG, H. H., An evaluation of stress corrosion cracking mechanisms. Fundamental Aspects of Stress Corrosion Cracking, R. W. Staehle, A. J. Forty and D.Van Rooyen eds., NACE, Houston, 86-91, 1969.

141. WESTWOOD, A. R. C. and KAMDAR, M. H., Concerning liquid metal embrittlement, particularly of zinc monocrystals by mercury. Phil. Mag., 8, 787-804,1963.

142. STOLOFF, N. S. and JOHNSTON, T. L., Acta Metall., 11, p.251, 1963.

143. UHLIG, H. H. and DUQUETTE, D. J., Alleged stress-corrosion cracking of pure copper. Corr. Sci., 9, 557-560, 1969.

144. GALVELE, J. R., Enhanced surface mobility as the cause of stress corrosion cracking. J. Electrochem. Soc., 133, 953-954, 1986.

145. GALVELE, J. R., A stress corrosion cracking mechanism based on surface mobility. Corr. Sci., 27, 1-33, 1987.

146. LYNCH, S. P., Cleavage fracture in face-centred cubic metals. Met. Sci., 15, 463-467, 1981.

147. TYSON, W. R., AYRES, R. A. and STEIN, D. F., Anisotropy of cleavage in bcc transition metals. Acta Met., 21, 621-627, 1973.

148. FLANAGAN, W. F., BASTIAS, P. and LICHTER, B. D., A theory of transgranular stress-corrosion cracking. Acta Metall. Mater., 39, 695-705, 1991.

149. FLANAGAN, W. F., ZHONG, LIJUN and LICHTER, B. D., A Mechanism for stress corrosion cracking, Met. Trans., 24A, 553-559, 1993.

150. STROH, A. N., The strength of Lomar-Cottrell sessile dislocations. Phil. Mag., 1, 489-502, 1956.

151. MAGNIN, T., CHIERAGATTI, R. and OLTRA, R., Mechanism of brittle fracture in a ductile 316 alloy during stress corrosion. Acta Metall. Mater., 38, 1313-1319, 1990.

152. THOMPSON, A. W. and BERNSTEIN, I. M., The role of metallurgical variables in hydrogen-assisted environmental fracture. Advances in Corrosion Science and Technology, 7, M. G. Fontana and R. W. Staehle eds., 53-175, 1980.

153. LATANISION, R. M., GASTINE, O. H. and COMPEAU, C. R., Stress corrosion cracking and hydrogen embrittlement: difference and similarities. Environment-Sensitive Fracture of Engineering Materials, Z. A. Foroulis ed., AIME, Warrendale, Pa, 48-70, 1978.

154. RICE, R. and THOMSON, R., Ductile versus brittle behavior of crystals. Phil. Mag., 29, 73-97, 1974.

155. BURNS, S. J., Crack tip dislocation nucleation observations in bulk specimens. Scripta Metall., 20, 1489-1494, 1986.

156. ANDERSON, P. M. and RICE, J. R., Dislocaton emission from crack in crystals or along crystal interfaces. Scripta Metall., 20, 1467-1472, 1986.

157. THOMSON, R., Brittle fracture in a ductile material with application to hydrogen embrittlement. J. Met. Sci., 13, 128-142, 1978.

158. WEERTMAN, J. Weertman, Fracture mechanics: a unified view for Griffith-Irwin-Orowan cracks. Acta Met., 26, 1731-1738, 1978.

159. LI, J. C. M., Computer simulaton of dislocatons emitted from a crack. Scripta Metall., 20, 1477-1482, 1986.

160. HIRTH, J. P., Crack nucleation in glide plane decohesion and shear band separation. Scripta Metall. Mater., 28, 703-707, 1993.

161. KAMDAR, M. H., Prog. Mat. Sci., 15, p.289, 1973.

162. WESTWOOD, A. R. C. and KAMDAR, M. H., Concerning liquid metal embrittlement, particularly of zinc monocrystals by mercury. Phil. Mag., 8, 787-804,1963.

163. PETCH, N. J., Phil. Mag., 1, p.331, 1956.

164. TROMANS, D., On surface energy and the hydrogen embrittlement of iron and steels. Acta Metall. Mater., 42, 2043-2049, 1994.

165. GILMAN, J. J., Stress-corrosion cracking in plastic solids including the role of hydrogen. Phil. Mag., 26, 801-812, 1972.

166. SHIMODAIRA, S. and TAKANO, M., Role of surface film in stress corrosion cracking. Fundamental Aspects of Stress Corrosion Cracking, R. W. Staehle, A. J. Forty and D.Van Rooyen eds., NACE, Houston, 202-210, 1969.

167. FORTY, A. J., The initiation and propagation of cracks in the stress-corrosion of α-brass and similar alloys. Physical Metallurgy of Stress Corrosion Fracture, T. N. Rhodin ed., Interscience, New York, 99-114, 1959.

168. HELDT, L. A., HINTZ, M. B. and KOSS, D. A., Localized Crack Chemistry and Mechanics in Environment Assisted Cracking, R. P. Gangloff ed., AIME, Warrendale, Pennsylvania.

169. CASSAGNE, T. B., FLANAGAN, W. F. and LICHTER, B. D., On the failure mechanism of chemically embrittled Cu_3Au single crystals. Met. Trans., 17A, 703-716, 1986.

170. CASSAGNE, T. B., FLANAGAN, W. F. and LICHTER, B. D., Transgranular stress corrosion cracking of disordered Cu-25Au in aqueous chloride and surfate media. Met. Trans., 19A, 281-292, 1988.

171. SIERADZKI, K., SABATINI, R. L. and NEWMAN, R. C., Stress-corrosion cracking of copper single crystals. Met. Trans., 15A, 1941-1946, 1984.

172. DEEGAN, D. C. and WILDE, B. E., The stress corrosion cracking behavior of ASTM A517 Grade ferritic steel in liquid ammonia environment. Stress Corrosion Cracking and Hydrogen Embrittlement of Iron Base Alloys, R. W. Staehle, J. Hochmann, R. D. McCright and J. E. Slater eds., NACE, Houston, TX, 663-670, 1977.

173. SCAMANS, G. M. and SWANN, P. R., High voltage electron microscopy of stress corrosion cracking of austenitis stainless steels. Corr.Sci., 18, 983-995, 1978.

174. NEWMAN, R. C., CORDERMAN, R. R. and SIERADZKI, K., Evidence for dealloying of austenitic stainless steels in simulated stress corrosion crack environments. Br. Corr. J., 24, 143-147, 1989.

175. BAKISH, R. and ROBERTSON, W. D., Acta Met., 3, p.513, 1955.

176. SWANN, P. R. and NUTTING, J., J. I. M., 88, p.471, 1960.

177. DOUGLASS, D. L., THOMAS, G. and ROSER, W. R., Ordering, stacking faults and stress corrosion cracking in austenitic alloys. Corrosion, 20, 15t-28t, 1964.

178. SWANN, P. R., Dislocation substructure vs transgranular stress corrosion cracking subsceptibility of single phase alloys. Corrosion, 19, 102t-112t, 1963.

179. EL OMARI, S., Effect da la ferrite delta sur la vitesse de fissuration en corrosion sous contrainte da l'acier inoxydable 316L, M. Sc. A. thesis, Ecole Polytechnique de Montreal, 1992.

180. Standard Test Method for Measurement of Fatigue Crack Growth Rates, Annual Book of ASTM Standards, 03.01, 569-596, 1994.

181. Heat Treating of Copper Alloys, ASTM Handbook, 4, 880-898, 1990.

182. MAREK, M. and HOCHMAN, R. F., Corrosion, 26, p.5, 1970.

183. NIELSEN, N. A., Hydrogen induced cracking of low strength stainless steels. Stress Corrosion Cracking and Hydrogen Embrittlement of Iron Base Alloys, R. W. Staehle, J. Hochmann, R. D. McWright and J. E. Slater eds., NACE, Houston, TX, 1108-1113, 1977.

184. HANNINEN, H. and HAKKARAINEN, T., Fractographic characteristics of a hydrogen-charged AISI 316 Type austenitic stainless steel. Met. Trans., 10A, 1196-99, 1979.

185. ELIEZER, P., CHAKRAPANI, D. G., ALTSTETTER, C. J. and PUGH, E. N., The influence of austenite stability on the hydrogen embrittlement and stress-corrosion cracking of stainless steel. Met. Trans., 10A, 935-941, 1979.

186. THOMPSON, A. W and J. A. BROOKS, Hydrogen performance of precipitation-strengthened stainless steels based on A-286. Met.Trans., 6A, 1431-1442, 1975.

187. GARBER, R., I. M. BERNSTEIN and THOMPSON, A. W., Effect of hydrogen in ductile fracture of spheroidized steel. Scripta Met., 10, 341-343, 1976.

188. ZAKROCZYMSKI, T., Entry of hydrogen into iron alloys from the liquid phase. Hydrogen Degradation of Ferrous Alloys, R. A. Oriani, J. P. Hirth and M. Smialowski eds., Noyes Publications, N.J.07656, p.215, 1985.

189. WEST, A. J. and LOUTHAN, M. R., Jr., Dislocation transport and hydrogen embrittlement. Met. Trans., 10A, 1675-1682, 1979.

190. TROIBIO, J., LANCHA, A. M. and ELICES, M., The tearing topography surface as the zone associated with hydrogen embrittlement processes in pearlitic steel. Met. Trans., 23, 1573-1584, 1992.

191. RITCHIE, R. O., Influence of microstructure on near-threshold fatigue crack propagation in ultra-high strength steel. Met. Sci., 11, 368-381, 1977.

192. TORIBIO, J., The role of crack tip strain rate in hydrogen-assisted cracking. Corr. Sci., 39, 1678-1697, 1997.

193. LUFRANO, J. and SOFRONIS, P., Numerical analysis of the interaction of solid hydrogen with the stress field of a crack tip. Int. J. Solids Struct., 33, 1709-1722, 1996.

194. OLTRA, R., BOUILLOT, C. and MAGNIN, T., The role of hydrogen in stress corrosion cracking of duplex stainless steels. Corrosion-Deformation Interactions CDI 96, T. Magnin ed. The Institute of Materials, 248-253, 1997.

195. YOSHINARI, O., SANPEI, K. and TANAKA, K., Hydrogen-solute interaction in nickel-based dilute alloys studied by internal fricition technique. Acta Metall. Mater., 39, 2657-1665, 1991.

196. DICKSON, J. I., TROMAN, D., LI, S., EL OMARI, S. and WU, X. Z., Implications on the mechanisms of transgranular SCC in f.c.c. metals from microfractography and fracture mechanics. Corrosion–Deformation Interactions CDI 92, T. Magnin and J. M. Gras eds., 643-657, 1992.

197. FLOWERS, J. W., BECK, F. H. and FONTANA, M. G., Corrosion, 19, p.186t, 1963.

198. LULA, R. A., Stainless Steel, ASM, Metals Park, Ohio, p.80.

199. HANNINEN, H. E., Influence of metallurgical varibles on environment-sensitive cracking of austenitic alloys. Inter. Mat. Rev, 24, 85-135, 1979.

200. DENHARD, F. E., Corrosion, 16, p.359t, 1960.

201. SHERMAN, D. H., DUQUETTE, D. J. and SAVAGE, W. F., Stress corrosion cracking behavior of duplex steel weldments in boiling $MgCl_2$ solution. Corrosion, 31, 376-380, 1975.

202. STALDER, F. and DUQUETTE, D. J., Slow strain rate stress corrosion cracking of Type 304 stainless steels. Corrosion, 33, 67-72, 1977.

203. FANG, Z., WU, Y. and ZHU, R., Stress corrosion cracking of Type 304 stainless less weldments in active state. Corrosion, 50, 171-175, 1994.

204. PERNG, T-P. and ALTSTETTER, C. J., Comparison of hydrogen gas embrittlement of austenitic and ferritic stainless steels. Met. Trans., 18A, 123-134, 1987.

205. PERNG, T-P. and ALTSTETTER, C. J., Cracking kinetics of two-phase stainless steel alloys in hydrogen gas. Met. Trans., 19A, 145-152, 1988.

206. THOMPSON, A.W., Ductility losses in austenitic stainless steels caused by hydrogen. Hydrogen in Metals, I. M. Bernstein and A. W. Thompson eds., 91-106, 1974.

207. BERNSTEIN, I. M. and THOMPSON, A. W., Alloy and Microstructure Design, J. K. Tien, G. S. Ansell eds., p.303.

208. MANDZIEJ, S. T., Mechanism of hydrogen assisted fracture of duplex stainless steel. Parkins Symposium on Fundamental Aspects of Stress Corrosion Cracking, S. M. Bruemmer, E. I. Meletis, R. H. Jones, W. W. Gerberich, F. P. Ford and R. W. Staehle eds., TMS, 215-230, 1992.

209. KAO, P. W., URE, R. W., Jr. and BYRNE, J. G., A study of hydrogen charging of nickel by positron drppler broadening. Phil. Mag., 39, 517-527, 1979.

210. KIMURA, A., MATSUI, H. and KIMURA, H., The work-hardening behavior of hydrogen-charged high purity iron single crystals at temperature between 296 to 200 K. Mat. Sci. Eng., 58, 211-222, 1983.

211. MANDZIEJ, S. T., Hydrogen and dislocation in high-chromium ferrite. Scripta Metall. Mater., 25, 213-218, 1991.

212. ULMER, D. G. and ALTSTETTER, C. J., Hydrogen induced strain localization and failure of austenitic stainless steels at high hydrogen concentration. Acta Metall. Mater., 39, 1237-1248, 1991.

213. HIRTH, J. P., Crack nucleation in glide plane decohesion and shear band separation. Scripta Metall. Mater., 28, 703-707, 1993.

214. BOND, A. P. and DUNDAS, J., Corrosion, 24, p.344, 1968.

215. TELELMAN, A. S. and ROBERTSON, W. D., Acta Metall., 11, p.415, 1963.

216. GELL, M. and ROBERTSON, W. D., An analysis of plastic deformation around stationary cleavage cracks. Acta Metall., 14, 481-490, 1966.

217. CHEN, X., FOECKE, T., LII, M., KATZ, Y. and GERBERICH, W. W., The role of stress state on hydrogen cracking in Fe-Si single crystals. Eng. Frac. Mech., 35, 997-1017, 1990.

218. GERBERICH, W. W., HUANG, H., ZIELINSKI, W. and MARSH, P. G., A dislocation-shielding predicition of the toughness transition during cleavage of semibrittle crystals. Met. Trans., 24A, 535-552, 1993.

219. HINOTANI, S., OHMORI, Y. and TERASAKI, F., Hydrogen cracking initiation and propagation in pure iron single crystals. Mat. Sci. Tech., 10, 141-148, 1994

220. BERNSTEIN, I. M., Hydrogen induced cracking in iron: Morphology and crack path dependence. Met. Trans., 1, 3143-3150, 1970.

221. NAKASATO, F. and BERNSTEIN, I. M., Crystallographic and fractographic studies of hydrogen-induced cracking in purified iron and iron-silicon alloys. Met. Trans., 9A, 1317-1326, 1978.

222. TAKANO, N., KIDANI, K., HATTORI, Y. and TERASAKI, F., Fracture surface of hydrogen embrittlement in iron single crystals. Scr. Metall. Mater., 29, 75-80, 1993.

223. DILLAMORE, I. L. and ROBERTS, W. T., Metall. Rev., 10, p.271, 1965.

224. DETERT, K., Acta Met., 7, p.589, 1959.

225. COHEN, L. J. R., CHARLES, J. A. and SMITH, G. C., Influence of cathodic hydrogen on microstructure of duplex stainless steel, Stainless Steel '87, The Institute of Matels, 363-374, 1988.

226. GAUTHIER, M., B. Sc. A. final project report, Ecole Polytechnique, 1993.

227. PINCHBACK, T.R., CLOUGH, S.P. and HLDT, L. A., Stress corrosion cracking of alpha brass in a tranishing ammoniacal environment: Fractrography and chemical analysis. Met. Trans., 6A, 1479-1483, 1975.

228. BAKISH, R. and ROBERTSON, W.D., Galvanic potentials of grains and grain boundaries in copper alloys. J. Electrochem. Soc., 103, 320-325, 1956.

229. HIRTH, P.B., Internal Stress and Fatigue in Matels, Elsevier, NY, p.139, 1958.

230. YEUNG, W. Y., Non-octahedral deformation activity in cold rolled 70:30 brass and its influence on the development of brass texture. Acta Metall. Mater., 38, 1109-1114, 1990.

231. NEWMAN, R.C. and SAITO, M, Anodic stress-corrosion cracking: slip-dissolution and film-induced cleavage. Corrosion–Deformation Interactions CDI 92, T. Magnin and J. M. Gras eds., 3-25, 1992.

232. CASSAGNE, T.B. and LICHTER, B.D., On the failure mechanism of chemically embrittled Cu_3Au single crystals. Met. Trans., 17A, 703-716, 1986.

233. BROWN, B. F., Stress corrosion cracking in high strength steels. The Theory of Stress Corrosion Cracking in alloys, J. C. Scully ed., NATO, Brussel, 186-203, 1971.

234. KERMANI, M. and SCULLY, J.C., Stress corrosion crack propagation in α-brass in 15N ammoniacal solutions. Corr.Sci., 18, 883-905, 1978.

235. FORSYTH, P. J. E., A unified description of micro and macroscopic crack behavior. Int. J. Fatigue, 5, 3-14, 1983.

236. FLANAGAN, W. F., ZHONG, LIJUN and LICHTER, B. D., A mechanism for stress corrosion cracking. Met. Trans., 24A, 553-559, 1993.

237.DAW, M. S. and BASKES, M. I., Embedded-atom method: derivation and application to impurities, surfaces and other defects in metals. Phys. Rev. B, 29, 6443-6453, 1984.

238.HENTZ, B., NETTLETON, L. J. and HELDT, L. A., Stress corrosion cracking of alpha-beta brass in distilled water and sodium sulphate solutions. Met. Trans., 16A, 971-978, 1985.

239.LYNCH, S. P., Concerning the mechanism of transgranular stress-corrosion cracking in α-brass. Scripta Metall., 18, 321-326, 1984.

240.HINTZ, M. B., Stress corrosion cracking and crack tip adsorption: Considerations regarding the role of alloy dissolution products. Scripta Metall., 19, 1445-1450, 1985.

241.DEMUTH, J. E., JEPSEN, D. W. and MARCUS, P. M., Crystallographic dependence of chemisorption bonding for sulfur on (001), (110) and (111) nickel. Phys. Rev. Lett., 32, 1182-85, 1974.

242.ORIANI, R. A., On the possible role of the surface stress in environmentally induced embrittlement and pitting. Scripta Metall., 18, 265-68, 1984.

IMAGE EVALUATION
TEST TARGET (QA-3)

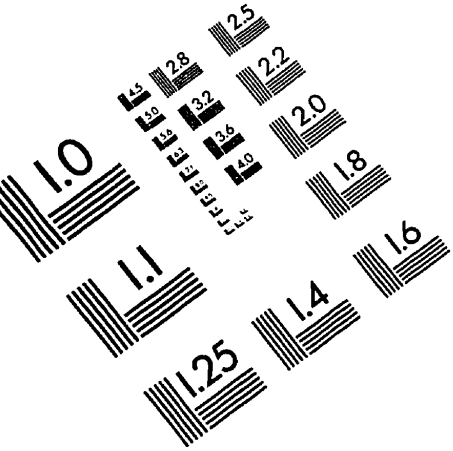
1.0
1.1
1.25
1.4
1.6
1.8
2.0
2.2
2.5
2.8
3.2
3.6
4.0
4.5
5.0
5.6
6.3
7.1
8.0
9.0
10.0
11.2
12.5
14.0
16.0
18.0
20.0
22.0
25.0
28.0
32.0
36.0
40.0
45.0
50.0
56.0
63.0
71.0
80.0
90.0
100.0
112.0
125.0
140.0
160.0
180.0
200.0
224.0
250.0
280.0
320.0
360.0
400.0
450.0
500.0
560.0
630.0
710.0
800.0
900.0
1000.0
1120.0
1250.0
1400.0
1600.0
1800.0
2000.0
2240.0
2500.0
2800.0
3200.0
3600.0
4000.0
4500.0
5000.0
5600.0
6300.0
7100.0
8000.0
9000.0
10000.0
11200.0
12500.0
14000.0
16000.0
18000.0
20000.0
22400.0
25000.0
28000.0
32000.0
36000.0
40000.0
45000.0
50000.0
56000.0
63000.0
71000.0
80000.0
90000.0
100000.0
112000.0
125000.0
140000.0
160000.0
180000.0
200000.0
224000.0
250000.0
280000.0
320000.0
360000.0
400000.0
450000.0
500000.0
560000.0
630000.0
710000.0
800000.0
900000.0
1000000.0
1120000.0
1250000.0
1400000.0
1600000.0
1800000.0
2000000.0
2240000.0
2500000.0
2800000.0
3200000.0
3600000.0
4000000.0
4500000.0
5000000.0
5600000.0
6300000.0
7100000.0
8000000.0
9000000.0
10000000.0
11200000.0
12500000.0
14000000.0
16000000.0
18000000.0
20000000.0
22400000.0
25000000.0
28000000.0
32000000.0
36000000.0
40000000.0
45000000.0
50000000.0
56000000.0
63000000.0
71000000.0
80000000.0
90000000.0
100000000.0
112000000.0
125000000.0
140000000.0
160000000.0
180000000.0
200000000.0
224000000.0
250000000.0
280000000.0
320000000.0
360000000.0
400000000.0
450000000.0
500000000.0
560000000.0
630000000.0
710000000.0
800000000.0
900000000.0
1000000000.0
1120000000.0
1250000000.0
1400000000.0
1600000000.0
1800000000.0
2000000000.0
2240000000.0
2500000000.0
2800000000.0
3200000000.0
3600000000.0
4000000000.0
4500000000.0
5000000000.0
5600000000.0
6300000000.0
7100000000.0
8000000000.0
9000000000.0
10000000000.0
11200000000.0
12500000000.0
14000000000.0
16000000000.0
18000000000.0
20000000000.0
22400000000.0
25000000000.0
28000000000.0
32000000000.0
36000000000.0
40000000000.0
45000000000.0
50000000000.0
56000000000.0
63000000000.0
71000000000.0
80000000000.0
90000000000.0
100000000000.0
112000000000.0
125000000000.0
140000000000.0
160000000000.0
180000000000.0
200000000000.0
224000000000.0
250000000000.0
280000000000.0
320000000000.0
360000000000.0
400000000000.0
450000000000.0
500000000000.0
560000000000.0
630000000000.0
710000000000.0
800000000000.0
900000000000.0
1000000000000.0
1120000000000.0
1250000000000.0
1400000000000.0
1600000000000.0
1800000000000.0
2000000000000.0
2240000000000.0
2500000000000.0
2800000000000.0
3200000000000.0
3600000000000.0
4000000000000.0
4500000000000.0
5000000000000.0
5600000000000.0
6300000000000.0
7100000000000.0
8000000000000.0
9000000000000.0
10000000000000.0
11200000000000.0
12500000000000.0
14000000000000.0
16000000000000.0
18000000000000.0
20000000000000.0
22400000000000.0
25000000000000.0
28000000000000.0
32000000000000.0
36000000000000.0
40000000000000.0
45000000000000.0
50000000000000.0
56000000000000.0
63000000000000.0
71000000000000.0
80000000000000.0
90000000000000.0
100000000000000.0
112000000000000.0
125000000000000.0
140000000000000.0
160000000000000.0
180000000000000.0
200000000000000.0
224000000000000.0
250000000000000.0
280000000000000.0
320000000000000.0
360000000000000.0
400000000000000.0
450000000000000.0
500000000000000.0
560000000000000.0
630000000000000.0
710000000000000.0
800000000000000.0
900000000000000.0
1000000000000000.0
1120000000000000.0
1250000000000000.0
1400000000000000.0
1600000000000000.0
1800000000000000.0
2000000000000000.0
2240000000000000.0
2500000000000000.0
2800000000000000.0
3200000000000000.0
3600000000000000.0
4000000000000000.0
4500000000000000.0
5000000000000000.0
5600000000000000.0
6300000000000000.0
7100000000000000.0
8000000000000000.0
9000000000000000.0
10000000000000000.0
11200000000000000.0
12500000000000000.0
14000000000000000.0
16000000000000000.0
18000000000000000.0
20000000000000000.0
22400000000000000.0
25000000000000000.0
28000000000000000.0
32000000000000000.0
36000000000000000.0
40000000000000000.0
45000000000000000.0
50000000000000000.0
56000000000000000.0
63000000000000000.0
71000000000000000.0
80000000000000000.0
90000000000000000.0
100000000000000000.0
112000000000000000.0
125000000000000000.0
140000000000000000.0
160000000000000000.0
180000000000000000.0
200000000000000000.0
224000000000000000.0
250000000000000000.0
280000000000000000.0
320000000000000000.0
360000000000000000.0
400000000000000000.0
450000000000000000.0
500000000000000000.0
560000000000000000.0
630000000000000000.0
710000000000000000.0
800000000000000000.0
900000000000000000.0
1000000000000000000.0
1120000000000000000.0
1250000000000000000.0
1400000000000000000.0
1600000000000000000.0
1800000000000000000.0
2000000000000000000.0
2240000000000000000.0
2500000000000000000.0
2800000000000000000.0
3200000000000000000.0
3600000000000000000.0
4000000000000000000.0
4500000000000000000.0
5000000000000000000.0
5600000000000000000.0
6300000000000000000.0
7100000000000000000.0
8000000000000000000.0
9000000000000000000.0
10000000000000000000.0
11200000000000000000.0
12500000000000000000.0
14000000000000000000.0
16000000000000000000.0
18000000000000000000.0
20000000000000000000.0
22400000000000000000.0
25000000000000000000.0
28000000000000000000.0
32000000000000000000.0
36000000000000000000.0
40000000000000000000.0
45000000000000000000.0
50000000000000000000.0
56000000000000000000.0
63000000000000000000.0
71000000000000000000.0
80000000000000000000.0
90000000000000000000.0
100000000000000000000.0
112000000000000000000.0
125000000000000000000.0
140000000000000000000.0
160000000000000000000.0
180000000000000000000.0
200000000000000000000.0
224000000000000000000.0
250000000000000000000.0
280000000000000000000.0
320000000000000000000.0
360000000000000000000.0
400000000000000000000.0
450000000000000000000.0
500000000000000000000.0
560000000000000000000.0
630000000000000000000.0
710000000000000000000.0
800000000000000000000.0
900000000000000000000.0
1000000000000000000000.0
1120000000000000000000.0
1250000000000000000000.0
1400000000000000000000.0
1600000000000000000000.0
1800000000000000000000.0
2000000000000000000000.0
2240000000000000000000.0
2500000000000000000000.0
2800000000000000000000.0
3200000000000000000000.0
3600000000000000000000.0
4000000000000000000000.0
4500000000000000000000.0
5000000000000000000000.0
5600000000000000000000.0
6300000000000000000000.0
7100000000000000000000.0
8000000000000000000000.0
9000000000000000000000.0
10000000000000000000000.0
11200000000000000000000.0
12500000000000000000000.0
14000000000000000000000.0
16000000000000000000000.0
18000000000000000000000.0
20000000000000000000000.0
22400000000000000000000.0
25000000000000000000000.0
28000000000000000000000.0
32000000000000000000000.0
36000000000000000000000.0
40000000000000000000000.0
45000000000000000000000.0
50000000000000000000000.0
56000000000000000000000.0
63000000000000000000000.0
71000000000000000000000.0
80000000000000000000000.0
90000000000000000000000.0
100000000000000000000000.0
112000000000000000000000.0
125000000000000000000000.0
140000000000000000000000.0
160000000000000000000000.0
180000000000000000000000.0
200000000000000000000000.0
224000000000000000000000.0
250000000000000000000000.0
280000000000000000000000.0
320000000000000000000000.0
360000000000000000000000.0
400000000000000000000000.0
450000000000000000000000.0
500000000000000000000000.0
560000000000000000000000.0
630000000000000000000000.0
710000000000000000000000.0
800000000000000000000000.0
900000000000000000000000.0
1000000000000000000000000.0
1120000000000000000000000.0
1250000000000000000000000.0
1400000000000000000000000.0
1600000000000000000000000.0
1800000000000000000000000.0
2000000000000000000000000.0
2240000000000000000000000.0
2500000000000000000000000.0
2800000000000000000000000.0
3200000000000000000000000.0
3600000000000000000000000.0
4000000000000000000000000.0
4500000000000000000000000.0
5000000000000000000000000.0
5600000000000000000000000.0
6300000000000000000000000.0
7100000000000000000000000.0
8000000000000000000000000.0
9000000000000000000000000.0
10000000000000000000000000.0
11200000000000000000000000.0
12500000000000000000000000.0
14000000000000000000000000.0
16000000000000000000000000.0
18000000000000000000000000.0
20000000000000000000000000.0
22400000000000000000000000.0
25000000000000000000000000.0
28000000000000000000000000.0
32000000000000000000000000.0
36000000000000000000000000.0
40000000000000000000000000.0
45000000000000000000000000.0
50000000000000000000000000.0
56000000000000000000000000.0
63000000000000000000000000.0
71000000000000000000000000.0
80000000000000000000000000.0
90000000000000000000000000.0
100000000000000000000000000.0
112000000000000000000000000.0
125000000000000000000000000.0
140000000000000000000000000.0
160000000000000000000000000.0
180000000000000000000000000.0
200000000000000000000000000.0
224000000000000000000000000.0
250000000000000000000000000.0
280000000000000000000000000.0
320000000000000000000000000.0
360000000000000000000000000.0
400000000000000000000000000.0
450000000000000000000000000.0
500000000000000000000000000.0
560000000000000000000000000.0
630000000000000000000000000.0
710000000000000000000000000.0
800000000000000000000000000.0
900000000000000000000000000.0
1000000000000000000000000000.0
1120000000000000000000000000.0
1250000000000000000000000000.0
1400000000000000000000000000.0
1600000000000000000000000000.0
1800000000000000000000000000.0
2000000000000000000000000000.0
2240000000000000000000000000.0
2500000000000000000000000000.0
2800000000000000000000000000.0
3200000000000000000000000000.0
3600000000000000000000000000.0
4000000000000000000000000000.0
4500000000000000000000000000.0
5000000000000000000000000000.0
5600000000000000000000000000.0
6300000000000000000000000000.0
7100000000000000000000000000.0
8000000000000000000000000000.0
9000000000000000000000000000.0
10000000000000000000000000000.0
11200000000000000000000000000.0
12500000000000000000000000000.0
14000000000000000000000000000.0
16000000000000000000000000000.0
18000000000000000000000000000.0
20000000000000000000000000000.0
22400000000000000000000000000.0
25000000000000000000000000000.0
28000000000000000000000000000.0
32000000000000000000000000000.0
36000000000000000000000000000.0
40000000000000000000000000000.0
45000000000000000000000000000.0
50000000000000000000000000000.0
56000000000000000000000000000.0
63000000000000000000000000000.0
71000000000000000000000000000.0
80000000000000000000000000000.0
90000000000000000000000000000.0
100000000000000000000000000000.0
112000000000000000000000000000.0
125000000000000000000000000000.0
140000000000000000000000000000.0
160000000000000000000000000000.0
180000000000000000000000000000.0
200000000000000000000000000000.0
224000000000000000000000000000.0
250000000000000000000000000000.0
280000000000000000000000000000.0
320000000000000000000000000000.0
360000000000000000000000000000.0
400000000000000000000000000000.0
450000000000000000000000000000.0
500000000000000000000000000000.0
560000000000000000000000000000.0
630000000000000000000000000000.0
710000000000000000000000000000.0
800000000000000000000000000000.0
900000000000000000000000000000.0
1000000000000000000000000000000.0
1120000000000000000000000000000.0
1250000000000000000000000000000.0
1400000000000000000000000000000.0
1600000000000000000000000000000.0
1800000000000000000000000000000.0
2000000000000000000000000000000.0
2240000000000000000000000000000.0
2500000000000000000000000000000.0
2800000000000000000000000000000.0
3200000000000000000000000000000.0
3600000000000000000000000000000.0
4000000000000000000000000000000.0
4500000000000000000000000000000.0
5000000000000000000000000000000.0
5600000000000000000000000000000.0
6300000000000000000000000000000.0
7100000000000000000000000000000.0
8000000000000000000000000000000.0
9000000000000000000000000000000.0
10000000000000000000000000000000.0
11200000000000000000000000000000.0
12500000000000000000000000000000.0
14000000000000000000000000000000.0
16000000000000000000000000000000.0
18000000000000000000000000000000.0
20000000000000000000000000000000.0
22400000000000000000000000000000.0
25000000000000000000000000000000.0
28000000000000000000000000000000.0
32000000000000000000000000000000.0
36000000000000000000000000000000.0
40000000000000000000000000000000.0
45000000000000000000000000000000.0
50000000000000000000000000000000.0
56000000000000000000000000000000.0
63000000000000000000000000000000.0
71000000000000000000000000000000.0
80000000000000000000000000000000.0
90000000000000000000000000000000.0
100000000000000000000000000000000.0
112000000000000000000000000000000.0
125000000000000000000000000000000.0
140000000000000000000000000000000.0
160000000000000000000000000000000.0
180000000000000000000000000000000.0
200000000000000000000000000000000.0
224000000000000000000000000000000.0
250000000000000000000000000000000.0
280000000000000000000000000000000.0
320000000000000000000000000000000.0
360000000000000000000000000000000.0
400000000000000000000000000000000.0
450000000000000000000000000000000.0
500000000000000000000000000000000.0
560000000000000000000000000000000.0
630000000000000000000000000000000.0
710000000000000000000000000000000.0
800000000000000000000000000000000.0
900000000000000000000000000000000.0
1000000000000000000000000000000000.0
1120000000000000000000000000000000.0
1250000000000000000000000000000000.0
1400000000000000000000000000000000.0
1600000000000000000000000000000000.0
1800000000000000000000000000000000.0
2000000000000000000000000000000000.0
2240000000000000000000000000000000.0
2500000000000000000000000000000000.0
2800000000000000000000000000000000.0
3200000000000000000000000000000000.0
3600000000000000000000000000000000.0
4000000000000000000000000000000000.0
4500000000000000000000000000000000.0
5000000000000000000000000000000000.0
5600000000000000000000000000000000.0
6300000000000000000000000000000000.0
7100000000000000000000000000000000.0
8000000000000000000000000000000000.0
9000000000000000000000000000000000.0
10000000000000000000000000000000000.0
11200000000000000000000000000000000.0
12500000000000000000000000000000000.0
14000000000000000000000000000000000.0
16000000000000000000000000000000000.0
18000000000000000000000000000000000.0
20000000000000000000000000000000000.0
22400000000000000000000000000000000.0
25000000000000000000000000000000000.0
28000000000000000000000000000000000.0
32000000000000000000000000000000000.0
36000000000000000000000000000000000.0
40000000000000000000000000000000000.0
45000000000000000000000000000000000.0
50000000000000000000000000000000000.0
56000000000000000000000000000000000.0
63000000000000000000000000000000000.0
71000000000000000000000000000000000.0
80000000000000000000000000000000000.0
90000000000000000000000000000000000.0
100000000000000000000000000000000000.0
112000000000000000000000000000000000.0
125000000000000000000000000000000000.0
140000000000000000000000000000000000.0
160000000000000000000000000000000000.0
180000000000000000000000000000000000.0
200000000000000000000000000000000000.0
224000000000000000000000000000000000.0
250000000000000000000000000000000000.0
280000000000000000000000000000000000.0
320000000000000000000000000000000000.0
360000000000000000000000000000000000.0
400000000000000000000000000000000000.0
450000000000000000000000000000000000.0
500000000000000000000000000000000000.0
560000000000000000000000000000000000.0
630000000000000000000000000000000000.0
710000000000000000000000000000000000.0
800000000000000000000000000000000000.0
900000000000000000000000000000000000.0
1000000000000000000000000000000000000.0
1120000000000000000000000000000000000.0
1250000000000000000000000000000000000.0
1400000000000000000000000000000000000.0
1600000000000000000000000000000000000.0
1800000000000000000000000000000000000.0
2000000000000000000000000000000000000.0
2240000000000000000000000000000000000.0
2500000000000000000000000000000000000.0
2800000000000000000000000000000000000.0
3200000000000000000000000000000000000.0
3600000000000000000000000000000000000.0
4000000000000000000000000000000000000.0
4500000000000000000000000000000000000.0
5000000000000000000000000000000000000.0
5600000000000000000000000000000000000.0
6300000000000000000000000000000000000.0
7100000000000000000000000000000000000.0
8000000000000000000000000000000000000.0
9000000000000000000000000000000000000.0
10000000000000000000000000000000000000.0
11200000000000000000000000000000000000.0
12500000000000000000000000000000000000.0
14000000000000000000000000000000000000.0
16000000000000000000000000000000000000.0
18000000000000000000000000000000000000.0
20000000000000000000000000000000000000.0
22400000000000000000000000000000000000.0
25000000000000000000000000000000000000.0
28000000000000000000000000000000000000.0
32000000000000000000000000000000000000.0
36000000000000000000000000000000000000.0
40000000000000000000000000000000000000.0
45000000000000000000000000000000000000.0
50000000000000000000000000000000000000.0
56000000000000000000000000000000000000.0
63000000000000000000000000000000000000.0
71000000000000000000000000000000000000.0
80000000000000000000000000000000000000.0
90000000000000000000000000000000000000.0
100000000000000000000000000000000000000.0
112000000000000000000000000000000000000.0
125000000000000000000000000000000000000.0
140000000000000000000000000000000000000.0
160000000000000000000000000000000000000.0
180000000000000000000000000000000000000.0
200000000000000000000000000000000000000.0
224000000000000000000000000000000000000.0
250000000000000000000000000000000000000.0
280000000000000000000000000000000000000.0
320000000000000000000000000000000000000.0
360000000000000000000000000000000000000.0
400000000000000000000000000000000000000.0
450000000000000000000000000000000000000.0
500000000000000000000000000000000000000.0
560000000000000000000000000000000000000.0
630000000000000000000000000000000000000.0
710000000000000000000000000000000000000.0
800000000000000000000000000000000000000.0
900000000000000000000000000000000000000.0
1000000000000000000000000000000000000000.0
1120000000000000000000000000000000000000.0
1250000000000000000000000000000000000000.0
1400000000000000000000000000000000000000.0
1600000000000000000000000000000000000000.0
1800000000000000000000000000000000000000.0
2000000000000000000000000000000000000000.0
2240000000000000000000000000000000000000.0
2500000000000000000000000000000000000000.0
2800000000000000000000000000000000000000.0
3200000000000000000000000000000000000000.0
3600000000000000000000000000000000000000.0
4000000000000000000000000000000000000000.0
4500000000000000000000000000000000000000.0
5000000000000000000000000000000000000000.0
5600000000000000000000000000000000000000.0
6300000000000000000000000000000000000000.0
7100000000000000000000000000000000000000.0
8000000000000000000000000000000000000000.0
9000000000000000000000000000000000000000.0
10000000000000000000000000000000000000000.0
11200000000000000000000000000000000000000.0
12500000000000000000000000000000000000000.0
14000000000000000000000000000000000000000.0
16000000000000000000000000000000000000000.0
18000000000000000000000000000000000000000.0
20000000000000000000000000000000000000000.0
22400000000000000000000000000000000000000.0
25000000000000000000000000000000000000000.0
28000000000000000000000000000000000000000.0
32000000000000000000000000000000000000000.0
36000000000000000000000000000000000000000.0
40000000000000000000000000000000000000000.0
45000000000000000000000000000000000000000.0
50000000000000000000000000000000000000000.0
56000000000000000000000000000000000000000.0
63000000000000000000000000000000000000000.0
71000000000000000000000000000000000000000.0
80000000000000000000000000000000000000000.0
90000000000000000000000000000000000000000.0
100000000000000000000000000000000000000000.0
112000000000000000000000000000000000000000.0
125000000000000000000000000000000000000000.0
140000000000000000000000000000000000000000.0
160000000000000000000000000000000000000000.0
180000000000000000000000000000000000000000.0
200000000000000000000000000000000000000000.0
224000000000000000000000000000000000000000.0
250000000000000000000000000000000000000000.0
280000000000000000000000000000000000000000.0
320000000000000000000000000000000000000000.0
360000000000000000000000000000000000000000.0
400000000000000000000000000000000000000000.0
450000000000000000000000000000000000000000.0
500000000000000000000000000000000000000000.0
560000000000000000000000000000000000000000.0
630000000000000000000000000000000000000000.0
710000000000000000000000000000000000000000.0
800000000000000000000000000000000000000000.0
900000000000000000000000000000000000000000.0
1000000000000000000000000000000000000000000.0
1120000000000000000000000000000000000000000.0
1250000000000000000000000000000000000000000.0
1400000000000000000000000000000000000000000.0
1600000000000000000000000000000000000000000.0
1800000000000000000000000000000000000000000.0
2000000000000000000000000000000000000000000.0
2240000000000000000000000000000000000000000.0
2500000000000000000000000000000000000000000.0
2800000000000000000000000000000000000000000.0
3200000000000000000000000000000000000000000.0
3600000000000000000000000000000000000000000.0
4000000000000000000000000000000000000000000.0
4500000000000000000000000000000000000000000.0
5000000000000000000000000000000000000000000.0
5600000000000000000000000000000000000000000.0
6300000000000000000000000000000000000000000.0
7100000000000000000000000000000000000000000.0
8000000000000000000000000000000000000000000.0
9000000000000000000000000000000000000000000.0
10000000000000000000000000000000000000000000.0
11200000000000000000000000000000000000000000.0
12500000000000000000000000000000000000000000.0
14000000000000000000000000000000000000000000.0
16000000000000000000000000000000000000000000.0
18000000000000000000000000000000000000000000.0
20000000000000000000000000000000000000000000.0
22400000000000000000000000000000000000000000.0
25000000000000000000000000000000000000000000.0
28000000000000000000000000000000000000000000.0
32000000000000000000000000000000000000000000.0
36000000000000000000000000000000000000000000.0
40000000000000000000000000000000000000000000.0
45000000000000000000000000000000000000000000.0
50000000000000000000000000000000000000000000.0
56000000000000000000000000000000000000000000.0
63000000000000000000000000000000000000000000.0
71000000000000000000000000000000000000000000.0
80000000000000000000000000000000000000000000.0
90000000000000000000000000000000000000000000.0
100000000000000000000000000000000000000000000.0
112000000000000000000000000000000000000000000.0
125000000000000000000000000000000000000000000.0
140000000000000000000000000000000000000000000.0
160000000000000000000000000000000000000000000.0
180000000000000000000000000000000000000000000.0
200000000000000000000000000000000000000000000.0
224000000000000000000000000000000000000000000.0
250000000000000000000000000000000000000000000.0
280000000000000000000000000000000000000000000.0
320000000000000000000000000000000000000000000.0
360000000000000000000000000000000000000000000.0
400000000000000000000000000000000000000000000.0
450000000000000000000000000000000000000000000.0
500000000000000000000000000000000000000000000.0
560000000000000000000000000000000000000000000.0
630000000000000000000000000000000000000000000.0
710000000000000000000000000000000000000000000.0
800000000000000000000000000000000000000000000.0
900000000000000000000000000000000000000000000.0
1000000000000000000000000000000000000000000000.0
1120000000000000000000000000000000000000000000.0
1250000000000000000000000000000000000000000000.0
1400000000000000000000000000000000000000000000.0
1600000000000000000000000000000000000000000000.0
1800000000000000000000000000000000000000000000.0
2000000000000000000000000000000000000000000000.0
2240000000000000000000000000000000000000000000.0
2500000000000000000000000000000000000000000000.0
2800000000000000000000000000000000000000000000.0
3200000000000000000000000000000000000000000000.0
3600000000000000000000000000000000000000000000.0
4000000000000000000000000000000000000000000000.0
4500000000000000000000000000000000000000000000.0
5000000000000000000000000000000000000000000000.0
5600000000000000000000000000000000000000000000.0
6300000000000000000000000000000000000000000000.0
7100000000000000000000000000000000000000000000.0
8000000000000000000000000000000000000000000000.0
9000000000000000000000000000000000000000000000.0
10000000000000000000000000000000000000000000000.0
11200000000000000000000000000000000000000000000.0
12500000000000000000000000000000000000000000000.0
14000000000000000000000000000000000000000000000.0
16000000000000000000000000000000000000000000000.0
18000000000000000000000000000000000000000000000.0
20000000000000000000000000000000000000000000000.0
22400000000000000000000000000000000000000000000.0
25000000000000000000000000000000000000000000000.0
28000000000000000000000000000000000000000000000.0
32000000000000000000000000000000000000000000000.0
36000000000000000000000000000000000000000000000.0
40000000000000000000000000000000000000000000000.0
45000000000000000000000000000000000000000000000.0
50000000000000000000000000000000000000000000000.0
56000000000000000000000000000000000000000000000.0
63000000000000000000000000000000000000000000000.0
71000000000000000000000000000000000000000000000.0
80000000000000000000000000000000000000000000000.0
90000000000000000000000000000000000000000000000.0
100000000000000000000000000000000000000000000000.0
112000000000000000000000000000000000000000000000.0
125000000000000000000000000000000000000000000000.0
140000000000000000000000000000000000000000000000.0
160000000000000000000000000000000000000000000000.0
180000000000000000000000000000000000000000000000.0
200000000000000000000000000000000000000000000000.0
224000000000000000000000000000000000000000000000.0
250000000000000000000000000000000000000000000000.0
280000000000000000000000000000000000000000000000.0
320000000000000000000000000000000000000000000000.0
360000000000000000000000000000000000000000000000.0
400000000000000000000000000000000000000000000000.0
450000000000000000000000000000000000000000000000.0
500000000000000000000000000000000000000000000000.0
560000000000000000000000000000000000000000000000.0
630000000000000000000000000000000000000000000000.0
710000000000000000000000000000000000000000000000.0
800000000000000000000000000000000000000000000000.0
900000000000000000000000000000000000000000000000.0
1000000000000000000000000000000000000000000000000.0
1120000000000000000000000000000000000000000000000.0
1250000000000000000000000000000000000000000000000.0
1400000000000000000000000000000000000000000000000.0
1600000000000000000000000000000000000000000000000.0
1800000000000000000000000000000000000000000000000.0
2000000000000000000000000000000000000000000000000.0
2240000000000000000000000000000000000000000000000.0
2500000000000000000000000000000000000000000000000.0
2800000000000000000000000000000000000000000000000.0
3200000000000000000000000000000000000000000000000.0
3600000000000000000000000000000000000000000000000.0
4000000000000000000000000000000000000000000000000.0
4500000000000000000000000000000000000000000000000.0
5000000000000000000000000000000000000000000000000.0
5600000000000000000000000000000000000000000000000.0
6300000000000000000000000000000000000000000000000.0
7100000000000000000000000000000000000000000000000.0
8000000000000000000000000000000000000000000000000.0
9000000000000000000000000000000000000000000000000.0
10000000000000000000000000000000000000000000000000.0
11200000000000000000000000000000000000000000000000.0
12500000000000000000000000000000000000000000000000.0
14000000000000000000000000000000000000000000000000.0
16000000000000000000000000000000000000000000000000.0
18000000000000000000000000000000000000000000000000.0
20000000000000000000000000000000000000000000000000.0
22400000000000000000000000000000000000000000000000.0
25000000000000000000000000000000000000000000000000.0
28000000000000000000000000000000000000000000000000.0
32000000000000000000000000000000000000000000000000.0
36000000000000000000000000000000000000000000000000.0
40000000000000000000000000000000000000000000000000.0
45000000000000000000000000000000000000000000000000.0
50000000000000000000000000000000000000000000000000.0
56000000000000000000000000000000000000000000000000.0
63000000000000000000000000000000000000000000000000.0
71000000000000000000000000000000000000000000000000.0
80000000000000000000000000000000000000000000000000.0
90000000000000000000000000000000000000000000000000.0
100000000000000000000000000000000000000000000000000.0
112000000000000000000000000000000000000000000000000.0
125000000000000000000000000000000000000000000000000.0
140000000000000000000000000000000000000000000000000.0
160000000000000000000000000000000000000000000000000.0
180000000000000000000000000000000000000000000000000.0
200000000000000000000000000000000000000000000000000.0
224000000000000000000000000000000000000000000000000.0
250000000000000000000000000000000000000000000000000.0
280000000000000000000000000000000000000000000000000.0
320000000000000000000000000000000000000000000000000.0
360000000000000000000000000000000000000000000000000.0
400000000000000000000000000000000000000000000000000.0
450000000000000000000000000000000000000000000000000.0
500000000000000000000000000000000000000000000000000.0
560000000000000000000000000000000000000000000000000.0
630000000000000000000000000000000000000000000000000.0
710000000000000000000000000000000000000000000000000.0
800000000000000000000000000000000000000000000000000.0
900000000000000000000000000000000000000000000000000.0
1000000000000000000000000000000000000000000000000000.0
1120000000000000000000000000000000000000000000000000.0
1250000000000000000000000000000000000000000000000000.0
1400000000000000000000000000000000000000000000000000.0
1600000000000000000000000000000000000000000000000000.0
1800000000000000000000000000000000000000000000000000.0
2000000000000000000000000000000000000000000000000000.0
2240000000000000000000000000000000000000000000000000.0
2500000000000000000000000000000000000000000000000000.0
2800000000000000000000000000000000000000000000000000.0
3200000000000000000000000000000000000000000000000000.0
3600000000000000000000000000000000000000000000000000.0
4000000000000000000000000000000000000000000000000000.0
4500000000000000000000000000000000000000000000000000.0
5000000000000000000000000000000000000000000000000000.0
5600000000000000000000000000000000000000000000000000.0
6300000000000000000000000000000000000000000000000000.0
7100000000000000000000000000000000000000000000000000.0
8000000000000000000000000000000000000000000000000000.0
9000000000000000000000000000000000000000000000000000.0
10000000000000000000000000000000000000000000000000000.0
11200000000000000000000000000000000000000000000000000.0
12500000000000000000000000000000000000000000000000000.0
14000000000000000000000000000000000000000000000000000.0
16000000000000000000000000000000000000000000000000000.0
18000000000000000000000000000000000000000000000000000.0
20000000000000000000000000000000000000000000000000000.0
22400000000000000000000000000000000000000000000000000.0
25000000000000000000000000000000000000000000000000000.0
28000000000000000000000000000000000000000000000000000.0
32000000000000000000000000000000000000000000000000000.0
36000000000000000000000000000000000000000000000000000.0
40000000000000000000000000000000000000000000000000000.0
45000000000000000000000000000000000000000000000000000.0
50000000000000000000000000000000000000000000000000000.0
56000000000000000000000000000000000000000000000000000.0
63000000000000000000000000000000000000000000000000000.0
71000000000000000000000000000000000000000000000000000.0
80000000000000000000000000000000000000000000000000000.0
90000000000000000000000000000000000000000000000000000.0
100000000000000000000000000000000000000000000000000000.0
112000000000000000000000000000000000000000000000000000.0
125000000000000000000000000000000000000000000000000000.0
140000000000000000000000000000000000000000000000000000.0
160000000000000000000000000000000000000000000000000000.0
180000000000000000000000000000000000000000000000000000.0
200000000000000000000000000000000000000000000000000000.0
224000000000000000000000000000000000000000000000000000.0
250000000000000000000000000000000000000000000000000000.0
280000000000000000000000000000000000000000000000000000.0
320000000000000000000000000000000000000000000000000000.0
360000000000000000000000000000000000000000000000000000.0
400000000000000000000000000000000000000000000000000000.0
450000000000000000000000000000000000000000000000000000.0
500000000000000000000000000000000000000000000000000000.0
560000000000000000000000000000000000000000000000000000.0
630000000000000000000000000000000000000000000000000000.0
710000000000000000000000000000000000000000000000000000.0
800000000000000000000000000000000000000000000000000000.0
900000000000000000000000000000000000000000000000000000.0
1000000000000000000000000000000000000000000000000000000.0
1120000000000000000000000000000000000000000000000000000.0
1250000000000000000000000000000000000000000000000000000.0
1400000000000000000000000000000000000000000000000000000.0
1600000000000000000000000000000000000000000000000000000.0
1800000000000000000000000000000000000000000000000000000.0
2000000000000000000000000000000000000000000000000000000.0
2240000000000000000000000000000000000000000000000000000.0
2500000000000000000000000000000000000000000000000000000.0
2800000000000000000000000000000000000000000000000000000.0
3200000000000000000000000000000000000000000000000000000.0
3600000000000000000000000000000000000000000000000000000.0
4000000000000000000000000000000000000000000000000000000.0
4500000000000000000000000000000000000000000000000000000.0
5000000000000000000000000000000000000000000000000000000.0
5600000000000000000000000000000000000000000000000000000.0
6300000000000000000000000000000000000000000000000000000.0
7100000000000000000000000000000000000000000000000000000.0
8000000000000000000000000000000000000000000000000000000.0
9000000000000000000000000000000000000000000000000000000.0
10000000000000000000000000000000000000000000000000000000.0
11200000000000000000000000000000000000000000000000000000.0
12500000000000000000000000000000000000000000000000000000.0
14000000000000000000000000000000000000000000000000000000.0
16000000000000000000000000000000000000000000000000000000.0
18000000000000000000000000000000000000000000000000000000.0
20000000000000000000000000000000000000000000000000000000.0
22400000000000000000000000000000000000000000000000000000.0
25000000000000000000000000000000000000000000000000000000.0
28000000000000000000000000000000000000000000000000000000.0
32000000000000000000000000000000000000000000000000000000.0
36000000000000000000000000000000000000000000000000000000.0
40000000000000000000000000000000000000000000000000000000.0
45000000000000000000000000000000000000000000000000000000.0
50000000000000000000000000000000000000000000000000000000.0
56000000000000000000000000000000000000000000000000000000.0
63000000000000000000000000000000000000000000000000000000.0
71000000000000000000000000000000000000000000000000000000.0
80000000000000000000000000000000000000000000000000000000.0
90000000000000000000000000000000000000000000000000000000.0
100000000000000000000000000000000000000000000000000000000.0
112000000000000000000000000000000000000000000000000000000.0
125000000000000000000000000000000000000000000000000000000.0
140000000000000000000000000000000000000000000000000000000.0
160000000000000000000000000000000000000000000000000000000.0
180000000000000000000000000000000000000000000000000000000.0
200000000000000000000000000000000000000000000000000000000.0
224000000000000000000000000000000000000000000000000000000.0
250000000000000000000000000000000000000000000000000000000.0
280000000000000000000000000000000000000000000000000000000.0
320000000000000000000000000000000000000000000000000000000.0
360000000000000000000000000000000000000000000000000000000.0
400000000000000000000000000000000000000000000000000000000.0
450000000000000000000000000000000000000000000000000000000.0
500000000000000000000000000000000000000000000000000000000.0
560000000000000000000000000000000000000000000000000000000.0
630000000000000000000000000000000000000000000000000000000.0
710000000000000000000000000000000000000000000000000000000.0
800000000000000000000000000000000000000000000000000000000.0
900000000000000000000000000000000000000000000000000000000.0
1000000000000000000000000000000000000000000000000000000000.0
1120000000000000000000000000000000000000000000000000000000.0
1250000000000000000000000000000000000000000000000000000000.0
1400000000000000000000000000000000000000000000000000000000.0
1600000000000000000000000000000000000000000000000000000000.0
1800000000000000000000000000000000000000000000000000000000.0
2000000000000000000000000000000000000000000000000000000000.0
2240000000000000000000000000000000000000000000000000000000.0
2500000000000000000000000000000000000000000000000000000000.0
2800000000000000000000000000000000000000000000000000000000.0
3200000000000000000000000000000000000000000000000000000000.0
3600000000000000000000000000000000000000000000000000000000.0
4000000000000000000000000000000000000000000000000000000000.0
4500000000000000000000000000000000000000000000000000000000.0
5000000000000000000000000000000000000000000000000000000000.0
5600000000000000000000000000000000000000000000000000000000.0
6300000000000000000000000000000000000000000000000000000000.0
7100000000000000000000000000000000000000000000000000000000.0
8000000000000000000000000000000000000000000000000000000000.0
9000000000000000000000000000000000000000000000000000000000.0
10000000000000000000000000000000000000000000000000000000000.0
11200000000000000000000000000000000000000000000000000000000.0
12500000000000000000000000000000000000000000000000000000000.0
14000000000000000000000000000000000000000000000000000000000.0
16000000000000000000000000000000000000000000000000000000000.0
18000000000000000000000000000000000000000000000000000000000.0
20000000000000000000000000000000000000000000000000000000000.0
22400000000000000000000000000000000000000000000000000000000.0
25000000000000000000000000000000000000000000000000000000000.0
28000000000000000000000000000000000000000000000000000000000.0
32000000000000000000000000000000000000000000000000000000000.0
36000000000000000000000000000000000000000000000000000000000.0
40000000000000000000000000000000000000000000000000000000000.0
45000000000000000000000000000000000000000000000000000000000.0
50000000000000000000000000000000000000000000000000000000000.0
56000000000000000000000000000000000000000000000000000000000.0
63000000000000000000000000000000000000000000000000000000000.0
71000000000000000000000000000000000000000000000000000000000.0
80000000000000000000000000000000000000000000000000000000000.0
90000000000000000000000000000000000000000000000000000000000.0
100000000000000000000000000000000000000000000000000000000000.0
112000000000000000000000000000000000000000000000000000000000.0
125000000000000000000000000000000000000000000000000000000000.0
140000000000000000000000000000000000000000000000000000000000.0
160000000000000000000000000000000000000000000000000000000000.0
180000000000000000000000000000000000000000000000000000000000.0
200000000000000000000000000000000000000000000000000000000000.0
224000000000000000000000000000000000000000000000